Design and Fabrication of an Autothermal Ultra-compact Membrane Reformer

Zur Erlangung des akademischen Grades eines
DOKTORS DER INGENIEURWISSENSCHAFTEN (DR.-ING.)

von der KIT-Fakultät für Chemieingenieurwesen und Verfahrenstechnik des
Karlsruher Instituts für Technologie (KIT)
genehmigte

DISSERTATION

von
M.Sc. Masoud Mahmoudizadeh
aus Dezful, Iran

Tag der mündlichen Prüfung:	11.09.2025
Erstgutachter:	Prof. Dr.-Ing. Roland Dittmeyer
Zweitgutachter:	Prof. Dr.-Ing. Gregor Wehinger

"The important thing is not to stop questioning. Curiosity has its own reason for existing. One cannot help but be in awe when he contemplates the mysteries of eternity, of life, of the marvelous structure of reality. It is enough if one tries merely to comprehend a little of this mystery every day."

-Albert Einstein

Abstract

As global energy demands increase and concerns about environmental sustainability intensify, the need for cleaner, more efficient energy technologies has become critical. Hydrogen, often seen as a key energy carrier for the future, holds great potential for decarbonizing various industrial sectors. However, producing hydrogen efficiently and sustainably remains a challenge. Among the existing methods, natural gas steam reforming is notable for its scalability, but its high energy consumption and associated CO_2 emissions call for innovation. This thesis presents a novel design for an autothermal membrane reformer system based on palladium membranes for hydrogen separation. The system integrates heat provided by catalytic combustion reaction in an ultra-compact planar design, offering a more efficient and environmentally friendly solution for hydrogen production. The hydrogen generated through methane steam reforming is separated in situ via the Pd membrane, providing highly pure hydrogen streams or hydrogen-nitrogen mixed streams for decentralized applications. The system's ultra-compact design operates under moderate conditions, with lower temperatures, faster reaction kinetics for natural gas conversion, and reduced installation requirements for heating and downstream separation processes.

The reformer's design maximizes catalyst and membrane surface area to volume ratio, leveraging advanced fabrication techniques aimed at reducing production costs and maintenance needs. The autothermal membrane reformer developed in this work produces a hydrogen-dilute stream in nitrogen, specifically designed for decentralized applications. The heat required for the methane steam reforming is supplied by catalytic combustion modules.

In this research, two novel metal-based catalysts with minimal loading on alumina supports were synthesized using a fast and precise technique, suitable for larger-scale powder production. These catalysts were applied using a screen-printing method, which ensures fast, reproducible coating of catalyst layers for microreactor technology. Catalyst coating parameters were optimized to achieve uniform 10 μm layers per print. Additionally, two plasma spraying techniques were evaluated to integrate Pd membranes into the reactor. However, challenges arose in producing dense Pd layers and during reactor assembly. To address these issues, thin commercial Pd foils were incorporated into the membrane reactor using laser welding. Results indicated that self-supported thin foils (5-12 μm) were prone to damage during the assembly of larger plates.

To overcome these challenges, further optimization of the reactor design was conducted using additive manufacturing with superalloy Crofer 22 APU, marking the first application of this material in such systems. Parameter optimization was performed for both dense and permeable parts using laser-based powder bed fusion of metals. This technique enabled the creation of complex structures for the ultra-compact membrane reactor, reducing the number of plates needed for assembly and thereby easing the scale-up process. Additionally, a detailed 2D model was developed to evaluate membrane reactors performance under conditions not tested experimentally. Based on simulation results, further novel designs were proposed for improved catalyst and fuel distribution, enhancing the temperature uniformity, a critical factor for preventing damage in prototype-scale membrane reactors.

Kurzfassung

Angesichts des weltweit steigenden Energiebedarfs und wachsender Sorgen um ökologische Nachhaltigkeit wird die Entwicklung sauberer und effizienter Energietechnologien zunehmend dringlicher. Wasserstoff, oft als zentraler Energieträger der Zukunft betrachtet, birgt großes Potenzial zur Dekarbonisierung verschiedener Industriesektoren. Allerdings bleibt die effiziente und nachhaltige Produktion von Wasserstoff eine Herausforderung. Unter den bestehenden Methoden zeichnet sich die Dampfreformierung von Erdgas durch ihre Skalierbarkeit aus, doch ihr hoher Energieverbrauch und die damit verbundenen CO_2-Emissionen erfordern Innovation. Diese Arbeit präsentiert ein neuartiges Design für ein autothermes Membranreformersystem auf Basis von Palladiummembranen zur Wasserstofftrennung. Das System integriert die durch katalytische Verbrennungsreaktion bereitgestellte Wärme in einem ultra-kompakten planaren Design und bietet damit eine effizientere und umweltfreundlichere Lösung für die Wasserstoffproduktion. Der durch Methandampfreformierung erzeugte Wasserstoff wird in situ über die Pd-Membran abgetrennt, wodurch hochreine Wasserstoffströme oder Wasserstoff-Stickstoff-Gemische für dezentrale Anwendungen bereitgestellt werden. Durch den kompakten Aufbau arbeitet das System unter moderaten Bedingungen mit vergleichsweise niedrigen Temperaturen, beschleunigter Reaktionskinetik bei der Erdgaskonversion sowie geringeren Anforderungen an Heiz- und nachgeschaltete Trennprozesse.

Das Reformerdesign nutzt moderne Fertigungsverfahren zur Maximierung der spezifischen Katalysator- und Membranoberflächen und zielt dabei auf eine kosteneffiziente, wartungsarme Systemarchitektur ab Der in dieser Arbeit entwickelte autotherme Membranreformer erzeugt einen wasserstoffverdünnten Stickstoffstrom und wurde speziell für den dezentralen Einsatz konzipiert Die für die

Methandampfreformierung erforderliche Wärme wird durch katalytische Verbrennungsmodule bereitgestellt.

Zwei neuartige, metallbasierte Katalysatoren mit niedriger Metallbeladung wurden im Rahmen dieser Arbeit auf Aluminiumoxidträgern synthetisiert. Zum Einsatz kam ein präzises, zeiteffizientes Verfahren, das sich für eine skalierbare Pulverproduktion im industriellen Maßstab eignet. Diese Katalysatoren wurden mittels Siebdruck aufgetragen, was eine schnelle und reproduzierbare Beschichtung von Katalysatorschichten für die Mikroreaktortechnologie gewährleistet. Die Parameter der Katalysatorbeschichtung wurden optimiert, um gleichmäßige 10 μm dicke Schichten pro Druckvorgang zu erreichen. Zusätzlich wurden zwei Plasmaspritzverfahren zur Integration von Pd-Membranen in den Reaktor evaluiert.

Die Herstellung dichter Pd-Schichten sowie die Assemblierung des Reaktors erwiesen sich jedoch als herausfordernd. Um diese Probleme zu lösen, wurden dünne kommerzielle Pd-Folien mittels Laserschweißen in den Membranreaktor integriert. Die Ergebnisse zeigten, dass selbsttragende Dünnfolien mit Dicken von 5–12 μm bei der Montage größerer Platten eine erhöhte Anfälligkeit für Beschädigungen aufwiesen. Zur Überwindung dieser Herausforderungen wurde das Reaktordesign mittels additiver Fertigung mit der Superlegierung Crofer 22 APU weiter optimiert. Es handelt sich dabei um die erste bekannte Anwendung dieses Materials in einem derartigen System. Die Parameteroptimierung erfolgte sowohl für dichte als auch permeable Bauteile mittels laserbasierter Pulverbettfusion von Metallen. Diese Technik ermöglichte die Herstellung komplexer Strukturen für den ultra-kompakten Membranreaktor, verringerte die Anzahl der benötigten Montageplatten und erleichterte so die Hochskalierung. Zusätzlich wurde ein detailliertes zweidimensionales Modell erstellt, das eine Bewertung der Membranreaktorleistung unter nicht experimentell erfassten Bedingungen ermöglicht. Auf Grundlage der Simulationsergebnisse wurden neue Designkonzepte entwickelt, die eine verbesserte Katalysator- und Brennstoffverteilung sowie eine höhere Temperaturhomogenität ermöglichen. Letztere ist entscheidend zur Vermeidung von Schäden in prototypischen Membranreaktoren.

Preface

This thesis is submitted in partial fulfillment of the requirements for the PhD degree at the Karlsruhe Institute of Technology (KIT). The research presented here was conducted at the Institute of Micro Process Engineering (IMVT), with the support of Arbeitsgemeinschaft industrieller Forschungsvereinigungen Otto von Guericke e.V. (AiF) under the agreement, ZF4591901ZG8.

I would like to express my deepest gratitude to my supervisor, Prof. Dr.-Ing. habil. Roland Dittmeyer, for establishing the framework of this project, encouraging alternative approaches, and providing invaluable insights and feedback across various areas of expertise throughout this work. I am also profoundly grateful to Dr. -Ing. Michael Rubin, my group leader, Prof. Dr. -Ing. Christoph Klahn, and Dr. Thomas Gietzelt, for their extensive guidance, which ranged from applied practical experience to detailed theoretical knowledge.

My heartfelt thanks go to all my colleagues at IMVT, whose collaborative and supportive environment made this journey rewarding. Their willingness to discuss complex results and assist with experimental challenges was invaluable.

Finally, I would like to thank my family and friends for their patience and understanding as they endured my enthusiastic explanations of obscure details, which, at the time, seemed of utmost importance (at least to me). I dedicate this work to Shadi, who not only endured these moments but often showed genuine interest, always offering unwavering support.

Contents

Abstract iii

Kurzfassung v

Preface vii

Acronyms and symbols xv

1 Introduction 1

2 Hydrogen production from natural gas and basics of methane steam reforming 3
2.1 Hydrogen production technologies from raw materials 3
2.2 Basics of catalytic methane steam reforming to produce hydrogen . 7

3 Decentralized hydrogen production methodology 11
3.1 Small-scale reformer units 12
3.2 Hydrogen separation techniques 13
3.2.1 Hydrogen selective membranes 13
3.3 Exploring the industrial advancements in the research and development of Pd-based membranes 26
3.3.1 Energy Research Center (ECN) 27
3.3.2 SINTEF Industries 27
3.3.3 NORAM/MRT/UBC 27
3.3.4 REB Research & Consulting Co. 28
3.3.5 TECNALIA 28
3.3.6 CACHET 28
3.3.7 CoMETHy 30

3.3.8 Micro-CHP . . . 33
3.3.9 Pilot plants . . . 37
3.4 Tubular membrane reactor development by IMVT-KIT, Linde engineering, and Plansee SE . . . 40
3.5 State of the art in ultra-compact planar membrane reformers . . . 41
3.6 Aim of this thesis . . . 47

4 Synthesis, preparation, assembly, and testing of Palladium-based membranes . . . 49
4.1 Membrane concept based on the tape-casted supports . . . 49
4.2 Experimental set-up for gas tests . . . 52
4.3 Plasma spraying coating . . . 54
4.3.1 Motivation . . . 54
4.3.2 Plasma spraying experiments . . . 56
4.3.3 Palladium powders . . . 58
4.3.4 Results of coated layers with SPS and VPS . . . 59
4.3.5 Gas test results of APS and VPS . . . 63
4.3.6 Concluding remarks on plasma spraying coating method for synthesis of Pd-composite membranes . . . 67
4.4 Foil-based membrane integration and assembly . . . 68
4.4.1 Assembly and sealing of Pd foils into the membrane module by laser welding . . . 69
4.4.2 Preparation of the Pd test modules for gas test . . . 73
4.4.3 Gas permeation test . . . 76
4.4.4 After test characterisation . . . 78
4.5 Summary and conclusion . . . 80

5 Catalyst preparation and testing for methane steam reforming and methane gas combustion . . . 81
5.1 Literature review . . . 81
5.1.1 MSR reaction mechanism and kinetics . . . 81
5.2 Catalyst synthesis . . . 83
5.3 Catalyst characterization in powder form . . . 86
5.3.1 Characteristics related to morphology and structure of catalyst for MSR . . . 86

5.3.2 Characteristics related to morphology and structure of catalyst for CCR . . . 89
5.3.3 Pore characteristics of synthesized catalysts powder for CCR and MSR . . . 93
5.4 Catalyst coating methodology . . . 94
5.5 Catalyst characterisation of the coated catalyst layers . . . 99
5.6 Experimental set-up and gas chromatography for gas test of catalysts used in MSR and CCR . . . 103
5.6.1 Test rig . . . 103
5.6.2 Gas chromatography . . . 103
5.6.3 Microstructured reactor . . . 105
5.7 Definitions . . . 106
5.8 Activity tests . . . 107
5.9 Summary and conclusion . . . 111

6 Prototype autothermal membrane reformer . . . 113
6.1 Design of the μ-EnH_2ancer V 3.0 . . . 114
6.2 Test set-up and operating conditions and definitions . . . 116
6.3 Reactor assembly . . . 118
6.4 Methane steam reforming reaction in μ-EnH_2ancer V 3.0 . . . 120
6.5 Combustion Reactor . . . 124
6.5.1 Effect of using Air distribution plate in μ-EnH_2ancer V 3.0 . . . 127
6.6 Membrane reformer . . . 132
6.6.1 Mathematical formula . . . 132
6.6.2 Autothermal modeling . . . 142
6.6.3 Model Validation; comparison of the results of 2D simulation with results of MicroEnhancer V 1.0 . . . 144
6.7 Characteristic timescales . . . 147
6.8 Results of non-isothermal simulation of MR . . . 149
6.9 Optimization of MR with advanced manufacturing techniques . . . 164
6.10 Summary and conclusion . . . 169

7 Additive manufacturing . . . 171
7.1 State of the art of the porous Crofer membrane supports . . . 171

7.2 Additive manufactured permeable structures . . . 172
7.3 Additive manufacturing of Crofer 22 APU for dense/permeable composite parts . . . 175
7.3.1 Characterization of dense parts . . . 177
7.3.2 Characterization of permeable parts . . . 181
7.4 Surface preparation for coating of active thin layers . . . 186
7.4.1 Microstructure of Crofer 22 APU before and after heat treatment . . . 186
7.4.2 Screen Printing Coating . . . 188
7.5 Results of additive manufactured permeable structures . . . 189
7.5.1 Results of coated porous parts . . . 189
7.5.2 Integration of AM parts into a MR system . . . 193
7.5.3 Using permeable parts for mixing air-fuel in microreactors . 195
7.6 Summary and conclusion . . . 198

8 Summary and outlook . . . 199
8.1 Summary . . . 199
8.2 Outlook . . . 201

A Appendix . . . 203
A.1 Equilibrium composition calculation . . . 203
A.2 Membrane . . . 205
A.3 Catalyst characterization techniques and test reactor sketch . . . 207
A.3.1 Electron Probe Microanalyzer . . . 207
A.3.2 Transmission Electron Microscopy . . . 207
A.3.3 Physi- and Chemisorption . . . 208
A.3.4 Rheometry . . . 210
A.3.5 Profilometer . . . 211
A.3.6 Inductively coupled plasma atomic emission spectroscopy . . 211
A.3.7 X-ray diffraction . . . 211
A.3.8 Test reactor sketch . . . 213
A.4 Autothermal membrane reformer . . . 214
A.5 Additive manufacturing . . . 217

List of Figures . . . 223

List of Tables **235**

List of Publications **239**
Journal articles 239
Conference talks 240
Book chapter 240
Patent application 240
Master thesis 241
Other publications 241
Permissions 241

Bibliography **243**

Acronyms and symbols

Acronyms

AM	Additive Manufacturing
APS	Atmospheric Plasma Spraying
ASU	Air Separation Process
ATR	Autothermal Reforming
BCC	Body-centered Cubic
BET	Brunauer-Emmett-Teller
CCM	Catalytic Combustion of Methane
CCR	Catalytic Combustion Reaction
CW	Continuous Wave
DBL	Diffusion Barrier Layer
DC	Direct Current
DLR	Deutsches Zentrum für Luft- und Raumfahrt
ECN	Energy Research Center
EDX	Energy-dispersive X-ray
EDS	Energy Dispersive Spectroscopy
ELP	Electroless Plating
FBMR	Fluidized Bed Membrane Reactor
FCC	Face-centered Cubic
FID	Flame Ionization Detector
FSP	Flame Spray Pyrolysis
FTT	Fast Fourier Transformation
GC	Gas Chromatography
H_2	Hydrogen

HAADF-STEM	High-angle Annular Dark-field Scanning TEM
HAGB	High-angle Grain Boundaries
HRTEM	High resolution TEM
HVOF	High Velocity Oxy-Fuel
ICP	Inductively Coupled Plasma
ICP-OES	ICP Optical Emission spectroscopy
IMVT	Institute for Microprocess Technology
KIT	Karlsruher Institute for Technology
LAGB	Low-angle Grain Boundaries
micro-CHP	Micro-combined Heat and Power
MMR	Microstructured Membrane Reactor
MR	Membrane Reactor
MSR	Methane Steam Reforming
NG	Natural Gas
NGCC	Natural Gas Combined Cycle
OPEX	Operational Costs
PBMR	Packed Bed Membrane Reactor
POX	Partial Oxidation of Methane
PrOX	Preferential Oxidation
PSA	Pressure Swing Adsorption
PSS	Porous Stainless Steel
PTFE	Polytetrafluoroethylene
PVD-MS	Physical Vapor Deposition Magnetron Sputtering
SADP	Selected Area Diffraction Patterns
S/C	Steam to Carbon ratio
SLM	Selective Laser Melting
SOEC	Solid Oxide Electrolytic Cells
SOFC	Solid Oxide Fuel Cells
SP	Screen Printing
SPS	Suspension Plasma Spraying
STEM	Scanning TEM
TEM	Transmission Electron Microscopy
TCD	Thermal Conductivity Detector

TOF	Turnover Frequencies
TPR	Temperature-programmed Reduction
VPS	Vacuum Plasma Spraying
WGS	Water Gas Shift
XRD	X-ray Diffraction
YSZ	Yttria-stabilized Zirconia

Constants

π	Pi: 3.141 59	-
R	Universal gas constant	$\mathrm{J\,mol^{-1}\,K^{-1}}$

Latin symbols and variables

a_S	Layer thickness	m
C	Concentration	$\mathrm{mol\,m^{-3}}$
C_p	Heat capacity	$\mathrm{J\,kg^{-1}\,K^{-1}}$
D	Diffusion coefficient	$\mathrm{m^2\,s^{-1}}$
Da	Damköhler number	-
d	Diameter	m
E	Activation energy	$\mathrm{J\,mol^{-1}}$
H	Enthalpy	$\mathrm{J\,mol^{-1}}$
H	Height	m
J	Flux	$\mathrm{mol\,m^{-2}\,s^{-1}}$
K	Thermodynamic constant	-
k	Kinetics coefficient	-
L	Length	m
L_c	Laser current	A
M	Molecular weight	$\mathrm{kg\,mol^{-1}}$
N	Channel number	-
n	Mole number	mol
P	Pressure	Pa
P_D	Point distance	m

Pe	Permeation number	-
P_L	Laser power	W
Q	Reaction heat	$\mathrm{J\,m^{-3}}$
R	Reaction rate	$\mathrm{kg\,m^{-3}\,s^{-1}}$
r	Reaction rate	$\mathrm{mol\,m^{-3}\,s^{-1}}$
S	Selectivity	-
S	Solubility	-
t	Time	s
T	Temperature	K
W	Width	m
X	Conversion	-
x	x-axis coordinate	m
y	y-axis coordinate	m
ν	Velocity	$\mathrm{m\,s^{-1}}$
ν_S	Scan speed	$\mathrm{m\,s^{-1}}$
h_S	Hatch distance	m

Greek symbols and variables

α	Building angle for AM	-
α	Thermal expansion coefficient	$\mathrm{K^{-1}}$
Δ	Difference	-
δ	Thickness	m
ϵ	Porosity	-
κ	Thermal conductivity	$\mathrm{W\,m^{-1}\,K^{-1}}$
λ	Mean free path	m
λ	Thermal conductivity	$\mathrm{W\,m^{-1}\,K^{-1}}$
λ	Wavelength	m
μ	Viscosity	$\mathrm{Pa\,s}$
ν	Velocity	$\mathrm{m\,s^{-1}}$
Ω	Kinetics parameter	-
Φ	Permeability	$\mathrm{mol\,m^{-2}\,s^{-1}\,Pa^{-0.5}}$
ρ	Density	$\mathrm{kg\,m^{-3}}$

τ	Time scale coefficient	-
τ	Tortuosity	-

Indices

abs	Absolute
cat	Catalyst
c	Critical
chem	Chemisorption
eff	Effective
ext	External
gas	Gas phase
ht	Heat transfer
i	Component index
in	Inlet
int	Internal
j	Reaction index
k	Knudsen
m	Mixture
out	Outlet
p	Particle
p	Pore
re	Reaction

1 Introduction

Hydrogen, the most abundant element in the universe, is a clean and non-toxic resource that was discovered almost three hundred years ago. While it is not a primary energy source, it serves as an energy carrier. Several aspects of hydrogen make it an attractive option for facilitating the shift to renewable energy [1]. There are diverse methods for H_2 production, broadly categorized into conventional and renewable technologies based on the raw materials and energy utilized. The first category is defined by conventional technologies which rely on fossil fuels and include methods such as hydrocarbon reforming and pyrolysis. The second category is based on biomass or water and renewable electrical energy. The former converts the biomass materials into hydrogen-rich gases through various processes like gasification or fermentation. The water-based production utilizes water electrolysis, solar-driven water splitting, or biological processes to generate hydrogen from water molecules [2].

Hydrogen is categorized into different colors based on its production technique. For example, the green hydrogen is produced using renewable energy sources like wind or solar power, while blue hydrogen is generated from natural gas with carbon capture and storage technology. Grey hydrogen is produced from fossil fuels without any capture step, leading to significant CO_2 emissions. Turquoise hydrogen is created through methane pyrolysis, resulting in solid carbon as a byproduct. Pink hydrogen is produced using nuclear energy, brown hydrogen is generated from coal gasification, which emits high levels of CO_2, and white hydrogen refers to naturally occurring hydrogen found in geological formations [3]. In various industries, especially the chemical and refining sectors, hydrogen finds extensive use in the production of valuable chemicals like ammonia and methanol, as well as in processes like hydrotreating within refineries [4]. To meet economic demands,

it is essential to separate and purify hydrogen. Current technologies employed for this purpose include wet scrubbing, dry scrubbing, pressure swing adsorption, membrane separation, and cryogenic distillation [5]. Membrane reactor technology combines steam reforming with hydrogen separation and membrane-based purification processes in a single device. In essence, a membrane selectively separates hydrogen through permeation while retaining other chemical components from the reaction system. The selectivity of this process largely depends on the membrane material used. This technology stands out due to its flexibility in operation, simplicity, energy efficiency, compactness, small footprint, environmental friendliness, and ease of integration with established industrial processes [6].

Unlike traditional reactors, a membrane reactor is not constrained by the reaction equilibrium. More specifically, the selective permeability of the membrane helps shift the thermodynamic equilibrium in favor of the desired product [7]. Various types of membrane reactors, such as Fluidized Bed Membrane Reactors (FBMRs), Micro-structured Membrane Reactors (MMRs), and Packed Bed Membrane Reactors (PBMRs) have been extensively studied and reported in the literature, with the majority of studies focusing on PBMRs [8–11]. However, it is essential to consider heat and mass transport aspects in these reactors. For instance, the presence of localized hot spots could potentially harm the membrane in a PBMR. Furthermore, in MMRs or FBMRs, it is theoretically possible to achieve the maximum permeability by mitigating the impact of mass transfer limitations [12–15].

2 Hydrogen production from natural gas and basics of methane steam reforming

2.1 Hydrogen production technologies from raw materials

Methane, with the highest hydrogen-to-carbon (H/C) ratio among feedstocks, has made natural gas the primary choice for hydrogen production. Over the years, various technologies have been developed and commercialized based on methane, including methane steam reforming (MSR), autothermal reforming (ATR), and partial oxidation of methane (POX). Of these, MSR is the most established and widely used. Recently, emerging technologies like dry reforming and methane decomposition have been explored, with the latter offering the added benefit of producing solid carbon as a valuable byproduct. However, these newer methods have yet to achieve commercial viability.

In the MSR process, natural gas is initially purified, typically through hydrodesulfurization, where sulfur compounds are transformed into H_2S and removed using a ZnO bed. The gas is then combined with steam at a steam-to-carbon (S/C) ratio of 2.5–3 to avoid carbon deposition on the catalyst. In some cases, the gas is pre-reformed over a Ni-based catalyst to remove heavier hydrocarbons. The gas mixture is then sent to a gas-fired steam reformer, where methane is converted into syngas (CO and H_2) over a Ni catalyst at high temperatures (850–920 °C) and pressures of 25–35 bar [16].

Several reformer configurations are commercially available. For instance, KT Kinetics Technology offers top-fired tubular reformers with ceiling-mounted burners that heat the catalyst-filled tubes [17]. Other suppliers like $CB\&I$ use similar designs [18]. Companies such as Haldor-Topsøe [19] provide side-fired reformers for more even temperature distribution, while others like Amec Foster Wheeler offer terrace wall furnaces, where furnaces are positioned at various levels within the reactor for better heat flux distribution.

After reforming, the syngas is cooled in a process gas boiler, producing steam that can be used to maintain the S/C ratio or for export. To enhance the hydrogen yield and carbon conversion, a water-gas shift (WGS) reaction is integrated into the MSR process. The configuration of the WGS section varies based on the technology provider and intended hydrogen application. For example, Haldor-Topsøe uses a single adiabatic WGS reactor operating at intermediate temperatures for optimal efficiency and heat integration, while other suppliers implement a two-stage WGS system. This approach includes a high-temperature WGS reactor, typically using a Fe-Cr catalyst at 320–350 $^{\circ}\mathrm{C}$ to accelerate the reaction, followed by a low-temperature reactor filled with Cu-Zn catalysts operating around 200 $^{\circ}\mathrm{C}$ to drive carbon monoxide conversion [20, 21].

The hydrogen-rich gas mixture is cooled down to ambient temperature, allowing the vapor to condense, and then directed to a pressure swing adsorption (PSA) unit. In the PSA, about 85–90% of the hydrogen is recovered with a purity exceeding 99.999%. This purified hydrogen is compressed to the required delivery conditions, with a small fraction recycled back into the process for the hydrodesulfurization step.

The remaining exhaust gas from the PSA is sent to the incinerator, mixed with fuel, and burned. The flue gases produced in the radiant section pass through the convective heat recovery area and are eventually released via a common stack. In top-fired reformers, the heat recovery section is located at the bottom of the reformer, while in other configurations, it may be installed in the upper part. The heat from the flue gas is used to preheat process streams and to generate high- and

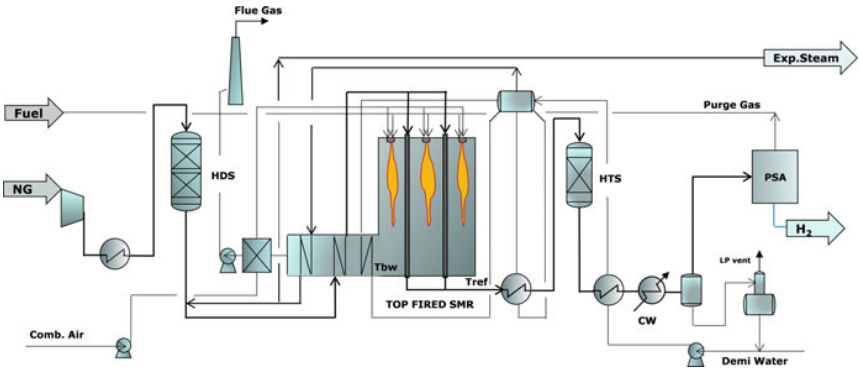

Figure 2.1: Schematic illustration of the methane steam reforming process, used with permission from Springer [16].

medium-pressure steam. A schematic of the MSR process can be found in Figure 2.1.

This technology has been well-established for decades, offering limited potential for further technological advancements or cost reductions. As a result, it is expected to remain the dominant method of grey hydrogen production worldwide for many years to come. Other prominent technologies in the market include ATR and POX. In ATR, sub-stoichiometric amounts of oxygen (either pure oxygen or atmospheric oxygen) are introduced into a burner at the top of the reformer, along with methane and steam. In this thermal section, oxygen reacts with a portion of the methane, generating the heat required for the catalytic reforming that occurs in the subsequent section. The resulting hot gas from the thermal section passes through a fixed bed containing reforming catalysts. Unlike MSR, where catalysts are distributed among several tubular reformers, ATR houses the entire catalyst in a single unit.

This technology simplifies the process and lowers operational costs (OPEX) due to its reduced S/C ratio (S/C $\approx$ 0.6–1), though the cost of oxygen must be factored into OPEX as well. However, the presence of oxygen reduces hydrogen selectivity, resulting in a lower H_2/CO ratio in the syngas and consequently lower reforming efficiency compared to MSR. Despite this, the highly integrated heat management

in ATR allows for a smaller equipment footprint, making it a widely adopted technology today. The primary disadvantage of ATR is the necessity for nearly pure oxygen, which is produced through an expensive cryogenic air separation process (ASU).

Table 2.1: Overview of key benefits and drawbacks of major hydrogen production technologies available in the market [16].

Technology	Strengths	Weaknesses
Natural gas as a feedstock		
MSR	• Well-established process • High energy efficiency based on LHV • Generates high H_2/CO ratio • Cost-effective method for hydrogen production	• Significant CO_2 emissions • High energy demand due to endothermic reactions • Requires external heat supply
ATR	• No external heat needed • Minimal methane slip • Compact design of the reactor	• Lower hydrogen yield compared to other methods • Requires ASU for oxygen supply
POX	• Negligible methane slip • No catalyst needed for the reaction • Compact reactor size • Flexible feedstock options	• Requires ASU • Low H_2/CO ratio • Difficult to regulate the reaction
Coal gasification	• High operational efficiency • Established technology	• Needs syngas purification • Produces high CO_2 emissions
Oil as a feedstock	• Hydrogen as a by-product • Simplified gas purification process	• High CO_2 output • Limited hydrogen production capacity
Biomass gasification	• Uses renewable resources • Substantially lower greenhouse gas emissions • Existing coal gasification plants can be modernized	• Lower efficiency compared to coal gasification • Requires preparation of raw materials • Limited operation under high pressure
Water splitting	• Environmentally friendly if powered by renewable energy • Hydrogen can be stored as an energy carrier • Produces high-purity hydrogen	• High electricity demand • Higher costs compared to natural gas reforming

There are other technologies to produce hydrogen from raw materials like coal, oil or biomass as well as by water electrolysis. The choice of technology for hydrogen production is influenced by several factors, including the cost and availability of the

energy source, the capacity for hydrogen production, and the purity of hydrogen. Regardless of these considerations, each of the technologies discussed in the previous section has distinct advantages and disadvantages that must be considered when selecting the most suitable option. These attributes are summarized in Table 2.1.

2.2 Basics of catalytic methane steam reforming to produce hydrogen

The initial documentation of the steam and methane catalytic reaction (MSR) dates back to 1924, as reported by Neumann and Jacob [22]. It was subsequently incorporated into industrial processes by 1930 [23]. Over the years, substantial advancements have been made in reactor design, sizing, thermodynamics, and catalysis associated with this process. Recent attention has focused on environmental considerations related to MSR, particularly due to the generation of CO_2 through the water-gas shift reaction. There is potential for separating and utilizing the produced CO_2 in various applications [24–26], or alternatively, it can be stored and sequestered geologically to mitigate carbon levels in the biosphere.

The MSR process involves the endothermic reaction outlined in Equation 2.1. Simultaneously, the excess water oxidizes CO in the system through the water-gas shift reaction, as depicted in Equation 2.2. In addition to these primary reactions, numerous side reactions, such as syngas formation and carbon-related processes like methane cracking and CO disproportionation, contribute to the complexity of MSR [27]. According to the literature, H_2 and CO_2 are also produced directly through CH_4 and H_2O as shown in 2.3 [28, 29].

$$\mathrm{CH_4 + H_2O \rightleftharpoons CO + 3\,H_2} \quad \Delta H^{\circ}_{298\ \mathrm{K}} = +206\ \mathrm{kJ/mol} \tag{2.1}$$

$$\mathrm{CO + H_2O \rightleftharpoons CO_2 + H_2} \quad \Delta H^{\circ}_{298\ \mathrm{K}} = -41\ \mathrm{kJ/mol} \tag{2.2}$$

$$\mathrm{CH_4} + 2\,\mathrm{H_2O} \rightleftharpoons \mathrm{CO_2} + 4\,\mathrm{H_2} \quad \Delta H^{\circ}_{298\ \mathrm{K}} = +165\ \mathrm{kJ/mol} \tag{2.3}$$

A thermodynamic analysis of the reaction system was conducted according to the description and formulation in Appendix A.1. The equilibrium constants for reactions 2.1, 2.2, and 2.3 were taken from the literature [30, 31], and the species involved were included in the calculations of the equilibrium concentrations. Figure 2.2 illustrates the logarithm of the thermodynamic equilibrium constants as a function of temperature for reactions 2.1, 2.2, and 2.3. It is observed that the endothermic reforming reactions are favored thermodynamically at elevated temperatures, whereas the exothermic WGS reaction is more favorable at lower temperatures.

The relevance of the two reactions that lead to carbon formation, specifically the Boudouard reaction (2.4) and the endothermic methane decomposition (2.5) depends on the steam-to-carbon (S/C) ratio.

$$2\,\mathrm{CO} \rightleftharpoons \mathrm{CO_2} + \mathrm{C} \quad \Delta H^{\circ}_{298\ \mathrm{K}} = -172\ \mathrm{kJ/mol} \tag{2.4}$$

$$\mathrm{CH_4} \rightleftharpoons 2\,\mathrm{H_2} + \mathrm{C} \quad \Delta H^{\circ}_{298\ \mathrm{K}} = +75\ \mathrm{kJ/mol} \tag{2.5}$$

Figure 2.2 B presents the equilibrium molar fractions and the equilibrium conversion of methane as a function of temperature, evaluated at a pressure of 1 bar, with a S/C ratio of 3. The elevated CO levels at high temperatures (Figure 2.2 B) can be shifted towards greater hydrogen production through the WGS within a downstream shift reactor operating at temperatures of 200-450 °C. Low residence time, combined with a selective catalyst, suppresses the Sabatier reaction (reverse of Reaction 2.1).

According to Le Chatelier's Principle, lower pressures promote product formation due to the volume expansion that occurs during methane steam reforming (see Figure 2.2 C). In industry, the process typically operates at pressures between 15

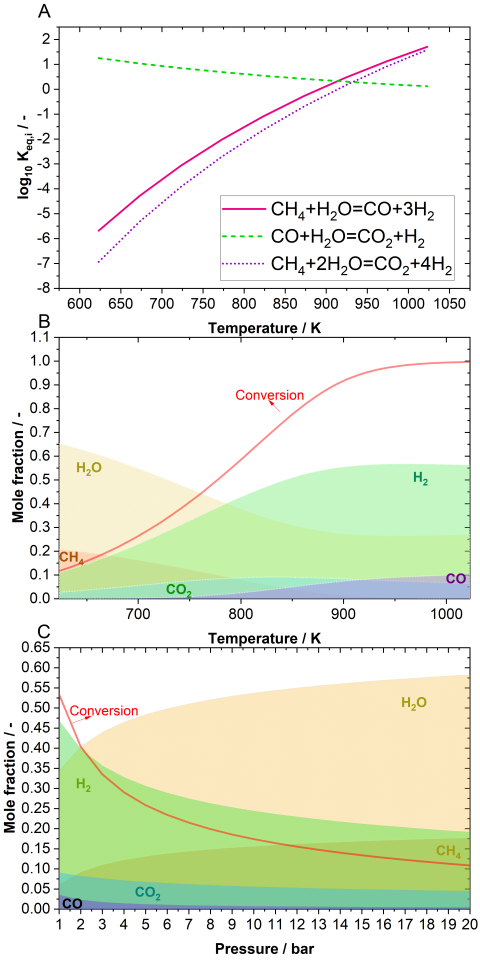

Figure 2.2: A) Equilibrium constants for reactions 2.1, 2.2, and 2.3 were determined as a function of temperature at a pressure of 1 bar. B) Mole fractions and CH_4 conversion of the components at equilibrium condition P:1 bar S/C:3 versus temperature. C) at constant temperature of 823 K and S/C:3 versus pressure.

and 30 bar, achieving an 80% conversion rate of NG in the reformer [32]. Higher pressures enhance process economics since the hydrogen produced is often used at elevated pressures. Although increased reactor pressure negatively impacts hydrogen yield, this is offset by a rise in temperature. The water-gas shift reaction is assumed to be in equilibrium under these reaction conditions. [33]. Above an S/C ratio of 2, thermodynamic predictions suggest that carbon formation is unlikely. However, it is important to note that carbon deposition on solid catalysts is frequently observed, particularly with Ni-based catalysts.

Typically, high S/C ratios are employed in hydrogen production via steam reforming, as they shift the equilibrium away from the regions where carbon formation occurs. This results in a reduced selectivity for carbon monoxide and an increased yield of hydrogen. Conversely, from an economic perspective, lower S/C ratios are advantageous since they require less feedstock for steam generation. The common S/C ratios for methane steam reforming range from 2.5 to 3.3, utilizing a base metal or noble metal-supported catalyst for the conversion process.

3 Decentralized hydrogen production methodology

Hydrogen can be categorized based on its usage into three types: captive hydrogen, fuel hydrogen, and merchant hydrogen. Captive hydrogen is utilized within industrial processes, such as fertilizer production and petroleum refining. Fuel hydrogen is employed in coal gasification and liquefaction, as well as in automotive, aircraft, and rocket fuels, and for heating or power generation. Merchant hydrogen is produced at one location and transported to another for various applications. These different uses necessitate distinct systems for production, storage, transmission, and transport, which are influenced by the production site's location, the customers' locations, and their anticipated demand [34].

The scale of hydrogen production and the proposed distribution methods can vary significantly, with both being closely tied to cost considerations. Downsizing conventional systems that use PSA for hydrogen purification is not economically feasible (see Section 3.1) and therefore the main motivation of this study is to focus on the decentralized hydrogen production units. As a result, small-scale MSR units are typically equipped with alternative purification processes, such as preferential oxidation (PrOX) or selective methanation. However, technological advancements are needed to further lower the costs of small-scale reforming and hydrogen purification. One potential solution for small-capacity and decentralized pure hydrogen production is steam reformer systems with integrated Pd membranes, which allow for the direct removal of hydrogen from the reactor (see Section 3.2). Section 3.3 introduces various types of membrane reactors developed and studied over the past decade. This section concludes with a review of the current status of microstructured membrane devices and reactors.

3.1 Small-scale reformer units

Conventional MSRs with tubular configurations and PSA hydrogen purification can be scaled down to a capacity of $3000\,\mathrm{m^3\,h^{-1}}$. However, the capital costs increase significantly from $\$80\mathrm{kW\,h\,d^{-1}}$ to $\$4000\mathrm{kW\,h\,d^{-1}}$ [35]. Major industrial companies, including Haldor-Topsøe, Howe-Baker, Hydrochem, KTI, and Foster Wheeler, supply these types of reformers for small-scale hydrogen production [35]. Other companies, such as Linde and Air Liquide, have developed small-scale reformer systems with capacities ranging from $50\,\mathrm{m^3\,h^{-1}}$ to $500\,\mathrm{m^3\,h^{-1}}$, utilizing PrOX or selective methanation for hydrogen purification [36, 37]. Table 3.1 provides a selection of available small-scale reformer units.

Table 3.1: Comparison of the commercial small reformer units after [36, 37].

Product	**Capacity** $[\mathrm{N\,m^3\,h^{-1}}]$	**Footprint** $[\mathrm{m^2\,h^{-1}\,N\,m^{-3}}]$	**Efficiency** [%]	$\mathbf{p_{H_2,exit}}$ [bar]
Hyos-R^{TM}	53 - 268	0.12 - 0.07	∼67	21.0
PRISM^{R}-HG	250	>0.12	∼70	6.9
Hygear HGS	42 - 82	0.24 - 0.18	∼45	6.5
Hyserve	30, 100	0.17 - 0.06	∼78	8.0
HydroPrime	300	0.11	>65	>15.0

The efficiencies listed in Table 3.1 were taken from [37]. Heat integration plays a critical role in small-scale reformers, as it enhances catalyst utilization and reduces overall energy consumption. While increased heat integration raises capital costs, it also improves efficiency and reduces operational expenses [36, 37]. These small-scale steam reformer systems typically operate at lower pressures to drive the reaction towards higher equilibrium conversions and reduce methane content in the reformate. For instance, methane steam reforming for fuel cell applications is conducted at lower pressures (around 3 bar) and lower temperatures (973 K) in concentric annular catalyst beds. Reported capacities range from 50 to 336 $\mathrm{m^3\,d^{-1}}$, with energy conversion efficiencies of approximately 70-80% [36].

However, the exit steam from these systems is at low pressure and thus has less value compared to high-pressure steam.

Technological advancements, such as microchannel process technology and membrane integration for an autothermal system, hold potential to further improve heat integration and increase the efficiency of small-scale reformers. The following chapters address the H_2 separation techniques.

3.2 Hydrogen separation techniques

3.2.1 Hydrogen selective membranes

The driving force for the separation of hydrogen with a membrane is the presence of a gradient of the chemical potential. Essentially, this involves subjecting one end of a completely sealed membrane to a mixture of gases at high pressure, while keeping the pressure relatively low on the opposing side. Because of this chemical potential gradient, a mass transport phenomenon occurs, during which hydrogen starts to traverse the membrane, leaving the impurity gases behind. There exist six primary categories of hydrogen-selective membranes, and one can assess their effectiveness and practical uses by examining different parameters associated with each type.

Table 3.2 presents a comprehensive overview of the properties linked to each membrane type, making it convenient for comparative analysis. In general, these membranes exhibit flexibility in their operation across a wide spectrum of temperatures and pressures, and they can be seamlessly adapted for both industrial and portable applications. Furthermore, the absence of moving components ensures that the system remains free from wear.

Table 3.2: Characteristics of the different types of hydrogen-selective membranes, derived from Kluiters [38].

	Dense Polymer	Micro-porous ceramic	Dense metallic	Porous carbon	Dense ceramic
Temperature range °C	<100	200-600	300-600	500-900	600-900
H_2 selectivity	Low	5-139	>1000	4-20	6-80
H_2 flux (1×10^{-10} mol m^{-2} s^{-1}) at ΔP = 100 kPa	Low	60-300	10-200	6-80	n.a.
Stability issues	Swelling, compaction, mechanical strength	Stability in H_2O	Phase transition	Brittle, oxidising	Stability in CO_2
Poisoning issues	HCl, SO_x, CO_2	n.a.	H_2S, HCl, CO	Strong adsorbing vapours, organics	H_2S
Materials	Polymers	Silica, alumina, zirconia, titania, zeolites	Pd alloy	Carbon	Proton conducting ceramics (mainly $SrCeO_{3-\delta}$, $BaCe_{3-\delta}$)
Transport mechanism	Solution/diffusion	Molecular sieving	Solution/diffusion	Surface diffusion; molecular sieving	Solution/diffusion (proton conduction)
Development status	Commercial by Air Products, Linde, BOC, Air Liquide	Prototype tubular silica membranes available up to 90 cm. Other materials only small samples (cm^2)	Commercial by Johnson Matthey; prototype membrane tubes available up to 60 cm	Small membrane modules commercial, mostly small samples (cm^2) available for testing	Small samples available for testing

The term "permeability" can have various interpretations, but within the scope of this study, it pertains to the measurement of certain gases' capacity to penetrate a solid substance. Permeability is quantitatively described and modeled using Fick's laws of diffusion. When it comes to hydrogen separation, a crucial factor to take into account is the hydrogen flux through the membrane. In this context, "flux" can be defined as the quantity of hydrogen molecules diffusing through a unit cross-sectional area perpendicular to the flow direction within a given time frame. The continuous flow of gases through a solid membrane at a constant rate can be expressed using Fick's first law, as illustrated in Equation 3.1:

$$J = -D\frac{\partial C}{\partial x} \tag{3.1}$$

In the provided equation, J represents the flux of the diffusing species, D stands for the diffusion coefficient or diffusivity, and $\frac{\partial C}{\partial x}$ denotes the concentration gradient. The negative sign is indicative of the direction of gas diffusion but can be disregarded in this derivation.

It's worth noting that the chemical potential gradient as the driving force for the separation process can be in the forms of gradients in concentration, pressure, temperature, and electromotive force within a system. Consequently, flux is fundamentally a function of the chemical potential gradient. For instance, in the case of reverse osmosis, two driving forces, concentration and pressure, are required. However, both of these parameters are interconnected through their impact on chemical potential. For simplicity, when considering gas permeation through a membrane, either the concentration or partial pressure gradient is typically taken into account. When the surface concentration of the gas is not known, Henry's law can be applied, as expressed in Equation 3.2 as follows:

$$S_H = \frac{C_{gas}}{P_{gas}} \tag{3.2}$$

In this equation, S_H is a constant and is defined as the ratio of the non-dissociative gas concentration in a solid or liquid at a dilute concentration (C_{Gas}) to its vapor

pressure (P_{Gas}). Given that it is relatively straightforward to measure the inlet and outlet gas pressures of a system, the concentration term in Fick's first law can be replaced with pressure. The proportionality constant in Equation 3.2, denoted as S_H, can alternatively be referred to as the solubility constant (S). The solubility constant (S) is expressed as the concentration per unit pressure. For diatomic molecules like hydrogen, they undergo dissociation into their atomic form before dissolving. Consequently, a modified version of Henry's Law is necessary to account for this behavior. The chemist Adolf Sieverts conducted research on the dissolution of gases in different metals and noticed that, owing to molecular dissociation, the solubility of hydrogen in metals is related to the square root of its pressure in the gas phase [39]. Sieverts subsequently adapted Henry's law (Equation 3.2) to formulate Equation 3.3, which is known as Sieverts' law:

$$S = \frac{C_H}{P_{H_2}^{0.5}} \tag{3.3}$$

By rearranging Equation 3.3 and substituting it into Equation 3.1, we obtain the expression shown in Equation 3.4:

$$J = DS\frac{\partial P_{H_2}^{0.5}}{\partial x} \cong DS\frac{\Delta P_{H_2}^{0.5}}{\Delta x} \tag{3.4}$$

Where $\Delta P_{H_2}^{0.5}$ is the square root of the pressure difference between the feed and permeate sides of the membrane, and Δx represents the membrane thickness, which can be simplified as x Equation 3.4 can be further manipulated to calculate the total number of moles (Q) that permeate through a dense metal membrane. This is achieved by multiplying both sides of the expression by the active membrane area (A) and the time (t) elapsed since gas permeation reached equilibrium, resulting in the following equation 3.5:

$$Q = JAt = DS\frac{A}{x}\Delta P_{H_2}^{0.5}.t \tag{3.5}$$

The constant DS is essentially the product of the diffusivity and solubility of hydrogen within the dense metal membrane, which leads to the term permeability,

denoted as Φ, as presented in Equation 3.6. It's important to note that all the terms in this equation are temperature-dependent.

$$\Phi = DS \tag{3.6}$$

When you differentiate Equation 3.5 to time (t), it yields a formula for determining the flow rate. Substituting this formula into Equation 3.6 leads to Equation 3.7.

$$\frac{dQ}{dt} = \Phi \frac{A}{x} \Delta P_{H_2}^{0.5} \tag{3.7}$$

If the conditions of the steady-state flow rate of hydrogen, the membrane's active area, its thickness, and the gas pressure on both sides of the membrane are known, the permeability is calculated. Alternatively, it is possible to determine the membrane's permeability by examining the slope of a straight line plot of Q versus t using Equation 3.7.

Equation 3.4 can be further simplified to yield Equation 3.8, which provides a general formula for calculating the hydrogen flux through a membrane.

$$J = \frac{\Phi(P_1^n - P_2^n)}{x} \tag{3.8}$$

In Equation 3.8, P_1 represents the hydrogen partial pressure on the feed side of the membrane, while P_2 is the hydrogen partial pressure on the permeate side. The value of the partial pressure exponent, denoted as n can vary depending on the assumed transport mechanism (Figure 3.1). For porous membranes, Henry's law applies, and it is typically assumed that n=1, resulting in what is known as Knudsen diffusion. In the case of hydrogen diffusion through a dense metal membrane, n=0.5, and Equation 3.8 simplifies to Sieverts' law. This equation highlights that the flux is inversely proportional to membrane thickness. It's worth emphasizing that permeability is a material constant that remains independent of membrane thickness [40]. Furthermore, permeability is a temperature-dependent parameter, and it can be expressed using the Arrhenius-type equation:

$$\Phi = \Phi_0 exp(\frac{-E_\Phi}{RT}) \tag{3.9}$$

In Equation 3.9, Φ_0 represents the maximum permeability at infinitely high temperatures, E_Φ stands for the activation energy for permeation, R is the universal gas constant, and T represents the absolute temperature. Similarly, diffusivity (D) and solubility (S) follow an Arrhenius-type relationship, as illustrated in Equations 3.10 and 3.11, respectively.

$$D = D_0 exp(\frac{-E_D}{RT}) \tag{3.10}$$

$$S = S_0 exp(\frac{-E_S}{RT}) \tag{3.11}$$

where D_0 and S_0 represent the diffusivity and solubility, respectively, at infinite temperature. E_D represents the activation energy for hydrogen diffusion, and E_S stands for the enthalpy of solution of hydrogen. Moreover, E_Φ, which appears in Equation 3.12, is defined as the activation energy for hydrogen permeation and is the sum of the activation energies for both diffusivity and solubility.

$$E_\Phi = E_D + E_S \tag{3.12}$$

3.2.1.1 Porous selective membranes

Porous membranes are typically effective at separating molecules that differ substantially in molecular weight, size, or shape. Four primary transport mechanisms are commonly identified (Figure 3.1): (1) Knudsen diffusion, (2) surface diffusion, (3) capillary condensation accompanied by liquid flow, and (4) molecular sieving.

Knudsen diffusion is limited in its separation capability, as it is most effective for systems with large molecular weight ratios, where the permeability ratio varies inversely with the square root of the molecular weight ratio. Surface diffusion

involves molecules adsorbed on pore walls moving along the surface due to concentration gradients in the adsorbed phase. This mechanism is often more effective for vapor separation compared to Knudsen diffusion. Capillary condensation with liquid flow occurs in very narrow pores, where one component of a vapor mixture condenses, blocking the pores and preventing non-condensable components from passing through. This method has proven highly efficient in various studies. Molecular sieving represents the ideal scenario for separating vapor compounds based on molecular size differences. Here, the pressure difference between the feed and permeate sides drives the transport through the pores [41].

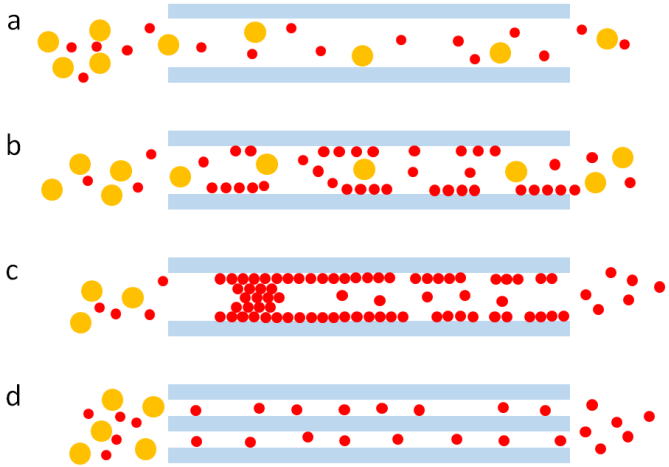

Figure 3.1: Illustration representing the four transport mechanisms through a porous membrane: (a) Knudsen diffusion, (b) surface diffusion, (c) capillary condensation, and (d) molecular sieving. This figure was regenerated according to reference [41].

3.2.1.2 Hydrogen in metals

Hydrogen permeates through the dense membrane material (as another type of selective membrane for hydrogen separation). Dense metal membranes offer very

high selectivity but have low flux, while porous membranes provide high flux but low selectivity. As previously discussed, the mechanism of hydrogen transport through dense metals relies on the solution-diffusion process. Additionally, it is important to elaborate on the models for hydrogen diffusion in metals. Kehr [42] has proposed several distinct mechanisms for hydrogen diffusion through metal lattices, all of which exhibit temperature dependence. Figure 3.2 illustrates these four types of diffusion.

At extremely low temperatures, where there is minimal thermal vibration, often referred to as phonons (Region I), hydrogen atoms can become "self-trapped" due to the relaxation of the surrounding metal lattice. It is then assumed that these hydrogen atoms proceed to the adjacent interstitial site through a quantum mechanical process known as "band propagation."

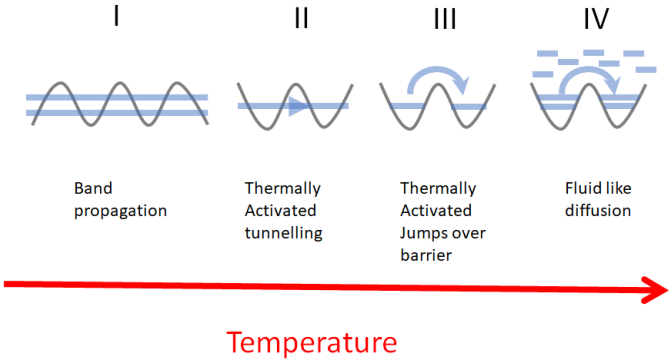

Figure 3.2: Diffusion model for hydrogen in metals according to Kehr's theory. This figure was regenerated according to reference [42].

As the temperature increases, hydrogen atoms are transported through a mechanism termed "thermally activated tunneling" (Region II), which involves the participation of phonons. At higher temperatures (Region III), the behavior of hydrogen atoms is modeled as that of classical particles, and they can perform

over-barrier jumps between neighboring interstitial sites. At even higher temperatures (Region IV), hydrogen atoms exhibit more fluid-like behavior, resembling the flow of liquids and gases rather than being confined to interstitial spaces.

It is important to note that these mechanisms are broad qualitative assumptions, where more than one method of transport can occur at a given temperature. Region III is particularly interesting because it is expected to occur between $200\,^{\circ}\mathrm{C}$ to $600\,^{\circ}\mathrm{C}$, which aligns with the operating temperature range of a metal membrane.

The crystal structure of a dense metal membrane has a significant impact on its solubility and diffusion mechanism. The body-centered cubic (BCC) crystal structure consists of atoms positioned at each corner of the cubic unit cell and one at the center. Various transition metals, including W, V, Cr, Rb, Nb, Mo, and Ta, form the BCC crystal structure.

The face-centered cubic (FCC) structure is another type of cubic unit cell, but in this arrangement, an atom is positioned at the center of each face of the cubic unit cell, as opposed to being located at the center of the 3D cell. This crystal structure is commonly adopted by materials like Pd and various Pd alloys. It is worth noting that the length of each dimension of the cubic unit cell is known as the lattice parameter.

Both crystal structures feature octahedral (O) and tetrahedral (T) interstitial sites that can be occupied by dissolved monatomic hydrogen. Table 3.3 provides information on the different concentrations and varying sizes of these interstitial sites within the BCC and FCC unit cells, which have a significant influence on the solubility of hydrogen and the transport mechanisms in these metals.

As shown in Table 3.3, there are three times more O and T sites available in a BCC crystal structure compared to that of the FCC crystal structure. However, it is important to note that the T sites surrounding the BCC O sites are severely distorted. Additionally, the T sites in the BCC crystal structure are larger than the O sites, while the reverse is true in the FCC crystal structure [43].

Theoretical calculations have indicated that hydrogen has a preference for occupying the tetrahedral (T) interstitial sites in BCC metals over the octahedral (O)

Table 3.3: Crystallographic information for metals with FCC and BCC structures [43].

Structure	BCC		FCC	
Space group	Im3m		Fm3m	
Interstitial site	Octahedral	Tetrahedral	Octahedral	Tetrahedral
Number per atom	3	6	1	2
Size relative to M atom radius	0.155	0.291	0.414	0.225
Packing density (%)	68		74	

sites [44–47]. Conversely, density of states (DOS) calculations have shown that hydrogen will tend to inhabit the O sites rather than the T sites in Pd systems, as the O interstitial sites are considered more stable [48, 49]. However, it is worth noting that there is literature suggesting that hydrogen can occupy both T and O sites within the Pd lattice. In-situ high-resolution neutron diffraction studies conducted at 310 °C on Pd loaded with 9 MPa of deuterium have revealed significant T site occupation [50].

Furthermore, it has been mentioned in the literature that the activation energy for the diffusion of hydrogen increases as the distance between interstitial sites increases. Consequently, diffusivity tends to be higher in metals with shorter lattice parameters [51].

The behavior of hydrogen solubility with temperature depends on the chemical properties of the host metal, which is determined by the tendency of the host metal to either form a solid solution or a stable metal hydride [52]. Examples of metals that exhibit an increase in hydrogen solubility as temperature rises include Mn, Fe, Co, and Ni, which are known as endothermic occluders. These metals form solid solutions with hydrogen occupying random sites within their crystal structure [43].

For hydrogen separation, metals like Pd, Ti, V, Nb, and Zr are commonly used and are categorized as exothermic occluders [53]. This is because they experience a decrease in hydrogen solubility with increasing temperature due to the propensity of the metal to form stable and ordered metal hydrides [43].

3.2.1.3 Metallic based membranes

Hydrogen can indeed diffuse rapidly through refractory metals, especially those with a BCC crystal structure. However, these metals tend to have highly inactive surfaces when it comes to catalyzing hydrogen dissociation and recombination, resulting in slow rates of absorption and desorption. Recognizing this challenge, Buxbaum and Marker [54] developed a membrane composed of Nb (a BCC metal) electroless plated with Pd (an FCC metal). This innovative approach yielded a membrane with relatively high hydrogen permeability, measured at 3.2×10^{-7} $\mathrm{mol\,m^{-1}\,s^{-1}\,Pa^{-0.5}}$ at $425\,^{\circ}\mathrm{C}$. Nevertheless, it was observed that the hydrogen flux deteriorated over time due to interdiffusion occurring between the Nb and Pd layers.

Table 3.4 provides information on the enthalpy of hydride formation for various metals. It shows that hydride formation is exothermic for metals such as Nb, Ta, V, Ni, and Pd. In exothermic reactions, hydrides readily form because they release energy. On the other hand, metals like Fe and Pt exhibit endothermic hydride formation. In endothermic reactions, external sources of heat are required to facilitate the formation of hydrides. Therefore, in the case of Fe and Pt, additional heat is needed to produce their respective hydrides.

Table 3.4: Hydrogen permeability in certain metals and the corresponding enthalpy for hydride formation.

Metal	crystal structure	Hydrogen permeability $500\,^{\circ}\mathrm{C}$ $\mathrm{mol/m/s/Pa^{0.5}}$ [39]	ΔH of hydride formation $\mathrm{kJ\,mol^{-1}}$ [55]
Nb	BCC	1.6×10^{-6}	-60 (NbH_2)
Ta	BCC	1.3×10^{-7}	-78 ($TaH_{0.5}$)
V	BCC	1.9×10^{-7}	-54 (VH_2))
Fe	BCC	1.8×10^{-10}	+14 (FeH)
Ni	FCC	7.8×10^{-11}	-6 ($NiH_{0.5}$)
Pd	FCC	1.9×10^{-8}	-40 ($PdH_{0.5}$)
Pt	FCC	2.0×10^{-12}	+26 (PtH)

3.2.1.4 Palladium membranes

At this point, it is important to understand why metals like Pd are widely favored in the field of hydrogen separation. Hydrogen can dissolve in a variety of metals, forming either interstitial solid solutions or metal hydrides. Some metals require high temperatures and pressures to absorb hydrogen, while others can readily form stable hydrides at room temperature. Palladium (Pd) possesses unique characteristics that make it ideal for hydrogen separation. One of its exceptional features is its ability to dissociate molecular hydrogen into its monatomic form, which allows for rapid diffusion through its lattice. Moreover, Pd can absorb approximately 600 times its volume in hydrogen while maintaining its physical properties and structural integrity. This property was discovered by Thomas Graham in 1866 [56].

Pd membranes were initially developed in laboratory settings, but it was not until the 1950s that they were scaled up for industrial use, particularly in the nuclear fission industry where there was a growing demand for separating hydrogen isotopes. Today, Pd membranes are more commonly employed in the production of ultra-pure hydrogen, particularly for the semiconductor industry [57].

Pd has a density of $12.023\,\mathrm{g\,cm^{-3}}$ and a melting point of $1555\,^{\circ}\mathrm{C}$. It was discovered by William Hyde Wollaston in 1803 and is a silvery-white metal that is malleable and easily worked. It finds wide application in the automotive industry, especially as a catalyst in catalytic converters.

In its free atomic state, Pd has an outer electron configuration of 1s2 2s2 2p6 3s2 3p6 3d10 4s2 4p6 4d10 5s0. There are overlapping energy bands between the 4d and 5s energy bands, which is typical of transition metals. This property gives Pd a high affinity for receiving donor electrons from other atoms, and it is responsible for the unique chemical and metallurgical interactions that Pd exhibits with other elements.

The Pd-H system consists of an interstitial solid solution phase (α) and a Pd hydride phase (β) (see Figure 3.3). Both phases have the FCC crystal structure, but they differ in lattice parameters. Pure Pd has a lattice parameter of 3.89 Å. At

room temperature, the α-phase exists up to a composition known as α_{max}, and it can coexist with the β_{min} phase up to a H/Pd atomic ratio of approximately 0.6, with each phase having lattice parameters of $3.895\,\text{Å}$ and $4.025\,\text{Å}$, respectively [58]. The coexistence of these two phases leads to a notable feature in the phase diagram, known as the miscibility gap. The critical temperature (T_c) for $\beta_{hydride}$ formation is approximately $295\,^{\circ}\text{C}$, above which this phase no longer occurs.

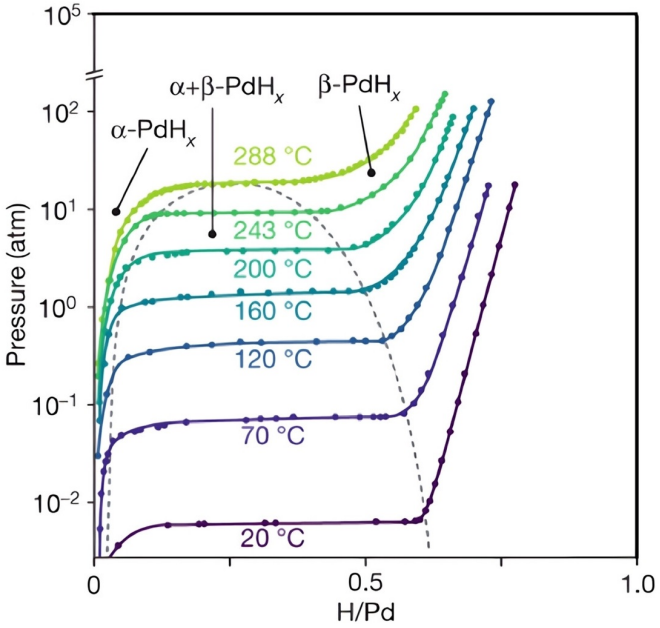

Figure 3.3: Phase diagram of palladium hydride as a function of pressure and temperature. Adapted from [59]; based on the original data from [60].

Cycling a Pd membrane through the miscibility gap can result in a significant lattice volume expansion, exceeding $10\,\%$. This expansion occurs due to the disparity between the lattice parameters of the α and $\beta_{hydride}$ phases. As more

hydrogen is absorbed within the Pd lattice, internal stresses are generated, ultimately leading to membrane failure. This phenomenon has been studied using transmission electron microscopy of a Pd-H alloy containing both α and β phases, providing clear evidence of dislocation production, which is a precursor to embrittlement [58]. To avoid the effects of embrittlement, it is essential to purge the membrane of any hydrogen before subjecting it to thermal cycling, preventing it from crossing the miscibility gap.

The α- and $\beta_{hydride}$ phases can coexist below the critical temperature (T_c). However, above this temperature, the $\beta_{hydride}$ phase may only occur at extremely high pressures [61]. According to Dolan [43], the formation of the $\beta_{hydride}$ phase is an exothermic process, and an increase in the content of this phase in metals like Pd can lead to a reduction in the hydrogen solubility of the $\alpha_{hydride}$. An FCC metal like Pd is inherently more resistant to hydrogen embrittlement than BCC metals like V since hydrogen solubility is relatively lower in Pd [43].

3.3 Exploring the industrial advancements in the research and development of Pd-based membranes

MR technology has been widely regarded as a promising innovation due to its ability to generate and separate hydrogen simultaneously [62]. Hydrogen production has traditionally relied on fossil fuel-driven steam reforming processes in industrial settings. Nevertheless, it is important to highlight that conventional reactors have drawbacks, including carbon formation, catalyst deactivation, elevated material expenses resulting from high temperatures, and, significantly, limitations imposed by reaction thermodynamics. To mitigate the drawbacks associated with conventional reactors, MRs are proposed [63].

The following presents a review of prominent manufacturers and research institutions actively involved in the advancement of Pd-based membranes. In the subsequent sections, a discussion is presented regarding various European-funded

projects that employ Pd-based membranes, encompassing CACHET, CoMETHy, FERRET, and FluidCELL. Finally, two distinct pilot plants are introduced, each having a unique plant architecture, within the scope of industrial process intensification.

3.3.1 Energy Research Center (ECN)

ECN, a division of TNO in the Netherlands, provides hydrogen separation modules for assessment under the name Hysep. These modules employ palladium composite membranes, incorporating a palladium layer deposited by Electroless plating (ELP) on a porous ceramic alumina support. Furthermore, ECN is involved in the development of innovative Pd alloy composite membranes, including Pd-Ag and Pd-Cu [64, 65].

3.3.2 SINTEF Industries

SINTEF Materials and Chemistry in Norway has been actively engaged in the development of palladium-based membranes through various national and international projects, such as CACHET, dating back to the 1990s. SINTEF holds several patents for methods facilitating the creation of Pd alloy thin films. One of the key patents pertains to the production of thin membranes composed of Pd alloys, with thicknesses ranging from $1\,\mu\mathrm{m}$ to $5\,\mu\mathrm{m}$ [66, 67].

3.3.3 NORAM/MRT/UBC

In 1998, the establishment of Membrane Reactor Technologies Ltd (MRT) took place, and later, NORAM Engineering acquired MRT upon making an investment and acquiring all their shares. MRT specialized in the fabrication of Pd/Pd-Ag alloy foils and thin films (with thicknesses ranging from $8\,\mu\mathrm{m}$ to $15\,\mu\mathrm{m}$) for membranes. They also secured a patent for a bonding technique that allowed for the

permanent attachment of membranes to support modules, creating a hydrogen-tight seal. Subsequently, NORAM, in collaboration with the University of British Columbia and their affiliated company, MRT, has been dedicating substantial efforts since 2000 to the development of industrial thin Pd-based composite membranes for the steam reforming of natural gas (NG) [68, 69].

3.3.4 REB Research & Consulting Co.

REB Research and Consulting Co., established in 1985 in the United States, specializes in the production and supply of various metal membranes. Their product range encompasses Pd-Ag alloy membranes, available in plain form, as well as coated with palladium-grey and coated with palladium-copper alloy variations [70, 71].

3.3.5 TECNALIA

TECNALIA Research and Innovation is the foremost center for applied research and technological development in Spain. They specialize in the production of various membrane types, including inorganic membranes like pore-filled Pd-membranes. TECNALIA, in collaboration with Eindhoven University of Technology, has actively participated in numerous European projects, such as FluidCELL, FERRET, and ReforCELL. They have successfully developed thin Pd-based membranes ($< 5\,\mu m$ thick) for hydrogen production, which find applicability in a wide range of applications [72, 73].

3.3.6 CACHET

The CACHET project (carbon dioxide capture and hydrogen production from gas fuels), funded under FP6-SUSTDEV, conducted an exploration of four distinct technologies aimed at reducing the expenses associated with carbon dioxide capture in power generation and hydrogen production. The project specifically

centered around a combined cycle gas turbine power plant fired by natural gas, with the inclusion of an optional pure H_2 side stream. The primary objectives of this endeavor were to achieve a $50\,\%$ reduction in CO_2 capture costs and sequester more than $90\,\%$ of the CO_2 emissions produced [74].

HyGenSys, an advanced steam methane reforming technology, emerged as a significant outcome of the CACHET project. This system, which was a pivotal component of the CACHET project, aimed to enhance the efficiency of the reforming process by incorporating heat from the exhaust gases of a gas turbine. The resulting H_2 was subsequently employed as fuel in a combined cycle gas turbine power plant for electricity generation. Notably, the reformer was purposefully engineered to operate under elevated pressure on the exhaust gas side of the unit, thereby facilitating improved heat transfer [75]. The project explored the application of Pd and Pd alloy membranes for the capture of CO_2 from syngas, either within a water gas shift reactor or directly from an integrated natural gas membrane reformer. In this process, a mixture of natural gas and steam was introduced into the feed side chamber of the membrane reformer, where simultaneous methane steam reforming and the extraction of H_2 through the membrane took place. Additionally, a sweep gas was employed to enhance the permeation process [76]. The development of these membranes involved collaborative efforts between SINTEF and DICP (Dalian Institute of Chemical Physics), employing different membrane manufacturing techniques to evaluate Pd alloy membranes. SINTEF's Pd-23wt%Ag membranes were produced using a two-step method. Initially, a thin ($2\,\mu m$) defect-free Pd-alloy film was created via sputtering deposition onto a silicon wafer. Subsequently, the membrane was detached from the wafer and affixed to a porous stainless steel support.

On the other hand, DICP's pure Pd membranes were manufactured on ceramic supports developed by ECN. ELP was utilized to deposit a Pd layer ($2\,\mu m$ to $3\,\mu m$ thick), with the pores of the support tubes pre-filled with an inorganic gel to ensure a smooth surface and prevent the Pd from entering into the pore structures [77].

Both the SINTEF and DICP membranes underwent thorough testing. SINTEF's membrane achieved a pure H_2 permeance of up to $1.4 \times 10^{-5}\ \mathrm{mol/m^2/s/Pa}$ at $400\,^{\circ}\mathrm{C}$, while DICP's membrane exhibited a pure H_2 permeance ranging from $7.2 \times 10^{-6}\ \mathrm{mol/m^2/s/Pa}$ to $9.7 \times 10^{-6}\ \mathrm{mol/m^2/s/Pa}$ at $100\,\mathrm{kPa}$ and $500\,^{\circ}\mathrm{C}$. Notably, both membranes demonstrated the ability to capture 90% of CO_2 in a Natural Gas Combined Cycle plant (NGCC) with significant selectivity.

Moreover, extended stability tests conducted over 150 days within a temperature range of $325\,^{\circ}\mathrm{C}$ to $400\,^{\circ}\mathrm{C}$ indicated a projected membrane lifetime of 2 to 5 years for temperatures exceeding $400\,^{\circ}\mathrm{C}$ [74].

In terms of the techno-economic analysis for electricity generation in NGCC cycles with pre-combustion CO_2 capture within the CACHET project, it was revealed that the water gas shift membrane offers a lower cost compared to the reforming membrane. Nevertheless, the overall projected costs remained relatively high due to the elevated price of natural gas and lower estimated efficiency [77–79].

3.3.7 CoMETHy

The CoMETHy project, funded by the Hydrogen and Fuel Cell Joint Undertaking (FCH-JU, FP7), focused on sustainable decentralized hydrogen production near end-users, using various renewable sources. CoMETHy had a strong focus on product development. The project involved designing a compact modular steam reformer that could be adapted to different heat sources, such as solar, biomass, and fossil fuels, to convert reformable fuels like methane into pure hydrogen. Notably, the project used the unique features of solar salt, specifically a molten nitrates mixture, to capture, store, and release solar heat in concentrated solar power systems, offering high heat transfer and storage capabilities, affordability, and minimal environmental concerns [80].

Typically, steam reforming processes operate at temperatures ranging from $850\,^{\circ}\mathrm{C}$ to $950\,^{\circ}\mathrm{C}$. However, the low-temperature steam reformer developed in this project

functioned at a maximum temperature of $550\,^{\circ}\mathrm{C}$, eliminating the need for expensive steel alloys. This low-temperature, single-stage hydrogen production and purification reformer necessitated the development of membranes and catalysts to achieve the intended objectives [81].

Various Pd-based membranes were initially selected for testing in the reactor, including different membrane supports (ceramic, metal, and self-supported), selective layer compositions (pure Pd and Pd-Ag), and selective layer deposition methods (such as ELP, sputtering, roll-to-roll fabrication of Pd foils, and self-supported membranes). Self-supported membranes were ultimately rejected due to mechanical issues, high costs, and scale-up challenges. An alternative approach considered Pd-Ag membranes supported on asymmetrical Porous Stainless Steel (PSS) supports with an inter-metallic ceramic layer for Pd-Ag deposition. However, the welding process introduced support roughness and defects, posing difficulties in this technology. Composite membranes with a thin Pd layer ($2\,\mu\mathrm{m}$ to $5\,\mu\mathrm{m}$) on a porous support tube were chosen as the most suitable option for scaling up. In preliminary laboratory testing, ceramic-supported membranes deposited by ELP exhibited hydrogen permeability of over $20\,\mathrm{Nm^3/h/bar^{0.5}}$, despite some permeance inhibition effects (about 65%) caused by mixture components, primarily methane. These Pd membranes, supported on porous ceramic tubes by ELP, were considered the best choice during pilot design and construction [82].

Figure 3.4 shows the ceramic-supported Pd membranes (10 tubes) installed by ECN. These membranes consisted of a selective Pd-based layer ($3\,\mu\mathrm{m}$ to $6\,\mu\mathrm{m}$) on a porous Al_2O_3 support with an outer diameter of $14\,\mathrm{mm}$, a length of $80\,\mathrm{cm}$, and an overall area of $0.35\,\mathrm{m^2}$.

To enhance the performance of the reformer for low-temperature steam reforming of methane, the project investigated the most efficient combination of active catalytic materials and support structures. Structured catalysts were explored to improve heat transfer throughout the catalytic bed, resulting in a flattened radial temperature gradient. The project also led to the development of structured open foam catalysts designed specifically for low-temperature steam reforming of methane and ethanol. These catalysts had minimal pressure drop, improved

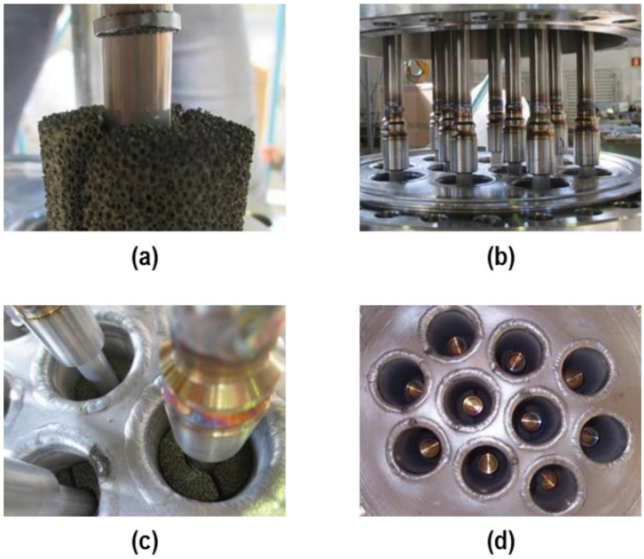

Figure 3.4: Images depicting the configuration of the catalyst-membrane assembly within the reformer tubes of the pilot membrane reformer operating with molten salt heating are presented. These images include a close-up perspective of the catalyst/membrane assembly (a), a lateral view (b), an overhead view (c), and a rearview that showcases the sealed end of the tubular membrane (d) [82] (re-printed with permission from Elsevier).

heat transfer, and simultaneously promoted steam reforming and water gas shift reactions [83, 84]. A bimetallic Ni-Pt-based catalytic foam was chosen for the reformer pilot plant due to its excellent catalytic activity for both methane and ethanol steam reforming, providing flexibility in terms of feedstock.

The evaluation of the CoMETHy membrane reactor's performance involved an examination of several operational factors. These factors encompassed the flow rate and temperature of the molten salt, the inlet methane flow rate, the steam-to-carbon ratio, and the sweep steam flow rate. It was observed that elevated temperatures had a stimulating effect on the endothermic reforming process. Specifically, as the temperature of the molten salt increased from $450\,^{\circ}\mathrm{C}$ to $540\,^{\circ}\mathrm{C}$, the methane conversion rate saw a significant improvement, escalating from 30% to 60%. A

comparable pattern was identified in the case of the hydrogen flow rate that passed through the membranes based on Pd. These results underscored the practical applicability of the CoMETHy membranes, as outlined in the final report summary [79, 82].

The techno-economic evaluation of this process took into account both decentralized ($1500\,\mathrm{N\,m^3\,h^{-1}}$) and centralized ($5000\,\mathrm{N\,m^3\,h^{-1}}$) solar steam reforming approaches. The "full solar" system exclusively relied on solar energy for providing the necessary heat, with or without the co-generation of electricity. In contrast, the "hybrid" steam reforming system combined the combustion of retentate off-gas with oxygen or air and a concentrating solar thermal plant to meet the heat requirements. A molten salt heat storage system ensured uninterrupted operation of the steam reforming plant, with backup support from a gas-fired heater when solar heat was unavailable.

In comparison to conventional steam reforming, the solar reforming process incurred a higher initial investment cost due to the inclusion of the concentrating solar thermal plant and its associated components. Nevertheless, when taking into consideration the relationship between the size of the solar field, thermal energy storage capacity, and annual operating hours, the hydrogen production costs fell within the range of $2.02\,\mathrm{Euro/kg}$ to $3.36\,\mathrm{Euro/kg}$. This cost range was comparable to the production cost of hydrogen through conventional steam reforming, which stood at $1.74\,\mathrm{Euro/kg}$. Furthermore, the integration of a solar energy system via a concentrating solar thermal plant that utilized molten salt for reforming processes proved to be an effective strategy for reducing hydrogen production costs while also facilitating CO_2 sequestration [85].

3.3.8 Micro-CHP

Worldwide, electricity generation primarily relies on a centralized grid structure, which comes with several drawbacks. These include transmission losses that negatively impact overall efficiency, increase emissions, and lead to long-term financial commitments. In response to these challenges, there is a growing need

for a more efficient system based on decentralized or distributed power generation, such as micro-combined heat and power (micro-CHP) systems. Micro-CHP systems are typically designed to provide electrical power up to $50\,\mathrm{kW}$ while concurrently generating low-temperature streams that can be utilized on-site. One of the key advantages of micro-CHP systems is their ability to recover and utilize waste heat [80, 86].

Furthermore, for remote communities in less-developed and developing countries that lack access to traditional grid infrastructure, distributed energy generation based on renewable energy sources offers a reliable, cost-effective, and sustainable source of clean energy [87]. Various technologies can be integrated into micro-CHP systems, including internal combustion engines, Stirling engines, micro-gas turbines, organic Rankine cycles, thermo-photovoltaics, and fuel cells [88].

In recent years, European Union projects like FERRET (FP7-JTI) and FluidCELL (FP7-JTI) have explored the potential of membrane reactors for hydrogen production and micro-CHP applications using different fuels. These initiatives aim to enhance the efficiency and sustainability of energy production and distribution. Within the FERRET project, the adaptability of a highly efficient micro-CHP system, specifically designed for this project, was investigated about the variable natural gas compositions found across Europe. Four distinct gas compositions, representing different European natural gas markets, were assessed. These compositions included the UK, Netherlands, Italy, and Spain. The natural gas sample from Italy was primarily composed of pure methane, while the UK composition featured an average natural gas composition. Additionally, the Netherlands had the lowest Wobbe index, while Spain had the highest [89].

A primary objective of the FERRET project was to maximize the net electric efficiency while minimizing the membrane surface area, a critical parameter that significantly influences the economic viability of the system. Consequently, a range of membranes was developed and put to the test as part of this project [90, 91].

These membranes consist of two layers: a thin PdAg ceramic-supported membrane with a thickness of approximately $0.8\,\mu\mathrm{m}$ to $2\,\mu\mathrm{m}$, which is then coated

with a thin mesoporous ceramic layer measuring less than $1\,\mu m$ in thickness. This mesoporous ceramic layer is composed of a mixture of 50% yttria-stabilized zirconia (YSZ) and 50% γ-Al_2O_3 (layers in series are ceramic support, thin PdAg layer and thin protective ceramic layer on top which is called double-skinned membrane). Additionally, another configuration involves a thin PdAg membrane with a thickness of $4\,\mu m$, which is supported on a ceramic-coated porous tube made of Hastelloy X.

The double-skinned membranes based on PdAg, with a selective layer thickness of $1\,\mu m$, when mounted on ceramic supports, exhibit notable characteristics. These membranes demonstrate substantial hydrogen permeances, with a rate of approximately $4.6 \times 10^{-6}\,mol\,m^{-2}\,s^{-1}\,Pa^{-1}$, and an ideal perm-selectivity for H_2/N_2 of around 26,000. These performance metrics are comparable to or even superior to those achieved by PdAg membranes on ceramic supports with a thickness ranging from $4\,\mu m$ to $5\,\mu m$ [80].

Furthermore, two different reactor configurations were proposed to enhance hydrogen permeation. One design utilizes vacuum at the permeate side, while the other employs a sweep gas. Both approaches aim to reduce the hydrogen partial pressure, thus increasing hydrogen flux and decreasing the required membrane area. According to the results obtained, the net electric efficiency in the case of the sweep gas configuration exceeds the project goals, reaching above 40% [89].

The FluidCELL project (FP7-JTI) aimed to develop a highly efficient micro-CHP system utilizing PEMFCs (proton exchange membrane fuel cells) and integrating a fluidized membrane reactor operating at low temperatures. This system was designed for use in off-grid applications and powered by bio-ethanol [92].

The primary objective of the FluidCELL project was to create an innovative bio-ethanol membrane reformer capable of producing pure hydrogen (approximately $3.2\,N\,m^3\,h^{-1}$) using membrane reactors. To achieve this, several PdAg (palladium-silver) membranes were developed and tested, including ultra-thin films (less than $2\,\mu m$) and thin films (approximately $4\,\mu m$ to $5\,\mu m$). Various

techniques were used to synthesize these membranes, including direct simultaneous Pd and Ag ELP, direct physical vapor deposition magnetron sputtering (PVD-MS), or a combination of PVD-MS and ELP.

The PdAg membranes, which were supported on asymmetric ceramic porous tubes (with outer and inner diameters of 10/7 mm), were prepared by ELP with different thicknesses and plating times. The plating time for ultra-thin films ranged from $30\,\mu\mathrm{m}$ to $70\,\mu\mathrm{m}$, while thin-film plating took about $4\,\mathrm{h}$ to $5\,\mathrm{h}$. Thin-film membranes were also developed on alumina asymmetric supports ($50\,\mathrm{cm}$ length) with a thicker wall (10/4 mm o.d./i.d.) [70, 93, 94].

PdAg films deposited directly on porous supports by PVD-MS were not dense and had a low ideal perm-selectivity for H_2/N_2, making them unsuitable for hydrogen purification. However, a combination of PVD-MS and ELP techniques used to prepare ultra-thin PdAg membranes demonstrated high hydrogen permeance and good hydrogen perm-selectivity. For stable membranes in a fluidized regime and ideal H_2/N_2 perm-selectivity above 8000, thin-film PdAg membranes of about $4\,\mu\mathrm{m}$ thickness prepared via simultaneous Pd and Ag ELP were selected for the prototype. Membrane stability over an extended period with sufficient perm-selectivity is a key feature that makes these membranes attractive for industrial-scale applications [95, 96].

It was determined that approximately $0.44\,\mathrm{m}^2$ of thin-film-supported Pd-based membranes were needed to separate $3.2\,\mathrm{N\,m^3\,h^{-1}}$ of H_2 using H_2O as the sweep gas. The final membrane reactor design for micro-CHP applications, validated by a model, achieved an overall hydrogen recovery factor of 67% and required substantially less catalyst (less than 3.5% by weight) in the fluidized bed [4].

The economic feasibility analysis for the FluidCELL system was conducted for 13 European countries, considering payback time, net present value, and internal rate of return. The studied countries included Austria, Finland, France, Germany, Greece, Ireland, Italy, Netherlands, Poland, Portugal, Spain, Sweden, and Switzerland [92].

To enhance the attractiveness of the system for customers, the economic analysis prioritized payback time. This assumption was based on the system operating at full load regardless of the season, adjusted to meet the minimum thermal requirements of dwellings. To reduce the payback time, end-users were expected to consume the entire thermal and electrical output of the system and maintain it at full capacity since higher efficiencies were achieved under these conditions. Therefore, the system needed to meet the energy demands of multiple dwellings, requiring a backup boiler. Considering all assumptions, investment costs, and varying electricity and natural gas costs in different EU countries, the analysis indicated a cost of $10.000\,\mathrm{Euro/kWe}$. On average across the countries studied, the payback time was eight years, assuming a service lifetime of ten years for the FluidCELL system [79].

Table 3.5 provides an overview of the Pd-membranes produced by Tecnalia for the prototype membrane reactors utilized in the FERRET and FluidCELL projects [73].

Table 3.5: Palladium-based supported membranes that were produced for the prototype membrane reactors [79].

Project	Reference period	Number of membranes	Membrane length after sealing step (cm)	Type of the MR prototype
FERRET	2014-2017	30	20	Fluidized-bed natural gas MR
FluidCELL	2014-2018	37	40	Fluidized-bed bio-ethanol MR

3.3.9 Pilot plants

In the context of the industrial process intensification trend aimed at enhancing process efficiency, selective membranes have been a prominent focus of scientific and technological research over the past two decades. Pd-based membranes can

be incorporated into steam reforming processes in two distinct configurations: open and closed architecture [97].

Open Architecture: In the open architecture configuration, hydrogen-selective membranes are assembled in separation modules downstream from catalytic reactors. This arrangement transforms the overall process into a series of reaction-separation units.

Closed Architecture: The closed architecture is characterized by the assembly of selective membranes inside the reactor close to the catalyst. This design ensures that the hydrogen produced is immediately removed from the reaction zone [98–100].

The Kinetics technology reformer and membrane module pilot plant, designed under the open architecture configuration, was established in 2009 as part of a research project funded by the Italian Ministry of Education, Universities, and Research. This semi-industrial plant aimed to investigate the integration of hydrogen-selective membranes in a real steam-reforming environment. The pilot unit had a capacity of $20\,\mathrm{N\,m^3\,h^{-1}}$, featuring two stages of reforming reaction and membrane separation for pure hydrogen production using natural gas sourced from the town grid. The plant underwent extensive testing for over $3000\,\mathrm{h}$ in a relevant industrial setting [101].

The process in the pilot plant involved desulfurizing natural gas up to 0.1 ppm using a desulfurization unit before combining it with process steam generated in a hot oil boiler at a controlled ratio. The superheated steam and natural gas mixture were preheated and directed to the reforming reactor, operating at an outlet temperature of $500\,^\circ\mathrm{C}$ to $600\,^\circ\mathrm{C}$. The two syngas streams produced in both reformers were cooled down with an air cooler to a temperature suitable for membrane operation. The retentate stream from the first membrane was recycled back into the second reformer for further feed conversion, which then passed through the second membrane separator for additional hydrogen recovery. The permeated streams exiting the membranes were combined and sent to the final cooling and condensate separation stage [97]. Figure 3.5 provides various views of the pilot plant. The initial membrane stage included two parallel modules

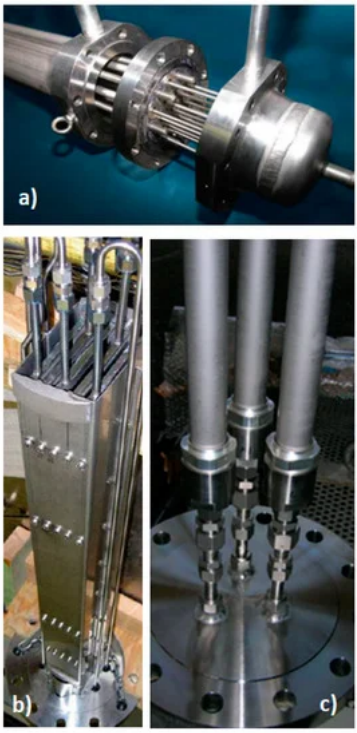

Figure 3.5: Photography of the membrane modules: (a) 13 tubular palladium membranes supported by alumina, (b) 5 plate PdAg (palladium-silver) membranes, (c) 3 tubular PdAg membranes supported by alumina [102].

with membrane areas of $0.4\,\mathrm{m}^2$ (ECN, Figure 3.5 (a)) and $0.6\,\mathrm{m}^2$ (MRT, 3.5 (b)). Additionally, the second membrane stage consisted of a module with an area of $0.13\,\mathrm{m}^2$ (Japanese Company supplier, 3.5 (c)). The steam reforming pilot plant, designed for the CoMETHy project as previously discussed, was developed by Processi Innovativi, a company owned by KT (Kinetics Technology). This pilot plant was constructed using a "closed architecture" configuration. The primary objective was to evaluate the integration of a palladium-based membrane reformer with solar-assisted molten salt heating. More information and characterization of

this pilot plant in the studies conducted by Giaconia et al. and Morico et al. are found in these references [83, 103].

3.4 Tubular membrane reactor development by IMVT-KIT, Linde engineering, and Plansee SE

With the goal of developing a membrane reformer for on-site hydrogen production, a cooperation was initiated in 2009 between the Austrian company Plansee SE, the Karlsruhe Institute of Technology (KIT), and the Linde Engineering division of the Linde Group . A primary objective of the three-year project was to demonstrate membrane reformer technology based on a newly developed tubular palladium composite membrane. For the development of a technical MR, practical operating parameters were theoretically determined (e.g., temperature of 600–650°C, pressure of 16 bar, and a S/C:3). In lab-scale experiments, two types of palladium composite membranes developed by Plansee and KIT were tested under these conditions. Both types exhibited excellent hydrogen permeability compared to literature values. By integrating the MR into the main production process, an efficiency of 77% was achieved, based on the higher heating values of hydrogen and natural gas or methane used for feed and fuel. To produce one mole of hydrogen, 0.418 moles of methane were required. An economic analysis of the MR system demonstrated that hydrogen can be produced in a MR with capacity of 50 $\mathrm{Nm^3/h}$ with membrane costs of less than 50,000 €, offering a 10% cost advantage compared to conventional small-scale reformer systems (51€ct/Nm^3 vs. 57 €ct/Nm^3 H_2) [36].

3.5 State of the art in ultra-compact planar membrane reformers

Extensive research has been conducted at IMVT-KIT on microstructured reactors. Notably, Cremers et al. [104] developed a compact reformer integrated with catalytic combustion, utilizing Nicrofer 3220 HT (Krupp VDM). Optimal results were achieved by firing the integrated combustor with a mixture of hydrogen and methane in co-flow with the reforming reaction. However, integrating a membrane for H_2 separation in such a planar system for hydrogen production through MSR was initiated with the first generation of μ-EnH_2ancer. A graphical representation of the functional plates (see Figure 3.6) associated with the μ-EnH_2ancer is presented, along with detailed dimensions outlined in Table 3.6. This design serves as a next generation to μ-EnH_2ancer V 1.0 and the autothermal version, μ-EnH_2ancer V 2.0, both developed at IMVT-KIT. Unfortunately, the outcomes from μ-EnH_2ancer V 2.0 were never experimentally tested. To elucidate the changes resulting from the design size, Figure 3.6 provides a sketch of each design, and the corresponding dimensions are delineated in Table 3.6.

Table 3.6: Characteristics of the μ-EnH_2ancer generations developed at IMVT.

MR	Pre-reforming W-H-L-N[a] (mm)	Reforming W-H-L-N (mm)	permeate W-H-L-N (mm)	combustion W-H-L-N (mm)	Air distributor W-H-L-N-D[b] (mm)	$(A/V)_{reactor}$ (m^2/m^3)	$(A_{reformer_{cat,bed}}/A_{plate})$ (m^2/m^3)
V 1.0	0.5-0.2-60-53	0.5-0.2-77-53	0.5-0.2-77-53	-	-	8	0.2-0.26
V 2.0	0.5-0.2-58-53	0.5-0.2-75-53	0.5-0.2-77-53	0.5-0.2-58-53	0.5-0.2-58-53-0.4	13	0.16-0.22
V 3.0	1.34-0.3-88-61	1.34-0.3-106-61	1.34-0.3-106-61	1.34-0.3-85-61	1.34-0.3-85-61-0.3	13	0.33-0.40

[a] W:channel width, H:channel height, L:channel length, N:number of channels

[b] W:channel width, H:channel height, L:channel length, N:number of channels, D: hole diameter

Therefore in this study, the version V 3.0 and V 4.0 (similar to V 3.0 but fabrication through 3D printing of metals) are addressed. Regarding the scale-up of the surface of the μ-EnH_2ancer V 3.0, the limiting factors were construction constraints due to chemical etching carried out by Ätztechnik GmbH for forming microchannels. It is worth mentioning that this fabrication size constraint was

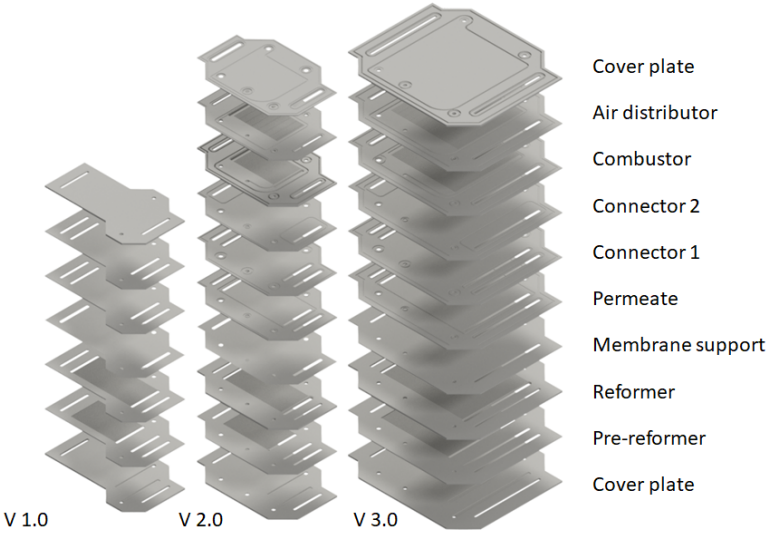

Figure 3.6: The evolution of the μ-EnH_2ancer from version V 1.0 to V 3.0 is marked by notable changes. In the case of V 1.0, testing was conducted under isothermal conditions. However, for version V 2.0, the focus shifted to incorporating a combustion plate reactor into the design, and V 3.0 aimed at increasing the area of reacting surface to volume of the module.

also encountered with 3D-printing devices for so-called version V 4.0. The latter will be discussed in Chapter 7.

In Figure 3.6, it is evident that the V 1.0 functions in an electrically heated, featuring an 8 mm overall thickness (module volume of approximately 61.03 cm^3) and generating $472\,\mathrm{N\,m^3\,m^{-3}\,h^{-1}}$ of H_2 per reactor volume. In V 2.0, while microchannel specifications remained constant, the addition of extra functional plates prompted a design modification, including the incorporation of two more plates (combustor and air distributor) into the module. The decision to include an air distributor was driven by the goal of uniformly distributing oxidant (air/oxygen) to the catalyst bed on the combustion plate to mitigate potential hot spots during

catalytic combustion reactions. Additional details are provided in the patent application by Pfeifer et al. [105]. This alteration resulted in an increase in module weight from $0.488\,\mathrm{kg}$ to $0.959\,\mathrm{kg}$ and a thickness increase to 13 mm (one combustion unit per membrane reformer). Notably, the ratio $(A_{reformer_{cat,bed}}/A_{plate})$ (area of the place for catalyst or membrane to the total area of the plate), representing the active area for H_2 production (e.g., reformer plate) compared to the surface area of the cover plate (top plate as a reference), decreased significantly from V 1.0 to V 2.0, declining from 0.26 to 0.22 for the reformer plate. This ratio serves as a crucial criterion when expanding the module's surface area. In the case of V 3.0, this factor reaches $0.4\,\mathrm{m}^2\,\mathrm{m}^{-3}$, presenting an advantageous aspect of the design by efficiently utilizing the area on each plate and constructing highly compact modules. This is not the only feature of the MR developed in this study. For the first time, advanced techniques for printing the plates of the μ-EnH_2ancer made of Crofer 22 APU have been utilized, providing flexibility between design and manufacturability with the aim of enhancing mass and heat transfer (V 4.0). This will be discussed in detail in Chapter 6 and Chapter 7. These three designs might have different features. The V 1.0 was constructed using Nicrofer alloy Nicrofer 3220H/Alloy 800 (1.4876, Thyssen-Krupp VDM, Germany), primarily composed of 30-32% Ni, 19-22% Cr, 46-51% Fe, and trace amounts of Mn, Si, Cu, Al, and Ti. However, in the V 2.0 and V 3.0, Crofer 22 APU was used for the plates.

Various methods of heat generation, primarily categorized to provide the heat for MSR (see Figure 3.7). However, when accounting for several device-level design constraints, such as compactness, energy efficiency, and long-term reliability, the range of suitable heat sources becomes limited. For instance, the heat source must be energy-dense to provide rapid heating while minimizing energy consumption to ensure efficient operation. Lastly, the source should offer long-term reliability, particularly for applications requiring all-day operation, as frequent component replacements are impractical.

While resistive heating both direct and indirect is clean and efficient, with rapid heat-up times and precise temperature control (see Figure 3.7), it can consume significant energy over extended periods. Other methods, such as solar-based

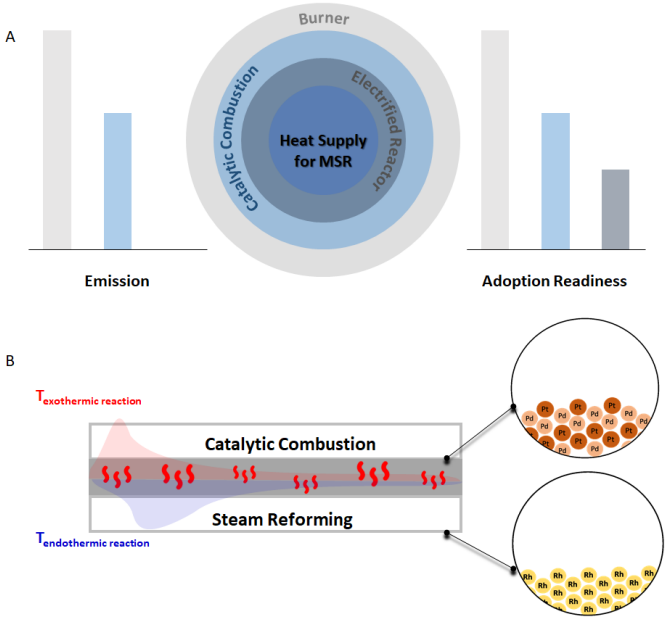

Figure 3.7: Different strategies to supply the heat needed for MSR.

heating, are less equipment-intensive but suffer from slower heating rates and intermittent functionality, limiting 24-hour operation.

Exothermic chemical reactions, like combustion-based heating, offer a potential solution to these challenges. With a higher energy density due to the high heating value of fuel, combustion can provide rapid and high-temperature heating.

As previously mentioned, traditional methods of providing the necessary heat for MSR involve using furnaces that burn non-catalytically NG with air. However, this approach has some limitations, which will be addressed here. The efficiency of endothermic processes is highly influenced by heat distribution. According to Le Chatelier's principle, the thermodynamics of steam methane reforming (Reaction 2.1) are negatively affected by pressure [106]. Yet, major consumers of syngas, such as ammonia, methanol, and Fischer-Tropsch synthesis, typically operate

at high pressure. To optimize plant economics, MSR is performed at elevated pressures (20-40 bar) to reduce overall compression costs [107]. Consequently, temperatures between $850\,^{\circ}\mathrm{C}$ to $950\,^{\circ}\mathrm{C}$ are necessary to achieve adequate methane conversion (see Figure 2.2).

Over decades, industrial reformers have evolved into systems with long, narrow tubular reactors where heat is supplied by combustion and transferred primarily via radiation [108, 109]. Despite reactor tube diameters being less than $12\,\mathrm{cm}$, heat transfer is often the limiting factor in performance rather than reaction kinetics. The extreme conditions of the process (over $850\,^{\circ}\mathrm{C}$, high steam partial pressures, and $30\,\mathrm{bar}$) require materials with ceramic properties which is achieved by additional coating of protective ceramic layers to ensure safe operation, such as resistance to corrosion and low thermal expansion. To meet these demands, expensive "superalloys" like Incoloy (FeNiCrAlTiC) are used for the reactor tubes, while catalyst pellets are made from a highly porous alumina-based support. However, the low thermal conductivity of these materials creates steep temperature gradients within the reactor walls and catalyst bed, limiting catalyst utilization [107, 110, 111].

In a typical industrial reformer, the catalytic effectiveness factor is between 2-10%, meaning that less than 10% of the catalyst's potential activity is utilized [31, 110, 112]. These steep temperature gradients induce thermal stresses, shortening reactor lifespan [107], and necessitating long startup times for the safe operation of industrial reformers [110]. Furthermore, high-temperature thermal gradients increase the risk of carbon deposition, which negatively impacts plant operations [113]. To mitigate this risk, the steam-to-carbon (S/C) ratio is carefully managed. Adding more steam improves methane conversion and lowers the risk of carbon formation, but higher S/C ratios also increase the energy required to heat the excess steam. Therefore, precise heating is essential to avoid hot spots, carbon deposition, and thermal stresses. The reactors are heated in large furnace chambers with strategically positioned burners to ensure optimal heat distribution. The combustion must occur several hundred degrees above the reaction temperature to generate the necessary heat flux, typically $60\,\mathrm{kW\,m^{-2}}$ to $150\,\mathrm{kW\,m^{-2}}$ [108, 110, 114]. The flame jets are often directed away from or

along the reactor tubes, transferring heat primarily through radiation and convection. Although uniform heat flux can be achieved, this comes at the cost of large furnace chambers, where typically less than 2% of the total volume is occupied by catalyst [108, 115]. Modern MSR plants operate with efficiencies (based on the lower heating values of H_2 to that of fuel) close to 95% [110, 116, 117], largely due to effective heat recovery and steam management, as the primary reformer only transfers about 50% of the fuel's energy to the process gas, with the remainder lost as latent heat in the flue gas at temperatures over $1000\,^{\circ}\mathrm{C}$ [108, 114]. The large furnace chambers, gas compression, and extensive heat recovery make large-scale operation economically favorable, a concept known as the economy of scale, which limits the feasibility of smaller, decentralized plants.

From an environmental standpoint, the combustion of fossil fuels for the highly endothermic reaction results in significant CO_2 emissions. A gas-fired MSR reformer produces between 7.7 and 10.4 kg of CO_2 per kg of H_2, depending on factors such as thermal efficiency, fuel, and feed, with 5.5 kg CO_2/kg H_2 coming from the stoichiometric reaction itself at full conversion [108, 118, 119]. To overcome the preheating demands typically associated with combustion, catalytic combustion can be introduced as an alternative heat source. Furthermore, in case of mitigating the emissions, by combining catalytic combustion with electric heating based on the renewable energy might be another option. This hybrid approach presents a promising solution for reducing electrical consumption in off-grid environments and other similar applications. However, this study focuses at the development of more efficient catalytic combustors (CR) and discussion over other techniques is out of the scope of this study. The structure for housing of such a system is based on the micro-reactor technology which in the following section will be detailed. In MSR, part of the fuel being reformed is combusted to meet the heat demands of the endothermic reaction [120]. These reactions are thermally integrated in spatially separated microchannels (see Figure 3.7 B), promoting effective heat transfer and resulting in a design similar to a plate heat exchanger. Such reactors demonstrate enhanced catalytic productivity compared to conventional fixed-bed or fluidized-bed reactors of similar size, due to surface-to-volume ratios that are $10\,\mathrm{m^2\,m^{-3}}$ to $100\,\mathrm{m^2\,m^{-3}}$ higher than their traditional

counterparts [121–125]. Additionally, they are modular, allowing for scaling by either externally "numbering-up" processors in parallel [126, 127], or more efficiently, by increasing the length and number of channels internally [128]. The high-efficiency heat transfer is attributed to the fact that reactions occur on or near the highly conductive (typically metallic) reactor walls, such as in microchannels separated by walls with deposited catalysts [129–131]. This design enables highly efficient heat recovery from exothermic reactions or heat supply to endothermic reactions while minimizing heat loss becomes crucial due to the enhanced thermal properties [132].

In terms of safety, microchannel reactors often benefit from structured flow paths, where flame combustion is suppressed due to the narrow channel dimensions (less than 1000 μm) and the high gas velocities through these channels [121]. Heat transfer to the reforming reaction requires a temperature gradient across the gas-tube-gas interface [129]. A greater thermal resistance at this interface necessitates a steeper temperature gradient, which in turn reduces process efficiency. Additionally, the flame heating used in industrial reformers can lead to the formation of nitrogen oxides due to the high temperatures of the flames [124, 129].

3.6 Aim of this thesis

Since the goal of this MR integrated with a CCR for autothermal operation is to enable decentralized applications and scale-up through modular replication, it is essential to design a module that maximizes the hydrogen production rate per reactor volume (or membrane area) with high mechanical and thermal stability. The core component of such a compact MR is a hydrogen-selective membrane that remains impermeable to other gases under operating conditions. While an ultra-thin Pd foil (12 μm thick) used in previous MR designs (V1.0) demonstrated excellent performance, its low mechanical stability and high production cost limit its practicality. This study therefore focuses on developing a cost-effective process for fabricating a Pd-based composite membrane with a Pd layer thickness of approximately 10 μm on a porous metallic substrate.

The key objectives of this study are:

- **Development of a thin, high-performance Pd-based composite membrane** with high hydrogen permeability, mechanical robustness, and thermal stability. Porous sintered metals such as Crofer 22 APU are one of the ideal substrates due to their compatibility with high-precision laser welding for module assembly and their compatibility with other components of the MR. To prevent Pd diffusion into the substrate, a DBL coating will be applied to the sintered metal carrier, ensuring long-term membrane stability. The Pd coating is carried out through plasma spraying, which is a fast coating technique with less chemical waste.
- **Development of a highly active catalyst layer for MSR and CCR** using flame spray pyrolysis (FSP) as catalyst synthesis method followed by screen printing (coating technique). A critical challenge lies in balancing hydrogen generation on the catalyst surface with hydrogen removal via the Pd membrane. Rh on Al_2O_3 and Pd-Pt on Al_2O_3 are synthesized and coated onto the microchannels for MSR and CCR.
- **Exploration of advanced manufacturing techniques, such as metal additive manufacturing (AM)**, for fabricating MR components, with emphasis on hybrid porous-dense plates that serve as membrane supports or gas distributors for CCR.
- **Development of a 2D model for the MR-CCR integrated system** to enable detailed analysis of potential concentration and temperature gradients. Moreover, this model can predict results in scenarios where experiments are not feasible.

4 Synthesis, preparation, assembly, and testing of Palladium-based membranes

This chapter focuses on preparation of composite planar membranes to be integrated into a membrane reformer. It starts first with idea of a composite membrane consists of tape-casted metallic supports which is coated with a DBL layer using dip-coating followed by Pd coating by plasma spraying. The final goal is to synthesis of a defect-free composite pd membrane with a thickness of Pd approximately $10\,\mu\mathrm{m}$, firstly, using small plates (only for lab tests) and then scaling to size needed for the membrane reformer.

4.1 Membrane concept based on the tape-casted supports

Among supported Pd-based membranes, metallic supports are generally preferred due to their weldability, which facilitates the integration of porous metal-based composite membranes into reactors. Considering the metallic supports, porous stainless steel supports are commonly utilized due to their widespread availability, excellent chemical resistance, and reasonable cost. However, more highly alloyed steels are required for demanding applications such as methane steam reforming. One of the promising metallic alloys for Pd-based composite membranes was ITM, developed by Plansee SE [36]. Generally , oxide dispersion-strengthened chromium-rich ferritic alloys like Fe-26Cr (Mo, Ti, Y_2O_3) [133] and Crofer 22

APU are particularly advantageous. These alloys offer desirable qualities such as strong corrosion resistance, low creep rate during operation, and compatibility in terms of thermal expansion coefficient with the YSZ support and the Pd membrane (see Figure A.1). However, since this alloy was not provided by the supplier, the alternative alloy (Crofer 22 APU) was used in this study.

The initial batch of Pd-composite membranes was formulated using Crofer 22 APU substrates. The process involved the initial preparation of porous sheet metals through tape-casting at the IEK-1 of Forschungszentrum Jülich.

Briefly, tape casting is often used for the production of substrates. In the tape casting process, the slurry runs onto a plastic film, which is continuously passed under the doctor blade at a controlled speed. A layer of slurry is formed on the plastic film (see Figure 4.1), whose thickness is adjusted with a height-adjustable doctor blade. This creates a smooth, even film. The thickness of the cast substrate depends on the adjustable gap of the doctor blade, the feed speed, the viscosity of the slurry, and the slurry level in the casting basin (hydrostatic pressure). After casting the slurry, the solvent is removed from the metal foil by drying. After drying, a self-supporting, flexible metal foil is obtained, which can be cut into any shape. Tape casting offers high production capacity and thus cost-effective production. Specifics about the tape casting procedure can be referenced in [134]. Subsequently, the fabricated porous sheets underwent laser welding at the IMVT to create a hybrid substrate. The cold-rolled sheets of Crofer 22 APU, with a thickness of 1 mm, were cut into rectangular shapes (refer to Figure 4.8) during this step and then welded to the porous sheets.

Selecting appropriate materials for the sintered metal support and the diffusion barrier layer is crucial for ensuring the long-term stability of the fabricated composite membrane. Table 4.1 displays a compilation of commercially available metallic supports from various companies. The criteria to consider when choosing metallic support include thermal expansion coefficients (e.g. ferritic stainless steels), compatibility with other membrane components like Pd, final surface quality for Pd coating, mechanical and chemical stability for applications such as steam reforming for hydrogen production, and thermal stability for long-term

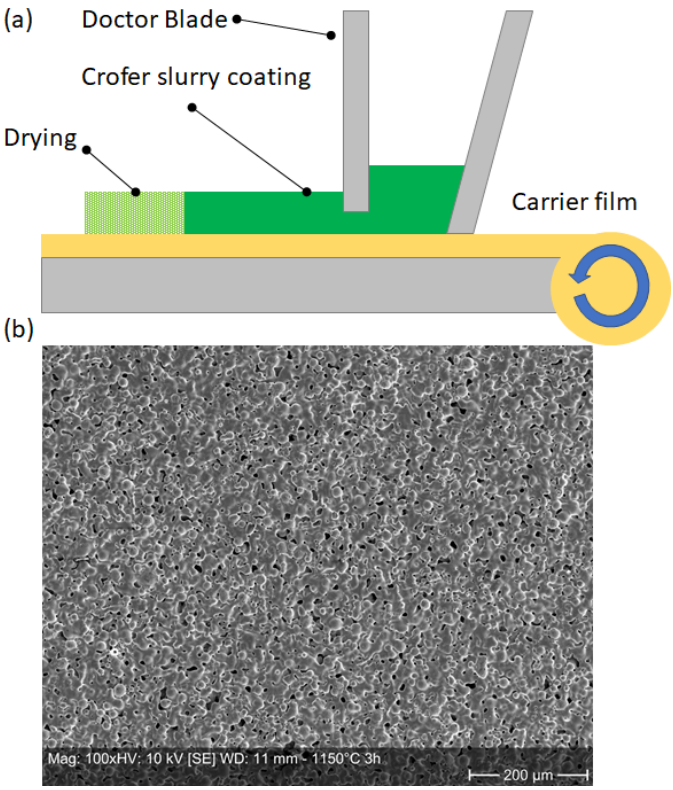

Figure 4.1: (a) Schematic of the tape-casting process for the fabrication of porous metallic substrates using Crofer 22 APU slurry, (b) Top view of the sintered tape-cast substrate after being treated under Ar at 1150 °C for 3 hours.

operation at moderate and elevated temperatures. For instance, Kot demonstrated that Crofer 22 APU steel combined with 8-YSZ is a suitable material combination for fabricating substrates for palladium composite membranes [134]. ITM support, being a ferritic stainless steel, also shows good compatibility. However, this study focuses on the combination of Crofer 22 APU, 8-YSZ, and Pd. Dip coating was used to coat the porous metallic supports at the IEK-1 of Forschungszentrum Jülich. The recipe and details can be found in [135].

Table 4.1: The thermal expansion coefficient of the principal elements in a metallic composite, Pd-based membrane designed for H_2 separation.

Material	Property	CET ($1 \times 10^{-6}\,K^{-1}$)	Ref.
Pd	selective towards H_2	12.26 at 525 °C	[136]
8-YSZ (TZ-8Y Tosoh)	reducing pores for Pd coating, metal inter-diffusion mitigation	10.5-10.7	
Crofer 22 APU	membrane support, MR body	10.3-11.2 at 500 °C	[137]
Hastelloy X	metallic filter	14.5-15.5 at 500 °C	[138]
Inconel 600	metallic filter	14-15.5 at 500 °C	[139]
AISI 316L	metallic filter	18 at 500 °C	[140]
AISI 304 SS	metallic filter	18 at 500 °C	[140]

4.2 Experimental set-up for gas tests

The arrangement of the experimental configuration employed for the investigation of gas separation tests on Pd membranes is delineated in Figure 4.2. The introduction of nitrogen and hydrogen into the membrane module was achieved through mass flow controllers (Instrument, Model SLA5800 series, thermal mass flow). The rates of permeate and retentate flow were assessed via a soap bubble flow meter or flow meter (MesaLabs Bios DryCal Definer 220) for inert gases e.g. N_2. The pressure on the retentate side was regulated using a Flowserve (Serie SmallFlow - 080037) regulating valve, a pressure sensor Bauemer (0-20 bar), and PID controllers (Eurotherm 4300) using Labview (National Instrument). During all experiments, the permeate side was consistently maintained at atmospheric pressure. The composite membranes were securely positioned within an electrically heated metallic apparatus made of stainless steel 1.4876 (Nicrofer 3220 H). The membranes were tightly enclosed using graphite gaskets for sealing purposes. This combined setup, along with the graphite gaskets, effectively sealed the membranes and hindered any potential leakage, as illustrated in Figure A.2 in the Appendix. The enclosure was subjected to electrical heating using three heating cartridges on each side. Both the feed gas and the optional sweep gas underwent preheating to match the temperature of the membrane apparatus.

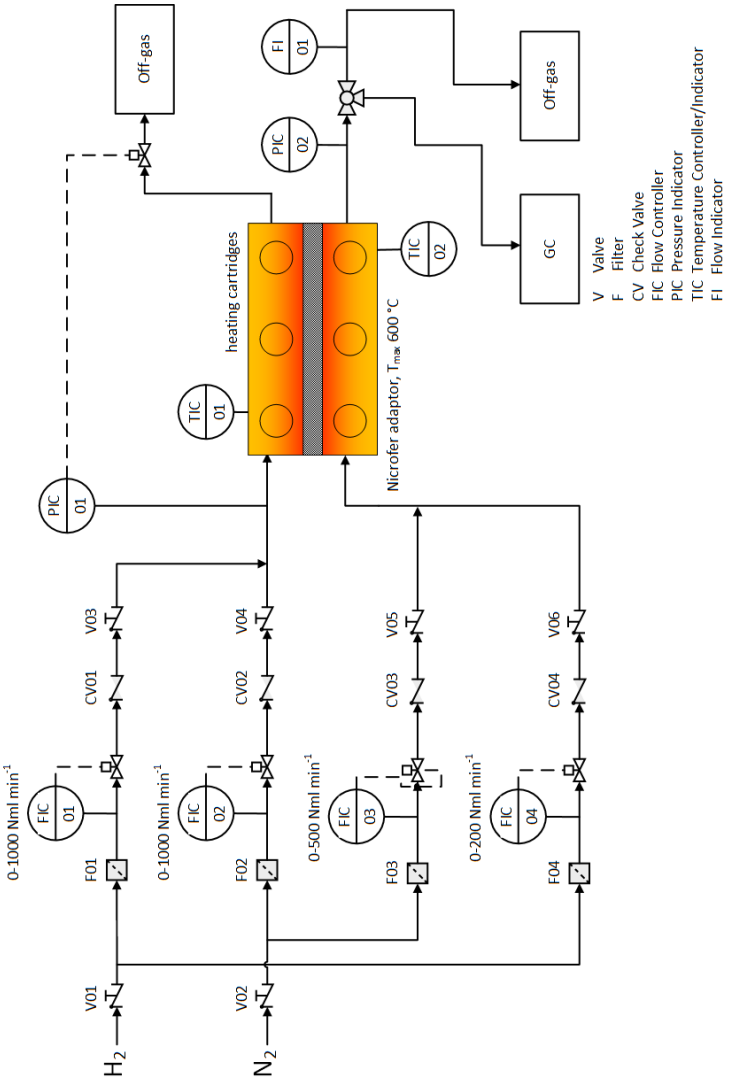

Figure 4.2: Schematic representation outlining the setup of the test apparatus for conducting experiments on the permeation of gases.

At the onset of the experiments, the membrane apparatus was gradually heated to the desired temperature at a rate of 1 $^{\circ}\mathrm{C}\,\mathrm{min}^{-1}$. During this period, nitrogen was passed through both the feed side and the permeate side for purging. Following this step, the nitrogen feed flow was gradually reduced to zero, and hydrogen was introduced into the feed side at a slow rate. The hydrogen flux was allowed to stabilize over the next 24 hours.

To ascertain the activation energy associated with hydrogen permeation, exclusively hydrogen with a relatively high volumetric flow rate (> 250 $\mathrm{mL}\,\mathrm{min}^{-1}$) was introduced on the feed side. No sweeping gas was employed on the permeate side, ensuring distinct hydrogen partial pressures on both sides of the membrane. Before each experiment was conducted under specific pressure and temperature conditions, the membrane was allowed to stabilize for 24 hours at the highest pressure and temperature within the defined parameter range (which varied for distinct membranes due to varying materials and thickness), unless otherwise specified in the pertinent section.

4.3 Plasma spraying coating

4.3.1 Motivation

Various preparation techniques for Pd-based membranes have been reported in the literature. Among these, electroless plating is the most commonly employed method for producing Pd membranes on a laboratory scale. However, methods that yield high-quality membranes in a laboratory setting may not be ideal for industrial applications due to factors such as lengthy and costly manufacturing processes [141]. High velocity oxy-fuel flame (HVOF) spraying is an attractive method for creating Pd layers in just a few minutes, generating less chemical waste compared to other techniques. This makes it particularly suitable for industrial applications. Plasma spraying typically employs metallic feedstock powders with particle sizes ranging from 20 to 60 $\mu\mathrm{m}$, resulting in thicker palladium membranes, usually between 45 and 60 $\mu\mathrm{m}$ [142, 143]. However, these membranes often exhibit poor

permeability due to their high thickness, and at times, they display insufficient selectivity towards hydrogen due to porosity and film instability. To address this issue, using nanosized powder feedstock for thinner coatings is an alternative. Yet, dry nanosized powders tend to cause particle agglomeration leading to amorphous films with high porosity. Moreover, they are pyrophoric due to their high surface area, which makes them prone to ignition when exposed to oxygen. For particles smaller than 1 μm, employing a solvent carrier is necessary to inject the powder into the plasma. The solvent evaporates within the plasma core, while the solid particles melt, accelerate, and impact on a substrate, forming a coating. Therefore, this process is referred to as suspension plasma spraying (SPS) [144–148]. Lee et al. [149] utilized colloidal spray deposition of Pd particles in the 100–300 nm range using water with a dispersing agent Darvan C as a solvent, accompanied by additional heating during spraying at 110 °C. This approach resulted in porous YSZ-supported Pd films with controllable homogeneous thickness (about 5–11 μm) and pores in the range of 3–7 μm after subsequent sintering.

In a similar study, Boeltken et al. [141] attempted a comparable method using a higher viscosity solvent in atmospheric plasma spraying (SPS). Particles ranging from 250 to 550 nm were mixed in diethylene glycol monobutyl ether stabilized (DGME) with 10 wt.% ethyl cellulose, and the suspension was heated at 65 °C for 24 h. Films of about 10 μm were formed on alumina and porous stainless steel with YSZ coatings used as a diffusion barrier layer, showing promising results in terms of hydrogen selectivity. However, both approaches faced challenges related to the stability of the suspensions, and no information was provided regarding the microstructure of the fabricated palladium membranes when using liquid suspension plasma spraying. An alternative technique involves using dried macro particles under vacuum conditions, referred to in this study as vacuum plasma spraying (VPS). Therefore, SPS is ideal for forming thin layers, while VPS can create coatings with lower porosity, higher density, and a higher deposition rate without particle oxidation. All the plasma spraying coatings were carried out by the project partner, Institute of Engineering Thermodynamics of Deutsches Zentrum für Luft- und Raumfahrt (DLR) in Stuttgart. In the following sections, firstly, it is focused on a Pd coating with a submicronic microstructure containing

a significant amount of low-angle grain boundaries (LAGBs) while suppressing high-angle grain boundaries (HAGBs). This is achieved using SPS and VPS techniques. Both processes were developed to produce dense Pd membranes on porous supports with the primary goal of achieving an optimal grain size (100–500 nm) with LAGBs for a stable membrane. Subsequent work will evaluate this microstructure for hydrogen flux and selectivity at operating temperatures in the hydrogen atmosphere. Then, the gas test results of the prepared test modules are presented and discussed.

4.3.2 Plasma spraying experiments

The thermal plasma generated in this study was produced through a direct current (DC) arc, resulting in a plasma jet with temperatures ranging from 8000 to 14,000 K and particle velocities in the range of 100 to 500 $\mathrm{m\,s^{-1}}$.

The temperature and momentum transfer from the plasma to the particles induced the melting of powder particles and their subsequent acceleration. The properties of these moving particles, along with the substrate temperature, were carefully controlled to achieve high bond strengths, low porosity, and the desired microstructure of the Pd coating. Typically, feedstock powders in thermal plasma processes are within the range of 10 to 100 $\mu\mathrm{m}$. Figure 4.3 provides a schematic illustration of the path taken by the liquid suspension in the SPS coating process. For comparison, the VPS chamber is depicted, demonstrating the process under vacuum conditions and utilizing pure micron-sized powder instead of a liquid suspension.

In the SPS experiments, investigations into the supply and injection of the suspension into the plasma jet were initially conducted using a pure solvent. It was crucial to fine-tune the injection parameters to ensure that the momentum of the particles matched that of the plasma jet. This adjustment aimed to allow the suspension to either bounce back from the plasma surface, traverse the plasma entirely, or reach the core of the jet, as opposed to other paths [151]. A summary of the impact of the injection pressure from the argon-pressurized tank (4 vs. 9

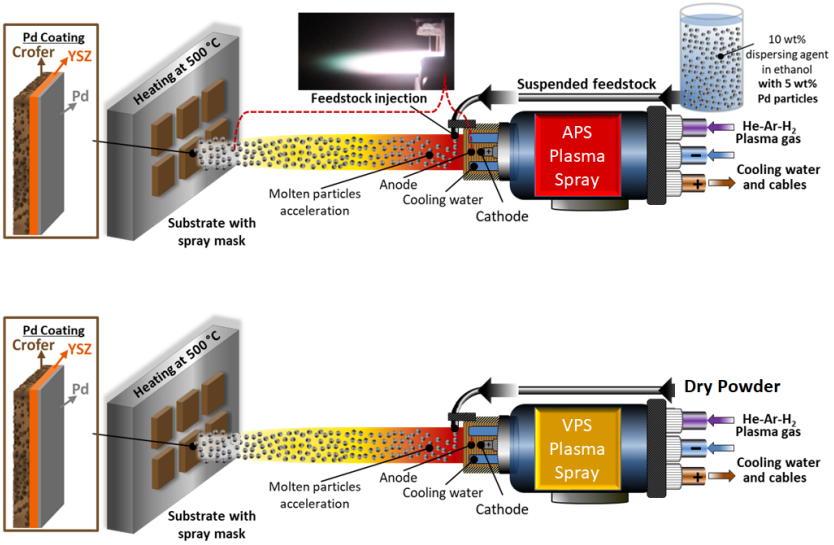

Figure 4.3: Schematic representation of the SPS (or APS) technique under atmospheric pressure (top) and VPS using dry powder of Pd (bottom) for preparation of Pd composite membranes [150].

bar) to deliver the suspension to the jet and the use of the injection nozzle aperture (0.2 mm vs. 0.3 mm) can be found here in our study [150]. It was determined that a 9-bar argon stream with a nozzle size of 0.2 mm represented the most suitable injection condition.

Subsequently, the suspension/powder was injected into the plasma, which utilized a Sulzer-Metco TriplexPro 200 torch at a constant pressure of 9 bar. All plasma parameters, including direct current (DC), argon, helium, and hydrogen flow, were carefully adjusted to optimize the treatment of the palladium particles, aiming to achieve a dense, thin coating [152]. Crofer 22 APU substrates coated with 8-YSZ were secured on the chamber holder and heated up to 500 °C throughout the entire process. The subsequent heating of the substrates facilitated better melting of the low-concentration particles, resulting in a denser microstructure in the final coating [150].

4.3.3 Palladium powders

In this study, two distinct types of powders were used including a nanopowder from Daiken Chemicals for the SPS coating suspensions and a micron-scale powder from C. Hafner GmbH for the VPS coating. Purification and particle size of the commercial palladium powders in forms of as-recieved were analyzed and the results are shown in in Figure 4.4. The Daiken Chemicals powder exhibited an average particle size of 150 nm, with some elongated areas and agglomerations. On the other side, the powder form C. Hafner GmbH had an average size of 8 $\mu\mathrm{m}$ with grain variations ranging from 1 to 16 $\mu\mathrm{m}$. ImageJ software facilitated the analysis of around 500 particles from various SEM images for each powder. Figure

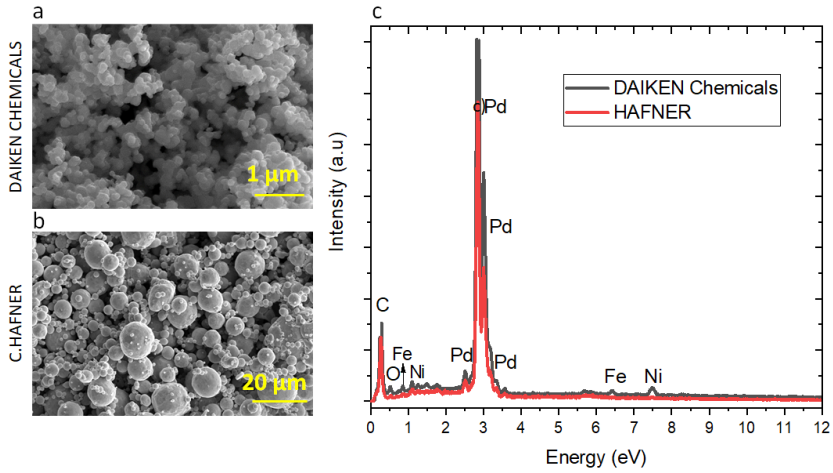

Figure 4.4: SEM images of the powders were captured using a voltage of 20 kV, a current of 1.6 nA, and an ETD detector. These images illustrate the average particle characteristics of the (a) Daiken Chemicals Pd powder, (b) C. Hafner powder, and (c) presents the EDX analysis of the powders, revealing insights into their purity levels [150].

4.4 presents the corresponding elemental analysis by EDX for both powders. In the case of the Daiken Chemicals powder, small impurities of iron and nickel

were detected, each constituting less than 2 wt.%. Both materials demonstrated a highly dense microstructure with minimal pores between the grains. To enhance the stability of the suspension in the case of the APS technique and prevent particle sedimentation while avoiding nozzle blockage during injection, TEGOMER DA 850 from EVONIK was chosen as an additive in pure ethanol. The viscosity of the final suspension, containing 10 wt.% Tegomer DA850, was measured using RheoSense μVISC and found to be approximately 1.8 $\mathrm{mPa\,sec}$ at room temperature. The solution exhibited a pH of 6.5, and its density was measured at 1.05 $\mathrm{g\,cm^{-3}}$.

The stability of the prepared suspension was crucial to meet the quality requirements for SPS coating. Given the short duration of the SPS process, it might be satisfactory enough if the suspension remains stable for several hours. To assess stability, photos were taken over a week. The suspension underwent a 30-minute treatment in an ultrasonic bath before initiating the process to simulate SPS conditions. It was found that the suspension exhibited significant stability for the first few hours, making it suitable for SPS as the coating is finished in a few minutes. Initial segmentation appeared after 5 h, with substantial segmentation after a few days. Importantly, any remaining suspension after the SPS process could be recovered for potential future use, if necessary [150].

4.3.4 Results of coated layers with SPS and VPS

In Figure 4.5, sample A, prepared using the Daiken Chemical Pd powder suspension in SPS, shows the density of the sample and an approximate coating thickness of $\approx 10\ \mu\mathrm{m}$. The 8-YSZ layer, shown in this Figure, showed a thickness of $\approx 25\ \mu\mathrm{m}$. The porosity of the Crofer 22 APU substrate is evident, and Figure 4.5 e, featuring EDX elemental mapping analysis, delineates the different layers and their well-defined interfaces.

In the VPS coating (Figure 4.5 c, d), fewer pores are apparent, and a denser structure is observable. The estimated thickness for this sample was also ≈ 10

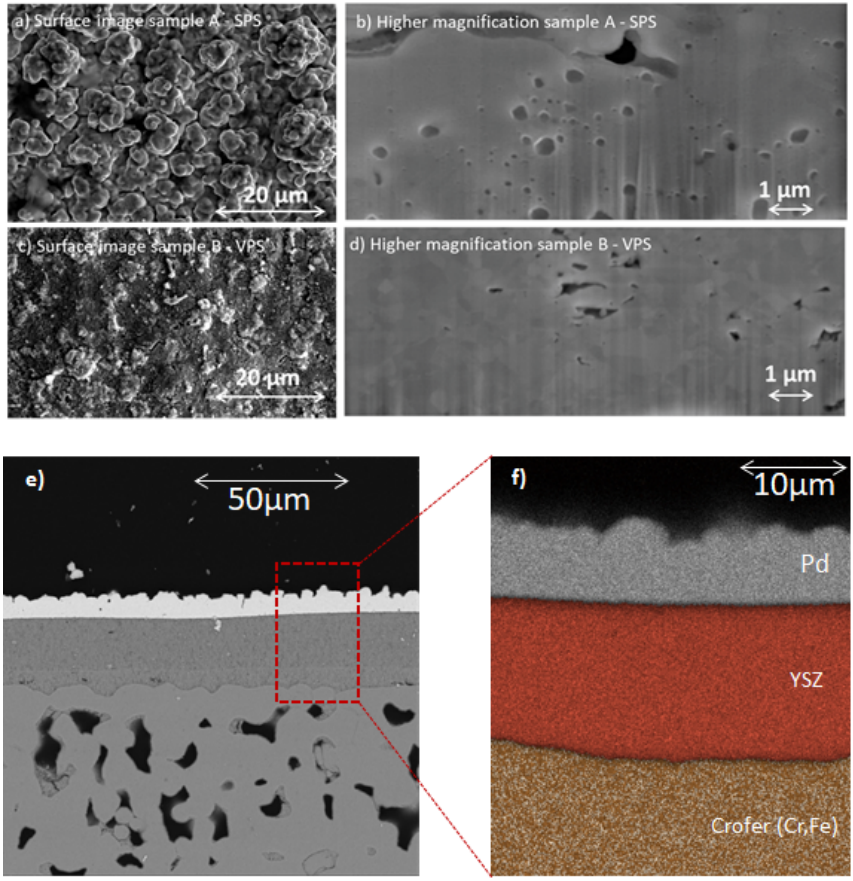

Figure 4.5: SEM images APS and VPS samples with a 30 kV, 1.6 nA beam. The surface morphology illustrates the layer roughness for SPS (a) and VPS (c) samples. Cross-sectional views of the SPS (b) and VPS (d) layers were also analyzed. Additionally, a backscattered detector cross-section image (e) and EDX elemental mapping analysis (f) were conducted for the SPS sample [150].

μm. Notably, in both cases, the pores had a diameter of less than 1 μm, and where they were isolated and not interconnected.

Figure 4.6 reveals the presence of 8-YSZ elements on the surface of the Pd layer coated with the VPS recipe, prompting inquiries about potential damage to the 8-YSZ during SPS. A point EDX analysis at the lower edge of the separated Pd layer indicated traces of Zr and Cu. The presence of Cu might be attributed to the copper mask employed to cover the samples before the SPS process.

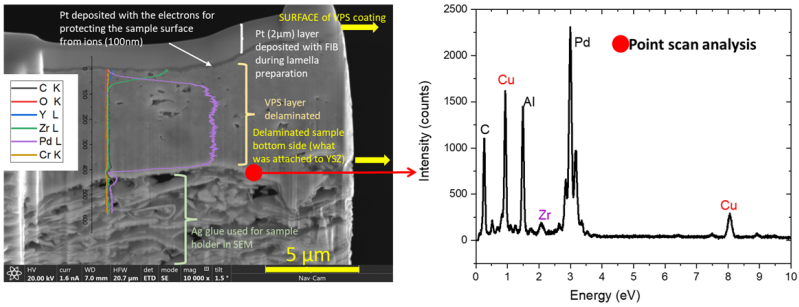

Figure 4.6: a) SEM images of the VPS samples with a 20 kV, 1.6 nA beam. This sample is the delaminated layer of Pd, lamella prepared for TEM analysis. b) Elemental mapping is shown as line and point in this Figure for the Pd layer and bottom of the Pd layer, respectively.

To explore the grain boundaries of the palladium coatings, a detailed examination of Sample APS was conducted through high-resolution imaging. The results revealed a scenario where two grains merged into a single particle. The grain boundary was distinctly identified along the line where a change in the fast Fourier transformation (FFT) of both grains occurred. In Figure 4.7, the depiction of two grains with their respective FFT highlights differing orientations, underscoring the importance of meticulous analysis for accurate grain size determination. To achieve this, numerous dark field images were acquired by tilting the beam to various orientations, ensuring that only one orientation was visible under the aperture during each instance. This rigorous procedure was consistently applied to both samples.

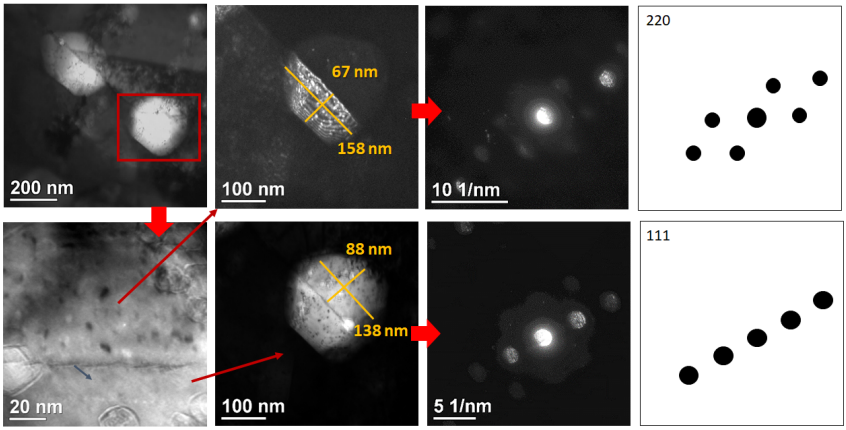

Figure 4.7: TEM analysis was conducted on two grains with distinct orientations in the APS sample [150].

Figure 4.8 presents the bright field images of both samples after the coating. In Figure 4.8 b for Sample APS and Figure 4.8 e for Sample VPS, dark field images are displayed, illustrating grains of various orientations. Each color corresponds to a distinct orientation, highlighting the random orientation of nanograins in both cases. For the APS sample, an average grain size of 540 nm was determined, with a broad range spanning from 1.2 $\mu\mathrm{m}$ to 190 nm. On the other hand, the VPS samples exhibited a slightly smaller grain size, averaging 400 nm, with grains ranging between 650 nm and 110 nm. The selected area diffraction patterns (SADP) of both samples affirmed the purity and crystallinity of the coatings, indexed to pure palladium.

Moreover, as part of the study, these samples were subjected to an H_2 atmosphere at 300 $^\circ\mathrm{C}$ and 20 bar. The findings revealed an expansion of grain boundaries from 100-500 nm to 536 nm for the APS sample, while it increased to 720 nm for the VPS sample. More in-depth discussions and detailed results can be found in our study [150]. While grain boundaries in APS and VPS samples may influence Pd membrane performance in terms of permeability, other critical factors such as layer thickness (affecting mass transfer resistance) and adhesion

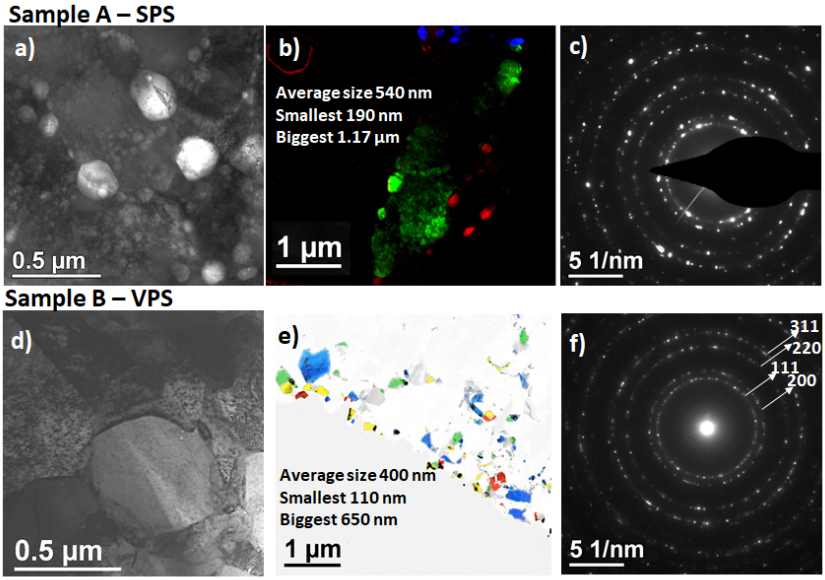

Figure 4.8: TEM bright field images of the samples are depicted in (a) and (d). Many dark field images of the coatings, superposed with different colors indicating various orientations and grain sizes, are shown in (b) and (e). The SADP of each sample, confirming the presence of pure palladium, are presented in (c) and (f) [150].

(determining coating stability) must also be considered when optimizing the membrane. To evaluate these aspects, gas permeation tests were conducted on the synthesized samples, and the discussion will continue based on the results of these experiments.

4.3.5 Gas test results of APS and VPS

In this section, the gas test results for the prepared samples of APS and VPS are discussed. The tests were carried out in the set-up explained in section 4.2.

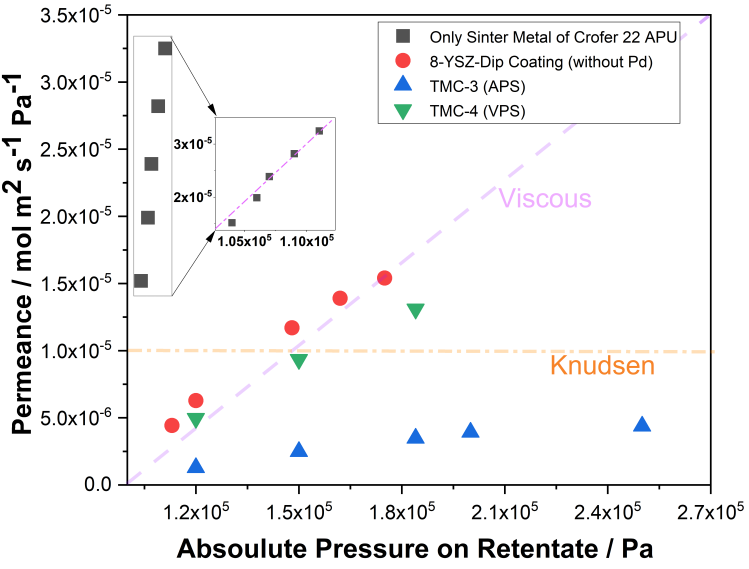

Figure 4.9: Gas test with N_2 at room temperature for samples of APS, VPS, metallic porous substrate of Crofer 22 APU (denoted as sinter metal), and dip-coated substrate with 8-YSZ.

In Table 4.2, several plasma spraying coatings were performed using two techniques, APS and VPS, on small substrates as detailed in section 4.1. In the initial examination of samples TMC-1 (APS) and TMC-2 (VPS), both were tested at room temperature under N_2 atmosphere to assess initial permeability against N_2. The coating thickness was approximately 65 μm for TMC-1 (APS) and 10 μm for TMC-2 (VPS), determined based on deposition weight. The modules were sealed with Viton sealings suitable for room temperature testing, and the adapter, explained in section 4.2, was fixed with screws. However, upon measuring the N_2 flux through the membrane, it was observed that modules TMC-1 and TMC-2 were not sufficiently dense, allowing a significant amount of N_2 to pass through. Both samples exhibited cracks and delamination after exposure to the N_2 flow, indicating an unstable coating.

Table 4.2: Samples of Pd-composite membranes prepared with plasma spraying coating with two techniques of APS and VPS in this study.

Sample	Composition	Technique of Pd coating	Thickness (μm)	Remark	Ref.
TMC-1	Crofer/8-YSZ/Pd	APS	65	delamination at RT	this study
TMC-2	Crofer/8-YSZ/Pd	VPS	10	delamination at RT	this study
TMC-3	Crofer/8-YSZ/Pd	APS	10	poor selectivity	this study
TMC-4	Crofer/8-YSZ/Pd	VPS	10	poor selectivity	this study
TMC-5	Crofer/8-YSZ/Pd	APS	10	Poor selectivity	this study
Tim Boeltken	Crofer/8-YSZ/Pd	APS	10	H_2/N_2 ideal selectivity : 45-60	[141]

For test pieces TMC-3 and TMC-4, although neither delamination nor significant cracks were observed after the test, the relatively high permeation rate of TMC-4 compared to a substrate with a diffusion barrier layer (DBL) such as 8-YSZ-Dip coating (Figure 4.9) suggests that the VPS technique may not produce dense Pd layers with plasma spraying and may not be suitable for a selective membrane for H_2 separation. In the case of TMC-3, the N_2 permeance ranged from $1.29 \times 10^{-6}\,\mathrm{mol\,m^{-2}\,s^{-1}\,Pa^{-1}}$ to $4.38 \times 10^{-6}\,\mathrm{mol\,m^{-2}\,s^{-1}\,Pa^{-1}}$ when the pressure on the retentate side was $1.2 \times 10^5\,\mathrm{Pa}$ to $2.5 \times 10^5\,\mathrm{Pa}$, respectively. Analyzing the trends of TMC-3 and TMC-4, the former exhibited behavior more dominant by viscous flow (permeance is linear dependent to pressure difference or flux is no-linearly dependent on pressure difference) rather than Knudsen diffusion, indicating significant defects in both the Pd layer and the 8-YSZ. The dominated viscous flow mechanism shows presence of micropores (larger than $1\,\mu\mathrm{m}$) that may originate from cracks or non-dense Pd coating.

In continuation, TMC-5, with a Pd layer coated using the APS technique, was tested at elevated temperatures for both N_2 and H_2. The test involved sealing the membrane with a graphite gasket, fixing N_2 flow rates at $100\,\mathrm{mL\,min^{-1}}$ on both sides and introducing a temperature ramp of $1\,\mathrm{K\,min^{-1}}$ until reaching 723 K. After reaching the set point, N_2 permeation testing was conducted, followed by transitioning from N_2 to H_2 with a ramp of $10\,\mathrm{mL\,min^{-1}}$ through a LABVIEW program. The H_2 flux versus different pressures on the retentate side was recorded, with the permeate pressure maintained at atmospheric pressure. The results are shown in Figure 4.10.

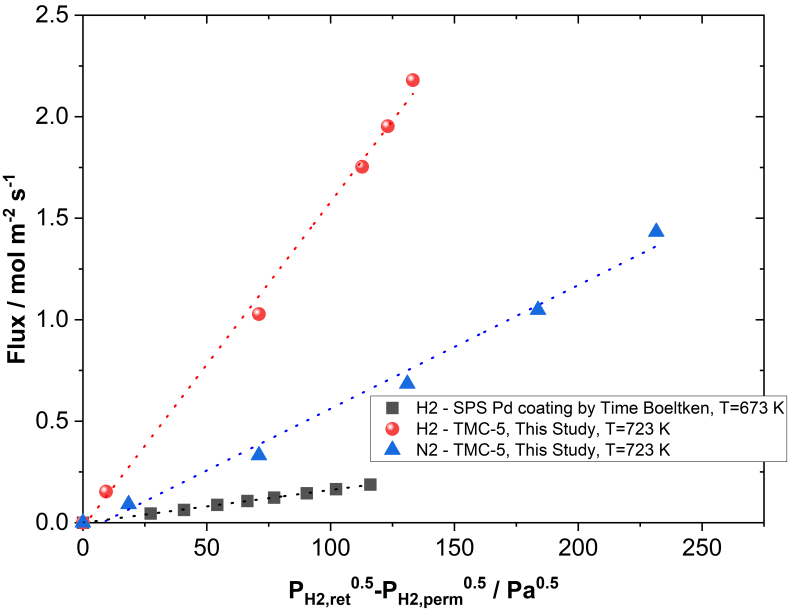

Figure 4.10: Gas test results for sample TMC-5 (APS) at T:723 K, for single gases of H_2 and N_2. For comparison, the results of the test module studied by Tim Boeltken [141] tested at 673 K is shown in the graph.

In Figure 4.10, it is evident that the H_2 flux for TMC-5 surpasses that of the sample prepared by Tim Boeltken using the SPS technique (for a pressure difference around 116 ($Pa^{0.5}$), with TMC-5 exhibiting a H_2 flux approximately one order of magnitude higher. Additionally, comparing the ratio of H_2 to N_2 flux for TMC-5 suggests a Knudsen diffusion-dominant diffusion mechanism, with a ratio of around 3.7.

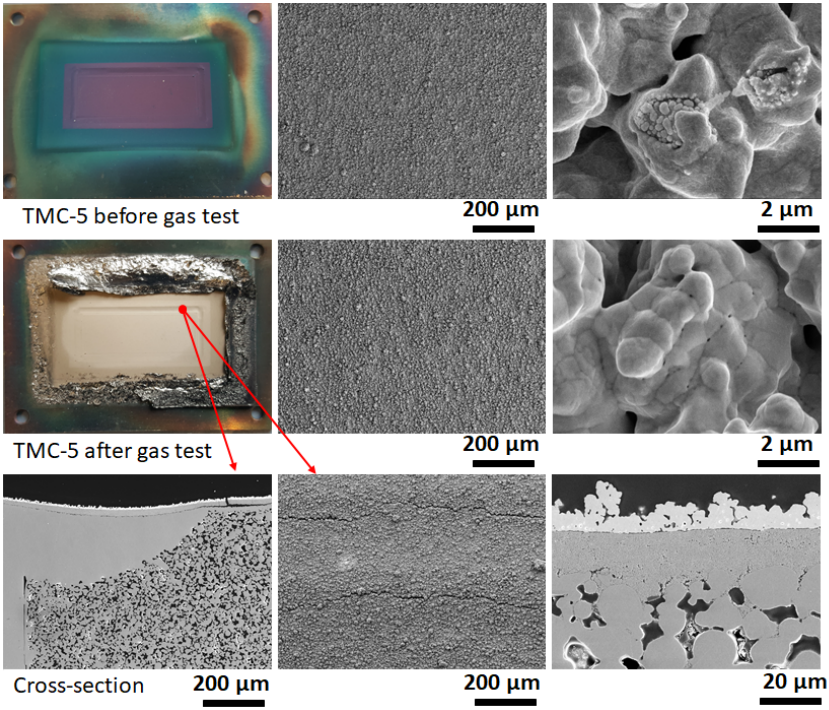

Figure 4.11: SEM analysis of TMC-5 with different magnification and views for before and after gas test of N_2 and H_2 at 723 K. Cracks were found after the assembly based on the images from the surface and cross-section view.

4.3.6 Concluding remarks on plasma spraying coating method for synthesis of Pd-composite membranes

Based on the observations made during the study of plasma spraying using two techniques, APS and VPS, several challenges were identified, which impede further progress in this particular study:

- Plasma spraying coating with both APS and VPS techniques did not result in a perm-selective membrane for H_2, as indicated by the findings in this study.
- Achieving very smooth surface roughness of DBL, with the aim of coating 8-YSZ to have Ra < 1 μm, proved challenging, leading to poor adhesion of the Pd layer to the DBL surface.
- The use of a planar metallic substrate with porous parts welded to a dense frame introduced non-uniform surfaces, particularly at the corners. This unevenness caused additional tension when clamping the test modules into the reactor, resulting in cracks.
- Both APS and VPS techniques caused the substrate plate to bend after the coating process, introducing additional stresses during assembly.

As part of this thesis, an alternative solution involving commercial thin foils of Pd and their integration using a laser-welding technique was considered to address the issues associated with the metallic substrate, and detailed discussions on this alternative approach will be presented in the following sections 4.4.

Nevertheless, for the Pd layer, the subsequent section will explain the integration of commercial Pd foils for the synthesis of the membranes, and this integration will be thoroughly discussed in the following section.

4.4 Foil-based membrane integration and assembly

In this study, two types of commercial thin foil of Pd-based membranes were employed and integrated into microstructured membrane modules. Goodfellow Special Metals provided cold-rolled Pd membranes with a thickness of 12.5 μm and Pd23Ag with thickness of 5 μm from SINTEF. The latter was only used for laser-welding tests.

In a previous study, an intensive study on integrating commercial thin Pd-based foils Pd, Pd-Cu, and Pd-Ag was carried out and the results can be found in reference [153]. This study aims at using these Pd foils to be integrated with Crofer 22APU substrates. In a previous study, the surface characteristics of the 12.5 μm Good Fellow were studied and the details are presented in [153]. The thickness of the membrane foil is provided by the manufacturer and is confirmed through cross-cut images during the analyses.

4.4.1 Assembly and sealing of Pd foils into the membrane module by laser welding

Laser welding is highly suitable for joining micro-process devices due to its advantageous attributes, such as high welding velocities and a minimized heat-affected zone. Its distinction from other methods, like diffusion bonding, lies in its applicability to various metals and high-melting alloys.

In the context of multilayer assemblies featuring mechanical microstructures, the geometry of the weld seam may be influenced by locally varying heat dissipation conditions, a consideration often overlooked at the macroscopic level. In instances of through welding, the transition to the next layer can act as thermal insulation, impacting the depth of welding penetration. The integration of thin membranes composed of different materials can introduce additional complexities, potentially leading to the occurrence of brittle phases. Nevertheless, when laser welding operates at high speeds, thermodynamic equilibrium is not achieved, and the formation of brittle phases can be circumvented.

Laser welding generally offers two modes of operation: continuous wave (CW) and pulsed mode. The cross-sectional geometry of the weld seam can be customized over a broad range based on specific application requirements. In the case of CW-mode, an energy density of approximately 1 $\mathrm{MW\,cm^{-2}}$ is necessary to generate a metal plasma keyhole, facilitating deep penetration welding. However, the high heat input per unit of time in this mode may induce internal stresses and thermal distortion. Alternatively, pulsed laser welding allows for adaptable energy

input per unit length or time, potentially reducing thermal distortion in assemblies made of thin sheets with low thermal mass for heat dissipation. Achieving vacuum gas tightness requires overlapping single pulses by around 75%, leading to remelting of some material multiple times, which, in turn, could contribute to crack formation. The likelihood of hot cracking during laser welding is significantly influenced by the solidification interval of alloys. A broad solidification range can result in the formation of hot cracks at grain boundaries, particularly where there is remaining melt. Mitigating this effect may involve reducing temperature gradients through pre- or post-heating. Austenitic stainless steels and nickel-based alloys in a solution-annealed condition demonstrate favorable weldability.

4.4.1.1 Parameter optimization for welding thin Pd foils to metallic substrates of Crofer 22 APU and 316L

Developing a reliable method for assembling membrane reactor plates that reduces time and costs is crucial. Unfortunately, the previously optimized parameters that facilitated the successful integration of thin Pd foils with stainless steel substrates could not be consistently replicated in the present study. The reason might be because of the aging of the laser-welding device. Consequently, an extensive and systematic investigation was required, involving not only Crofer 22 APU but also stainless steel 316L.

The compositions and physical properties of the steel alloys and Pd are illustrated in Table 4.3. While 316L is FCC, Crofer 22APU possesses a BCC structure and it is ferromagnetic as well. The bcc structure contributes to a lower coefficient of thermal expansion in Crofer 22APU, and its heat conductivity is approximately twice that of 316L. Additionally, the solidus temperature of Crofer 22APU is 135 K higher than that of 316L.

The coefficients of thermal expansion for both palladium and 8-YSZ (see Table 4.1 or Figure in Appendix A.1), which serve as a diffusion barrier layer for palladium to stainless steel, align well with the bcc structure of Crofer 22 APU. However, it

Table 4.3: Compositions and physical properties of the material used in parameter study for laser welding in this section.

Material-No.	1.4404	1.4760 [137]	Pd
Trade name	316L	Crofer 22 APU	
short name	X2CrNiMo17-12-2	X1CrTiLa22	
C	<0.03	<0.03	
Cr	16.5-18.5	20-24	
Ni	10-13		
Mn	<2	0.3-0.8	
Ti		0.03-0.2	
Mo	2-2.5		
Si	<1	<0.5	
Cu		<0.5	
Al		<0.5	
Fe	balance	balance	
La		0.04-0.2	
P	<0.045	<0.05	
S	<0.015	<0.02	
N	<0.11		
Solidus Temperature (°C)	1375	1510	
Liquid Temperature (°C)	1400	1530	1555
Melting interval (K)	25	20	0
Thermal conductivity ($\mathrm{W\,m^{-1}\,K}$)	15	26	72
Thermal expansion coefficient ($1\mathrm{E}-6/\mathrm{K}$)	16	10.3	11

Table 4.4: Integration of Pd23Ag ($5\,\mu\mathrm{m}$, SINTEF) to Crofer 22 APU and SS 316L via laser welding.

Nr.	P (W)	P (W)	Frequency (Hz)	Pulseduration (ms)	Velocity (m/min)	Focus (mm)	Remark
1	1000	-	-	-	3.0	1	enough welding depth, well Pd bound, pore in the seam
2	1000	-	-	-	3.0	2	not enough welding depth
3	800	-	-	-	1.50	1	well integration of Pd, pore in the seam
4	800	-	-	-	1.50	2	not enough welding depth, pore in the seam
5	1500	-	-	-	5.0	1	enough welding depth, well Pd bound, break next to the seam
6	1500	-	-	-	5.0	2	not enough welding depth, well integration of Pd
7	1200	360	400	0.75	2.40	1	Well integrated Pd foil but low welding depth
8	1500	120	100	0.80	0.60	2	no integration of pd
9	2000	80	50	0.80	0.30	2	no integration of pd
10	2000	160	50	1.60	0.30	2	pore and cracks in and next to the weld seam

is important to note that the cubic structures differ between palladium and Crofer 22 APU.

In this context, a plate with a thickness of 1 mm, composed of the selected materials, was carefully chosen as the substrate for welding. This plate served as the base for attaching a 12.5 $\mu\mathrm{m}$-thick Pd foil and an additional compartment plate made of the same material. The next phase of the investigation involved the deliberate adjustment of various parameters, as detailed in Table 4.4, followed by a thorough analysis of the results using SEM imaging (see Figure 4.12 and Figure 4.13).

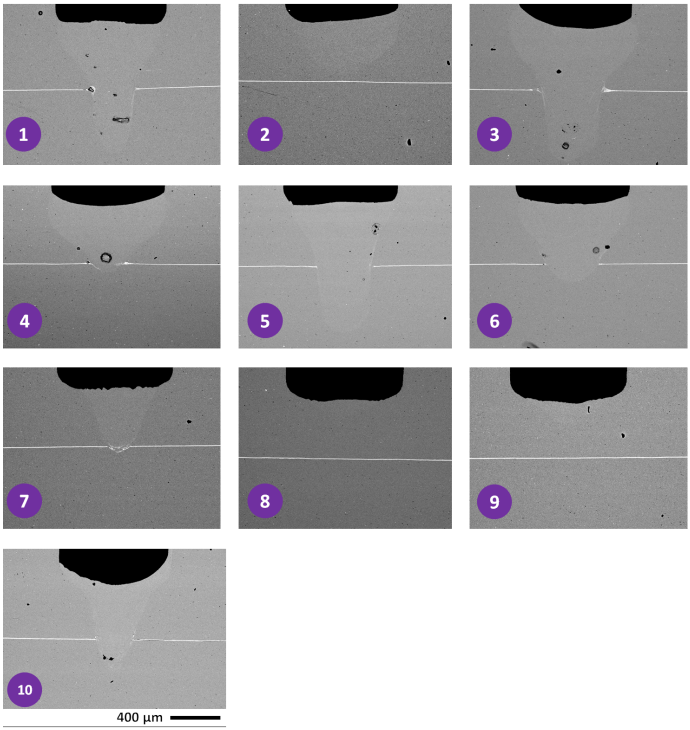

Figure 4.12: Results of the welded pieces of Crofer 22 APU to Pd-membrane based on the numbers listed in Table 4.4.

The results display significant variations: the integration of the Pd-membrane in sample 5, employing the CW technique, as depicted in Figure 4.12 and Figure 4.13, appears well-alloyed with sufficient depth of melting. However, small defects are observable for both alloys. Unfortunately, none of the He-leak tested samples with recipe 5 exhibited gas tightness. The sole instance of gas tightness was observed in sample 7, where the impulse technique was employed, despite potential reproducibility concerns related to the depth of melting. Nevertheless, after at least three samples were prepared with these parameters, the sample demonstrated He tightness.

From this point onward, Pd foils are welded using parameters from No. 7 (Table 4.4), irrespective of the material used (either Crofer 22 APU or 316L). However, for non-Pd foil welding, No. 5 was considered.

Table 4.5: Leak test of the welded modules at different stages.

Name[a]	foil Leak rate (before welding)[c] Int./Ext. (mbarl/s)	Leak rate (after welding) Int./Ext. (mbarl/s)	Leak rate (after gas test) Int./Ext. (mbarl/s)	welding technique/parameter[b]	configuration
TMF-1	<1E-8/<1E-8	<1E-8/<1E-8	<1E-8/<1E-8	Impulsed W./7	MC-Pd-MC[d]
TMF-2	-	4E-3/<1E-8	-	Impulsed W./7	MS-Pd-SM[e]

[a] Test module- membrane type- number
[b] Parameters according to those listed in Table 4.4
[c] Internal/external leak rate
[d] Micro channel made of Crofer 22 APU with weld seam 0.5 mm in depth, 12.5 μm Pd
[e] Microsieve made of Aluchrom YF with 0.2 mm thickness, 12.5 μm Pd, porous sinter metal made of Crofer 22 APU with 1 mm thickness

4.4.2 Preparation of the Pd test modules for gas test

Practically, a successful welding criterion is defined based on the vacuum He leak test (PHOENIX Quadro Leckdetektor, Leybold). In order to prevent any damage to thin foils during the suction/de-suction, a needle valve was installed before the permeate side to gently control the vacuum atmosphere on the membrane.

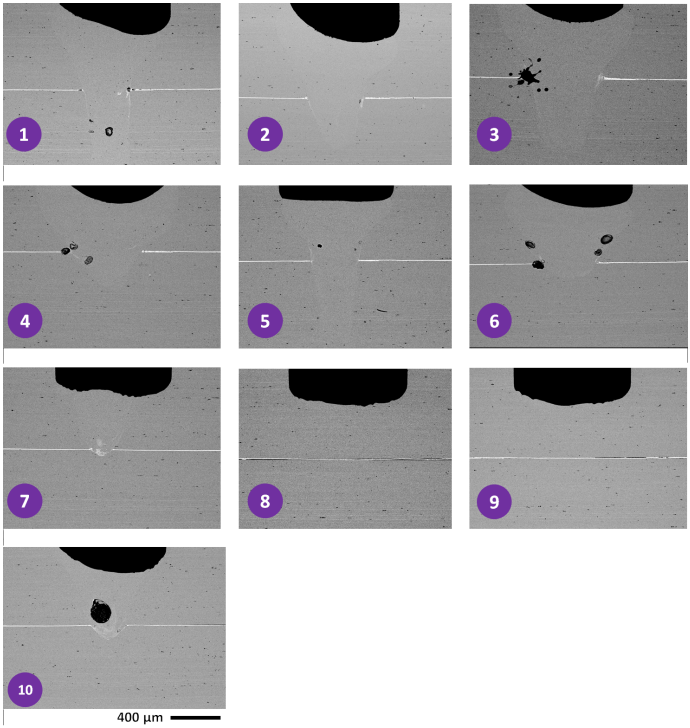

Figure 4.13: Results of the welded pieces of SS-316L to Pd-membrane based on the numbers listed in Table 4.4.

It is worth noting that although the commercial Pd foils were initially certified as light-tight by the supplier, an additional helium leak test was conducted to confirm their integrity before welding. Particular emphasis is required to ensure the precise clamping of multiple layers during the through-penetration welding procedure. The primary aim is to achieve welding seams that exhibit robust vacuum integrity. Gaps between these layers must be completely avoided, as they act as potent thermal insulators. These insulating gaps present challenges by hindering the attainment of consistent and predictable welding seam geometries. This obstruction can lead to the formation of shrinking holes or compromise the uniformity of the weld. Similar challenges arise when dealing with layers

featuring oxidized surfaces. In this context, conducting comprehensive parameter tests becomes essential to determine the optimal welding depth and the cross-sectional configuration of the weld seam.

Furthermore, critical considerations include the complex interaction between apparatus design and welding parameters, which significantly impacts the thermal field during the welding process. This interaction is crucial for minimizing potential distortions or the formation of cracks, especially when working with delicate membranes. The relationship between the heat conduction properties of the apparatus and the rate of heat conduction adds further complexity to the process. Notably, while uniform energy deposition per unit length can be achieved by adjusting welding parameters, this does not necessarily guarantee consistent welding outcomes. Consequently, parameter combinations that produce satisfactory results may not easily transfer to different structural designs.

In the fabrication of metal-based systems, such as the one under consideration, the process involves laser welding across a variety of materials. A significant challenge in this context is the difficulty of bridging gaps without the use of filler material. The concave nature of welding seams, often referred to as the "humping effect," can cause plate bending issues, particularly when welding the microstructured stack from an upper position. To address this issue, laser parameters were carefully adjusted, leading to the development of an effective mitigation strategy. More broadly, the inherent interplay between dissimilar materials within the reformer system is further explored in the following section:

Table 4.6: Module specification for the samples of TMF-1 and TMF-3.

Module	Metallic substrate	DBL (coating technique)	$A_m (cm^2)$	thickness of DBL	Height of channel (μm)
TMF-1	Micro Channel (Crofer 22 APU)	-	1.5	-	$\approx 150\,\mu$m to $170\,\mu$m
TMF-3	Sinter Metal (Crofer 22 APU)	ZrO_2 (screen printing)	1.5	$\approx 13\,\mu$m to $19\,\mu$m	$\approx 30\,\mu$m to $134\,\mu$m

4.4.3 Gas permeation test

Figure 4.14 shows the H_2 flux as a function of the square root of the H_2 partial pressure difference. As it is seen in Table 4.6, TMF-1 and TMF-3 are configured differently with similar Pd membranes (12.5 μm, Good Fellow). However, TMF-3 is supported on both sides with porous substrates. This configuration might not control the Pd volume expansion when exposed to H_2, however, it allows the user to work at higher operating pressures. Such an extra supports the probable cost of extra mass transfer resistances, especially for gas mixtures.

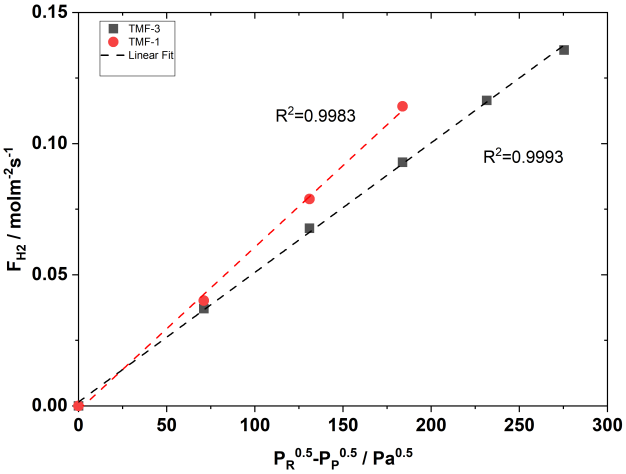

Figure 4.14: Flux of H_2 gas versus pressure difference of retentate and permeate side with power of 0.5 for modules TMF-1 and TMF-3 at 623.15 K.

The observed hydrogen flux versus the hydrogen partial pressure difference aligns well with Sieverts' law, characterized by a hydrogen partial pressure exponent of 0.5, as described in Equation 3.8. This suggests that hydrogen transport is primarily governed by the bulk diffusion of hydrogen atoms within the dense membrane. Permeance and permeability values for all pure hydrogen experiments

were derived via linear regression based on the experimental data, as indicated by dotted lines in Figures 4.14 and Figure 4.15. In case of N_2 permeation, no permeation was seen neither at room temperature nor at elevated temperatures.

As anticipated, the hydrogen flux through the membrane increases with rising trans-membrane hydrogen partial pressure difference, as justified by Equation 3.8. For instance, the H_2 flux through the 12.5 um Pd membrane was 0.078 $\mathrm{mol\,m^{-2}\,s^{-1}}$ at a feed pressure of 130 kPa, increasing to 0.11 $\mathrm{mol\,m^{-2}\,s^{-1}}$ at a feed pressure of 183 kPa for TMF-1.

Figure 4.15 shows the temperature-dependent permeance of each membrane, suggesting that the Arrhenius law can be applied to the experimental data. The apparent activation energies for Pd and PdAg membranes, deduced from the linear fit of experimental values, fall within the range of 8.75 $\mathrm{kJ\,mol^{-1}}$.

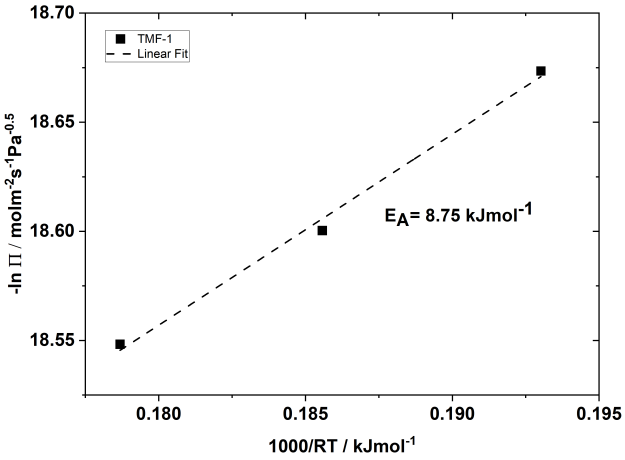

Figure 4.15: Estimation of activation energy and permanence coefficient based on an Arrhenius plot for sample TMF-1.

Table 4.7: Review of the experimental gas test results for Pd membranes in literature and this study as a comparison. $P_{H_2,perm}$: 101.3 kPa id permeate side was atmospheric pressure and no other stand in the paper. CR: cold-rolled, CHF: ceramic hollow fiber, ELP: electroless plating, MC: microchannel, PSS: porous stainless steel.

Membrane /PM/support	s_{Pd} (μm)	$P_{H_2,R}$ (kPa)	$P_{H_2,P}$ (kPa)	T (K)	Q0 (1×10^{-7} mol/sec/Pa$^{0.5}$)	E_A (kJ mol^{-1})	QT$_{350^\circ C}$ (1×10^{-8} mol/sec/Pa$^{0.5}$)	S (-)	Ref.
Pd/ELP/PSS	19-28	100-600	101.3	350-700	n.a.	16.4	n.a.	n.a.	[154]
Pd/CR/-	25	0.133-3.325	Ar sweep	100-350	n.a.	11	n.a.	n.a.	[155]
Pd/ELP/PC	0.5	200	101.3	350-500	0.149	9.7	0.229	846-1359	[156]
Pd/ELP/PC	0.5	200	101.3	350-500	0.363	10.3	0.497	1132-2185	[156]
Pd/ELP/CHF	2-3	115-265	98.5	350-450	n.a.	14.6	n.a.	$\simeq 1000$	[157]
Pd/ELP/CHF	2-3	190	10.3	335-400	n.a.	15.8	n.a.	>1000	[158]
Pd/CR/MC	12.5	250-450	101.3	350-400	2.59	14.6	1.56	>30000	[153]
Pd/CR/MC	12.5	250-450	101.3	350-400	4.21	8.7	0.777	not measured	TMF-1

The obtained permeability and activation energy for the for TMF-1 is illustrated in Table 4.7 where the other values from the literature for a Pd membrane are presented.

4.4.4 After test characterisation

In order to see the real configuration after assembly and laser welding, for each sample is only possible after-test SEM imaging. In this way, the samples TMF-1 and TMF-3 were cut and mounted in epoxy for cross-sectional analysis.

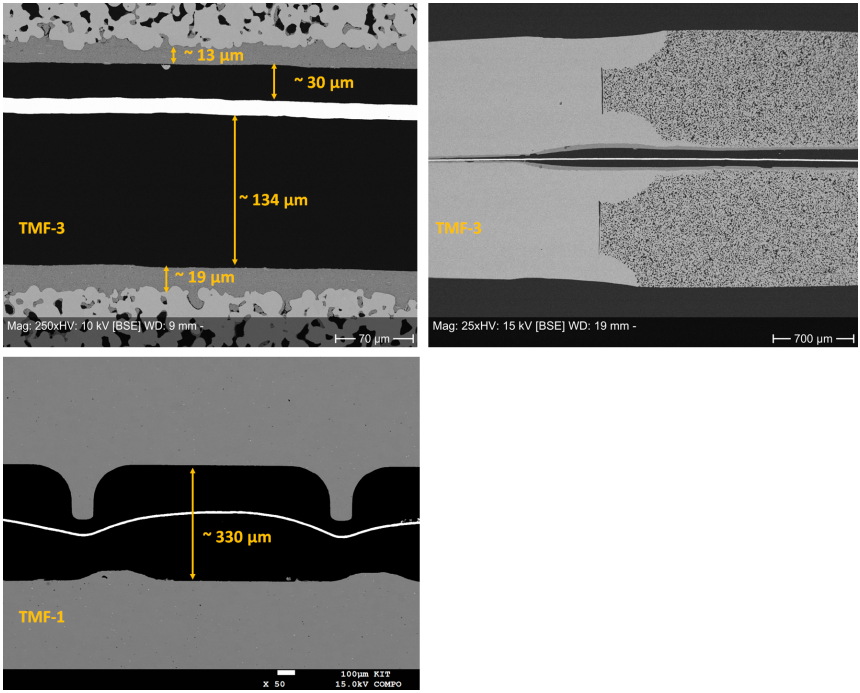

Figure 4.16: Cross-section view of samples TMF-1 and TMF-3 after gas test for estimation of the size of each layer.

Figure 4.16 illustrates the cross-sectional views of TMF-1 and TMF-3. TMF-1 experienced bending due to the higher pressure on the retentate side. This general configuration is not ideal, as the Pd membrane may either come into direct contact with the fins or become unstable at higher operating pressures. For the TMF-3 sample, the Pd foils are shielded by an 8-YSZ coating. However, the curvature of the substrate, where the dense frame is welded to the porous section, creates an additional gap between the top and bottom plates, preventing the Pd foil from being properly tightened.

One issue that remains as a question for using Pd membranes for long-term operation is the changes in the substrate. It is important to note that metallic supports cannot be used at operational temperatures exceeding 550°C due to the potential risk of inter-metallic diffusion between the palladium membrane and the metallic support [159].

4.5 Summary and conclusion

In this chapter, various topics are discussed, including the fabrication of hybrid metallic supports made from Crofer 22 APU using tape-casting, and the application of a DBL coated with 8-YSZ using dip-coating. Additionally, the chapter covers the coating of an active Pd layer using plasma spraying with two techniques, APS and VPS, as well as the use of commercial Pd foils.

Regarding the fabrication of the tape-casted metallic substrates, it was observed that increasing the size of the sheets for the porous part of the substrates resulted in non-reproducible, crack-free plates after laser welding assembly. To address this challenge, AM was explored, as detailed in Chapter 7, to fabricate the entire hybrid porous-dense plate in one step, eliminating the need for laser welding.

In the context of applying an active thin layer of Pd coating using plasma spraying, neither VPS nor APS proved effective for creating a dense, perm-selective layer for H_2 separation. This indicates that further study is needed to find the optimal conditions for using the plasma spraying coating technique which was outside the time period of this project. Consequently, commercial Pd foils with a thickness of $12.5\,\mu\mathrm{m}$ were used, demonstrating that these foils are suitable only for small-sized plates at the lab scale when integrated with substrates using laser welding techniques.

5 Catalyst preparation and testing for methane steam reforming and methane gas combustion

In this chapter, catalysts required for MSR and CCR were synthesized and coated into the microchannels of reactor plates. For MSR, Rh on Al_2O_3 was synthesized based on the optimal sample reported by Yu et al. [160]. For CCR, an optimal bimetallic Pd-Pt on Al_2O_3 was identified and synthesized by varying the metal loadings. The synthesized catalysts were then optimized for coating stable and active layers into microchannels, a necessary step for assembling an ultra-compact membrane reformer. Activity tests of the prepared layers were conducted using lab-scale reactors to evaluate their performance.

5.1 Literature review

5.1.1 MSR reaction mechanism and kinetics

MSR relies on a catalyst to lower the energy barrier of the process. This catalyst typically consists of the active metal, the catalyst support, and occasionally a promoter or dopant. The support acts as the physical framework, maintaining the catalyst within the reacting system, and it should possess good thermal and mechanical stability, potentially contributing some catalytic activity [161]. The support serves as a foundation for the active metal in the highly energetic reaction system and aids in the dispersion of the active metal [162].

The predominant catalyst for MSR is Ni/γ-Al_2O_3, owing to its widespread use due to low cost and favorable catalytic activity [163, 164]. Beyond γ-Al_2O_3, refractory oxides like magnesium aluminates and calcium aluminates find broad application [165]. Despite Ni's advantageous properties, such as cost-effectiveness and catalytic activity, it is prone to sintering and coking. Various strategies have been employed to address Ni's limitations, including the use of alternative supports to γ-Al_2O_3 for stronger metal-support interactions, thereby reducing sintering [166].

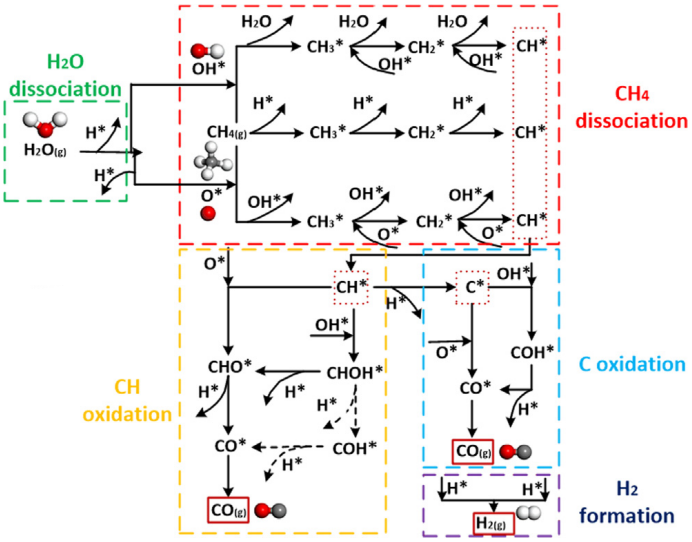

Figure 5.1: Potential reaction pathways for MSR as outlined by Niu et al. [167]. The reaction network for MSR is segmented into five parts: H_2O dissociation (enclosed in a dashed green rectangle), CH_4 dissociation (enclosed in a dashed red rectangle), CH oxidation (enclosed in a dashed orange rectangle), C oxidation (enclosed in a dashed light blue rectangle), and H_2 formation (enclosed in a dashed dark blue rectangle). (reprinted with permission from Elsevier).

The MSR process can take various reaction pathways, as depicted in Figure 5.1. Catalysis is crucial as it facilitates specific reaction pathways to enhance hydrogen production. Many reactions illustrated in Figure 5.1 are inherent to MSR systems.

The catalytic influence on these pathways involves reducing the activation energy barrier for particular reactions through the active sites on the catalyst [168]. Consequently, the dominant pathways depend on the chosen catalyst type and the characteristics of its active sites. Figure 5.1 demonstrates the dissociation of water into . H and . OH (as the sole radical species). In contrast, methane dissociation follows three mechanisms: . OH-assisted activation, direct dissociation, and . O-assisted dissociation [167]. The . CH radical generated from these pathways undergoes various oxidation routes, yielding CO and H_2. Specifically, . CH can be oxidized to . CHO by O_2 or . CHOH by . OH, serving as precursors for CO formation (alongside . H production). Alternatively, . CH can be reduced to C (with . H production), potentially deposited on the catalyst. Depending on the presence of oxygenated species in the reaction environment, C either oxidizes to CO and CO_2 or remains on the catalyst, leading to deactivation. The . H in the reacting systems contributes to H_2 formation. As indicated in Figure 5.1, the MSR system encompasses five possible reaction pathways: CH_4 dissociation, H_2O dissociation, C oxidation, CH oxidation, and H_2 formation.

5.2 Catalyst synthesis

The Flame Spray Pyrolysis (FSP) was used to prepare the catalysts for MSR and CCR in this work. The setup is shown in Figure 5.2.

The support flame is generated by burning a mixture of CH_4 and O_2 which were fed with flow rates of $0.6\,\mathrm{L\,min^{-1}}$ and $1.9\,\mathrm{L\,min^{-1}}$, respectively. The metal precursor solution flow rate to the flame is adjusted to $5\,\mathrm{L\,min^{-1}}$ by a syringe pump (PHD UltraTM, Harvard). An O_2 stream as dispersion gas was fed through the precursor solution nozzle. Additional $5\,\mathrm{L\,min^{-1}}$ of oxygen is provided by a sintered metal plate ring as sheath gas for supporting and stabilising the flame. The product particles are collected either in batches on a glass fibre filter (Whatman GF/D, $25.7\,\mathrm{cm}$ in diameter) placed at the top of the FSP cylinder with the aid of a vacuum pump or semi-continuously in a bag-house filter (Wegner Consulting, Zürich). In order to load noble metals of Rh, Pt, or Pd onto Al_2O_3 support,

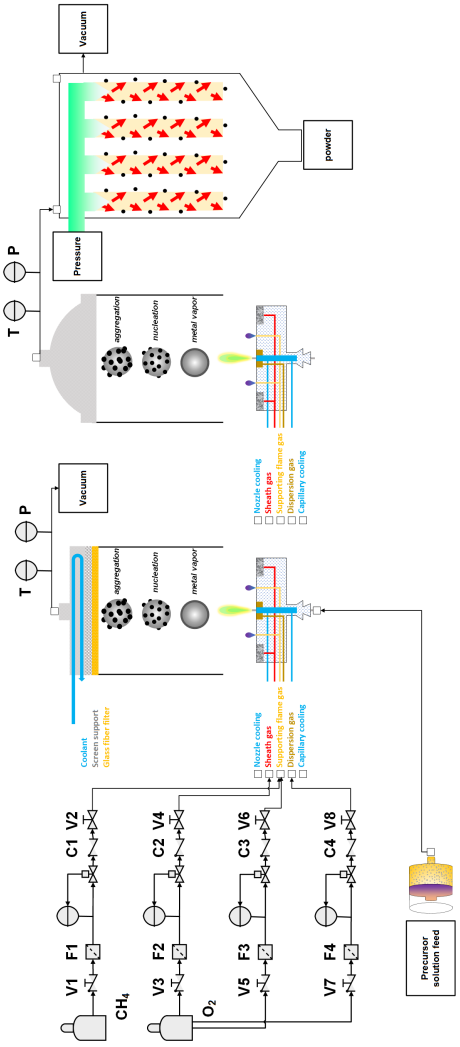

Figure 5.2: Schematic of FSP system for synthesis of catalyst in this study. The left drum shows the batch configuration and the right drum shows the semi-continuous configuration.

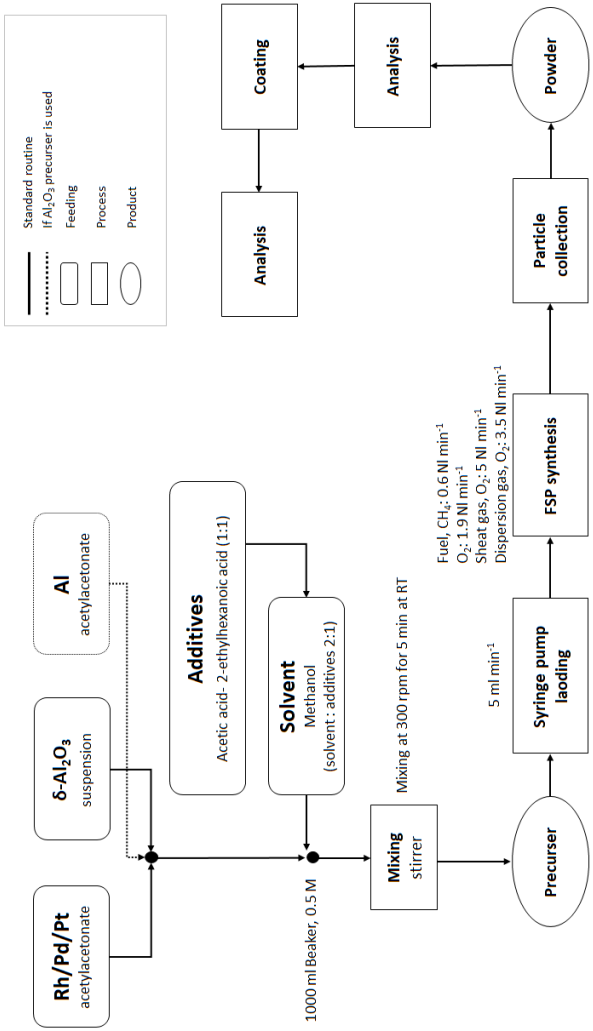

Figure 5.3: The flowchart showing the procedure for catalyst preparation for MSR and CCR in this study.

a commercial Al_2O_3 suspension was used (Alfa Aesar, $20\,\%$ stabilized Al_2O_3 in H_2O). In this work, all prepared catalysts from this suspension are denoted as SAL. This suspension is mixed with the Rh/Pd/Pt acetylacetonate precursor (in 1:1:2 acetic acid/ethyhexanoic acid/methanol solution) and then sprayed into the flame [160, 169]. To control the temperature of the flame nozzle and the filter, two lines of cooling water are used. The deposited particles are collected carefully from the filter by scratching the glass fiber filter with a spatula after cooling down in batch mode. In a semi-continuous system, particles are collected by a vacuum pump and bag-house filters, where 4 polytetrafluoroethylene (PTFE) filters supported by metallic cages are installed inside a drum. In detail, to collect catalyst powder, after stopping the vacuum pump, the pressurized air with the pressure of 5 bar was pulsed for $0.05\,\mathrm{s}$ every $5\,\mathrm{s}$ into the 4 PTFE filters from an electrically controlled tank. The catalyst powder is then collected at the bottom of the drum. Unlike the glass fiber filter, the Bag-house collection system is not limited to particle collection. It does not need to take more time to separate and scratch the filter for every synthesis and finally, the powder has a higher purity compared to batch-FSP [170].

5.3 Catalyst characterization in powder form

The prepared catalysts and coated layers (in the following sections) were characterized by different techniques. These are explained in detail in Appendix A.3.

5.3.1 Characteristics related to morphology and structure of catalyst for MSR

The catalyst for MSR has already been optimized and more information can be found here [160]. Briefly, two sets of catalysts based on Rh were successfully synthesized using FSP on both flame-made and preformed support particles. This was done to understand the factors that influence the catalytic activity of

such catalysts in MSR. Among the catalysts tested, the 1Rh/SAL catalyst showed the highest CH_4 conversion at a weight hourly space velocity (W/F) of 0.374 $\mathrm{g_{cat}/mol_{CH4}}$ and $600\,^\circ\mathrm{C}$. Generally, catalysts supported on preformed Al_2O_3 exhibited higher turnover frequencies (TOF) compared to those on flame-made Al_2O_3, and the values surpassed those reported in the literature for Rh catalysts. It was observed that approximately one-third of Rh was incorporated into the Al_2O_3 support in Rh catalysts supported on flame-made Al_2O_3, resulting in reduced accessibility of active Rh sites. Moreover, Rh reduction and H_2 spillover were facilitated on catalysts made with preformed Al_2O_3 particles, indicating that the support plays a significant role in the catalytic activity of Rh. Therefore, the catalytic performance of flame-made catalysts can be significantly improved by using preformed Al_2O_3 supports [160]. For MSR, 1Rh/SAL was reproduced and characterized before the coating process. The results of X-ray diffraction (XRD) and temperature-programmed reduction (TPR) analysis have already been reported in a previous study [160], therefore they are not presented here.

The BET surface area of 1RhSAL catalyst was measured to be $42\,\mathrm{m^2\,g^{-1}}$. The particle size of Al_2O_3 in the suspension was reported to be $80\,\mathrm{nm}$ to $100\,\mathrm{nm}$ by the manufacturer. TEM images revealed a larger particle size distribution of $50\,\mathrm{nm}$ to $200\,\mathrm{nm}$ for SAL. As a result, the low surface area of SAL was attributed to its relatively large particle size and lack of intraparticle porosity.

Scanning transmission electron microscopy (STEM) was employed to examine the morphology of Rh nano-clusters on the SAL support, as well as to analyze the distribution of elements on the catalyst. STEM images of 1RhSAL are depicted in Figure 5.4.

The Rh particles appeared as distinct, bright, spherical dots on the spherical Al_2O_3 support particles in the high-angle annular dark-field scanning transmission electron microscopy (HAADF-STEM) images. It was observed that the SAL support comprised large spheres with a size ranging from 50 to 200 nm. Moreover, Rh particles were found to be limited to the surface of the SAL support. The lattice distances of the Rh clusters corresponded to the Rh(111) and Rh(200) planes, as identified by previous studies [171]. The Rh particles exhibited a

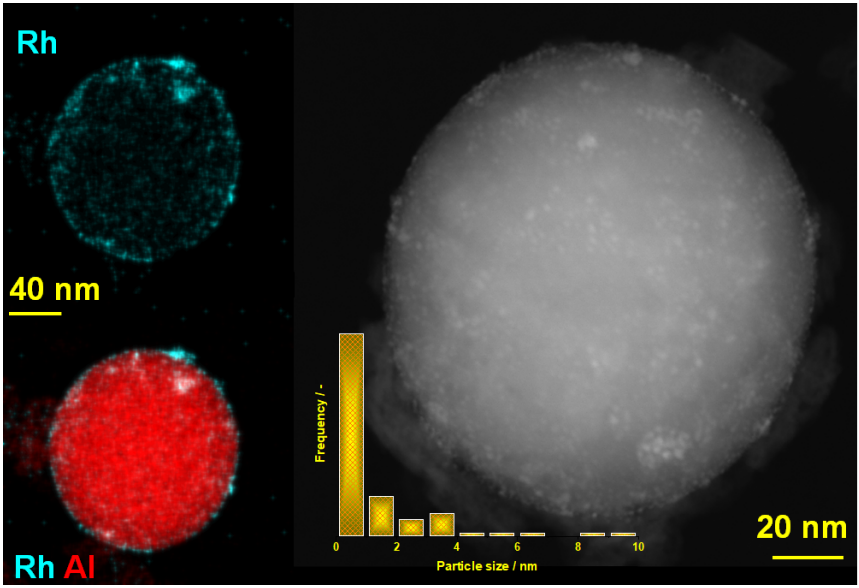

Figure 5.4: High-angle annular dark-field scanning transmission electron microscopy (HAADF-STEM) images were captured for 1RhSAL catalyst (up). The SAL particle size seen by STEM images (down).

broad distribution in particle sizes, ranging from 1 to 4 nm, as depicted in the insets of Figure 5.4. Table 5.1 summarizes the characterization results obtained from inductively coupled plasma (ICP), pulse H_2 chemisorption, and transmission electron microscopy (TEM) methods. The Rh particle size was calculated using Equation A.12 based on the Rh dispersion determined by H_2 chemisorption, and the amount of Rh active sites was estimated from the observed Rh particle size by TEM using the same equation.

Using the mentioned techniques might come with errors in estimation when calculating e.g. particle size of the Rh. For instance, results of the chemisorption might not be accurate if factors, such as strong metal-support interaction, H_2 spillover, or reactive adsorption of H_2 on the support surface happen. The metal-support interaction results in an exaggerated assessment, while the latter two result

Table 5.1: Charactersitics of the 1Rh/SAL based on the H_2 chemisorption and TEM analysis.

Catalyst	Rh loading from ICP	H_2 chemisorption results			TEM results		Ref.
		Rh active sites	Rh dispersion	Rh particle size	Rh particle size	Rh active sites	
	(%)	$(A_{chem})(\mu\text{mol}/\text{g}_{\text{cat}})$	(%)	$(P_{chem})^a$(nm)	$(P_{TEM})^b$(nm)	$(A_{TEM})^c(\mu\text{mol}/\text{g}_{\text{cat}})$	
1RhSAL	0.84	59	73	1.5	1.7	53	[160]
1RhSAL	0.86	-	64	-	1.4	-	this study

[a] Calculated based on the H_2 chemisorption and Equation A.12.
[b] Estimated from Rh particles from TEM results.
[c] Calculated from the dispersion obtained from particle size P_{TEM} based on the Equation A.12.

in an underestimated metal particle size. However, it is particularly noted that strong metal-support interaction is not anticipated to have a significant effect on the catalyst synthesized in this study [160]. Conversely, conventional TEM techniques may not be able to identify metal particles when they are extremely small when metal concentrations are very low (e.g. loading of metals $< 1\,\text{Wt.}\%$), or when there is poor contrast between the metal and support. Generally, this situation can result in an overestimation of the average size of the metal particles and an underestimation of the metal dispersion. Furthermore, TEM methods can only examine microscopic sample sections, which means that variations in macroscopic sample properties may not be fully reflected. Additionally, TEM methods are not able to detect metal particles that are covered by Al_2O_3, which means that such incorporated metal particles will not be accessible to H_2 or reactants. As a result, the number of catalytically active Rh sites may be overestimated based on TEM analyses. Therefore, the average size of the metal particle obtained by TEM should be viewed as an upper limit, and the derived active Rh site density should also be considered if the partial coverage of metal particles by the support is a concern [160].

5.3.2 Characteristics related to morphology and structure of catalyst for CCR

The FSP method (explained in Section 5.2) was utilized to synthesize the catalyst for this reaction as well. Initially, the support was prepared using both SAL

and (flame-made Al_2O_3) FAL methods to synthesize $0.5\,\mathrm{Wt.\%}$ to $1.5\,\mathrm{Wt.\%}$ of Pd on pre-formed Al_2O_3. The characteristics results showed 1PdSAL as the optimum for second metal loading (Pt). Finally, Pd-PtSAL catalysts with various Pt were synthesized and their compositions, particle sizes, and Inductively Coupled Plasma Optical Emission Spectroscopy (ICP-OES) analysis results are presented in Table 5.2.

Table 5.2: Prepared catalysts with different loadings of Pd and Pt onto SAL and FAL for CCR.

Sample	Nominal composition Pd loading by ICP Pt loading by ICP P_{TEM}			
	Pd:Pt	(wt.%)	(wt.%)	(nm)
0.5PdSAL	0.5:0	-	-	-
1.0PdSAL	1:0	0.852	-	-
1.5PdSAL	1.5:0	1.280	-	6.000[a]
0.5PdFAL	0.5:0	-	-	-
1.0PdFAL	0.5:0	-	-	-
0.5PdFAL	1.5:0	1.290	-	2.500[b]
0.5Pt1.5PdSAL	0.5:1.5	1.340	0.171	-
1.0Pt1.5PdSAL	1.0:1.5	-	-	-
1.5Pt1.5PdSAL	1.5:1.5	1.270	0.504	0.875[c]

[a] Pd particles are only measured.
[b] Pd particles are only measured.
[c] Pd and Pt particles are only measured.

5.3.2.1 XRD results

Figure 5.5 displays the XRD pattern of PdSAL with $0.5\,\mathrm{Wt.\%}$ and $1.0\,\mathrm{Wt.\%}$ of Pd loading. The pattern reveals that the peaks of $0.5\,\mathrm{Wt.\%}$ are generally a bit sharper and more intense than those of $1.0\,\mathrm{Wt.\%}$. However, as there is no big difference between the Pd loading of the samples, it is not expected to see a very sharp difference in the peaks. The peaks at $34.38°$,$41.72°$, $60.64°$, and $71.82°$ indicate the presence of the PdO phase, while the peak at $66.84°$ indicates the presence of only small amounts of metallic Pd in both samples. Most of the peaks in both samples do not exhibit a significant shift from one another [172–174].

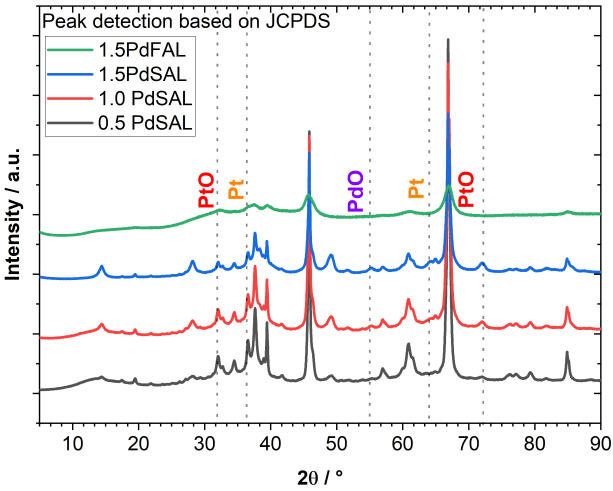

Figure 5.5: The XRD patterns of different loading of Pd onto SAL and FAL for as prepared catalysts by FSP.

As observed, there is a significant difference in the number of peaks between SAL and FAL. This could be due to the presence of either nanoparticles with a crystalline size in the FAL sample (which could not be detected) or an amorphous structure. It is important to note that peaks related to Pd or Pd-Pt alloy are concealed by peaks of γ-Al_2O_3. Most of the peaks in both samples are attributed to alumina. One possible factor affecting the crystallinity results is that in FAL, metal particles may form on both the surface and in the matrix of the substrate.

The XRD pattern in Figure 5.6 displays the impact of Pt loading on 1.5PdSAL, where Pt loading varied between $0.5\,\mathrm{Wt.\%}$ to $1.5\,\mathrm{Wt.\%}$. With an increase in Pt loading, the peaks became narrower and sharper. The peaks at $34.29°$ and $71.07°$ indicate the presence of PtO, while the peak at $55.23°$ represents the presence of PdO. The peaks at $39.39°$ and $66.90°$ are possibly related to the presence of Pt in all samples. Moreover, according to the XRD patterns between $20°$ to $80°$, the δ-phase of alumina was found in all three catalysts [172–174].

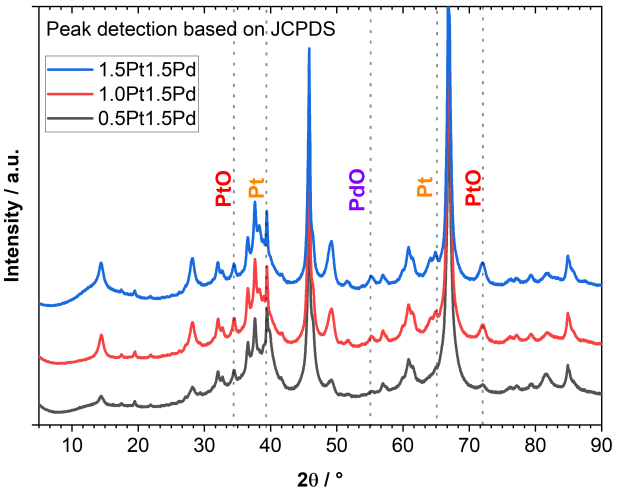

Figure 5.6: The XRD patterns of different loading of Pt onto 1.5PdSAL for as prepared catalysts by FSP.

5.3.2.2 TEM results

TEM analysis examined the arrangement of metal (oxide) particles such as Pd and Pt onto/into alumina particles. Figures 5.7 and 5.8 present some TEM images of 1.5PdSAL and 1.5PdFAL, respectively. The SAL support was composed of large spheres with a size ranging from 40-200 nm and large Pd particles were observed on the surface of the SAL support in Figure 5.7.

On the other hand, Pd particles in FAL were distributed within a broader size range of 0.5 to 4.5 nm, with an average Pd particle size of 2.5 nm based on the TEM images. Furthermore, the elemental mapping of Pd, O, and Al in 1.5PdSAL and 1.5PdFAL is shown in Figures 5.7 and 5.8. The results showed that many Pd clusters were formed on the surface of the SAL particles (see Figure 5.7), possibly due to the relatively high Pd loading and the low surface area of this support (SAL). In contrast, Pd particles are well dispersed on the FAL support

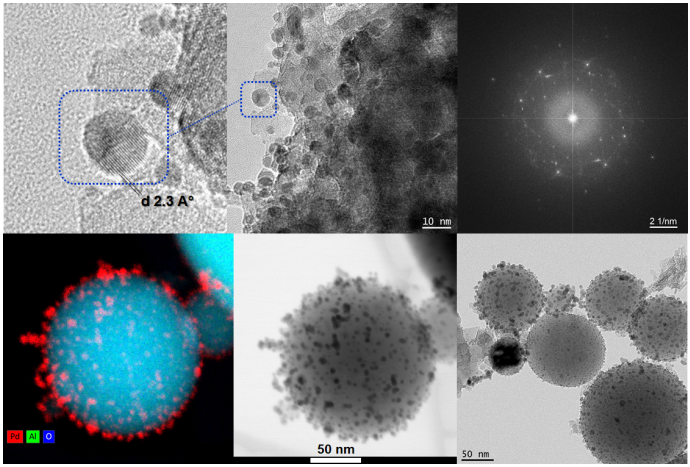

Figure 5.7: TEM images of 1.5PdSAL with different magnifications and elemental mapping.

(see Figure 5.8). Figures 5.7 and 5.8 also display HRTEM images for 1.5PdSAL and 1.5PdFAL samples.

5.3.3 Pore characteristics of synthesized catalysts powder for CCR and MSR

Figure 5.9 illustrates the N_2 adsorption-desorption isotherms and the pore size distribution for the 1RhSAL and 1.5PdSAL catalysts. Both samples exhibit (as they are based on the same support) a type IV isotherm with a hysteresis loop at high relative pressures, characteristic of capillary condensation within mesopores (Figure 5.9 top) [175–177]. Based on IUPAC classification, the hysteresis loop is of type H2, indicating a complex mesoporous structure with poorly defined pore size and shape distributions [178, 179]. This type of loop is typically associated with a pore structure resembling interconnected bottlenecks, where the pore mouth is narrower than the body [180]. The presence of the hysteresis loop at high pressure indicates a wide pore size distribution and a large specific surface

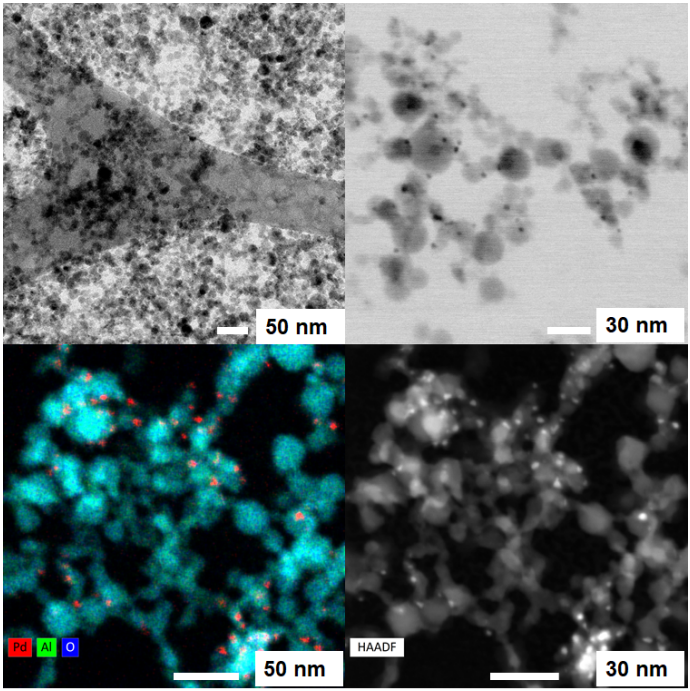

Figure 5.8: TEM images of 1.5PdFAL with different magnifications and elemental mapping.

area [181]. As shown in Figures 5.9 bottom, the pore size distribution for the 1RhSAL and 1.5PdSAL samples spans 2–100 nm, with a peak around 10–20 nm.

5.4 Catalyst coating methodology

For large-scale production, screen-printing is regarded as the most effective method for loading catalysts because of its rapid processing, consistent performance, and versatility in handling different pastes. Each screen printer is composed of several key components, including a frame with a stretched mesh, a photo stencil of the desired design attached to the mesh, a squeegee, a printable

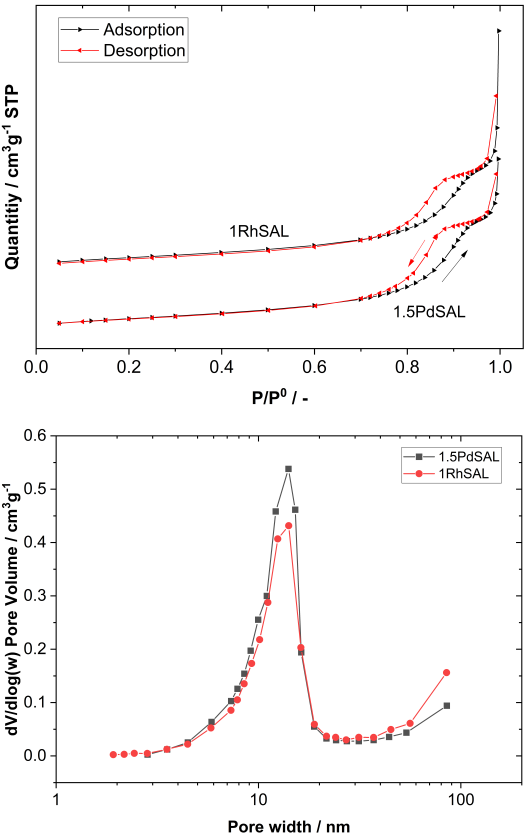

Figure 5.9: N_2 adsorption-desorption isotherms (top) and porse size distribution (bottom) for samples 1.5PdSAL and 1RhSAL in the fresh mode and after calcination at 550 °C. It should be noted that the isotherms for the 1RhSAL sample are shifted upwards by 50 units to clearly distinguish the results within a single graph.

paste, and the substrate on which the printing is carried out. The printing process involves the movement of the paste with a squeegee across the screen. The screen, positioned at a defined distance from the substrate, is brought into contact with the substrate. As the squeegee moves in the printing direction, it creates an applied shear rate on the paste, pushing it through the screen. Upon returning

to the starting position, the flood squeegee is lowered, refilling the screen mesh with printing paste in preparation for the next print. The quality of the layer is influenced by the substrate, the screen, and various process parameters [170]. The layer thickness typically ranges from a few μm up to 100 μm and is dependent on factors such as the distance between the screen and the substrate (snap-off distance), the screen mesh type, printing speed, pressure, squeegee hardness, and the rheological properties of the paste [170]. The following advantages can be regarded when opting for screen printing as a coating technique:

- Screen printing can be effectively used for structured substrates, such as microstructured foils
- Flexibility in design and material selection
- High resolution patterns
- Coating reproducible layers with a fast procedure
- Higher layer thickness in comparison to inkjet printing

This section represents the results related to catalyst synthesis for MSR and CCR and their coating into the microchannels with screen printing technique.

The catalyst synthesis involved loading active metals such as Rh, Pd, Pt, or bimetallic Pd-Pt on/into alumina as the support. The catalysts were applied to the microchannels using a screen printing technique, which provides a straightforward and rapid coating method suitable for industrial applications. Each set for MSR and CCR was evaluated to meet the following points:

- Development of a fast and reproducible technique for catalyst synthesis with a semi-industrial approach
- Employing and parameter optimization for catalyst coating with screen printing technique as a fast and precise method

Several methods can be employed to coat particulate media onto a planar substrate. In this study, screen printing is chosen as the primary coating process to apply the desired material from a paste into the channels of micro-structured metallic support foils with a specified layer thickness. Compared to other coating methods, such as inkjet printing, screen printing offers several advantages, including the ability to produce relatively thicker coatings with highly reproducible paste and layer properties. This technique was employed not only for coating the synthesized catalysts but also for applying the diffusion barrier layer, as described in Chapter 7. In this section, a homemade paste with the recipe and procedure described in Figure 5.10 was used. The coated plates were dried and calcined. Afterward, the weight of the depositions was calculated to adjust the operating conditions for the reactor test.

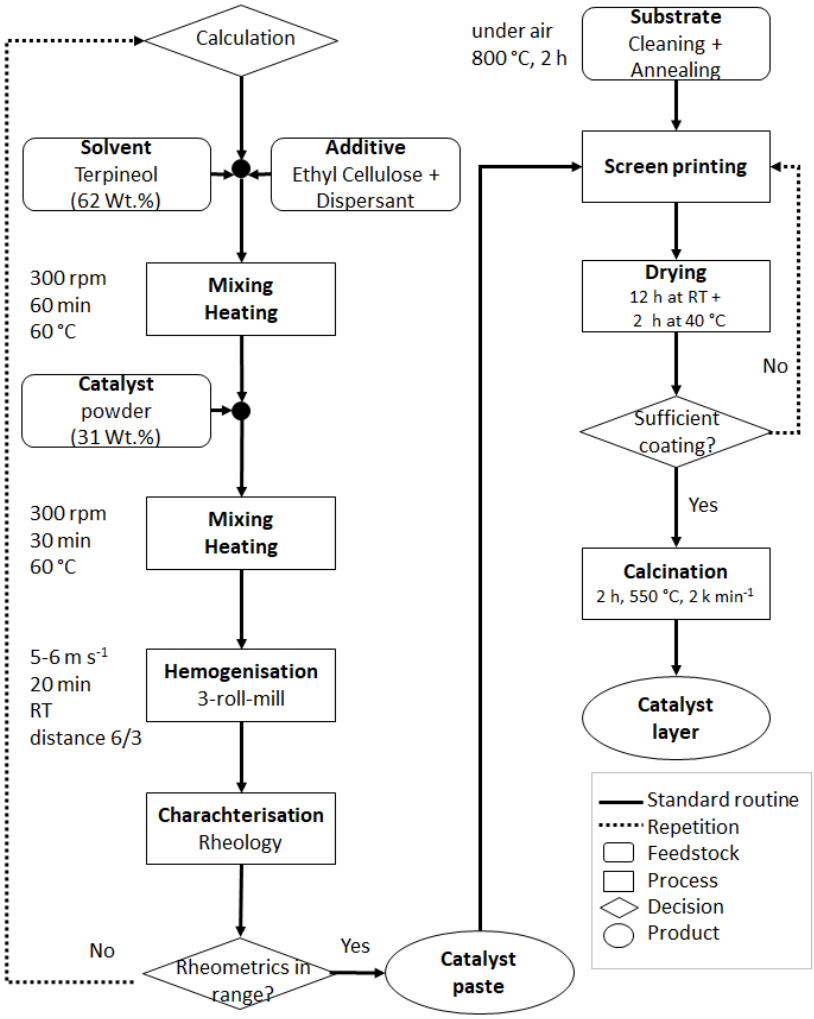

Figure 5.10: Flowchart of the paste preparation and coating with screen printing.

5.5 Catalyst characterisation of the coated catalyst layers

Figure 5.11 illustrates the Energy Dispersive Spectroscopy (EDS) of the 1RhSAL coated catalyst, highlighting various elements. Notably, Rh exhibits effective dispersion within the layer after screen printing coating. The analysis focuses on layers produced after a single step of catalyst printing, resulting in a layer approximately $\simeq 10\ \mu\mathrm{m}$ thick. Furthermore, both surface examination and additional scanning probes conducted during the analysis reveal an absence of cracks. The layer's topology appears sufficiently porous, suggesting probably no significant hindrance to the effective diffusion coefficient of reactants or products to/from the layer during the reaction.

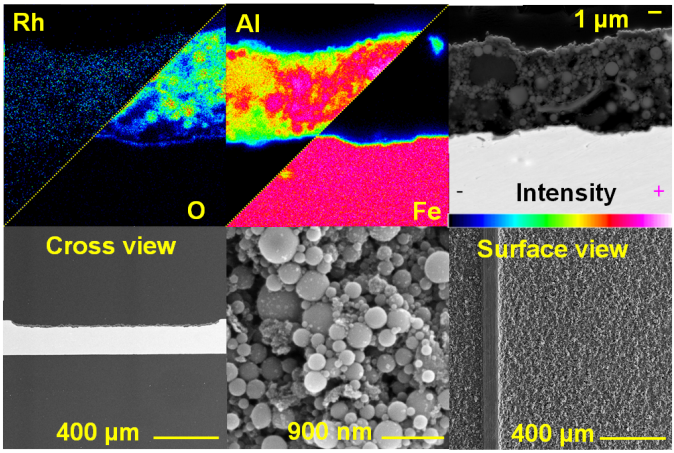

Figure 5.11: Cross sectional view and surface view of the coated catalyst of 1RhSAL into the microchannels with screen printing technique.

For the CCR reaction catalyst, a paste containing 1.5Pd1.5Pt catalyst was printed into microchannels similar to those used for MSR. The results of the freshly coated catalyst, with screen printing, are depicted in Figure 5.12. The cross-sectional

views reveal a layer thickness of approximately $\simeq 20\ \mu\mathrm{m}$. In particular, the proportion of Pt is observed to be less than that of Pd, in alignment with their respective compositions in the powder synthesis, as discussed in Section 5.3.2. It should be noted that, similar to the MSR case, no cracks were identified in the layers resulting from this paste.

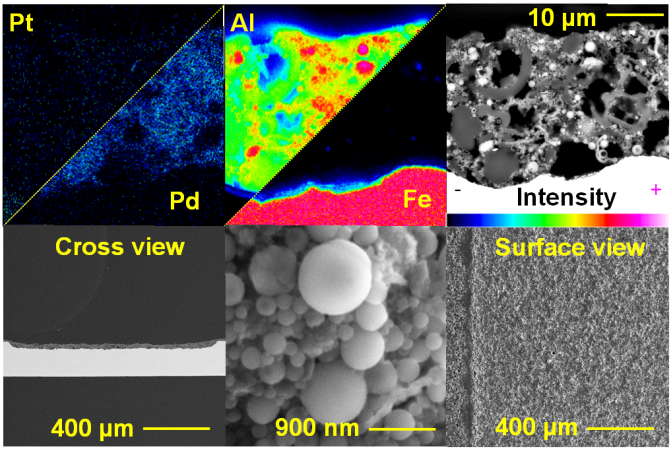

Figure 5.12: Cross sectional view and surface view of the coated catalyst of 1.5Pd1.5PtSAL into the microchannels with screen printing technique.

Figures 5.13 illustrate the shear stress and viscosity of the individual pastes as a function of shear rate. Both pastes exhibit shear-thinning behavior. Notably, from initial shear rates to a shear rate of approximately 25 s^{-1}, the RhSAL pastes demonstrate lower shear stress with a relatively similar viscosity value compared to the 1.5Pd1.5Pt paste. After that, the 1RhSAL shows more shear stress while viscosity remains still close to 1.5Pd1.5Pt paste. Both pastes exhibit an overall trend of elevated shear stress and reduced viscosity as the shear rate increases. This observation aligns with the findings of Somalu et al., who emphasized the importance of understanding paste behavior within the shear rate regime encountered during the screen-printing process [182].

To ensure a successful screen-printing process, it is crucial for the applied pastes to display low viscosity at high shear rates (during actual printing) and vice versa (for distributing the paste on the sieve) [183]. In line with this requirement, a 3-interval thixotropic test was conducted to simulate the conditions during screen printing. Initially, the shear rate was held constant at $0.1\mathrm{s}^{-1}$ for the first 240 s. Subsequently, it was abruptly increased to 100 s^{-1} over the next 45 s before being reduced again to 0.1 s^{-1} for the final 200 s.

Figure 5.13 depicts the results of the thixotropic test for each considered paste. Both pastes adhere to typical shear thinning and thixotropic behavior. The prepared pastes align with the suggested literature range and the pastes have been shown to result in satisfactory layers, making them suitable for coating using screen printing. The reproducible was also carried out for several trials and the deviation was less than 1%. No falling test was carried out for the coated substrates, but recording their weight before and after long gas experiments showed trivial loss (less than 3%) for small substrates. Factors such as solid content, particle size, surface area of the particle, and binder content influence layer quality. The amount of binder plays a crucial role in the rheological properties of the paste. An optimal balance between solid and binder content is essential to control the ink's rheology, as too much binder can hinder printability, while too little can lead to cracking during drying. In the case of nano-sized powders, high surface area may result in low solid content, enhancing interparticle interaction and increasing viscosity and viscoelastic properties even at low solid contents. Reducing the amount of catalyst was necessary to lower the yield stress values and obtain a paste suitable for printing. This adjustment is crucial for extrapolating the preparation of the paste and its components when starting materials have comparable structural properties. This aligns with Somalu et al. research [182], indicating that paste viscosity is influenced not only by solvent and binder loading but also by the powder's surface area to be printed.

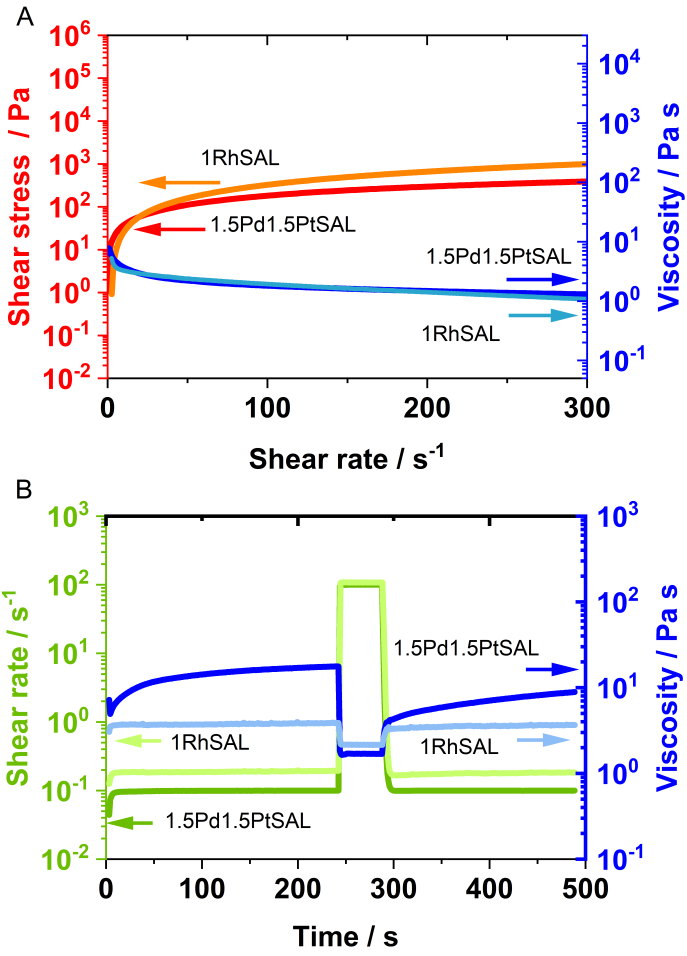

Figure 5.13: Rheological properties of the pastes prepared based on 1RhSAL and 1.5Pd1.5PtSAL catalysts for screen printing; (A) shear stress and viscosity versus shear rate, (B) shear rate and viscosity versus time.

5.6 Experimental set-up and gas chromatography for gas test of catalysts used in MSR and CCR

5.6.1 Test rig

Figure 5.14 indicates the flow chart of the set-up used for the activity catalyst test. The gases were dosed through mass flow controllers (MFC, Brooks Instrument, Model SLA5800 series, thermal mass flow).

The pressure of the reactor was regulated via a regulating valve Flowserve (Serie SmallFlow- 080037) and sensing and reading the pressures with a pressure sensor Baumer 0-20 bar, and pressure indicators West 8010+. In order to control the heating, pressure, and flow rates a LABVIEW (National Instrument) program was used, and the whole data was recorded for every 10 sec. P&ID controllers of Eurotherm 2408 and Elotech R2500S were used. The reactants' ratio and compositions were analyzed through a bypass stream equipped with two three-way valves before or during the reaction.

5.6.2 Gas chromatography

The gas compositions were analyzed with a gas chromatograph (GC, Agilent Technologies 7890B). It was equipped with a thermal conductivity detector (TCD), and a flame ionization detector (FID). The GC was equipped with an HP-Plot/Q 19095P-Q04 and 5A-Mole sieve 19095P-MS6. The HP-Plot Q column has a length of 30 m, a diameter of 530 mm, and a film thickness of 40 mm.

Ar was used as a carrier gas as well as a reference gas for the TCD to enable the detection of H_2 with sufficient high sensitivity towards CO. Due to GC calibration of all present gaseous species, including O_2 and H_2O, the C-, H-, and O-balances could be calculated. Laboratory gas mixtures provided by different suppliers (Air Liquide, Basi) were used for GC calibration.

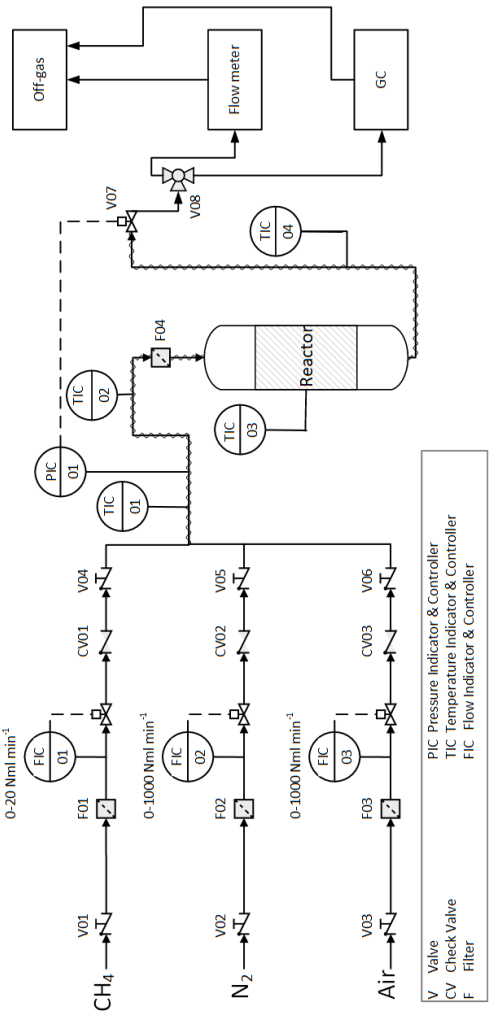

Figure 5.14: Test rig flow diagram for a microchannel reactor used for catalyst activity tests for MSR and CCR in this work.

5.6.3 Microstructured reactor

Figure A.3 illustrates the microreactor employed in CCR tests. The reactor comprises a tube and a housing cell, made of stainless steel 1.4571 and 1.4435 (316L), while the latter was fabricated using selective laser melting technology. To create parallel microchannels for testing, the coated foils were cut with a cutter to fit within the housing. Subsequently, the cell (housing) was placed into a tube reactor along its length, ensuring a snug fit to the inner diameter of the tube reactor to prevent any flow from bypassing the catalytic channels. Standard swagelock connections with metric connectors were used for the reactor sealings.

5.6.3.1 Microstructured foils

The bed for catalyst coating was a plate consisting of microchannels L $240\,\mathrm{mm}$, W $1.34\,\mathrm{mm}$, H $300\,\mu\mathrm{m}$, and N $14\,\mathrm{mm}$ for small plates and L 850-110 mm, and N $61\,\mathrm{mm}$ for big plates in this work. The plates were made of Crofer 22 APU (VDM Metals gmbh). Its composition is listed in Table 5.3;

Table 5.3: Chemical composition of Crofer 22 APU in [%] by min. and max. by specification [137] and analysis of the virgin powder.

	C	Cr	Fe	S	Mn	Si	Ti	Cu
Min.		20.0	Bal.		0.30		0.03	
Max.	0.03	24.0		0.020	0.80	0.50	0.20	0.50
Analysis	<0.01	22.21	Bal.	<0.003	0.38	0.02	0.06	0.01

	P	Al	La	Mo	Ni	V	W	Co
Min.			0.04	n.s.	n.s.	n.s.	n.s.	n.s.
Max.	0.050	0.50	0.2	n.s.	n.s.	n.s.	n.s.	n.s.
Analysis	0.006	0.013	<0.005	0.02	0.02	0.01	<0.01	0.01

The microstructured foils/plates were pre-treated with cleaning with detergent agents and water and then cleaned in an ultrasonic-bath with isopropanol for 15 min. Then they were dried and annealed at Air atmosphere for 2 h at $800\,^{\circ}\mathrm{C}$ in an oven to form an oxide layer on the surface that provides the coated catalyst layer a better adhesion to the substrate [184].

5.7 Definitions

In this section, general correlations or equations used in catalyst activity definitions are described. The residence time as a parameter to calculate the contact time of the reactants into the reactor and consequently on the catalyst sites is defined as;

$$\frac{W}{F} = \frac{m_{cat}}{\dot{N}_{CH_4}} \tag{5.1}$$

where equation 5.1 gives the modified contact time with parameters of m_{cat}, $\dot{N}_{CH_4}$ as the catalyst mass (g) and the methane flow rate in $\mathrm{mol\,h^{-1}}$, respectively. The CH_4 conversion, H_2 and CO (for reformed gas catalytic combustion) are defined based on their molar flow rates in the inlet and outlet of the reactor as below;

$$X_{CH_4} = \frac{\dot{N}_{CH_4,in} - \dot{N}_{CH_4,out}}{\dot{N}_{CH_4,in}} \tag{5.2}$$

$$X_{H_2} = \frac{\dot{N}_{H_2,in} - \dot{N}_{H_2,out}}{\dot{N}_{H_2,in}} \tag{5.3}$$

the CO and CO_2 selectivity's are defined as followings:

$$S_i = \frac{\dot{N}_{i,out}}{\dot{N}_{CH_4,in} - \dot{N}_{CH_4,out}} \tag{5.4}$$

where i denotes the gas CO or CO_2 molar flow rate.

As a check and pass routine for the activity tests, for each experiment point, an elemental mass balance is defined based on C, H, and O elements as written in the Equation 5.5 (e.g. for C^- balance, but the others are calculated identically).

$$C = (1 - \frac{\dot{N}_{CH_4,out} + \dot{N}_{CO,out} + \dot{N}_{CO_2,out}}{\dot{N}_{CH_4,in} + \dot{N}_{CO,in} + \dot{N}_{CO_2,in}}) \cdot 100\% \tag{5.5}$$

5.8 Activity tests

In this section, the catalyst for the MSR reaction has been extensively examined and detailed in [160]; consequently, no additional tests were conducted, either in powder form or as a coating in a small lab scale. The results are directly addressed and discussed in Section 6.4 concerning the prototype reactor. Therefore, the subsequent section focuses on the discussion of CCR catalysts. The tests were executed in the reactor outlined in Appendix A.3.

In this series of experiments, a blank test was conducted under atmospheric pressure at 550 $^\circ$C using a diluted mixture of 1% CH_4 in air. The analysis of the gas at the reactor outlet revealed no detection of any product gas. This result indicates that, under these operating conditions, the reaction solely occurred with the catalyst, and no additional product gases were formed.

Before conducting tests with the synthesized catalysts, a preliminary investigation was carried out using a commercial catalyst, specifically 1Wt.%Pd on Alumina in its reduced form (Alfa Aesar, 300 $\mathrm{m^2\,g^{-1}}$, lot No. 0969000). This commercial catalyst (denoted as 1PdAl-comm) served as a reference for behavior analysis and comparison with the synthesized catalysts.

To prepare the reactor for the test, the catalyst was initially pelletized and subsequently sieved within the range of 200-300 μm. Additionally, SiC (silicon carbide) particles, ranging from 200-300 μm, were incorporated as inert diluting particles at a 1:4 ratio with the catalyst. In the first test, 25.6 mg of catalyst and 107.3 g of SiC were thoroughly mixed in a beaker before loading into the reactor.

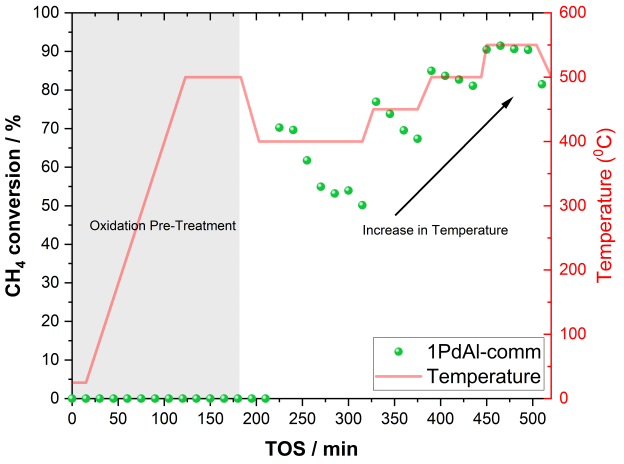

Figure 5.15: CH_4 conversion versus time on stream for catalyst 1PdAl-comm at P_{abs}:1 bar, Air/CH_4:10, W/F:0.0064 $gr_{cat}.min/ml_{CH_4}$.

The feed compositions for the test comprised only CH_4 (4 $\mathrm{N\,mL\,min^{-1}}$) and synthetic air (200 $\mathrm{N\,mL\,min^{-1}}$). The loading procedure involved placing a layer of silicon wool inside the tube reactor, followed by loading the powder mixture and sealing the top with another layer of silicon wool.

As observed In Figure 5.15, there is instability over time at relatively lower temperatures. The instability in single metal Pd catalysts is a well-known drawback, leading to a significant decrease in activity during the reaction, as highlighted in literature [172, 185–188]. The literature currently lacks a definitive conclusion regarding the cause of this deactivation. For instance, Narui et al.[186] suggested that it might be attributed to PdO particle sintering during the reaction, although this explanation has been challenged by others who demonstrated that aging does not significantly affect dispersion.

One potential factor contributing to this issue could be the inhibiting effect of water, which is generated as a product during the oxidation process [189–194]. Water can lead to the formation of inactive hydroxyl groups on the catalyst's

surface, blocking active sites for methane dissociation. Therefore, it becomes crucial in the synthesis of Pd-based catalysts to develop methods that enhance the catalyst's resistance to water. The results indicate that both methane conversion and stability increase with a temperature rise from 400 to 500 °C. This could be attributed to the possibility that at higher temperatures, water, formed as a product, more easily leaves the catalyst's surface, reducing the blockage of active sites.

Additionally, according to the literature, low loading of Pd on Alumina can undergo oxidation with a broad peak observed from 200-700 °C for 1wt.%Pd/Al_2O_3 [195]. This information contributes to the understanding of the catalyst behavior and oxidation characteristics at different temperature ranges.

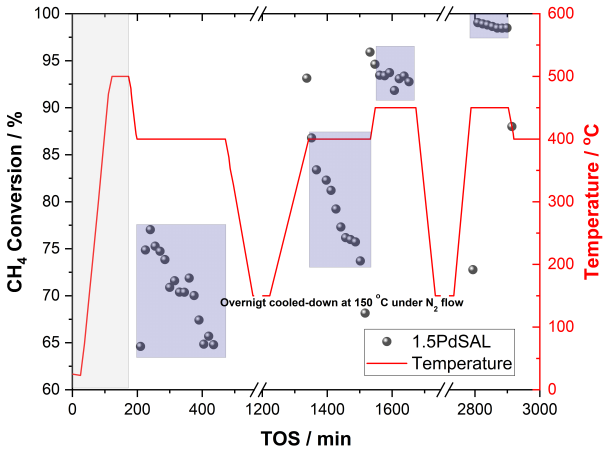

Figure 5.16: CH_4 conversion versus temperature for catalyst 1.5PdSAL at P_{abs}:1 bar, Air/CH_4:10, W/F:0.0082 $gr_{cat}.min/ml_{CH_4}$.

In Figure 5.16, the activity of the 1.5PdSAL is presented at ambient pressure versus various temperatures. Following the pre-oxidation step and subsequent cooling

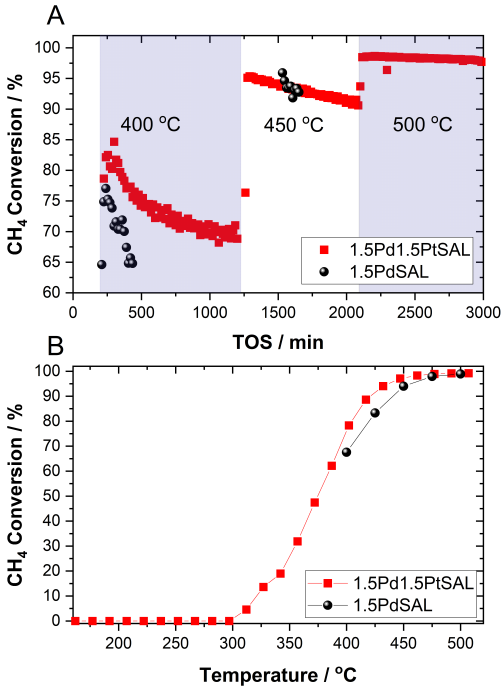

Figure 5.17: CH_4 conversion; (A) versus time for (B) against temperature catalyst; for 1.5PdSAL and 1.5Pd1.5PtSAL , P_{abs}:1 bar, Air/CH_4:10, W/F:0.0082 $gr_{cat}.min/ml_{CH_4}$.

of the reactor to 400 °C for the initiation of GC measurements, the catalyst's activity diminishes progressively throughout the entire measurement period at this temperature. This behavior mirrors the observed trend in the 1PdAL-COMM catalyst. Following this segment, the reactor underwent a transition from a fuel/air atmosphere to N_2, followed by cooling to 150 °C, an overnight holding period, and subsequent heating to 400 °C for the commencement of measurements. Interestingly, there is an increase in CH_4 conversion compared to the previous day's measurements. This phenomenon, reported by Persson et al. [172], suggests a potential for recovering catalyst activity. During this process, rapid changes in

particle morphology or desorption of substances from the catalyst surface may occur, influencing the blocking of active sites [172].

Furthermore, activity tests were conducted on the 1.5PdSAL at 500 °C with 30-minute intervals, alternating the feed stream between Air and N_2 while closing the CH_4 valve. Results indicate the possibility of catalyst activation (regeneration), but with an increase in the number of cycles, the efficiency of reactivation tends to decrease.

Figure 5.17 A shows the the CH_4 conversion versus time which as it is seen, the addition of Pt to the catalyst stabilizes the catalyst for the gathered data at 400 and 450 °C. In Figure 5.17 B, the catalyst activity plotted against a defined heat ramp (1 $\mathrm{K\,min^{-1}}$) for the 1.5Pd1.5PtSAL catalyst. The activity initiates at approximately 320 °C and reaches full conversion around 475 °C. To provide a basis for comparison, key data points for the 1.5PdSAL catalyst are also included in the graph. However, to draw a comprehensive conclusion regarding the activity of the catalyst with the combined loading of Pd and Pt, additional experiments are needed.

5.9 Summary and conclusion

Catalysts based on noble metals, specifically Rh for MSR and Pd-Pt for CCR, were synthesized using an efficient method suitable for large-scale production. Both catalyst series utilized pre-formed commercial γ-Al_2O_3 particles, which provide excellent access for reactants to the active metals on their surfaces. The synthesized catalysts were characterized and then coated into microchannels using a screen printing technique. Each pass of the printer deposited a layer approximately 10 μm thick, allowing for rapid and uniform catalyst layering. The coated layers were analyzed, and activity tests were conducted to evaluate the catalysts' performance. For MSR, 1RhSAL was identified as the optimal catalyst due to its high activity. For CCR, 1.5Pd1.5PtSAL was chosen as the optimal catalyst, demonstrating high activity and good stability in the MR system.

6 Prototype autothermal membrane reformer

The outcomes and experimental results described in the preceding chapters have shaped the trajectory for the development and arrangement of a third generation of the microstructured membrane reactor (μ-EnH_2ancer V 3.0), which incorporates a Pd membrane and operates autothermally for on-site generation of pure hydrogen. However, for this generation, μ-EnH_2ancer V 3.0 should be operated autothermally; therefore, a catalytic combustor should also be integrated into the system.

Therefore, it should meet the following additional requirements:

- Ultra-compact design to enable high heat transfer from the heat source to the heat sink
- Dedicated air distribution in the combustion part to avoid potential hot spots on the catalytic combustion part
- Material selection in terms of thermal stability for the membrane reformer

In this chapter, the third version of μ-EnH_2ancer, inspired by versions 1.0 and 2.0, is presented along with its improvements over the previous versions. The plates of the membrane reformer, μ-EnH_2ancer V 3.0, were coated with a catalyst based on the optimal cases discussed in Chapter 5. For Pd membrane integration, a thin layer of $12\,\mu\mathrm{m}$ was used. The experiments were initially conducted on a module that included pre-reforming, reforming, combustion, and an air distributor. In another set of experiments, all the components of μ-EnH_2ancer V 3.0 were

welded together; however, a sealed Pd membrane was not achieved. Therefore, no experimental results are reported for the membrane reformer in this chapter. Instead, the performance of such a system is reported theoretically using a multi-domain, multiphysics 2D simulation. Further development of the membrane reformer, based on the simulation results, was studied, and flexible designs were printed using AM, which will be shown in Chapter 7.

6.1 Design of the μ-EnH_2ancer V 3.0

In this study, a microstructured membrane reactor with the specified characteristics was designed, constructed, and partially tested. The detailed internal guidance of the gas flow within the microchannels, the welding procedure enabling the modularity of the μ-EnH_2ancer V 3.0, and the precise adjustment of the microstructured plates without causing damage (manufacturability) were developed as part of this research.

The microstructured plates were laser-welded in a leak-tight manner layer by layer, for the entire assembly, except in the case where the plates were integrated with Pd foil. The reformer comprises a housing with inlets for methane, water, and a sweep gas, as well as outlets for the reformate and separated hydrogen. The number of membrane modules integrated into the reactor housing depends on the desired hydrogen production capacity. Each membrane module is seamlessly integrated through laser welding, and the specific layout of the μ-EnH_2ancer V 3.0 is presented in detail below. To facilitate module replacement in the event of membrane defects, the laser-welded membrane modules are sealed together using graphite rings. The housing and membrane modules are constructed using a Crofer 22 APU which shows excellent corrosion resistance up to $900\,^{\circ}\mathrm{C}$ in the relevant gas atmospheres.

The stacking arrangement of the μ-EnH_2ancer V 3.0 is illustrated in Figure 6.1. It shows photographic and schematic representations of the MR integrated with CCR. Each module consists of a 'pre-reforming' zone, where methane or natural

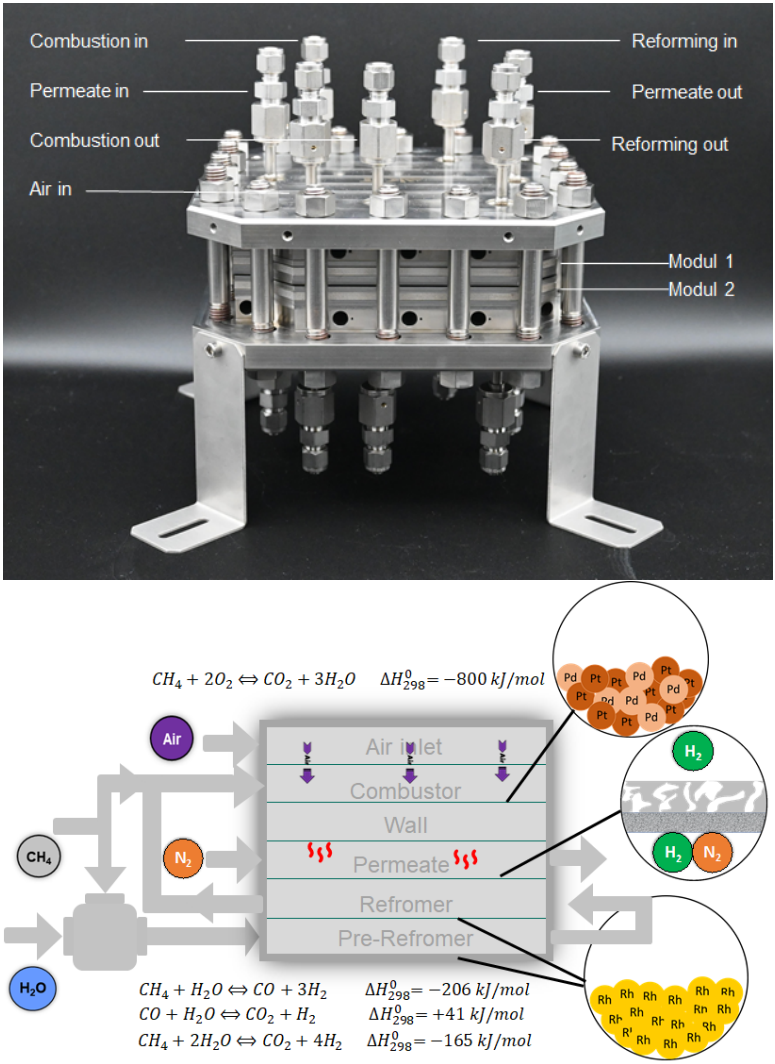

Figure 6.1: The top illustration depicts the stacking principle of the modular microstructured membrane reactor, while the bottom schematic showcases the channel configuration within the microchannel membrane module, highlighting heat integration through combustion.

gas is converted with water vapor. Ideally, a hydrogen partial pressure slightly greater than the permeate pressure is generated to avoid back-permeation from the permeate side of the membrane. The subsequent reforming zone is in contact with the Pd-based membrane which separates and purifies the generated H_2 and further enhances the methane conversion and the hydrogen recovery along the microchannel. The microchannels were created using wet chemical etching. In the 'pre-reforming' zone, there are 61 microchannels with dimensions of 1340 μm x 300 μm x 87 mm (width x depth x length), while the microchannels in the 'reforming' zone, which are in contact with the membrane, only vary in length (105 mm). The microstructured plates currently have a thickness of 1 mm, but the reforming plate is designed based on a 2 mm thick plate (see Table 3.6).

6.2 Test set-up and operating conditions and definitions

The test rig used for methane steam reforming (see Figure 6.2) was modified for the experimental investigation of the μ-EnH_2ancer. The flow chart of the modified test rig is shown in Figure 6.2. The microstructured membrane reactor was installed into the test rig, and 8 heating cartridges width 8 thermocouples on each side of the housing were used for temperature control and measurement. The pressure drop along the microchannels was negligible ($<$100 mbar).

The initial concentration of the feed was adjusted through a bypass, while the reactor underwent flushing with N_2. Gas concentrations in the retentate were assessed using gas chromatography (GC, Agilent Technologies 7890B) featuring TCD and FID detectors. The outlet gas volume flows were measured by using a bubble flow meter and their mole fractions were analyzed with GC. Depending on the type of the experiment for each study, the outlet of the reforming section was investigated immediately after the reactor outlet or was delivered to the combustor where excess air was ad-mixed, and then the combustor outlet was measured and analyzed. Given the absence of a successfully assembled MR, the reaction pressure was intentionally maintained at a low level. This decision was made as

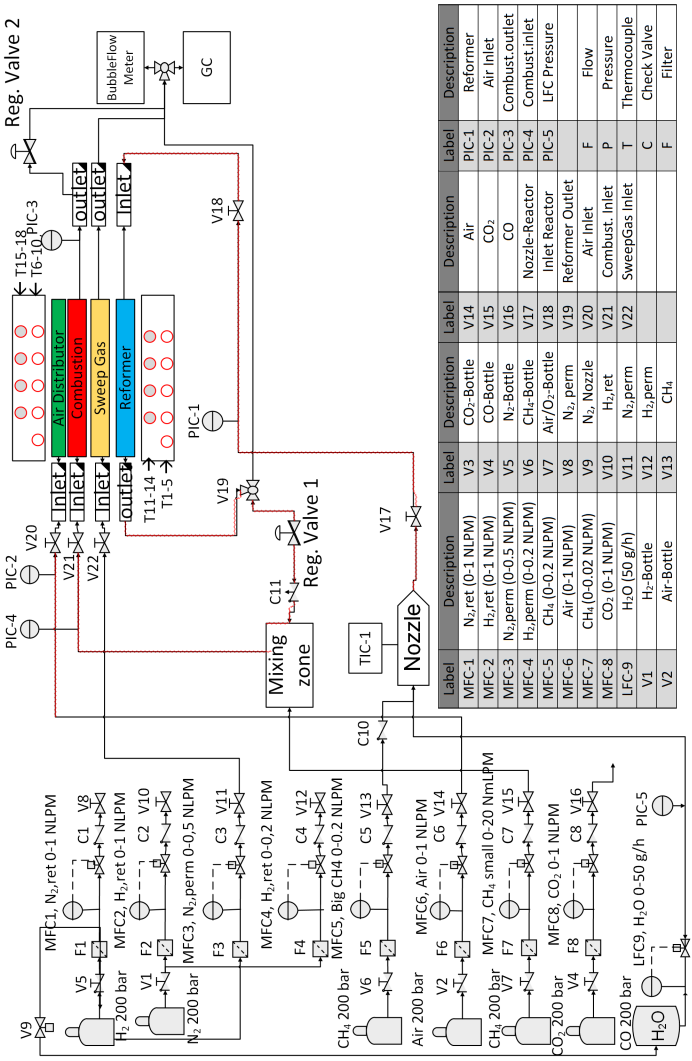

Label	Description	Label	Description	Label	Description	Label	Description
MFC-1	N_2,ret (0-1 NLPM)	V3	CO_2-Bottle	V14	Air	PIC-1	Reformer
MFC-2	H_2,ret (0-1 NLPM)	V4	CO-Bottle	V15	CO_2	PIC-2	Air Inlet
MFC-3	N_2perm (0-0.5 NLPM)	V5	N_2-Bottle	V16	CO	PIC-3	Combust.outlet
MFC-4	H_2perm (0-0.2 NLPM)	V6	CH_4-Bottle	V17	Nozzle-Reactor	PIC-4	Combust.inlet
MFC-5	CH_4 (0-0.2 NLPM)	V7	Air/O_2-Bottle	V18	Inlet Reactor	PIC-5	LFC Pressure
MFC-6	Air (0-1 NLPM)	V8	N_2, perm	V19	Reformer Outlet		
MFC-7	CH_4 (0-0.02 NLPM)	V9	N_2, Nozzle	V20	Air Inlet	F	Flow
MFC-8	CO_2 (0-1 NLPM)	V10	H_2,ret	V21	Combust. Inlet	P	Pressure
LFC-9	H_2O (50 g/h)	V11	N_2,perm	V22	SweepGas Inlet	T	Thermocouple
V1	H_2-Bottle	V12	H_2,perm			C	Check Valve
V2	Air-Bottle	V13	CH_4			F	Filter

Figure 6.2: The diagram illustrating the flow scheme of the test rig utilized to experimentally assess the μ-EnH_2ancer V 3.0.

the focus of the experiment did not involve studying the pressure effects in the absence of a membrane.

6.3 Reactor assembly

Considering the laser welding process as a crucial step in the design and assembly. Table 6.1 provides details on the characteristics of the alloys utilized in the membrane reformer in this study.

Table 6.1: Parameters applied for laser welding of μ-EnH_2ancer V 3.0 components.

Trenches depth (mm)	P (W)	P (W)	Frequency (Hz)	Pulse duration (ms)	Velocity (m/min)	Focus (mm)	Width (mm)	Material
Foil	1200	360	400	0.75	2.40	-	1	Pd
0.3	600	-	CW	-	3	+1	-	Crofer 22 APU
1.3	850	-	CW	-	3	+1	-	Crofer 22 APU

To join the plates together, a laser welding technique was used. It, as a general practice, is characterized by a minimal heat input, resulting in a narrow or potentially negligible heat-affected zone. More details were discussed in Section 4.4.

Figure 6.3 shows the assembly procedure for the μ-EnH_2ancer V 3.0 involving a step-by-step welding process for different weld seams. The initial phase includes the membrane substrate, utilizing either Pd composite membranes on metallic substrates or Pd foils with adjacent plates, such as the micro-sieve configuration in V.01 or without it as in V.03. Following the welding of each new plate, a leakage test with He is conducted to ensure the module is gas-tight. However, in this step, the assembled modules were not He leak-tight as the Pd foil damaged (see Figure 6.3 b). Proceeding with additional plates in both directions from the first plate (membrane plate) may induce thermal and mechanical stresses on the module, particularly affecting the Pd layer.

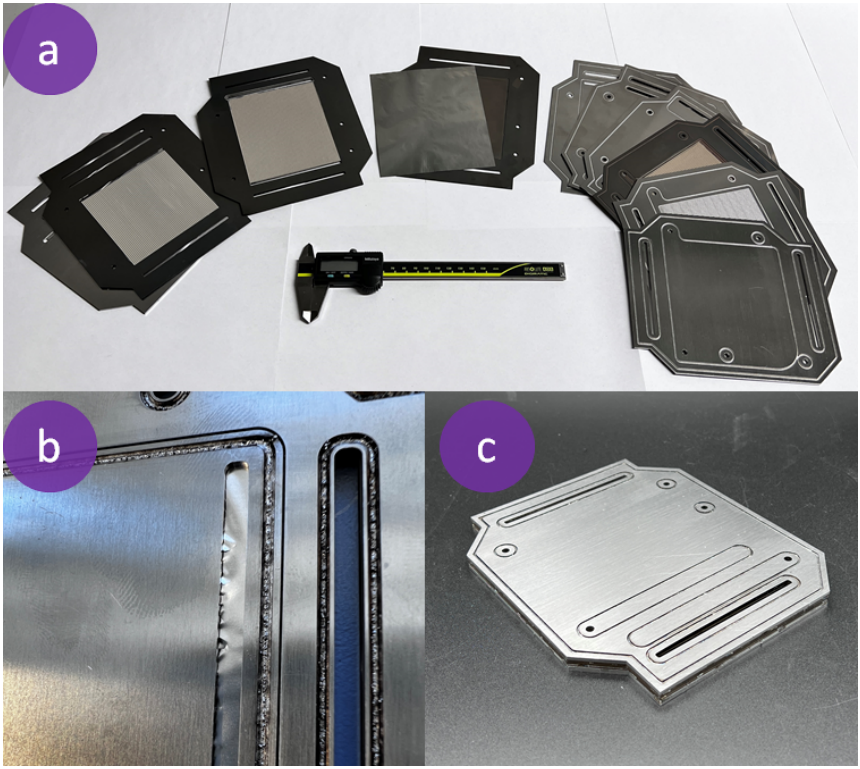

Figure 6.3: Assembly procedure for μ-EnH_2ancer V 3.0 plates: a) Integration of all plates, a porous substrate (Crofer 22 APU), and a 12.5 μm Pd foil. b) Foil cracking occurred during the He test due to mechanical force applied during rubber tightening. c) Successful testing and coupling of the reactor without the membrane part in this configuration.

6.4 Methane steam reforming reaction in μ-EnH_2ancer V 3.0

In this section, an electrically-heated examination of the MSR was conducted experimentally in the prototype reactor. Regarding the modeling, it was assumed that infinitely fast heat transfer occurs without any temperature gradient in the catalyst layers. Since the thickness of the catalyst layer, which could create cold spots, is very small compared to the housing of the reactor, and any heat loss is compensated by heating cartridges, this assumption might be correct for this system. The properties of both the catalysts and the coated layer are outlined in Table 6.2.

Table 6.2: Parameters for catalyst characteristics implemented in prototype reactor.

Sample	Weight	Thickness	Catalyst composition	Density	Porosity[a]	Tortuosity[b]	Particle size [c]	Pore Diameter [d]
	(gr)	(μm)	(-)	(kg m^{-3})	(-)	(nm)	(nm)	(nm)
PT-PR-1	0.45	40	1RhSAL[e]	1493	0.5	$\tau = \epsilon^{-1/3}$	100	20
PT-R-1	0.20	17	1RhSAL	1493	0.5	$\tau = \epsilon^{-1/3}$	100	20
PT-C-1	0.41	40	1.5Pd1.5PtSAL	1220	0.5	$\tau = \epsilon^{-1/3}$	100	20

[a] It is assumed from our previous knowledge based on the catalyst coating on the small plates
[b] For saturated porous media τ is calculated from Millington and Quirk correlation: $\tau = \epsilon^{-1/3}$
[c] Average size taken from TEM results
[d] Average size taken from N_2 chemisorption results
[e] SAL is preformed γ -Al_2O_3

The graph in Figure 6.4 illustrates the CH_4 conversion as a function of temperature in the range of 600 to 900 K at nearly atmospheric pressure (P_{abs}= 1.14 bar). The steam-to-carbon ratio was maintained at 3.7, and the modified contact time (W/F) was set at 1.53 $\mathrm{gr_{cat}\,h/mol_{CH_4}}$. To facilitate result comparison and explore the reactor's behavior theoretically, two kinetic models were employed. The first, proposed by Xu and Froment [28], is associated with a $NiMgAl_2O_4$ catalyst, while the second, studied by Halabi et al. [29, 196], refers to a Rh/Ce_α $Zr_{1-\alpha}O_2$ catalyst. A mathematical 2D model was used to simulate the reformer section of the reactor, with the model's details and formulation explained in Section 6.6.

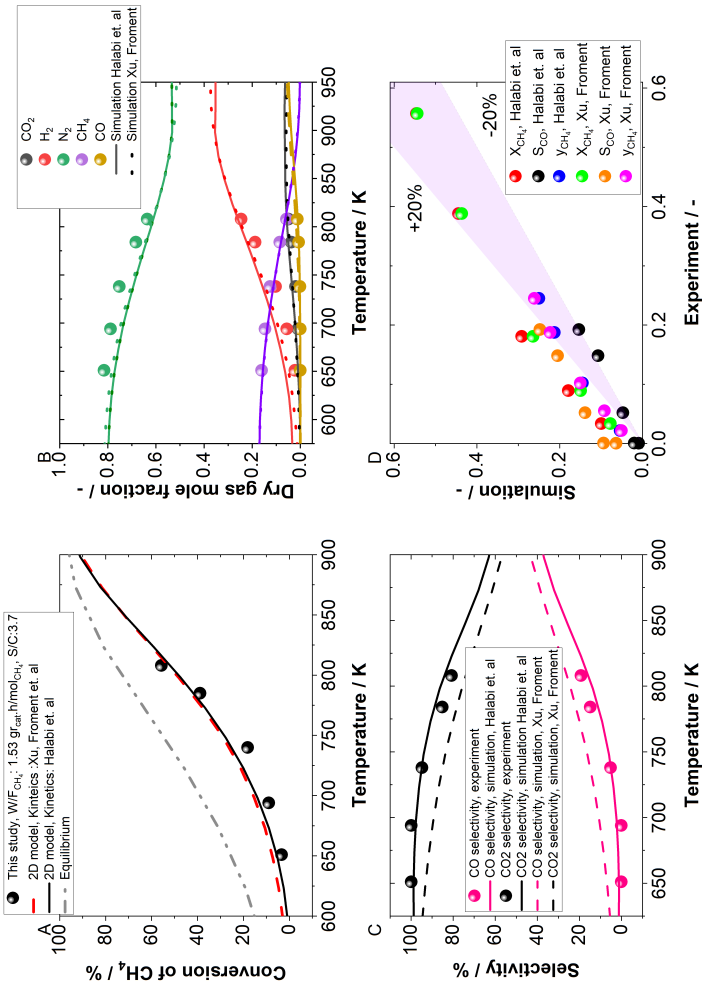

Figure 6.4: MSR test at μ-EnH_2ancer V 3.0 plates: A) conversion of CH_4 versus temperature B) Dry gas molar fraction of the gases C) CO selectivity and CO_2 selectivity versus temperature D) 2D model validation against experiments. The 2D model was simulated based on the kinetics of Halabi et. al and Xu, Froment at S/C:3.7 and W/F:1.53 $\mathrm{gr_{cat}\ h/mol_{CH_4}}$.

In Figure 6.5 A, it is observed that as the temperature is increased from 651.15 to 808.15 K, the conversion increases from 3.4% to 55.7%, accompanied by a shift in CO selectivity from 0.08% to 19.3% (see Figure 6.5 C). No experiments were conducted to assess mass transport resistance or limitations, and this aspect is solely addressed by the model in the following section.

As shown in Figure 6.5, the behavior of the reaction is different for the two kinetic models used. The performance of the Rh/$Ce_{\alpha}Zr_{1-\alpha}O_2$ catalyst and its kinetic model were evaluated by Halabi et. al [29, 196] in comparison to the traditional Ni-based catalyst for steam reforming, using the kinetics proposed by Xu and Froment [28]. The steady-state CH_4 conversion profiles along the relative length of a 5 cm fixed bed reactor were compared for both catalysts at 550 °C and 1.5 bar, employing a gas composition of (7.0 kPa CH_4, 28.0 kPa H_2O, and 4.0 kPa H_2). Initially, 10 mg of catalyst loading was used for both. According to Xu and Froment kinetics [28], the Ni-based catalyst yielded a maximum CH_4 conversion of 64%. In contrast, the kinetic model derived from Halabi et al. [29, 196] for the Rh-based catalyst predicts a maximum CH_4 conversion of 79%, highlighting the superior activity of the Rh catalyst compared to the Ni catalyst. They found out that the Ni catalyst weight loading needs to be increased 14 times to match the activity of the Rh catalyst, underscoring the significant performance difference between the two catalysts.

As evident from Figures 6.4 D, both models exhibit deviations from experiments, exceeding $\pm$ 20 %. One main reason might be the assumption of the isothermal condition which makes temperature gradients along the channels. Another reason might be the necessity of a kinetic study for the synthesized catalysts. However, since it falls outside the scope of this investigation, the kinetics model proposed by Halabi et al. [29, 196] is adopted as the primary model in this section and subsequent sections as it is based on using novel metal of Rh.

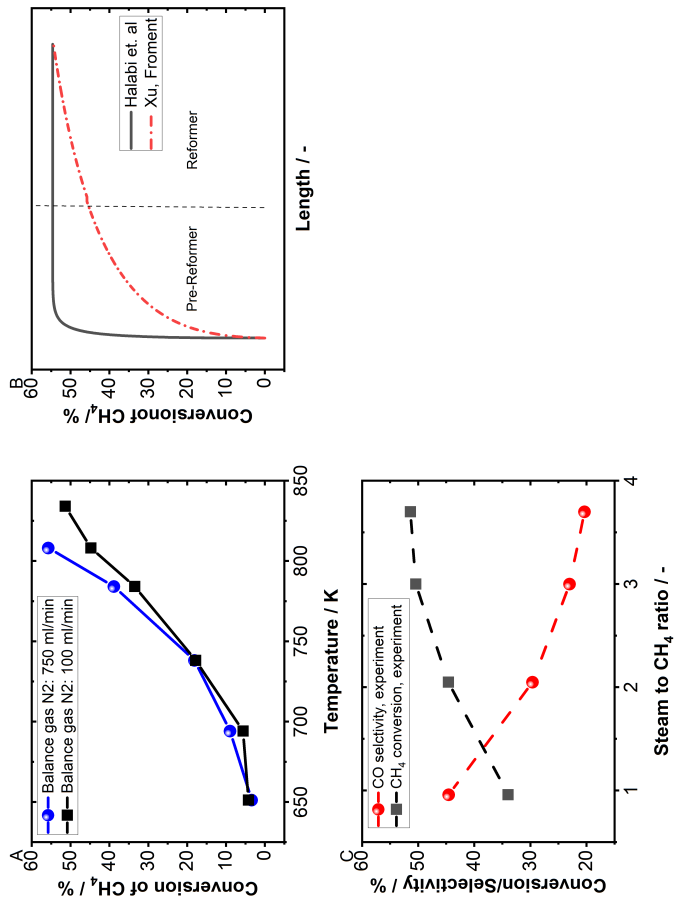

Figure 6.5: MSR test at μ-EnH_2ancer V 3.0 plates: A) conversion of CH_4 versus temperature for different N_2 flow rates B) conversion of CH_4 along the reactor length for kinetics of Halabi et al. and Xu, Froment (simulation) at T:808 K, S/C:3.7 W/F:1.53 $\mathrm{gr_{cat}\ h/mol_{CH_4}}$, C) conversion and CO selectivity versus S/C ratio T:808 K, P:1 bar, W/F:1.53 $\mathrm{gr_{cat}\ h/mol_{CH_4}}$.

6.5 Combustion Reactor

In this section, a specialized test was performed to evaluate the efficiency of the air distributor and optimize the air-to-fuel ratio for the microenhancer. This test specifically targeted the components of the combustion plates. The assembly process, executed via laser welding (see Figure 6.6), is explained in detail in the preceding section. The catalyst weight and layer properties are provided in Table 6.2.

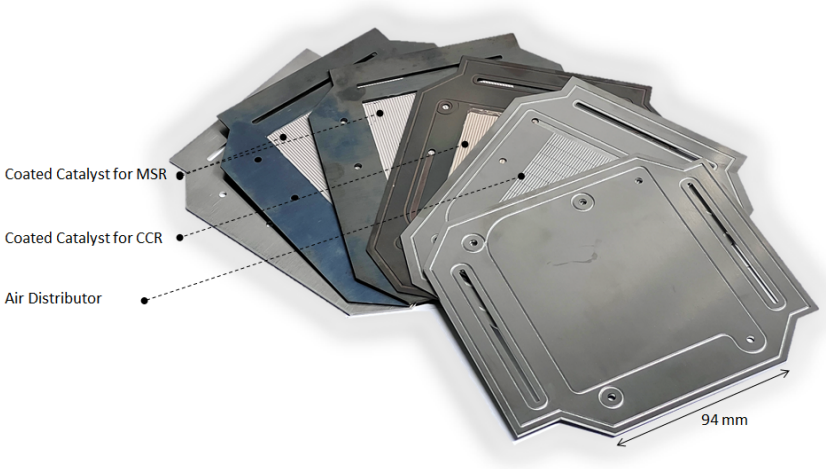

Figure 6.6: Air distributor plate used in the CCR test for controlling the heat reduce along the reactor bed.

For tests conducted with pre-mixed feed for the CCR, it is important to note that the air inlet is closed, and the only entry point for the feed is through the fuel stream. In both simulation and activity tests, the dead zone where gas could

reach the air distribution plate is ignored and assumed to have no impact on CCR performance.

Figure 6.7 shows the performance of the plate combustor with a configuration of a pre-mixed gas inlet, where the air and fuel are combined beforehand and introduced into the channels from the bottom plate (catalyst bed). The second configuration, which involves the air distributor, is discussed in the following section. To estimate the activation energy of the catalyst, a temperature variation experiment was conducted, ensuring that methane conversions remained below 20%. A power-law model was used to define the reaction rate as follows:

$$r_{CH_4} = K_0 exp(-E/RT) C_{CH_4}^{\alpha} C_{O_2}^{\beta} \tag{6.1}$$

It is assumed that the reaction rate changes to CH_4 with a power of 1 (α=1) and for O_2 with a power of zero (β=0) since the reaction is carried out under lean condition (excess air). Using the Arrhenius equation, the activation energy was calculated to be approximately $77\,\mathrm{kJ\,mol^{-1}}$, and the frequency factor was determined to be $1.4 \times 10^8\,\mathrm{s^{-1}}$ for the simulation phase. To validate these findings against experimental data, a 2D multiphysics simulation was conducted under isothermal conditions, using 16 heating cartridges to regulate the temperature for the catalyst test. As shown in Figure 6.7 A, the temperature and mole fraction of the components (dry gas) are in good agreement with the simulation (Figure 6.7 B). All data from the isothermal condition simulation were collected based on the CCR outlet. Figure 6.7 C illustrates the effect of the air-to-fuel ratio on the conversion of CH_4 versus temperature. As seen, with an increase in the air ratio from 5 to 15, the conversion decreases from around 95% to 65% at 400 $^{\circ}\mathrm{C}$. This may be due to higher velocity in the channel, which limits the diffusion of the fuel to the catalyst layer. Additionally, Figure 6.7 D shows an increase in the W/F ratio from 3.85 to 15.4 $\mathrm{gr_{cat}\,h/mol_{CH_4}}$ results in an increase in CH_4 conversion from approximately 60% to 85%.

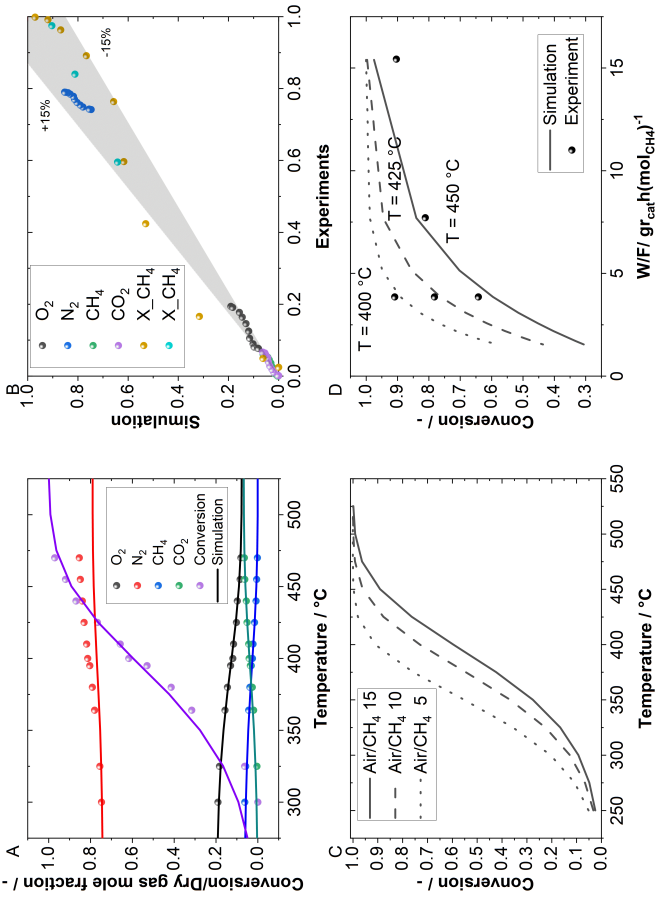

Figure 6.7: CCR test at μ-EnH_2ancer V 3.0 plates: A) conversion of CH_4 and mole fraction of the dry gas in the outlet of the reactor for 40CH4600Air ($\mathrm{N\,mL\,min^{-1}}$), W/F:3.85 $\mathrm{gr_{cat}\,h/mol_{CH_4}}$ B) simulation results against experiments C) effect of air to CH_4 versus temperature for different Air to CH_4 ratios D) Conversion versus at different temperatures versus W/F:3.85-15.4 $\mathrm{gr_{cat}\,h/mol_{CH_4}}$. Tests were carried out at atmospheric pressure.

6.5.1 Effect of using Air distribution plate in μ-EnH_2ancer V 3.0

In this section, the air enters the reaction bed through a separate distributor aimed at managing heat across/along the reactor bed when hot spots occur (see Figure 6.6). In the literature, many studies have been allocated to the use of special configurations for mixing fuel and oxygen/air to improve the heat distribution e.g. CCR [197–199].

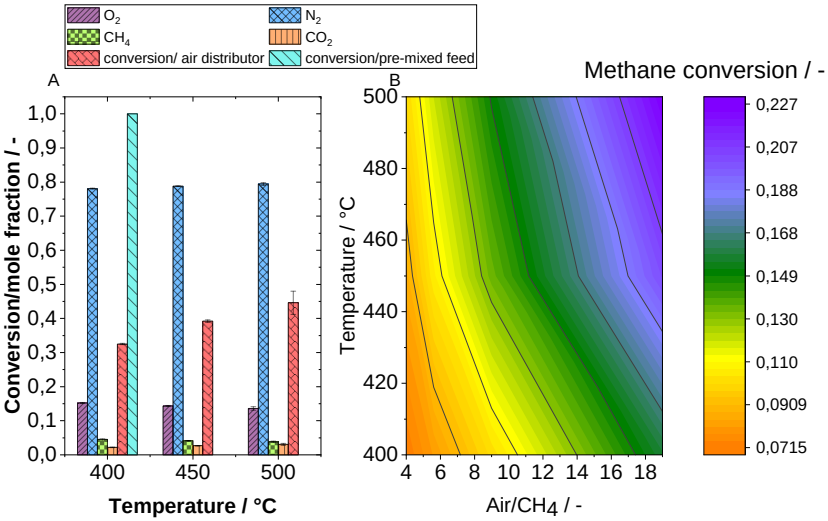

Figure 6.8: Effect of air for tests carried out at A) conversion of CH_4/mole fraction of the gases (dry basis) 5$CH_4$75Air ($N\,mL\,min^{-1}$), W/F:30 $gr_{cat}\,h/mol_{CH_4}$, and B) conversion of CH_4 versus temperature and Air to CH_4 ratios.

As observed in Figure 6.8, after conducting experiments in both pre-mixed feed mode and with the use of an air distributor plate to distribute air along and across the catalytic plate, it was found that incorporating the air distributor leads to a

significant reduction in CH_4 conversion, down to approximately 30%, compared to the pre-mixed mode at 400 °C. At higher temperatures, for the configuration with air distribution, methane conversion increases progressively with temperature. A 2D model along a single channel, with the bottom surface coated with a catalyst layer, was considered suitable only for the pre-mixed feed case and was therefore used as the base case, as discussed in detail in Section 6.9. However, based on experimental findings (Figure 6.8), a 2D single-channel model cannot fully capture the effect of air distribution along the channel, since air is first distributed across multiple channels. A 3D model is therefore more appropriate, as it allows a more realistic simulation of air–fuel mixing. In order to save the computation time, the 3D simulation was carried out under the assumption that no catalytic reactions occur on the catalyst surface, focusing solely on the mixing behavior. To evaluate this effect, a simplified mass and momentum balance was employed to study mixing behavior under different feed flow rate conditions.

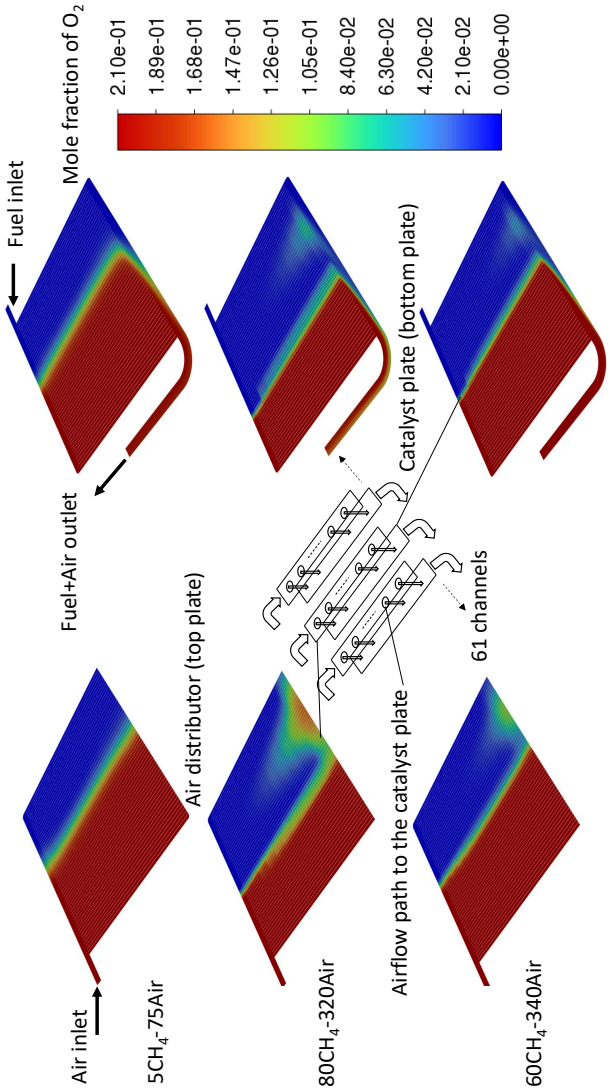

Figure 6.9: Mole fraction of O_2 in mixture of CH_4 and air with different flow rates of $5CH_4$-75Air, $80CH_4$-320Air, and $60CH_4$-340Air $\mathrm{mL\,min^{-1}}$ where no reaction term is considered.

As shown in Figure 6.9, the mixing of CH_4 and air (O_2 in this case) is incomplete at the selected flow rate ratios. This suggests that a significant portion of the catalyst bed is not adequately supplied, as the O_2 to CH_4 ratio falls below the stoichiometric ratio. It becomes clear that only a small part of the reactor bed is actively participating in the reaction, which may contribute to the lower activity observed in the air-distributor configuration compared to a pre-mixed air and fuel system.

Based on the observation from Figure 6.10, the velocity perpendicular to the reactor bed varies among different channels due to mal-distribution and also along the channels. Generally, across all channels, the middle holes contribute the least flow directed toward the catalyst bed. Regardless of the configuration, assuming a uniform distribution for all channels in the catalyst plate, the flow distribution is further scrutinized in the subsequent study through a 2D model. This involves proposing alternative designs using AM techniques.

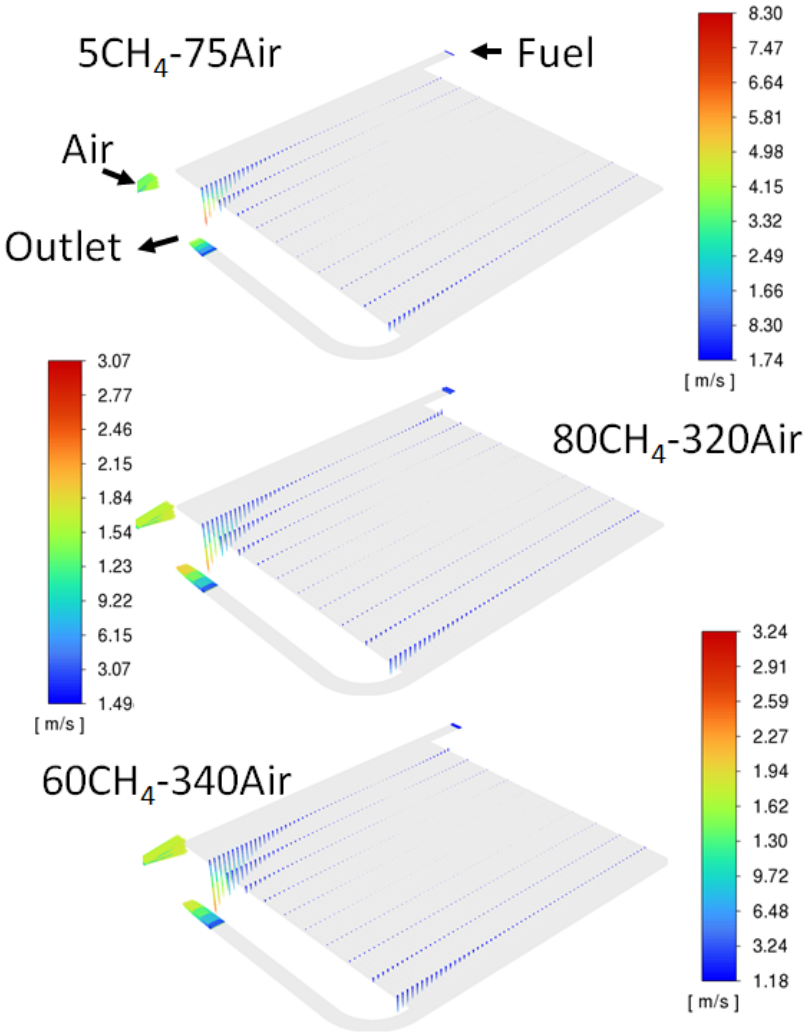

Figure 6.10: Velocity vector in direction of the micro-hole depths of O_2 in mixture of CH_4 and air with different flow rates of 5CH_4-75Air, 80CH_4-320Air, and 60CH_4-340Air $\mathrm{mL\ min^{-1}}$ where no reaction term is considered.

6.6 Membrane reformer

Since successful integration of either a Pd composite membrane or a Pd foil into μ-EnH_2ancer V 3.0 was not achieved, the experiments for an autothermal membrane reformer remained incomplete in this study. However, despite encountering technical challenges in assembling such a complex and fragile system, it is worthwhile to proceed with simulating the system based on the insights gained from this thesis and previous studies.

To this end, a non-isothermal 2D model is described initially, followed by validation of the results against simulation data from a previous study based on an electrically heated membrane reformer (μ-EnH_2ancer V 1.0) [37]. Subsequently, the model was further developed for a non-isothermal mode with integrating the combustion module with membrane reformer based on the design of μ-EnH_2ancer V 3.0.

6.6.1 Mathematical formula

In order to model such a compact system includes four main parts endothermic reaction part (MSR), exothermic reaction part (CCR), permeate side of Pd membrane, and conductive Crofer 22 APU walls. Regarding the integration of the combustion section, one approach is to fabricate the combustor cell separately using laser welding and then connect it to the membrane reformer solely through graphite gaskets. Alternatively, as demonstrated in this study, all components can be directly integrated into a single cell. Figure 6.11 shows a cross-cut view of such a system and also a simplified sketch with the same size as the real geometry for one cell. When comparing with a cell structure, the model, particularly the heat transfer, was considered only for the central rectangular section. Moreover, as shown in the base case, no air distributor was included.

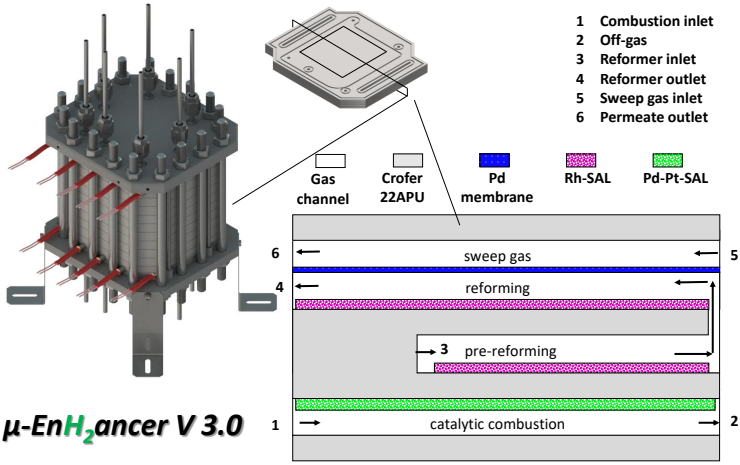

Figure 6.11: A graphical representation of the stacked cells of the autothermal membrane reformer and a cross view of one cell for a 2D modeling.

The mathematical formulation for a 2D heterogeneous model is presented below. To illustrate the desired set of equations corresponding to each section in Figure 6.11, all formulas are organized into subcategories. These subcategories include the bulk gas phase, the porous structure representing the catalyst-coated layer for each reaction, and the solid structure (in the case of non-isothermal simulations) representing the solid walls of Crofer 22 APU.

6.6.1.1 Free-flow channel

- momentum transfer and mass conservation

momentum in x direction

$$\rho_{mix}(u_x\frac{\partial u_x}{\partial x}+u_y\frac{\partial u_x}{\partial y})=-\frac{\partial P}{\partial x}+\frac{\partial}{\partial x}(2\mu_{mix}\frac{\partial u_x}{\partial x}-\frac{2}{3}\mu_{mix}(\frac{\partial u_x}{\partial x}+\frac{\partial u_y}{\partial y}))+\frac{\partial}{\partial y}(\mu_{mix}(\frac{\partial u_x}{\partial y}+\frac{\partial u_y}{\partial x})) \tag{6.2}$$

momentum in y direction

$$\rho_{mix}(u_x\frac{\partial u_y}{\partial x}+u_y\frac{\partial u_y}{\partial y})=-\frac{\partial P}{\partial y}+\frac{\partial}{\partial y}(2\mu_{mix}\frac{\partial u_y}{\partial y}-\frac{2}{3}\mu_{mix}(\frac{\partial u_x}{\partial x}+\frac{\partial u_y}{\partial y}))+\frac{\partial}{\partial x}(\mu_{mix}(\frac{\partial u_x}{\partial y}+\frac{\partial u_y}{\partial x})) \tag{6.3}$$

continuity equation

$$\rho_{mix}(\frac{\partial u_x}{\partial x}+\frac{\partial u_y}{\partial y})+(u_x\frac{\partial \rho_{mix}}{\partial x}+u_y\frac{\partial \rho_{mix}}{\partial y})=0 \tag{6.4}$$

In this equation, ρ_{mix} represents the density of a gas mixture, which is estimated using the ideal-gas state equation. Meanwhile, μ_{mix} denotes the viscosity of the gas mixture, which is estimated using the Wilke method as reported by Poling et al. [200].

- heat transfer and energy conservation

$$\rho_{mix}C_{p,mix}(u_x\frac{\partial T}{\partial x}+u_y\frac{\partial T}{\partial y})=k_{mix}(\frac{\partial^2 T}{\partial x^2}+\frac{\partial^2 T}{\partial y^2}) \tag{6.5}$$

In this context, $C_{p,mix}$ denotes the heat capacity of a gas mixture, which is determined by computing the weighted average heat capacity of the chemical

species involved. Additionally, k_{mix} represents the thermal conductivity of the gas mixture, which is estimated utilizing the Mason and Saxena method as reported by Poling et al. [200].

- mass transfer

$$\begin{aligned}\rho_{mix}((u_x\frac{\partial\omega_i}{\partial x}+u_y\frac{\partial\omega_i}{\partial y})+\omega_i(\frac{\partial u_x}{\partial x}+u_y\frac{\partial u_y}{\partial y}))\\ =\frac{\partial}{\partial x}(\rho_{mix}\omega_k\sum_{j=1,j\neq i}^{n_g}D_{ji}^F(\frac{\partial x_j}{\partial x}+\frac{\partial x_j}{\partial y}\\ +(\frac{x_j-\omega_j}{P})(\frac{\partial P}{\partial x}+\frac{\partial P}{\partial y})))+\frac{\partial}{\partial y}(\rho_{mix}\omega_k\sum_{j=1,j\neq i}^{n_g}D_{ji}^F(\frac{\partial x_j}{\partial x}+\frac{\partial x_j}{\partial y}\\ +(\frac{x_j-\omega_j}{P})(\frac{\partial P}{\partial x}+\frac{\partial P}{\partial y})))\end{aligned} \tag{6.6}$$

where ω and x respectively denote the mass fraction and mole fraction of chemical species. The multicomponent Fick diffusivities, denoted as D_{ij}^F, are related to the Maxwell-Stefan diffusivities as follows [201]:

$$D_{ij}^{MS}=\frac{x_ix_j\sum_{k\neq i}D_{ij}^F(adjB_i)_{kj}}{\omega_i\omega_j\sum_{k\neq i}(adjB_i)_{kj}};where(B_i)_{jk}=-D_{jk}^F+D_{ik}^F \tag{6.7}$$

In the context of multicomponent diffusion in gases at low density, the Maxwell-Stefan diffusivities D_{ij}^{MS} can be substituted with the binary diffusivities D_{ij} [201]. These binary diffusivities are estimated using the Fuller equation as reported by Poling et al. [200].

- Boundary conditions

Inlet conditions as shown in Figure 6.11

- fully developed flow with an inlet velocity $u_x = u_{in}$

- temperature $T = T_{in}$
- mass fraction $\omega_i = \omega_{i,in}$

conditions at the outlet

- pressure $P = P_{out}$
- zero flux $\frac{\partial w_i}{\partial x} = 0; \frac{\partial T}{\partial x} = 0$

at $y = y_{outlet,boundary}$

- $\frac{\partial u_x}{\partial y} = 0; \frac{\partial \omega_i}{\partial y} = 0; \frac{\partial T}{\partial y} = 0$

at the interface of the catalyst layer and flow channel

- no slip $u_x = 0$
- heat flux continuity $\overrightarrow{n}.(N_{channel} - N_{catalyst}) = 0$
- zero flux $\frac{\partial \omega_i}{\partial y} = 0$

boundary condition for the interface between retentate (feed) and permeate sections, the flux of H_2 is as follows:

$$-n.(-D_i \nabla c_{H_2} + u c_{H_2}) = J_{H_2,0} \tag{6.8}$$

it is worth mentioning that, in the sweep channel (permeate side) a tiny amount is considered (in case of no sweep gas) which prevents negative concentration errors during the solving of the simulations.

6.6.1.2 Porous catalyst layer and porous parts of Crofer 22 APU printed by SLM

- Momentum and mass conservation

momentum in x direction

$$\frac{\mu_{mix}}{\kappa}u_x = -\frac{\partial P}{\partial x} + \frac{\partial}{\partial x}(2\frac{\mu_{mix}}{\epsilon}\frac{\partial u_x}{\partial x} - \frac{2}{3}\mu_{mix}(\frac{\partial u_x}{\partial x} + \frac{\partial u_y}{\partial y})) + \frac{\partial}{\partial y}(\frac{\mu_{mix}}{\epsilon}(\frac{\partial u_x}{\partial y} + \frac{\partial u_y}{\partial x})) \tag{6.9}$$

momentum in y direction

$$\frac{\mu_{mix}}{\kappa}u_y = -\frac{\partial P}{\partial y} + \frac{\partial}{\partial y}(2\frac{\mu_{mix}}{\epsilon}\frac{\partial u_y}{\partial y} - \frac{2}{3}\mu_{mix}(\frac{\partial u_x}{\partial x} + \frac{\partial u_y}{\partial y})) + \frac{\partial}{\partial x}(\frac{\mu_{mix}}{\epsilon}(\frac{\partial u_x}{\partial y} + \frac{\partial u_y}{\partial x})) \tag{6.10}$$

continuity equation

$$\rho_{mix}(u_x\frac{\partial u_x}{\partial x} + \frac{\partial u_y}{\partial y}) + (u_x\frac{\partial \rho_{mix}}{\partial x} + u_y\frac{\partial \rho_{mix}}{\partial y}) = 0 \tag{6.11}$$

In this equation, κ represents the permeability of the porous media, which is calculated based on the Kozeny-Carman equation [202]. Additionally, ϵ denotes the volume void fraction (porosity) of the porous media, which is assumed to be 0.4 for the catalyst layer.

- heat transfer and energy conservation

$$\rho_{mix}C_{p,mix}(u_x\frac{\partial T}{\partial x} + u_y\frac{\partial T}{\partial y}) = k_{eff}(\frac{\partial^2 T}{\partial x^2} + \frac{\partial^2 T}{\partial y^2}) + \nu r_j \Delta H \tag{6.12}$$

In this expression, H represents the enthalpy of the reaction, while k_{eff} denotes the effective thermal conductivity for a porous catalyst domain, which is computed using a volume-weighted average. The thermal conductivity of the solid catalyst ($k_{cat/crofer}$) is estimated based on alumina and is given in Table 6.3. Therefore, the k_{eff} is calculated as follows:

$$k_{eff} = \epsilon k_{mix} + (1-\epsilon) k_{cat/crofer} \tag{6.13}$$

$$Q_{reaction} = (1-\epsilon) \sum \Delta H_{reaction,j} r_{reaction,j} \tag{6.14}$$

where k_{mix} represents the gas mixture thermal conductivity and $k_{cat/crofer}$ is the porous (catalyst or Crofer) layer thermal conductivity. The ΔH is the reaction heat for endothermic and exothermic reactions in the coated layers. The thermal conductivity of the catalyst, which mainly consists of Al_2O_3, is calculated using the following correlation [203]:

$$k_{cat} = 5.85 + \frac{15360 e^{-0.002T}}{T + 516} \tag{6.15}$$

where T is the temperature (°C) and k_{cat} has $\mathrm{W\,m^{-1}\,K^{-1}}$ unit.

- mass transfer

$$\begin{aligned} &\rho_{mix}((u_x \frac{\partial \omega_i}{\partial x} + u_y \frac{\partial \omega_i}{\partial y}) + \omega_i (\frac{\partial u_x}{\partial x} + \frac{\partial u_y}{\partial y})) \\ &= \frac{\partial}{\partial x}(\rho_{mix} \omega_k \sum_{j=1, j\neq i}^{N_g} D^F_{ij,eff} (\frac{\partial x_j}{\partial x} + \frac{\partial x_j}{\partial y} + (\frac{x_j - \omega_j}{P})(\frac{\partial P}{\partial x} + \frac{\partial P}{\partial y}))) \\ &+ \frac{\partial}{\partial y}(\rho_{mix} \omega_k \sum_{j=1, j\neq i}^{N_g} D^F_{ij,eff} (\frac{\partial x_j}{\partial x} + \frac{\partial x_j}{\partial y} + (\frac{x_j - \omega_j}{P})(\frac{\partial P}{\partial x} + \frac{\partial P}{\partial y})) \\ &+ \nu r_{com} \end{aligned} \tag{6.16}$$

for calculation of $D_{ij,eff}$ the following equation was used

$$D_{ij,eff} = D_{ji,eff} = \frac{\epsilon}{\tau} \frac{1}{2} (\frac{1}{\frac{1}{D^k_i} + \frac{1}{D_{ij}}} + \frac{1}{\frac{1}{D^k_j} + \frac{1}{D_{ji}}}) \tag{6.17}$$

In this equation, D_i^k and D_j^k represent the Knudsen diffusion coefficients of chemical species i and j respectively. D_{ij} and D_{ji} denote the binary diffusion coefficients of chemical species i and j. The values of tortuosity (τ) are calculated using the Bruggeman correlation [204].

- boundary conditions

interface boundary between the catalyst layer and the gas channel

- continuity: the momentum, mass, and heat flux components normal to the boundary remain continuous across the boundary; $\overrightarrow{n}.(N_{channel} - N_{porous}) = 0$

Table 6.3: Physical properties of the porous parts (coated catalysts and printed Crofer 22 APU) used for simulation.

Material	K ($\mathrm{W\,m^{-1}\,K^{-1}}$)	ρ ($\mathrm{kg\,m^{-3}}$)	C_p ($\mathrm{J\,kg^{-1}\,K^{-1}}$)	ϵ (-)	τ (-)	d_p (μm)	Permeability (κ) ($\mathrm{m^2}$)
Crofer 22 APU	25	7700	760	0.3[a]	$\tau = \epsilon^{-1/3}$	-	1×10^{-12}[b]
Al_2O_3	Equation 6.15	-	1100	-	-	0.1	$\frac{d_p^2 \epsilon^3}{180(1-\epsilon)^2}$[c]

[a] It is taken from results of the optimal case in Chapter 7
[b] Permeability of the printed porous parts can be tuned by parameters of SLM (see Chapter 7)
[c] It is taken form Kozney-Carman equation

6.6.1.3 Solid plate of Crofer 22 APU

- heat transfer

$$\frac{\partial^2 T}{\partial x^2} + \frac{\partial^2 T}{\partial y^2} = 0 \tag{6.18}$$

- boundary conditions

- heat flux continuity in the interface between the gas channel and solid plate; $\overrightarrow{n}.(N_{channel} - N_{porous}) = 0$

6.6.1.4 Pd membrane

To calculate the flux of H_2 across the membrane a pure Pd membrane with a thickness of $12.5\,\mu\mathrm{m}$ was used and the expression for the permeability of H_2 is as follows which is taken from [153].

$$Q = 1.58 \times 10^{-7} exp(\frac{-12.14(\frac{kj}{mol})}{RT}) \frac{mol}{msPa^{0.5}} \tag{6.19}$$

Furthermore, hydrogen recovery is defined as:

$$\phi_{H_2} = \frac{F_{H_{2,perm}}}{F_{H_{2,ret}+F_{H_{2,perm}}}} \tag{6.20}$$

6.6.1.5 Equilibrium conversion

In order to calculate the equilibrium constants and the conversion of CH_4 as a function of H_2 recovery when using a Pd membrane (as explained in Appendix A.1), the relevant parameters were computed. Additionally, a factor was introduced for each equilibrium constant to account for the removal of H_2 from the reactor, representing the degree of H_2 recovery. This factor adjusts the equilibrium calculations by reflecting the continuous extraction of H_2, which shifts the reaction towards the further conversion of CH_4, enhancing the overall efficiency of the process.

6.6.1.6 Kinetics model

Definition and coefficients of the kinetics parameters of the model proposed by Halabi et. al [29, 196] are as follows:

$$R_1 = \frac{k_1}{p_{H_2}^{2.5}}(p_{CH_4}p_{H_2O} - \frac{p_{H_2}^3 p_{CO}}{K1}) \times \Omega_1\Omega_s \tag{6.21}$$

$$R_2 = \frac{k_2}{p_{H_2}}(p_{CO}p_{H_2O} - \frac{p_{H_2}p_{CO_2}}{K2}) \times \Omega_1\Omega_s \tag{6.22}$$

$$R_3 = \frac{k_3}{p_{H_2}^{3.5}}(p_{CH_4}p_{H_2O}^2 - \frac{p_{H_2}^4 p_{CO_2}}{K3}) \times \Omega_1\Omega_s \tag{6.23}$$

$$\Omega_1 = \frac{1}{1 + k_{CH_4}p_{H_2}/p_{H_2}^{0.5} + k_{CO}p_{CO} + k_{CO_2}p_{CO_2} + k_{H_2}p_{H_2}} \tag{6.24}$$

$$\Omega_s = \frac{1}{1 + k_{H_2O}p_{H_2O}/p_{H_2} + k_{H_2}p_{H_2}} \tag{6.25}$$

Table 6.4: Arrhenius kinetic parameters.

Reaction, j	k_{j0} $[mol/kg_{cat}s]$	E_j $[kJ/mol]$
1	$1.62 \times 10^8\ kPa^{0.5}$	83.8
2	$2.34 \times 10^5\ kPa^{-1}$	15.1
3	$4.55 \times 10^8\ kPa^{0.5}$	89.2

Table 6.5: Van't Hoff adsorption parameters

Species, i	K_{i0} [kPa^{-1}]	ΔH_i [kJ/mol]
CH_4	1.49×10^{-8}	-98.8
CO	2.34×10^{-8}	-111.2
CO_2	8.33×10^{-10}	-115.6
H_2	3.88×10^{-7}	-88.2
H_2O	2.91×10^{6}	112.3

6.6.2 Autothermal modeling

In this section, considering the simulation results for the μ-EnH_2ancer V 3.0 system, energy balances for the system have been performed, and the simulation outcomes for μ-EnH_2ancer V 3.0 are discussed. The energy balances take into account heat losses, energy input requirements, and the efficiency of the H_2 recovery process, allowing for a comprehensive evaluation of the system's performance in various operating conditions. In simulations of the autothermal system, convergence failures were observed for very thick catalyst layers e.g. δ=100 μm and at high fuel flow rates. To ensure consistent convergence across operating conditions, β = 0.5 was applied in Equation 6.1, thereby imposing a small positive apparent oxygen order which improves Jacobian conditioning and mitigates O_2 -depletion-induced stiffness, allowing robust solver convergence. The activation energy of 77 kJ mol^{-1} and the frequency factor of 1.4×10^8 s^{-1} were retained as specified earlier for Equation 6.1. Moreover, a heat transfer to the ambient is considered with heat transfer coefficient of U=4 W m^{-2} K^{-1} defined on the top and bottom surface of the MR.

6.6.2.1 Description of simulation input

The cross-sectional view of the membrane reformer in its real geometry reveals a non-symmetric structure, including intricate features such as weld seams used in

the assembly process. For the purposes of simulation, these complex features are ignored, and a simplified schematic is presented in Figure 6.11.

The characteristics of the catalyst layers are derived from the isothermal model and experimental data presented in the previous section. Kinetic data for the reactions occurring within the reformer are provided in Table 6.4 and 6.5. The heat generated by the combustion reaction in the coated layer is calculated using the enthalpy change of the reaction, $\Delta H_{\text{reaction}}$.

In the simulation, the membrane is modeled as a self-supported thin layer of Pd, welded between micro-structured plates responsible for both permeation and reforming. Given that this system is intended for decentralized plants, operating pressure is kept relatively low to avoid the need for a costly compressor, while also simplifying the system. Additionally, since the dimensions and number of microchannels are identical on both the retentate and permeate sides, no additional hindrances were assumed for the accessible membrane area.

The parameters specific to Crofer 22 APU, which forms the solid structure and housing of the membrane reactor, were taken from the manufacturer's data sheet [137]. This simplification allows for more straightforward modeling while maintaining a focus on operational feasibility for decentralized applications.

6.6.2.2 Solver configuration

The simulations in this study were solved using COMSOL multiphysics version 6.2. The solver of the parallel sparse direct solver (PARDISO) with a fully coupled physics was used. The relative tolerance of 1×10^{-6} was considered as termination criteria for all simulations. The mesh was created using an automated function, resulting in smaller domains near walls and corners, and larger ones in central areas with lower expected gradients. Mesh convergence was verified by comparing settings from coarse to extremely fine settings (see Figure A.4 in Appendix). The simulation was done using a workstation with AMD Ryzen Threadripper 3960X 24-Core Processor 3.79 GHz processor, 64 GB RAM.

6.6.3 Model Validation; comparison of the results of 2D simulation with results of MicroEnhancer V 1.0

Given the unsuccessful integration of a Pd membrane into μ-EnH_2ancer V 3.0, the initial step involves comparing the results of a 2D simulation under assumption of isothermal conditions for the electrically-heated membrane reformer, utilizing the same Pd membrane characteristics and Rh-based catalyst, with data from a study conducted by a previous study at IMVT [205]. Based on the data presented in Reference [205] and the experimental results obtained in this study, the layer thicknesses in the pre-reforming and reforming zones were assumed to be 40 μm and 17 μm, respectively (data from Table 6.2).

Figure 6.12 A depicts the methane conversion and CO selectivity plotted against the W/F ratio. These results are obtained from an assumed isothermal condition for simulation conducted under operating conditions with a retentate pressure of 6 bar at 773 K.

According to thermodynamics of the reaction, methane conversion in steam reforming decreases with increasing system pressure. However, with the presence of a Pd membrane, the equilibrium is shifted due to continuous hydrogen removal, allowing for higher methane conversions. This conversion increases with residence time. At the lowest W/F ratio of 0.33 $\mathrm{gr_{cat}\,h/mol_{CH_4}}$, a S/C ratio of 3, and without sweep gas, a methane conversion of 38% was achieved while the simulation showed around 35%. This experiment value is approximately presents a higher conversion compared to the corresponding equilibrium conversion without the membrane. This increased conversion suggests that the partial pressure of hydrogen exceeded 1 bar at the end of the "pre-reforming" zone, preventing H_2 diffusion from the permeate to the retentate side, thus enhancing reactor performance. At the same time, CO selectivity decreases with an increase in residence time showing an improving WGS reaction which converts further CO in this reaction. Using sweep gas that removes H_2 on the permeate side keeps the partial pressure gradient of H_2 (driving force) on both sides of the membrane high and

therefore increases the CH_4 conversion as more H_2 is removed from the reaction passage through the membrane.

In Figure 6.12 B, the graph illustrates the methane conversion, both measured and simulated, for the "no sweep gas" mode, plotted against H_2 recovery. The experimental values of methane conversion align closely with the thermodynamic equilibrium, which means the rate of the H_2 separation keeps up with its production rate through MSR. The simulated values, considering the residence time values from Figure 6.12 B, approach the equilibrium, indicating an increase in residence time. The deviation from the equilibrium curve is, however, relatively higher for the simulation results. This trend shifts closer to the equilibrium curve for space velocities larger than W/F = 0.81 $\mathrm{gr_{cat}\,h/mol_{CH_4}}$, suggesting that as residence time increases, the system approaches equilibrium with a more pronounced change in CH_4 conversion (dX/d(W/F) becomes larger), indicating that hydrogen removal could be the rate-limiting step. According to Sieverts' law for a Pd-based membrane, higher reaction pressures result in increased hydrogen flux and subsequently greater hydrogen recovery (Figure 6.12 D), and, thus to a decreased partial pressure of hydrogen in the reforming passage. This causes the equilibrium to shift further towards the product side, leading to higher methane conversions at increased reaction pressures. The influence of reaction pressure on methane conversion at a constant W/F ratio is illustrated in Figure 6.12 C. Although thermodynamic equilibrium conversion decreases with increasing pressure, the actual conversion in the MR shows the opposite trend due to the continuous removal of hydrogen which is promoted by the higher trans-membrane pressure difference. By comparing the predicted results from a 2D simulation with assumption of isothermal condition with experimental data taken from μ-EnH_2ancer V 1.0 [205], it is needed to develop to model for an autothermal model where the combustion module is integrated with the membrane reformer according the data and characteristics of EnH_2ancer V 3.0.

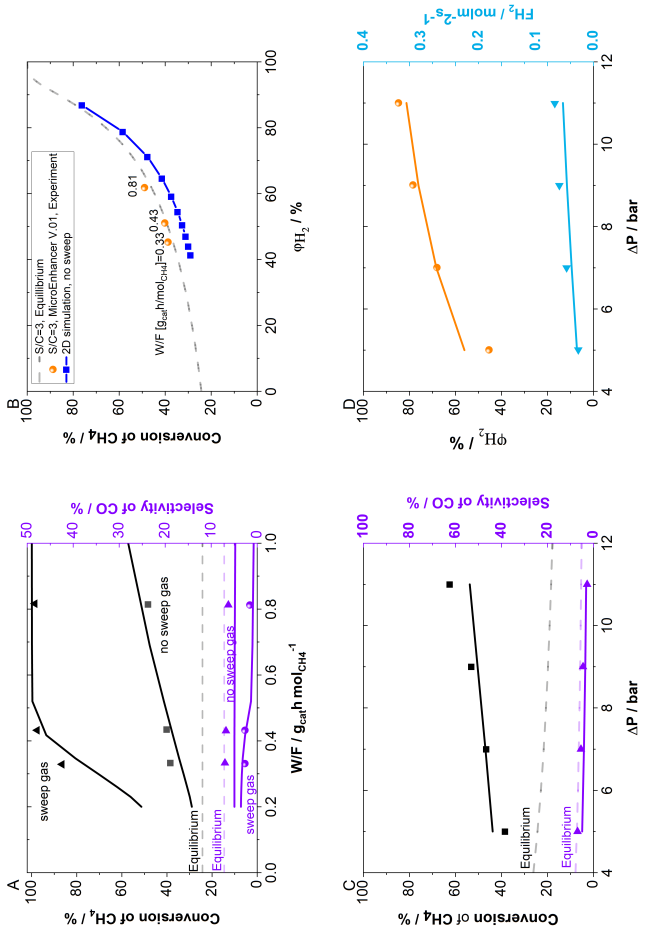

Figure 6.12: Validation of 2D simulation vs experimental results μ-EnH_2ancer V 1.0 [205] under assumed isothermal condition. A) CH_4 conversion (left axis) and CO selectivity (right axis) against residence time (W/F), B) CH_4 conversion versus hydrogen recovery. C) CH_4 conversion (left axis) and CO selectivity (right axis) against pressure difference (bar) at W/F 0.33 $\mathrm{gr_{cat}\,h/mol_{CH_4}}$ D) hydrogen recovery and flux of permeated H_2 against pressure difference (bar) at W/F 0.33 $\mathrm{gr_{cat}\,h/mol_{CH_4}}$ and without sweep gas. Operating conditions are T=773 K, P_{ret}=6 (A,B), P_{perm}=1 bar and S/C=3. The solid lines, dashed lines, and points present the 2D simulation results, equilibrium curves, and experiments, respectively.

6.7 Characteristic timescales

A typical sequence of steps in a heterogeneous catalytic reaction, leading to the production of a product, involves bulk diffusion, internal diffusion, adsorption, reaction, and desorption [106]. To identify the limiting factors in the reaction, characteristic timescale analysis is employed. In the case of an endothermic reaction, the relevant timescales include external mass transfer, internal mass transfer, heat transfer, reaction, and contact time [206].

Contact time, a crucial factor in such analyses, is determined utilizing spacetime instead of the average residence time. This choice is influenced by the consistently laminar flow at all locations, evident in a Reynolds number below 1200, significantly lower than the turbulence transition threshold at 2100. The concept of space-time is formally defined as [207]:

$$\tau_s = \frac{x_c}{u_{xc}} \tag{6.26}$$

The axial position in the reactor center ($H_{\text{channel}}/2$) is indicated by x_c and u_{xc} represents the linear velocity, evaluated at position x_c. In contrast to the average reaction time, which is measured at the entrance ($x_c = 0$), the space-time is calculated based on the velocity in the center of the channel. This is distinct from residence time, which is determined by dividing the volume by the flow.

The external mass transport time coefficient is defined as follows [208–210]:

$$\tau_{ext} = \frac{(H_{channel} - \delta_{catalyst})^2}{D_{m,CH_4}} \tag{6.27}$$

where $(H_{channel} - \delta_{catalyst})$ represents the height of the channel, excluding the thickness of the catalyst layer, and D_{m,CH_4} is the average diffusion coefficient for CH_4.

The time coefficient for internal mass transfer (in the catalyst-coated layer) is [211]:

$$\tau_{int} = \frac{\delta^2_{catalyst}}{D_{m,eff,CH_4}} \tag{6.28}$$

where $\delta_{catalyst}$ is the thickness of the coated catalyst and D_{m,eff,CH_4} is the effective diffusion of the CH_4 in the gas mixture in the porous layer of catalyst as follows [212]:

$$D_{eff} = \frac{\epsilon}{\tau}(\frac{1}{D_k} + \frac{1}{D_m})^{-1} \tag{6.29}$$

$$\tau = \epsilon^{-1/2} \tag{6.30}$$

where ϵ and τ are the porosity and tortuosity of the catalyst layer, and latter is calculated based on the Bruggeman correlation. Moreover, D_m is the mixture-averaged bulk diffusing coefficient (here for CH_4 in mixture), and D_k which is the Knudsen diffusion is defined as follows [212]:

$$D_k = \frac{d_{pore}}{3}\sqrt{\frac{8RT}{\pi M_{avg}}} \tag{6.31}$$

In this context, d_{pore} denotes the mean pore diameter, M_{avg} represents the average molecular weight of the gas species, R is the gas constant, and T denotes the temperature. To simplify the calculation of tortuosity, a straightforward correlation is employed, as variations in tortuosity approximations exert minimal influence on moderate porosities [213].

The timescale coefficient for heat transfer is written as [106]:

$$\tau_{ht} = \frac{\delta^2 \rho C_p}{k} \tag{6.32}$$

here, k represents thermal conductivity, ρ is the material density, and C_p denotes the specific heat capacity. Throughout, the coat consistently acts as the limiting factor in comparison to heat transfer across the reactor wall ($\tau_{wall} < \tau_{coating}$).

The reaction time is another time scale that can be defined as follows.

$$\tau_{re} = \frac{C_{CH4}}{R_{CH_4}} \tag{6.33}$$

In the written equation, C_{CH_4} denotes the concentration of the methane and R_{CH_4} is the the overall consumption rate of methane. This time scale is calculated based on the values on the surface of the catalyst layer. The results comparing the different characteristic time scales are presented and discussed in the following section (see Figure 6.18).

6.8 Results of non-isothermal simulation of MR

Based on the defined model and geometry in previous sections, several parameters were selected to be evaluated in the following sections. First, by varying two parameters of the CCR, the total performance of the MR is shown in Figure 6.13 and Table A.2 in the Appendix. In this regard, the efficiency of the membrane reformer (MR) which is integrated with combustion module (CCR) is defined based on the H_2 permeated through the membrane in the permeate side to the inlet CH_4:

$$\eta_{MR} = \frac{F_{H_{2,perm}} LHV_{H_2}}{F_{CH_{4,in,MSR}} LHV_{CH_4} + (F_{CH_{4,CCR,in}} - F_{CH_{4,CCR,out}}) LHV_{CH_4}} \tag{6.34}$$

where F represents the flow rate of each stream, and LHV stands for the lower heating values of the corresponding species.

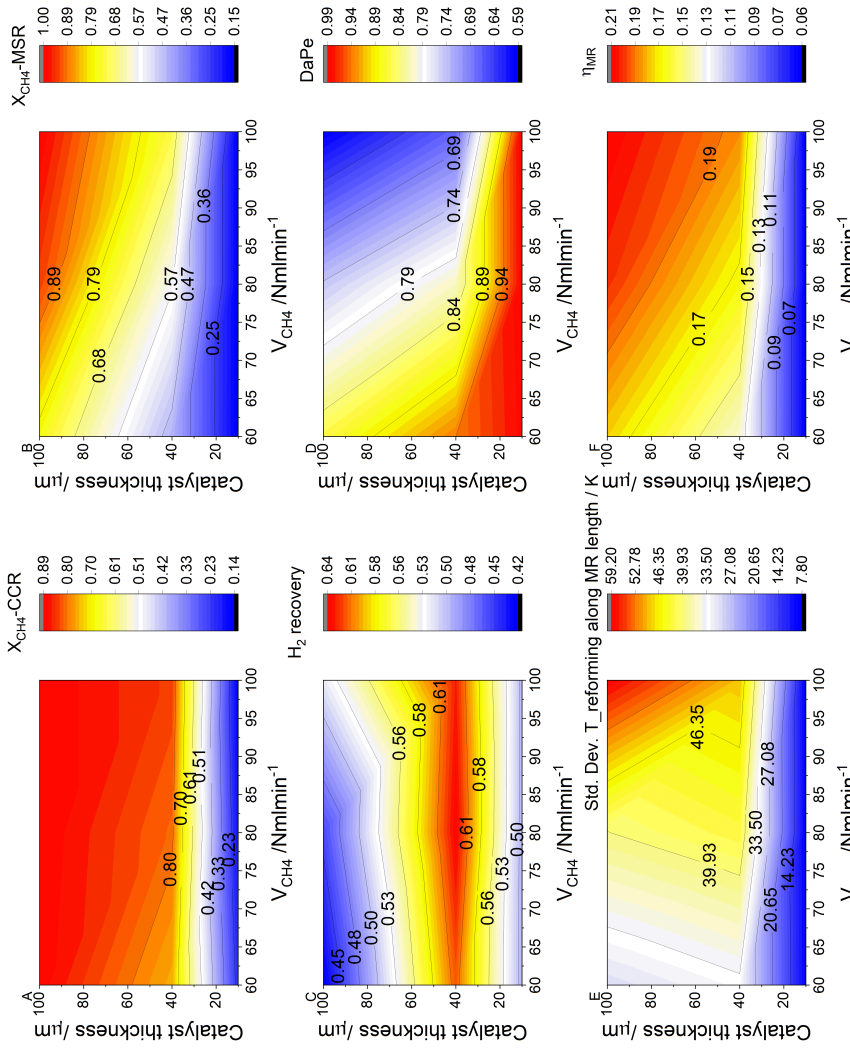

Figure 6.13: Results of the simulation for a non-isothermal MR by changing flow rate of CH_4 and thickness of coating in CCR. The conditions are $W/F_{reforming}$ 1.80 $gr_{cat}h/mol$ and Sweep gas of N_2: 500 N mL min^{-1}, T_{inlet}=673 K, P_{ret}=1.5 bar, P_{perm}=1 bar, Air/CH_4:10 and S/C=3.

To assess the overall performance of the MR, objective metrics such as the efficiency index (η_{MR}) and H_2 recovery, with relatively high CH_4 conversion, can be defined. Referring to the graph in Figure 6.13, Table A.2, and Figure A.5 in Appendix (the green line in that graph with circular markers represents the optimal condition compared to other scenarios), the optimal conditions for the next step can be evaluated. In this optimal track, the flow rate of CH_4 is set at $100\,\mathrm{N\,mL\,min^{-1}}$, with a coated layer thickness for the CCR of $40\,\mu\mathrm{m}$. This configuration results in CH_4 conversion rates of $83\,\%$ and $72\,\%$ for the CCR and MSR, respectively.

Additionally, since unconverted gases in the reformate, such as CH_4, CO, and H_2 can be redirected to the CCR inlet, it is important to consider the ratio of CH_4 flow rate at the CCR inlet compared to the MSR outlet. A ratio of less than 1 indicates that the reformate gas can be utilized in the CCR without requiring additional make-up gas. A high value of this index signifies that the CH_4 in the MSR is largely converted to products.

To identify the temperature gradients across and along the model, the flow rate of CH_4 on the combustion side (fuel) and the catalyst loading (by varying the layer thickness) were studied. The temperature profiles along the membrane reformer are shown in Figure 6.14 and Figure 6.15.

With the comparison of the results for different flow rates of CH_4, temperature increases alongside the MR from the inlet of CCR to rightwards. This trend is kept, however, for a flow rate of $100\,\mathrm{N\,mL\,min^{-1}}$, it tends to give a hot spot in relative axial position alongside MR between 0.5-0.6. As shown, this generated heat is transferred through conduction towards the outlet of the reformer and permeate sections. To stay within the limits of Crofer 22 APU thermal stability, input parameters were selected to ensure the temperature does not exceed $900\,^{\circ}\mathrm{C}$. In such a system, due to the removal of hydrogen by membrane, the MSR process can operate at lower temperatures, such as $550\,^{\circ}\mathrm{C}$. However, this temperature is considered a constraint due to the reactor material stability.

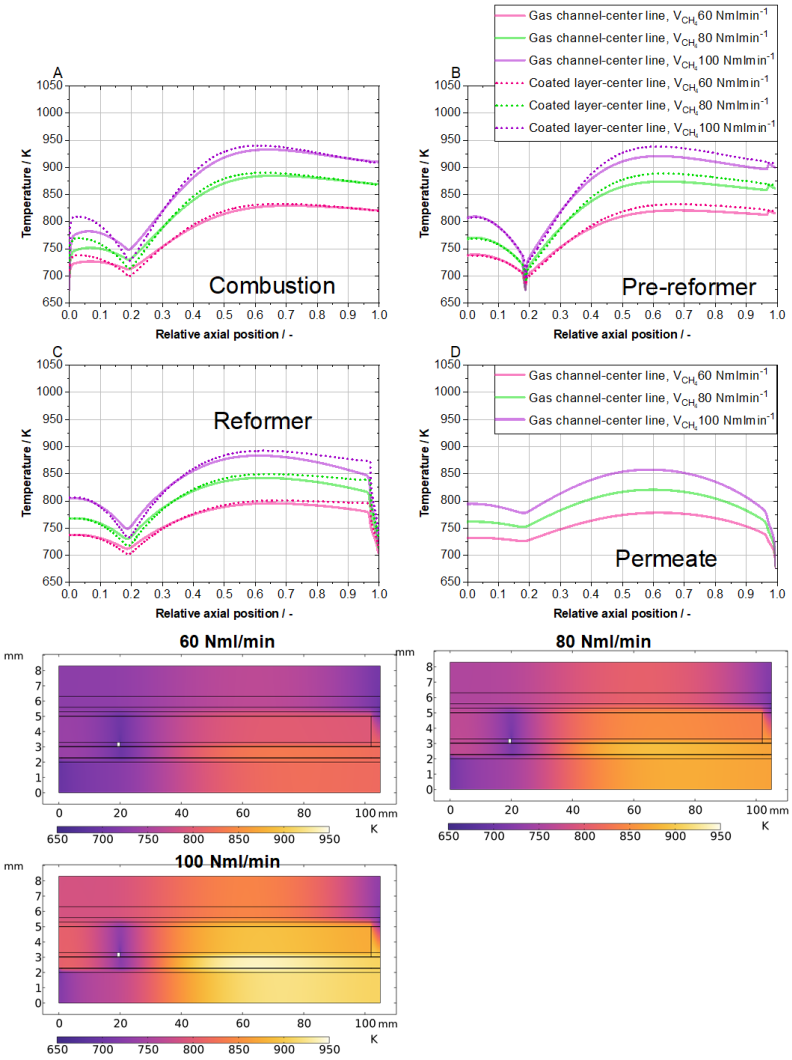

Figure 6.14: Temperature profile of different sections of the autothermal MR for different flow rates of fuel (CH_4) at combustion section A) Combustion section, B) Pre-reforming section, C) Reforming section, and D) Permeate section and temperature profile of the whole geometry. The conditions are $W/F_{reforming}$ 1.80 $\mathrm{gr_{cat}\ h/mol_{CH_4}}$ and Sweep gas of N_2: 500 N mL $\mathrm{min^{-1}}$, $\delta_{\mathrm{cat,CCR}}$: 40 μm, T_{inlet}=673 K, P_{ret}=1.5 bar, P_{perm}=1 bar, Air/CH_4:10 and S/C=3.

The temperature profile shown for the catalyst layer (center line) corresponds to a heat generation by CCR channel (per volume of channel, surface average value) of approximately 93 to 171 $\mathrm{W\,cm^{-3}}$ when increasing the fuel flow rate from 60 to 100 $\mathrm{N\,mL\,min^{-1}}$. This range of value is significantly comparable to industrial-scale gas-fired reformers, where heat values typically range from $0.5\,\mathrm{W\,cm^{-3}}$ to $7.5\,\mathrm{W\,cm^{-3}}$ [108, 110]. Additionally, in gas-fired microreactors, this value can increase significantly, reaching up to $65\,\mathrm{W\,cm^{-3}}$ within the reaction zone [214].

One major advantage of such a compact system is its ability to mitigate the steep temperature gradients observed in industrial-scale reformers. In traditional setups, reformer tubes placed inside a furnace experience high heat flux from the furnace and low thermal conductivity within the catalyst-packed tubes, leading to substantial temperature variations. In contrast, catalyst-coated reactors offer a much shorter length scale, effectively minimizing temperature gradients between the heat source and heat sink. As seen in Figure 6.15, with an increase in the thickness of the coated catalyst layer in the CCR to $\delta_{\mathrm{cat,com}} = 100\,\mu\mathrm{m}$, an undesirable heat peak develops in the first 20% of the MR. On the other hand, for a thickness of $\delta_{\mathrm{cat,com}} = 10\,\mu\mathrm{m}$, the system becomes inefficient in terms of providing the necessary heat for conducting the MSR.

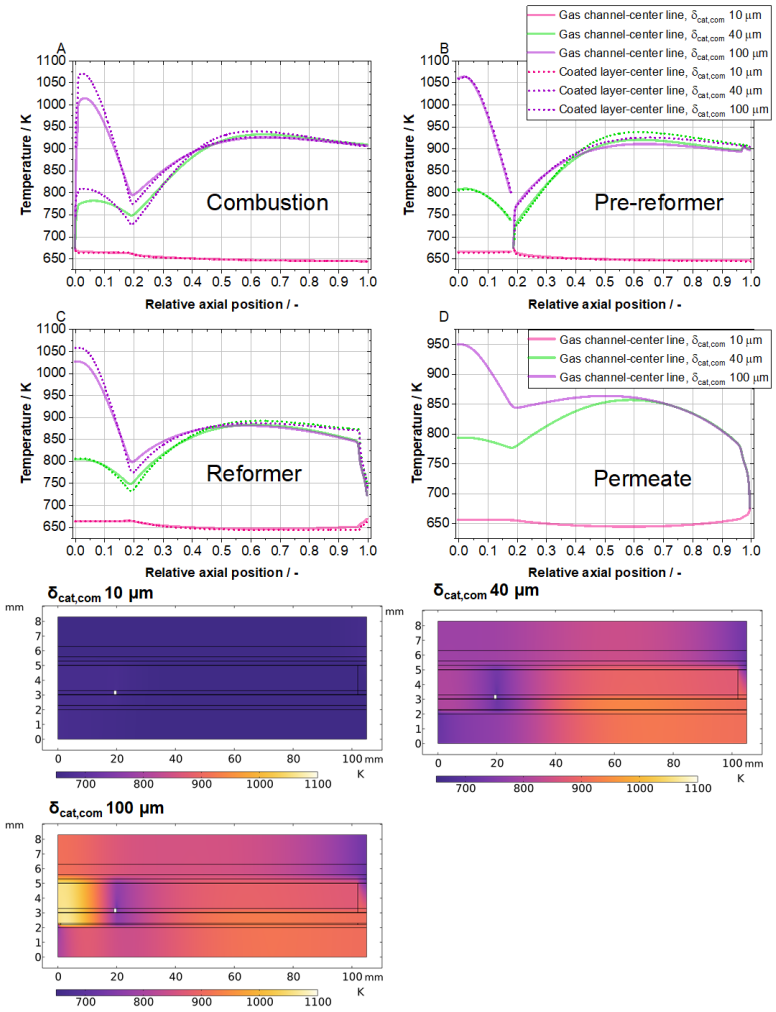

Figure 6.15: Temperature profile of different sections of the autothermal MR for different coating thicknesses at combustion section A) Combustion section, B) Pre-reforming section, C) Reforming section, and D) Permeate section and temperature profile of the whole geometry. The conditions are $W/F_{reforming}$ 1.80 $gr_{cat}h/mol$ and Sweep gas of N_2: 500 N mL min^{-1}, F_{CH4}:100 N mL min^{-1}, T_{inlet}=673 K, P_{ret}=1.5 bar, P_{perm}=1 bar, Air/CH_4:10 and S/C=3.

Figure 6.16 illustrates the CH_4 conversion and CO selectivity for MSR across different sections, including pre-reforming and reforming, for various CH_4 feed flow rates and catalyst thickness of $40\ \mu m$ at CCR channel. As observed, increasing the fuel feed flow rate in the combustor enhances CH_4 conversion for MSR. This is due to the greater amount of heat produced by the exothermic reactions at higher fuel flow rates. Comparing the results with the equilibrium values calculated for each temperature profile indicates that in the pre-reformer, the conversion of CH_4 approaches the equilibrium value near the end of the channel. In the reformer channel, where H_2 is separated through the membrane, the conversion exceeds the equilibrium value.

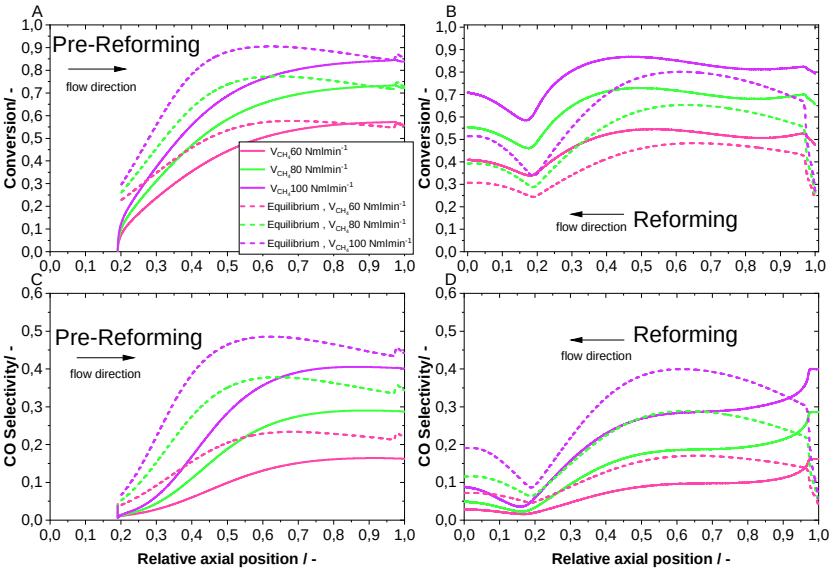

Figure 6.16: CH_4 conversion and CO selectivity of MSR for different flow rates of fuel (CH_4) at combustion section A) conversion in pre-reforming section, B) conversion in reforming section, C) selectivity in pre-reforming section, and D) selectivity in reforming section. The conditions are $W/F_{reforming}$ 1.80 gr_cath/mol and Sweep gas of N_2: $500\,Nml/min$, $\delta_{cat,CCR}$: 40 μm, T_{inlet}=673 K, P_{ret}=1.5 bar, P_{perm}=1 bar, Air/CH_4:10 and S/C=3.

However, as shown in Figure 6.17, the location of the heat source in the catalytic combustion reactor (CCR) does not align perfectly with the heat sink in the MSR for $\delta_{cat,CCR}$:100 μm. This misalignment causes a sharp temperature rise on the left-hand side of the MR and an increased CH_4 conversion at the reformer outlet. Moreover, Figure 6.17 shows that in the "reforming" for case $\delta_{cat,CCR}$:100 μm, as the temperature in regions "reforming" and "permeation", the rate of H_2 permeation falls behind its production by MSR in the last 15% of its path in the flow direction. It requires introducing the DaPe number which is explained in the following section.

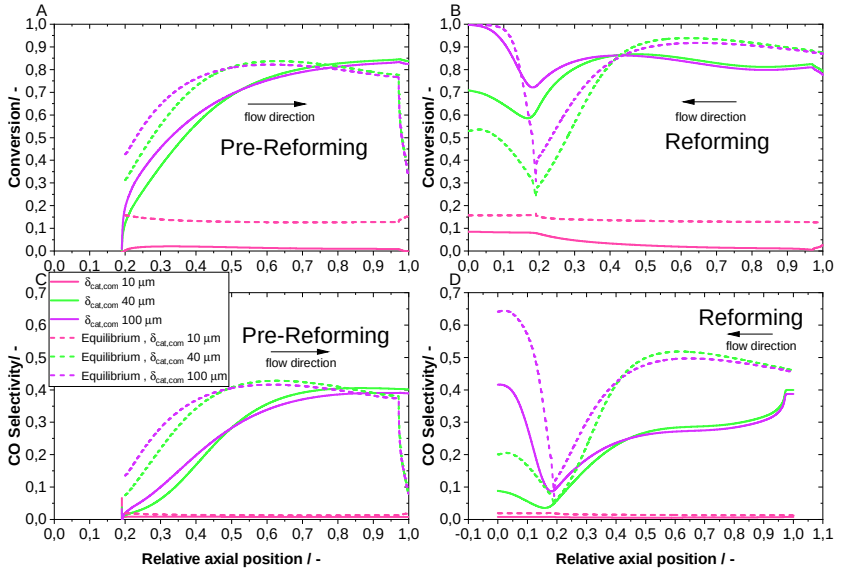

Figure 6.17: CH_4 conversion and CO selectivity of MSR for different coating thicknesses at combustion section A) conversion in pre-reforming section, B) conversion in reforming section, C) selectivity in pre-reforming section, and D) selectivity in reforming section. The conditions are $W/F_{reforming}$ 1.80 $gr_{cat}h/mol$ and Sweep gas of N_2: 500 N mL min^{-1}, F_{CH4}:100 N mL min^{-1}, T_{inlet}=673 K, P_{ret}=1.5 bar, P_{perm}=1 bar, Air/CH_4:10 and S/C=3.

To assess the membrane's performance under the specified operating conditions, additional parameters need to be defined. Dimensionless analysis is a widely used approach for quickly identifying characteristic time and length scales within a system, making it an essential tool in chemical engineering, fluid dynamics, and heat and mass transfer. In the design of membrane reactors, two critical dimensionless numbers are particularly relevant: the Damköhler number and the permeation (Péclet) number. These numbers provide valuable insights into the system's behavior and are defined here by Tsuru et al. [215]:

$$Pe = \frac{P_{H_2}^{0.5} A_{mem} L Q}{F_{CH_{4,0}}} \tag{6.35}$$

$$Da = \frac{R_1^{max} W_{cat}}{F_{CH_{4,0}}} \tag{6.36}$$

where

$$R_1^{max} = k_1 (P_{CH_4} P_{H_2O}) / P_{H_2^{2.5}} / \Omega 1 \Omega s \tag{6.37}$$

where DaPe is defined as the ratio of Da number to Pe number. In the mentioned equations, $P_{H_2}^{0.5}$ is the maximum driving force of partial pressure of H_2 at the retentate side. Q is the permeance according to Equation 6.19. $F_{CH_{4,0}}$ is the molar flow rate of CH_4 in the inlet of the reactor. R_1^{max} is the forward reaction of MSR as the maximum H_2 production rate. Parameters $\Omega 1$ and Ωs can be calculated from Equations 6.24 and 6.25, respectively.

Figure 6.18 illustrates the time scales for various transport mechanisms within the bulk and porous catalyst layer. The space-time serves as the primary limiting factor for all cases. As the coating thickness of the CCR increases from 10 to 100 μm, τ_{ext} decreases because the thicker coating reduces the bulk gas diffusion path. Comparing τ_{ext} with τ_{re} suggests for effect of thickness shows that for $\delta_{\text{cat,CCR}}$: 10 μm, reaction limitations may occur. For τ_{int}, its value increases with coating thickness but remains lower than τ_{re}, indicating no limitation due to internal diffusion (Figure 6.18 B). Additionally, τ_{ht} is the fastest transport mechanism and shows no limitations for all coating thicknesses. When considering the effect of

the CH_4 flow rate (60-100 $\mathrm{N\,mL\,min^{-1}}$) in the fuel chamber, τ_{ext} shortens for the first 25% of the MR length.

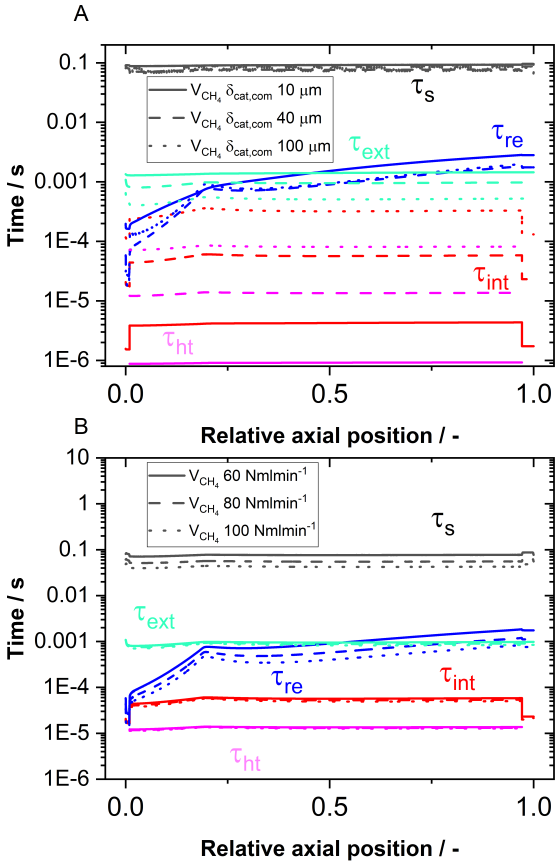

Figure 6.18: Time scales for different fuel flow rates and CR coating thicknesses. The conditions are $\delta_{cat,com}$:10-100 μm, combustion fuel flow of CH_4: 60-100 $\mathrm{N\,mL\,min^{-1}}$ $W/F_{reforming}$ 1.80 $gr_{cat}h/mol$ and Sweep gas of N_2: 100-500 $\mathrm{N\,mL\,min^{-1}}$, T_{inlet}=673 K, P_{ret}=1.5-2.5 bar, P_{perm}=1 bar, Air/CH_4:10 and S/C=3.

Figure 6.19 (and Table A.3 in Appendix) shows the simulation results for different values of input parameters related to MSR. These set of simulations was carried out based on the picked $\delta_{cat,CCR}$:40 μm, and combustion fuel flow rate of CH_4:100 $\mathrm{N\,mL\,min^{-1}}$ as the optimum condition from the previous step. It is noted that the CCR and MR are supposed to be operated at the same operating pressure when operating MR. Therefore, increasing the pressure of MR for higher permeation of H_2 is inevitable for operating conditions in CCR.

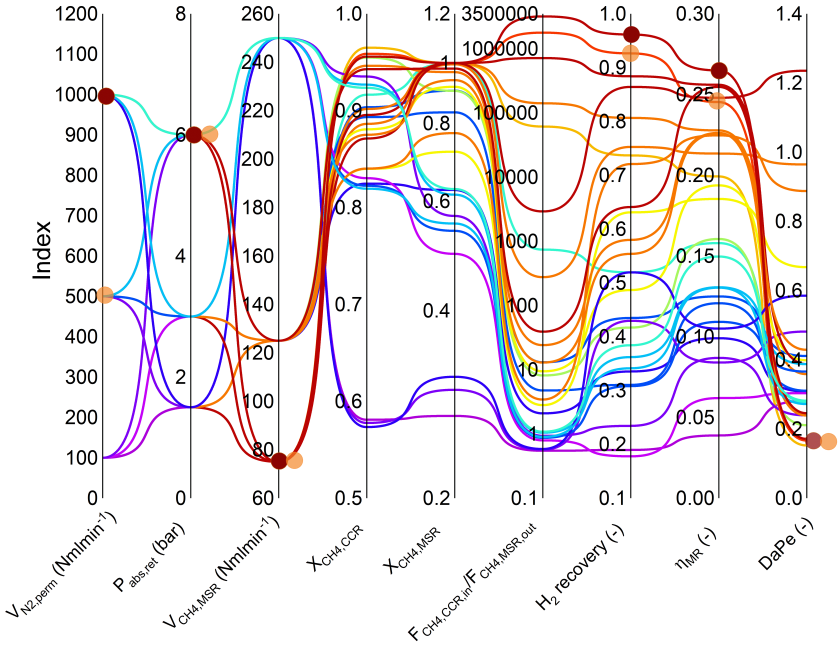

Figure 6.19: CH_4 conversion and H_2 recovery, MR efficiency, and DaPe number. The conditions are $\delta_{cat,com}$:40 μm, combustion fuel flow of CH_4: 100 $\mathrm{N\,mL\,min^{-1}}$ $W/F_{reforming}$ 1.80 gr_cath/mol and Sweep gas of N_2: 100-1000 $\mathrm{N\,mL\,min^{-1}}$, T_{inlet}=673 K, P_{ret}=1.5-6 bar, P_{perm}=1 bar, Air/CH_4:10 and S/C=3.

As observed, the DaPe parameter exhibits varying behavior for each set of conditions due to temperature or pressure changes in the reformer channel, which

are influenced by the combustor section. When DaPe exceeds 1, the membrane reactor (MR) is constrained by the membrane's performance. Comparing this with Figure6.17 B, it is evident that in the first 20% of the relative axial position, where the combustor section overheats the MR, H_2 production is higher, though its permeation lags, aligning with equilibrium values. Based on the results from Figure 6.19, η_{MR} reaches to maximum 26% with a H_2 recovery of 96% for the case shown with dark brown circle. It requires indeed high sweep gas flow rate of 1000 $\mathrm{N\,mL\,min^{-1}}$, pressure of 6 bar and W/F_{CH4} 3 $gr_{cat}h/mol$. By reducing the sweeping flow rate to 500 $\mathrm{N\,mL\,min^{-1}}$, the performance of MR still remains in a good range in terms of MR efficiency, H_2 recovery, and CH_4 conversion.

Figure 6.20 illustrates that as the sweeping flow rate of N_2 (used as a sweep gas) increases from $100\,\mathrm{N\,mL\,min^{-1}}$ to $1000\,\mathrm{N\,mL\,min^{-1}}$, a concentration polarization develops. This polarization reduces the concentration to approximately 3% and 10% near the membrane surface, highlighting the inhibitory effect of N_2 sweep gas through diffusion. However, increasing the flow rate of the sweeping gas improves the flow rates of the permeated H_2 on the permeate side by improving the driving force on both sides of the membrane. In applications where a diluted N_2-H_2 mixture is required, such as in steel or glass plants as a reducing agent, no further separation of the permeate stream is necessary. It can be supplied directly to these industries.

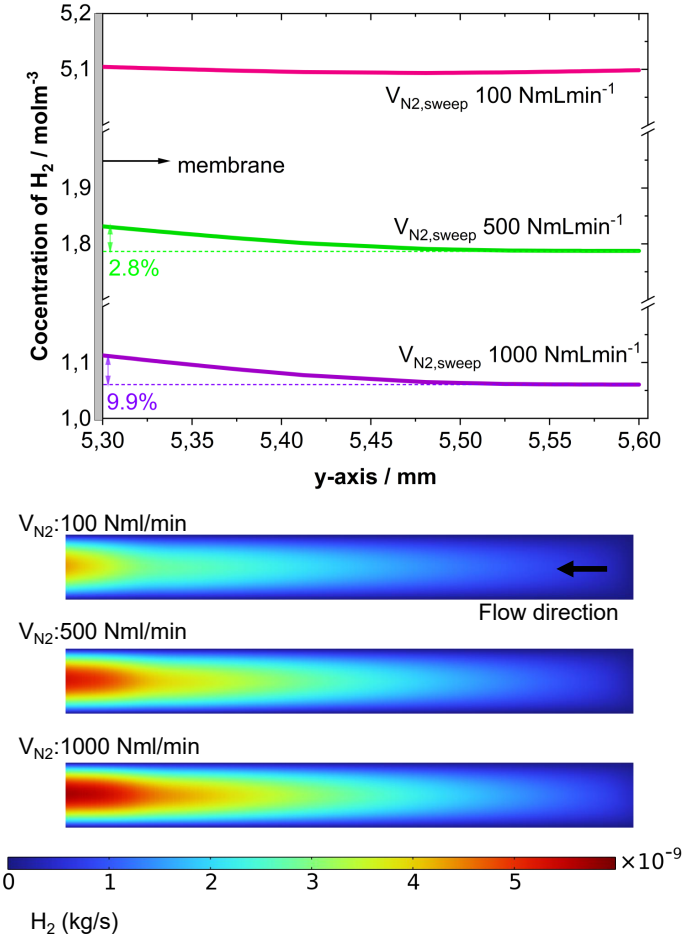

Figure 6.20: Effect of sweeping gas N_2 flow rate at conditions of $\delta_{cat,com}$:40 μm, combustion fuel flow of CH_4: 100 N mL $\min^{-1}$ $W/F_{reforming}$ 3 $\mathrm{gr_{cat}\ h/mol_{CH_4}}$ and Sweep gas of N_2: 100-1000 N mL $\min^{-1}$, T_{inlet}=673 K, P_{ret}=6 bar, P_{perm}=1 bar, Air/CH_4:10 and S/C=3.

Figure 6.21 illustrates the impact of trans-membrane pressure difference on the performance of the MR. Both the CCR and the MSR operate under the same inlet temperature and pressure conditions. It is observed that a higher fuel concentration in the CCR causes a temperature peak in the first 20% of the MR's axial position when the pressure increases from 1.5 to 6 bar.

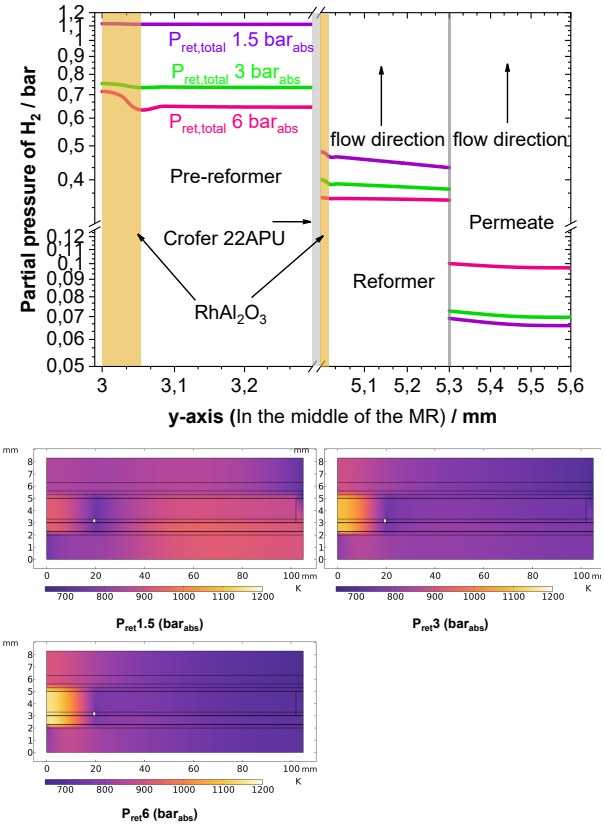

Figure 6.21: Effect of pressure of MSR at conditions of $\delta_{cat,com}$:40 μm, combustion fuel flow of CH_4: 100 N mL min^{-1} $W/F_{reforming}$ 3 $\mathrm{gr_{cat}\ h/mol_{CH_4}}$ and Sweep gas of N_2: 1000 N mL min^{-1}, T_{inlet}=673 K, P_{perm}=1 bar, Air/CH_4:10 and S/C=3.

Additionally, Figure 6.21 shows the partial pressure of H_2 in the pre-reformer, reformer, and permeate sections. Here, H_2 is produced within the coated catalyst layers and migrates to the membrane surface to pass through. As pressure increases, the driving force also increases (in the case of isothermal conditions). However, since the MR temperature distribution is influenced by the CCR's operating pressure, at the same cross-section of the MR (middle of the MR), a higher pressure of 6 bar results in a lower driving force (difference between partial pressure profiles) compared to 1.5 bar, due to the relatively higher temperature at that position for the latter.

Due to the high concentration of fuel in the CCR and the low velocities of the reactants causing temperature spikes, it is necessary to optimize the MR with innovative design ideas. The following section will discuss these ideas thoroughly.

6.9 Optimization of MR with advanced manufacturing techniques

As identified in the previous section, when there is a mismatch between the exothermic and endothermic reactions, significant heat peaks persist within the first 20% of the reactor. In this section, it is proposed to distribute the heat source more along the reactor length, either through segmentation of the catalyst layers or by incorporating additively manufactured air distributors.

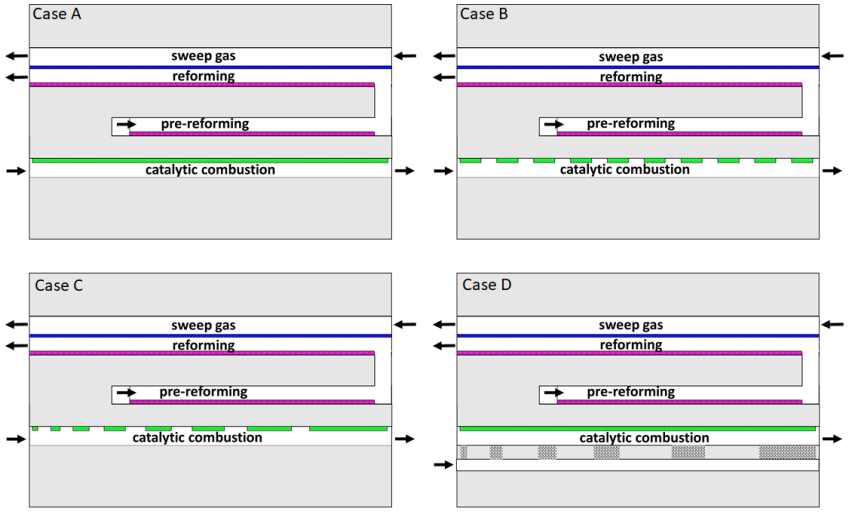

Figure 6.22: Comparison of different configurations for CR, Case A: base case where air and fuel are pre-mixed with uniform coated layer, Case B: pre-mixed inflow with uniform segmented catalyst layer, Case C: additively manufactured porous segments for air distribution along the CR with descending design, and Case D: additively manufactured porous segments with ascending design.

Without performing shape optimization for the segmented catalyst layer, a uniform segmented model is proposed, referred to as design "B." The base case from the previous section is treated as design "A". Furthermore, segmented coating with

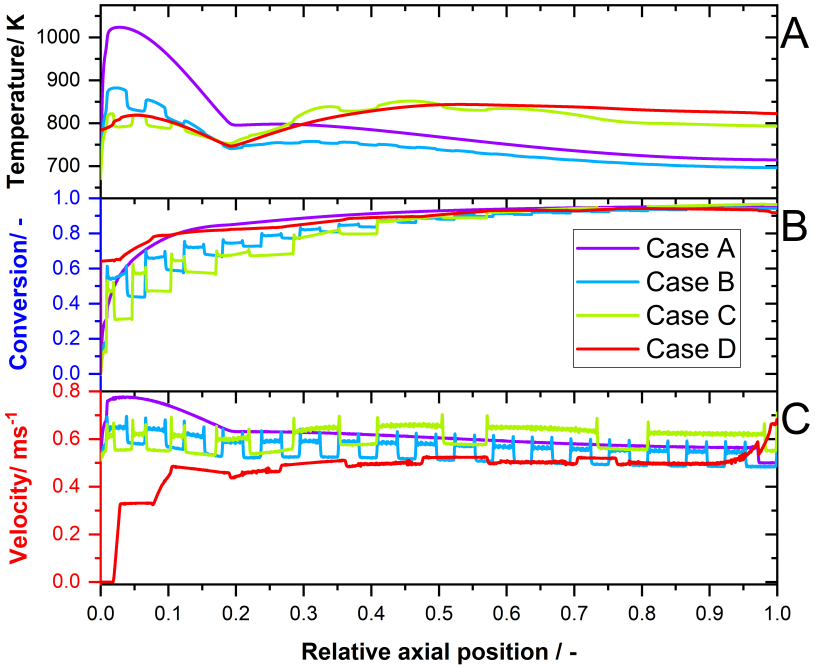

Figure 6.23: Results of the simulated configurations of CCR, A) Temperature in the gas channel (fuel section) along the reactor, B) CH_4 conversion of CCR, and C) velocity magnitude in the center-line of fuel channel. The conditions are $\delta_{cat,com}$:40 μm, combustion fuel flow of CH_4: 100 N mL min^{-1} $W/F_{reforming}$ 3 $\mathrm{gr_{cat}\ h/mol_{CH_4}}$ and Sweep gas of N_2: 1000 N mL min^{-1}, T_{inlet}=673 K, P_{ret}=6 bar, P_{perm}=1 bar, Air/CH_4:10 and S/C=3.

increment design is termed design "C" and an SLM printed fuel distributor with the ascending design of porous segments is labeled as "D". Figure 6.22 presents a general overview of these different configurations.

Figure 6.23 presents the simulation outcomes for case A-D. As shown in Figure 6.23 A, the temperature peak within the first 20% of the MR found for base case A is significantly reduced in cases C and D, followed by case B. The catalyst weight varies for cases B and C, while Cases A and D have a uniform coating. In case B, the temperature decreases after the relative axial position of 20%, where the

MSR starts and continues to decrease until the end of the MR. When comparing the mass of the CCR catalyst, cases B and C have approximately 50% and 60% of the catalyst mass compared to cases A and D, respectively. Therefore, in case B, the heat released by the CCR is insufficient to increase the temperature along the MR. In case C, because the longer catalyst layers are at the end of the MR, the temperature increases after the initial drop. This trend is similar to Case D, where fuel is added incrementally to the CCR channel.

In Figure 6.23 A and B, the temperature profile and CH_4 conversion along the MR for the CCR is shown. Comparing cases B and C with the base case A reveals that fuel conversions slow down initially and then increase slightly compared to Case A, reaching similar values by the end of the MR axis. For case D, the conversion proceeds comparable to case A.

It is also obvious that for case A, that with nearly 10% CH_4 in the air, fuel consumption is rapid as it enters the reactor. This poses a challenge when the reactor is scaled up, as most of the heat is released at the entrance of the reactor. Case C exhibits the highest fuel concentration in the bulk flow compared to Cases A, B, and D. Conversely, Case D shows the lowest concentration, as its supply to the catalyst chamber is controlled by a porous fuel distributor (for a 2D profile, see Figure 6.24). Higher fuel concentration in the bulk flow leads to higher reaction rates and, consequently, greater heat generation. Furthermore, a higher fuel concentration in the bulk flow reduces diffusion limitations, thereby decreasing reaction inhibition and enhancing combustion performance. Figure 6.23 C shows the gas velocity along the center line of the CCR channel (gas bulk). The velocity is affected by the temperature and, consequently, the space time of the reactants in the gas channel.

Figure 6.24 illustrates the performance of the proposed designs in terms of CH_4 conversion, H_2 recovery, and MR efficiency. It also shows 2D profiles of temperature and CH_4 mole fraction. The temperature distribution along and across the MR is improved in cases C and D compared to case A (based on the standard deviation of temperature along MR for reforming channel, interface between catalyst layer and bulk flow). Additionally, H_2 recovery decreases by about 15% in

case B compared to case A, possibly due to the average velocity in the reformer-permeate channels. Comparing cases A-D, it is concluded that cases C and D have a higher potential for avoiding temperature spikes when running a CCR and controlling fuel distribution. Notably, under similar operating conditions, case C uses approximately 60% less catalyst weight than case D, which is a crucial factor in reactor design.

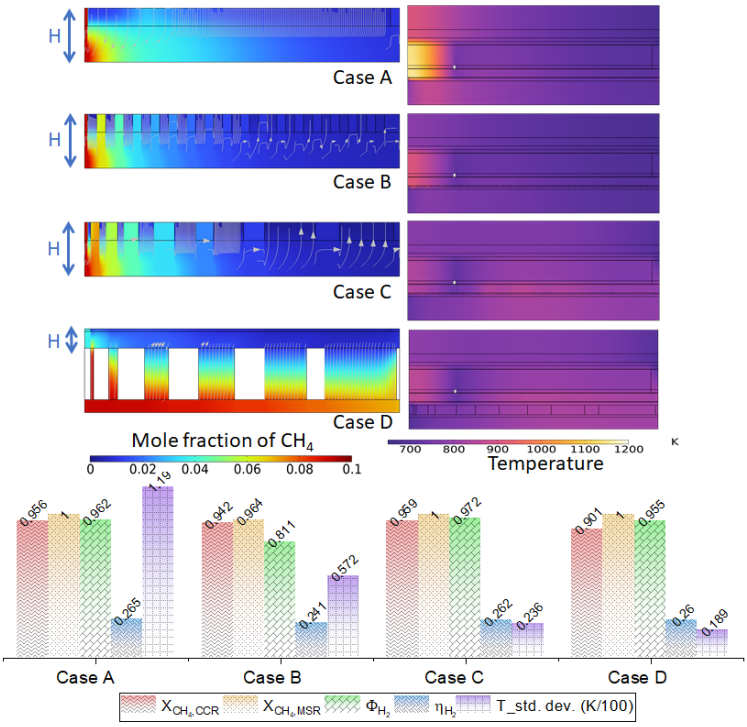

Figure 6.24: Results of the simulated configurations of CR, A) Temperature in gas channel (fuel section) along the reactor, B) CH_4 conversion of CR, C) concentration ratio of O_2 to CH_4, and D) velocity magnitude in the center-line of fuel channel. The conditions are $\delta_{cat,com}$:40 μm, combustion fuel flow of CH_4: 100 N mL min^{-1} $W/F_{reforming}$ 3 $\mathrm{gr_{cat}\ h/mol_{CH_4}}$ and Sweep gas of N_2: 1000 N mL min^{-1}, T_{inlet}=673 K, P_{ret}=6 bar, P_{perm}=1 bar, Air/CH_4:10 and S/C=3.

6.10 Summary and conclusion

In this chapter, μ-EnH_2ancerV 3.0 was presented as a potential solution for decentralized applications. This new version features a higher surface-to-volume ratio for the reactor. Based on the designs, it was fabricated and prepared for testing at IMVT. While the reaction part was successfully tested, attempts to implement a Pd membrane inside it failed, both with coating and commercial thin foils. Although smaller MRs used the latter successfully, it failed in this study. Additionally, a 2D simulation was developed to evaluate the autothermal performance of μ-EnH_2ancer V 3.0. The study found that heat management is crucial, as increased fuel concentration can cause temperature spikes, potentially damaging the MR housing. Consequently, an innovative design was suggested to better control the heat generated by the CCR section.

7 Additive manufacturing

Additive manufacturing (AM) of metals has attracted significant attention across various industries. However, its adoption in certain chemical and energy sectors remains constrained by the absence of optimized alloys tailored for high temperatures and corrosive environments. This chapter explores the laser-based powder bed fusion processing of Crofer 22 APU for the first time to date of this thesis. Systematic optimization of laser parameters including laser power, hatch distance, point distance, and building angles was conducted for both dense and porous objects. Additionally, an 8-YSZ coating applied via screen printing demonstrated the impact of hatch distance and laser power on surface quality. The combination of AM of Crofer 22 APU and screen printing of 8-YSZ simplifies the preparation of metallic supports for Pd-based membranes, reducing fabrication time and cost by shortening the number of preparation steps. This technique offers a promising approach for scaling up membranes and membrane reactors.

7.1 State of the art of the porous Crofer membrane supports

Although laser welding is an efficient technique, its weld seam (see Figure 7.1) causes problems in subsequent coatings. Xie and Dittmeyer [216] have described these challenges and proposed a possible solution of an additively manufactured plate. However, the proof-of-concept part was still made of stainless steel 316L which is not the optimal choice concerning compatibility with Pd and working at elevated temperatures e.g. above $500\,^{\circ}\mathrm{C}$. Our recent studies on AM motivated

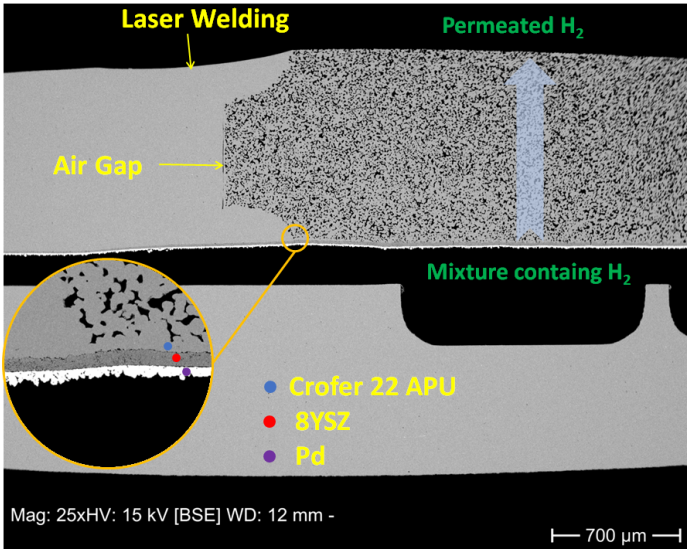

Figure 7.1: Cross-sectional view of a composite Pd membrane consisting of porous sinter metal of Crofer 22 APU, 8YSZ diffusion barrier layer, and Pd layer (selective towards hydrogen) for hydrogen separation from a gas mixture. More details regarding the Pd coating can be found in [150].

us to make use of this technique for a practical MR system by developing metal additive manufacturing process parameters for Crofer 22 APU.

7.2 Additive manufactured permeable structures

The AM technology of Laser-based Powder Bed Fusion of Metals (PBF-LB/M) is a mature production process for complex monolithic parts and individualized designs. The field of process engineering already benefits from these well-known properties in the form of optimized and compact chemical devices [217–219].

A literature review found no suitable AM high-temperature alloys for Pd membrane supports. The classification of high-temperature alloys is based on a functionality working in the range of 30 % to 70 % of the desired alloy's melting temperature [220]. Temperature is one of the important parameters to select the material for a system especially a multi-component system like a MR. Rizzi et al. [220] present a good review of alloys for high-temperature applications in chemical industries. Nevertheless, none of the commercially available AM materials for high temperatures are deemed suitable material. The integration of functions in monolithic additive manufactured parts is a design option. The proposed design of the membrane reactor plates (see Section 7.5.2 and Figure 7.11) require a dense, leak-tight frame and backside as well as a permeable surface to support the membrane coating. The dense/permeable composite is a key feature of the design. The feasibility of permeable, additive-manufactured material has been demonstrated for other materials and applications.

Stoffregen et al. [221] distinguish two approaches to produce permeable AM material: The creation of an undefined pore structure by choosing process parameters with a lower energy input or the creation of a geometrically defined structure. Gu and Shen [222] produced permeable 316L (1.4404) stainless steel by adjusting the laser process parameters. Yadroitsev et al. [223] demonstrated with stainless steels 316L and 904L (1.4539) that a geometrically defined approach offers more control over the size, shape, and distribution of pores. Thin walls with intermediate gaps are formed by placing the individual melt tracks on top of each other. The resulting porosity consists mostly of through pores that contribute to the permeability of the material while undesired blind or closed pores are avoided. Blind and closed pores reduce the strength and fatigue life of a part without contributing to the permeability. We favor the term permeable material for such material to distinguish the functional structure from an undesired random porosity.

The permeability of geometrically defined structures is not necessarily isotropic. The permeable material consists of an arrangement of straight walls made from stacked melt tracks with open gaps between the walls. The arrangement of melt tracks in the scan strategy defines the orientation of gaps and therefore the main direction of flow [224, 225] equipped parts with large permeable areas

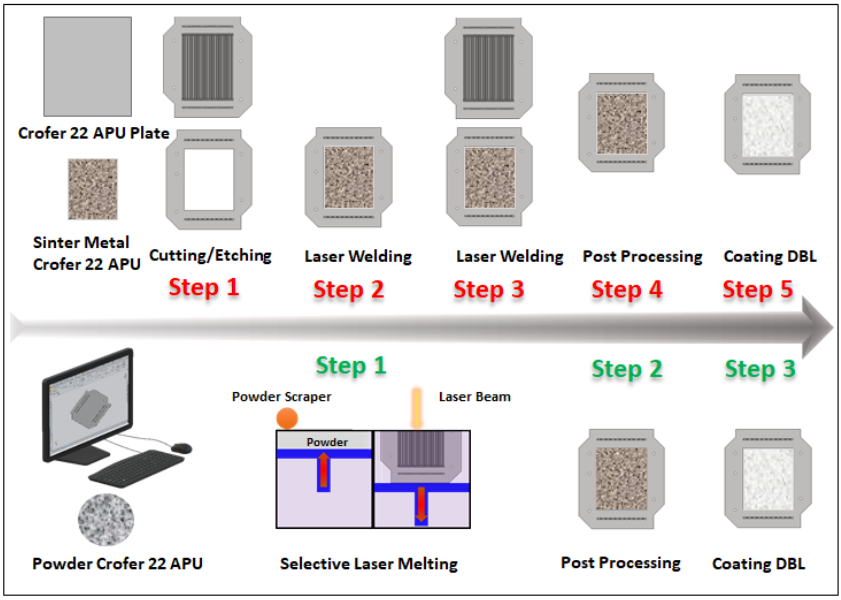

Figure 7.2: Comparison of preparation of planar metal-based membrane support through PBF-LB/M and tape-casting plus welding techniques.

with a direction of flow in the build direction. He demonstrated the viability of such permeable structures made from tooling steel Maraging 300 (1.2709) in the mechanically challenging application of pneumatic ejectors for injection molding tools. Xie and Dittmeyer [216] developed a scan strategy for large, planar surfaces with a flow direction perpendicular to the build direction. Later their approach was extended to tubular parts with a flow radial to the build direction [226].

The most common approach for permeable/dense composite parts is to separate the parts into individual 3D models for each type of material. Klahn [224] and Xie et al. [226] demonstrated the feasibility and design opportunities of multiple types of permeable materials in an integrated part. A suitable parameter set is assigned to each of the 3D models to achieve different gap sizes, orientations, or

patterns. Li et al. [227] proposed a similar approach for undefined pore structures to create a gradient porous structure with different pore sizes.

The stacked melt tracks provide less volume for heat conduction and as heat sinks. Thus the melt temperature rises and melt volume increases. The increased melt volume leads to elevated melt tracks. Yasa et al. [228] associates elevated edges to melt flow and process parameters. Manufacturing permeable material requires an adaptation of the process parameters of the laser-based powder bed fusion process. Documented process parameters for permeable material show a decrease of laser power P_L and an increase in scan speed v_S to reduce the energy density of the laser-based powder bed fusion process [216, 222, 224].

7.3 Additive manufacturing of Crofer 22 APU for dense/permeable composite parts

The membrane reactor requires a high-temperature steel with a thermal expansion coefficient similar to the one of the ceramic coating. The stainless steel Crofer 22 APU exhibits these properties because it was developed for Solid Oxide Fuel Cells (SOFC) and Solid Oxide Electrolytic Cells (SOEC) stacks [137]. These applications require high temperature and corrosion resistance as well as a thermal expansion coefficient that matches the ceramics typically used in fuel cells.

Crofer 22 APU (1.4760, X1CrTiLa22, ASTM A240) is a ferritic stainless steel. The composition is listed in Table 7.1. The alloy manufacturer VDM Metals states that the material may contain other elements for technical reasons [137]. The analysis of the virgin powder used in this study by the powder supplier Rosswag shows that the material is within the specifications of the alloy manufacturer, except for a lower concentration of Lanthanum (La).

Despite the impact on alloy properties due to the reduction in La content during gas atomization, Crofer 22 APU remains suitable for applications at temperatures below $900\,^{\circ}\mathrm{C}$. At such elevated temperatures, the volatility of chromium oxide becomes a concern, and the addition of a minimal amount of La effectively

Table 7.1: Chemical composition of Crofer 22 APU in [%], min. and max. by specification [137] and analysis of the virgin powder.

	C	Cr	Fe	S	Mn	Si	Ti	Cu
Min. [137]		20.0	Bal.		0.30		0.03	
Max. [137]	0.03	24.0		0.020	0.80	0.50	0.20	0.50
Analysis	<0.01	22.21	Bal.	<0.003	0.38	0.02	0.06	0.01

	P	Al	La	Mo	Ni	V	W	Co
Min. [137]			0.04	n.s.	n.s.	n.s.	n.s.	n.s.
Max. [137]	0.050	0.50	0.2	n.s.	n.s.	n.s.	n.s.	n.s.
Analysis	0.006	0.013	<0.005	0.02	0.02	0.01	<0.01	0.01

addresses this issue. However, for processes like MSR that operate within a range from moderate to relatively high temperatures, Crofer 22 APU remains a favorable choice. Its ferritic nature and compatibility with Pd in an MSR system make it a robust and viable selection. The Crofer 22 APU bulk material was gas atomized into a fine powder with spherical particles. Figure 7.3 depicts the particle size distribution of the virgin powder.

A parameter study on a DMG Realizer SLM-125 laser-based powder bed fusion machine identified the parameters in Table 7.3 for the production of dense and permeable structures. The scan strategy for dense parts is a typical island strategy with $5\,\mathrm{mm}$ squares and a variation of the island positions and orientations between layers. The permeable parts are manufactured by increasing the hatch distance h_s to create a gap between neighboring melt tracks. The melt tracks are unidirectional and parallel to the direction of flow of the membrane reactor. This pattern is constant across all layers of the permeable section of the membrane part.

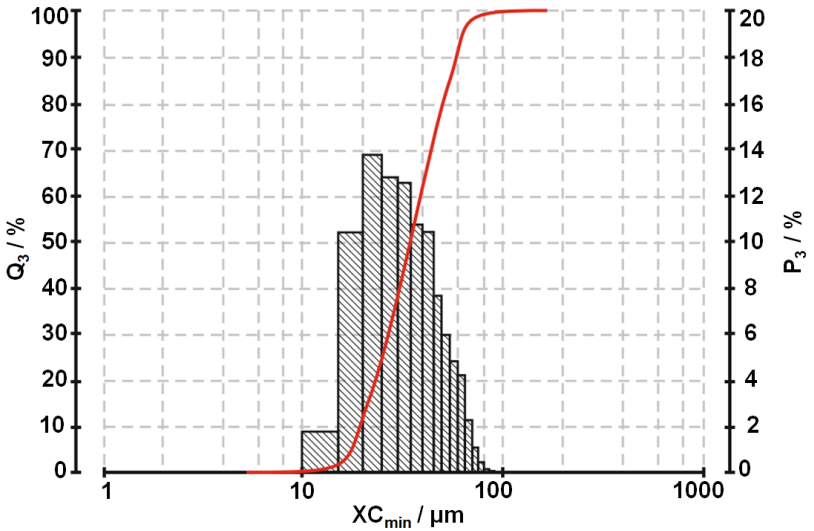

Figure 7.3: Particle size distribution of the Crofer 22 APU powder.

7.3.1 Characterization of dense parts

7.3.1.1 Relative density

To find the optimal parameter for printing a gas-tight part (dense part), a set of hatching parameters was considered (illustrated in Table S1). The printed objects were in the form of cubes with a length of $10\,\mathrm{mm}$. After the build job, the samples were separated from the build plate and rinsed with isopropanol to remove loose powder particles. They were subjected to polishing treatment before imaging as follows. To achieve a mirror-polished finish for the printed samples, essential for analyzing porosity and defects, the ATM SAPHIR 550 polishing machine was utilized, featuring a holder and a cooling water system. The stepwise polishing procedure involved the successive use of finer polishing papers: starting with the number 320, followed by 400, 600, and 1200, each for 2 minutes at a rotation speed of 300 rpm. Subsequently, an additional 2 minutes of polishing with paper

number 2500 at a reduced speed of 150 rpm was carried out. In the final stages, the samples were polished with Dia-COMPLETE poly pastes, first with 3 µm and then with 1 µm pastes, each for an additional 2 minutes at 150 rpm. This consistent treatment approach was also applied to polish the cross-sections of the samples, preparing them for subsequent SEM analysis. All samples underwent measurement using a single SENSOFAR SNEOX optical profilometer, employing various techniques for quantitative characterization. The measurement techniques of Imaging Confocal Microscopy were used for whole samples. Consistent conditions were maintained with 10x magnification at identical Region of Interest (ROI) locations (at least 3 spots on each sample) for the measuring technique, covering an area of 1.75x1.32 mm^2. Data processing was carried out using SensoSCAN 6.4 software. Initially, non-measured points were computed as a performance indicator and then reconstructed by interpolation using the "smooth shape calculated from the neighbors" algorithm. A least-squares plane fitting, implemented as the F-operator, removed the global form of the surfaces analyzed in the study. No L-filter (high-pass filter) was applied, preserving all topographic features of the AM process. A set of topographical parameters from ISO 25178, related to height (S_q, S_{sk}, S_{ku}, S_a), spatial (S_{al}), and hybrid (S_{dr}) were calculated on the primary surface.

A MATLAB code was used to determine the potential pore quantity and diameter on the surface from the images. Briefly, in the quantitative analysis of 3D-printed samples across diverse research domains using MATLAB, the initial step involved the conversion of images into a binary format. This conversion required assigning gray values to pixels within the range of 0 to 255. Consequently, the binary images exhibited a clear black-and-white contrast, effectively revealing the internal structure. In this binary representation, pixels with a value of 0 represented black and corresponded to pores, while pixels with a value of 255 were depicted as white, signifying the non-porous area. The binarization process was executed using MATLAB's native "Color Thresholder" application. After having the images, binary images are generated. Further analysis includes calculating parameters such as image porosity, and pore size distribution were carried out. The 'size' function in MATLAB is utilized to identify and extract pixels in the

binary image. Employing the built-in 'bwarea' function, the total number of image points, representing the sum of black and white pixels, can be obtained. The porosity is calculated based on dividing the black pixels by the whole pixels. Additionally, to analyze the distribution of pore radius, the 'bwlabel' function in MATLAB is utilized (see Figure A.7).

The results showed that the sample with the hatching parameter H08 (Laser current L_C: $2000\,\mathrm{mA}$, point distance P_D: $35\,\mu\mathrm{m}$, scan speed v_s :$1750\,\mathrm{mm\,s^{-1}}$) represents the minimum defects and a relative density of 99.99%.

7.3.1.2 Surface roughness

The surface quality for different orientations and the need for support structures are also affected by process parameters. In this regard, the surface roughness Sa depending on the down-facing angles of the objects is characterized on samples depicted in Figure 7.4 [229]. The design was chosen because it allows the evaluation of up- and down-facing surfaces in two opposing orientations. The size of samples allows for measuring at least 5 points on each surface according to the reference [229]. This set of samples allows the characterization of surfaces with angles $\alpha = 25°$, $35°$, $45°$, $90°$, $135°$, $145°$ and $155°$. The roughness was measured based on areal average roughness (S_a). By comparing Table 7.2, Table S1, and also Figure A.10, it is seen that samples with contour parameters C02 and C03 show lower surface roughness (L_c: $1400\,\mathrm{mA}$ and P_D: $30\,\mu\mathrm{m}$ and $40\,\mu\mathrm{m}$, respectively), compared to the those of other samples except the angle $25°$. Compared to up-facing surfaces $135°$-$155°$, the down-facing surfaces are susceptible to dross formation as the penetration of melt pool into the powder bed increases causing higher surface roughness. Such a high roughness could be critical when coating onto a printed reactor wall, as it may hinder the formation of an even and homogeneous layer. However, defining one set of parameters that meets the surface quality for all regions of a complex geometry remains a challenge. Ferchow et al. [230] extended the feasibility of overhanging geometries by assigning different parameter sets to different regions. They showed that it is possible to reduce the post-processing efforts. Accordingly, depending on the

target geometry for a reactor body, sets of parameters can be selected from Table 7.2.

Table 7.2: Arithmetical mean height of the surface Sa of additive manufactured Crofer 22 APU with a surface angle α to the build plate.

Sample	down-facing surfaces				up-facing surfaces		
	25°	35°	45°	90°	135°	145°	155°
C01	83.86±8.27	49.89±2.22	32.99±2.05	33.76±2.00	37.46±3.51	44.03±2.85	51.68±7.78
C02	61.65±3.80	47.05±2.33	41.27±1.48	26.15±2.57	31.34±2.77	28.98±2.92	34.24±1.85
C03	62.57±6.80	45.74±3.85	41.55±2.06	26.68±1.29	28.43±3.87	30.49±2.94	40.09±1.51
C04	50.82±4.99	49.95±1.84	44.89±4.32	27.11±0.61	43.64±2.56	39.74±4.09	44.96±5.30
C05	106.47±9.18	94.05±5.10	60.56±4.59	14.08±2.22	30.03±5.36	38.35±2.60	44.87±6.83
C06	89.18±4.08	109.32±11.31	78.60±13.17	18.31±0.69	30.62±2.97	41.98±9.33	49.81±5.52
C07.90°	114.06±12.84	104.76±15.80	55.58±4.67	13.31±0.56	25.09±5.11	37.90±7.99	43.76±7.50
C08.90°	102.10±14.20	88.49±7.48	67.76±10.62	12.42±0.17	33.78±5.56	54.07±8.01	53.23±11.48

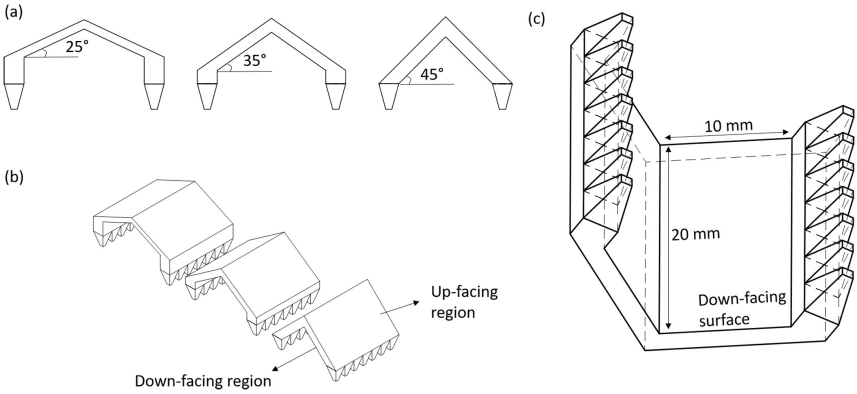

Figure 7.4: Sample for the evaluation of surface roughness of AM Crofer 22 APU, (a) Front view of manufactured test pieces showing all three printed angles 25°, 35° and 45°, (b) isometric view of printed test pieces and (c) view of down-facing surface of all test pieces (the schematic was reprinted with permission from Elsevier) [229].

As a conclusion, Table 7.3 lists the optimal parameters to print dense parts from Crofer 22 APU. The parameters on Realizer machines are converted into the usual PBF-LB/M parameters. With these parameters we achieve a relative density of

99.99% and a surface roughness Sa = 41.27±1.48 at α:45°) and Sa = 26.15±2.57 at α: 90°). In the following the permeable section is discussed.

Table 7.3: Process parameters for dense part printing with Crofer 22 APU powder.

	Hatch (H08)	Contour (C02)
Laser power P_L (W)	180	180
Scan speed v_s ($\mathrm{mm\,s^{-1}}$)	1750	750
Hatch distance h_s (µm)	80	-
Layer thickness s (µm)	50	50

7.3.2 Characterization of permeable parts

After achieving a rather defect-free wall, the next step was the study of the permeable parts. Eight cubes were manufactured with the parameters S1-S8 in Table 7.4. They were polished and mounted in epoxy, which is shown in Figure 7.5. This figure shows that, with increasing the hatch distance from $0.12\,\mathrm{mm}$ to $0.16\,\mathrm{mm}$, the porosity based on the surface images, increases by approximately $19\,\%$ and $14\,\%$ for a laser current $1000\,\mathrm{mA}$ and $1200\,\mathrm{mA}$, respectively.

In another print job, the samples were printed in a plate shape with dense frames for a water permeability test. The test was carried out on the as-received samples using a flow cell system to estimate the superficial velocity versus pressure drop. The permeability assessment involved utilizing a flow cell system to measure the pressure loss at various flow rates of water passing through the test sample. The initial step included polishing the dense part through polishing for better sealing. Subsequently, sealing through the dense part of the tested sample was accomplished using rubber sealings. Pressure measurements were conducted using a Baumer PBSN pressure sensor, which had a range from $0\,\mathrm{bar}$ to $2.5\,\mathrm{bar}$ absolute and a standard error of measurement of ± 0.03% FSP.

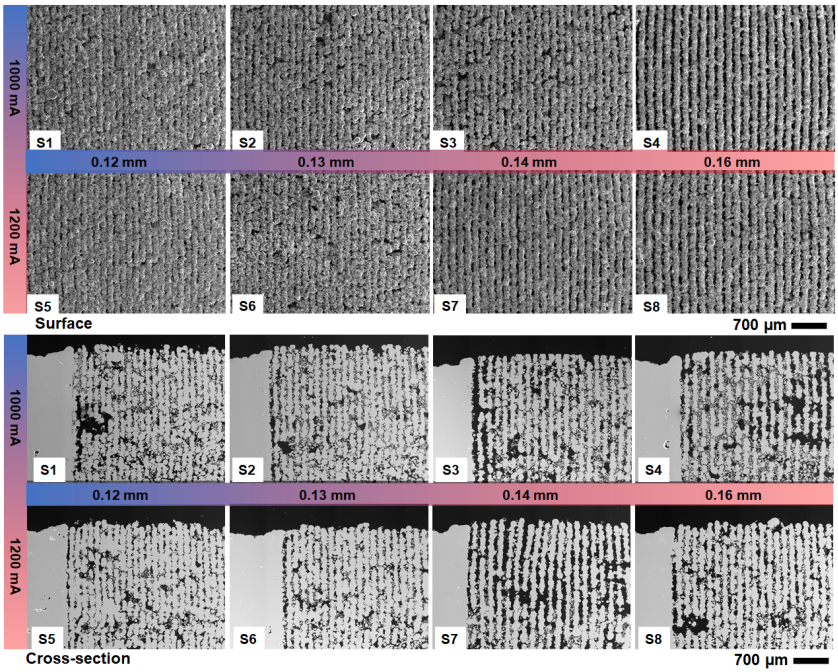

Figure 7.5: Top view and cross-sectional view of printed samples with different hatch distances and laser power (hatch distance 0.12-0.16 mm and laser current 1000-1200 mA).

The Verdergear VG 1000 basic gear pump controlled the water flow rate, and the flow rate, which was adjusted within the range of 30% to 80% of the maximum rating of 4000 rpm, with 10% intervals. The precise determination of each setting was achieved by measuring the amount of water permeating over 2 minutes. Before each permeation test, the flow cell system ran for 30 minutes to ensure stable conditions, including complete wetting of the sample, a constant flow rate, and pressure loss. Throughout the measurement procedure, the system was allowed to equilibrate for at least 5 minutes after setting a higher flux before measuring the corresponding pressure loss. The superficial velocity was then calculated based on the amount of water permeating within 120 seconds using the formula specified in Equation 7.1.

$$\nu = \frac{m_{H_2O}}{\Delta t} \rho_{H_2O}^{-1} A_{porous}^{-1} \tag{7.1}$$

where ρ_{H_2O} =998 $\mathrm{kg\,m^{-3}}$ and A_{porous} =2.2 $\mathrm{cm^2}$ were used for calculations. The flow behavior in the porous media is addressed in different ways [231–234]. Darcy's Law predicts the flow behavior in porous media, stating that the pressure gradient is linearly proportional to the fluid velocity. However, this linear dependency is only valid for low-pressure gradients or small flow velocities [235]. As the flow reaches a turbulent regime, a non-linear dependency of pressure gradient versus flow velocity is expected. Brinkman's equation describes the macroscopic fluid flow for laminar and turbulent regimes as follows:

$$\frac{\Delta p}{L} = \mu \frac{v}{K_D} + \rho \frac{v^2}{K_F} \tag{7.2}$$

with the speed v ($\mathrm{m\,s^{-1}}$), pressure drop Δp (Pa) through the porous medium, the permeable part thickness L (m), fluid density ρ ($\mathrm{kg\,m^{-3}}$) based on the inlet pressure, Darcy's K_D ($\mathrm{m^2}$), and Forchheimer's terms K_F (m). To estimate the porosity of the additively manufactured samples, porous parts with parameters S1-S8 were printed in disk shape with a diameter of $22\,\mathrm{mm}$ and a thickness of $1.1\,\mathrm{mm}$. Equation 7.3 was used to estimate the corresponding porosity ϕ for each sample (see Table 7.2)

$$\phi = 1 - \frac{\frac{m_{\text{exp}}}{V_{\text{exp}}}}{\rho_{\text{Crofer}}} \tag{7.3}$$

where m_{exp} denotes the weight of samples measured by a balance (accuracy $0.1\,\mathrm{mg}$) and V_{exp} is the volume of the printed disks. The density is $\rho_{\text{Crofer}} = 7.7\,\mathrm{g\,cm^{-1}}$ according to the material certificate [137].

Figure 7.6 shows the results of the water permeability for samples S1-S8. It is observed that the permeability K_D increases from $2.77 \times 10^{-12}\,\mathrm{m^2}$ to

$1.98 \times 10^{-9}\,\mathrm{m}^2$ for S1 (hatch distance $0.12\,\mathrm{mm}$) compared to S4 (hatch distance $0.16\,\mathrm{mm}$). The permeability also changed from $1.55 \times 10^{-12}\,\mathrm{m}^2$ to $1.57 \times 10^{-11}\,\mathrm{m}^2$ for S5-S8. Comparing S5 to S1, it is found that a laser current increase from $1000\,\mathrm{mA}$ to $1200\,\mathrm{mA}$ lowers K_D approximately $44\,\%$. These results confirm the feasibility and permeability for all parameters. The final choice of a parameter set depends on the ability to screen print a homogeneous layer of 8-YSZ onto the permeable surface.

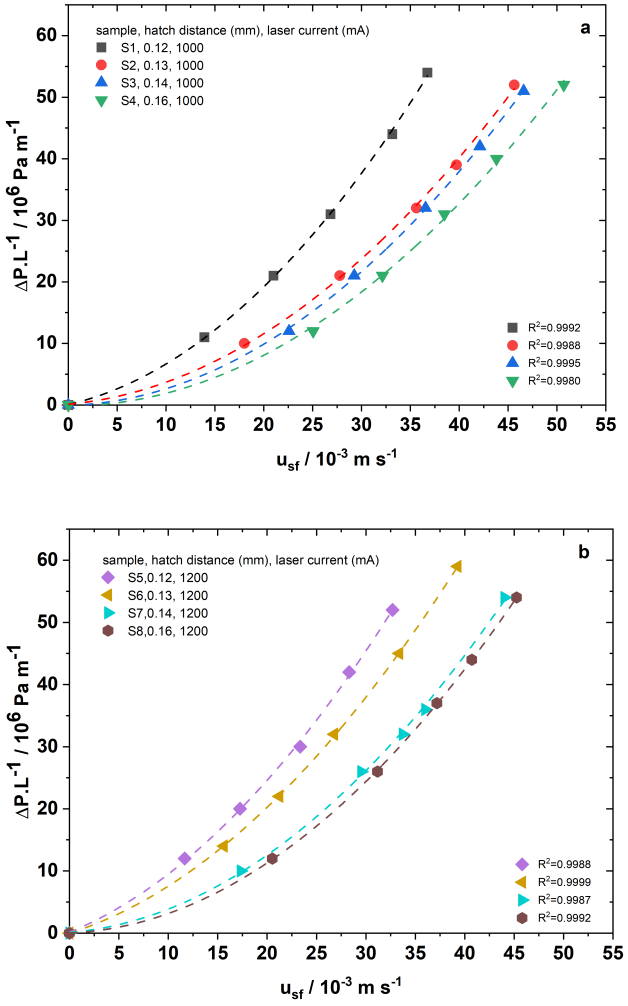

Figure 7.6: Water permeability of additively manufactured samples, the effect of hatch distance ranging from 0.12 mm to 0.16 mm, a: Laser current 1000 mA, b: 1200 mA.

7.4 Surface preparation for coating of active thin layers

Typically, preliminary treatments and modifications to metallic support are carried out to enhance the overall quality of the membrane. Beyond standard initial cleaning procedures, the emphasis in most of these modifications lies in improving layer adhesion, reducing average pore sizes, and smoothing the support surface to achieve thin and defect-free Pd layers. These treatments can be categorized into three main types: (i) chemical treatment such as using a corrosive solution, (ii) physical treatment e.g. polishing, and (iii) incorporation of an intermediate layer. In this regard, the following, two techniques of heat treatment and ceramic layer coating (as an intermediate layer) are discussed.

7.4.1 Microstructure of Crofer 22 APU before and after heat treatment

Annealing the metal leads to the formation of a thin oxide layer that acts as a protective coating in the reactor. This oxide layer also enhances coating stability by providing a stable anchor for the coated layer. One sample (sample S5 which showed the lowest porosity among the samples) was heated up to $800\,^{\circ}\mathrm{C}$ for $2\,\mathrm{h}$. The EDS analysis was conducted on the surface of the porous part. Figure 7.7 shows sample S5 before (denoted as the fresh sample, after printing) and after annealing treatment. As seen, a layer of around $500\,\mathrm{nm}$ to $1000\,\mathrm{nm}$ on the outer surface is formed. Comparing the growth of the oxide layer, which reaches a maximum of approximately $1\,\mathrm{mm}$, with the surface roughness reported for S5 (see Table 7.4), it appears that heat treatment has minimal impact on the surface roughness. Instead, it seems that the primary role of the formed layer is to act as a protective layer for the Pd layer. The formed layer shows a triangle structure for the grains near the surface.

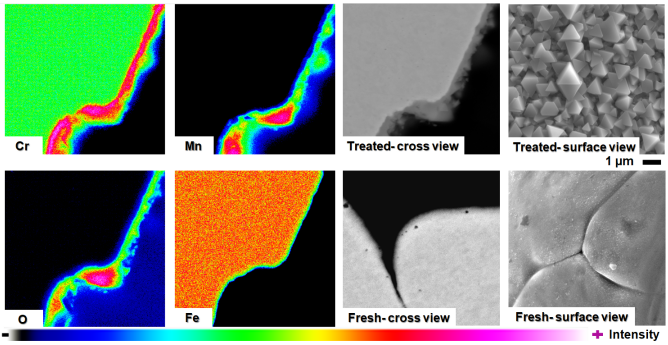

Figure 7.7: Heat treatment under Air atmosphere for sample S5, at 800 °C for 2 h.

In the literature, there are several examples of ferritic stainless steels forming two-layer oxide scales, with particular attention given to SS 430 [236–238]. Alloys of the Fe-Cr-Mn type exhibit a rapid formation of an initial Cr_2O_3 layer during oxidation. Saeki conducted a comprehensive study utilizing a combination of X-ray photoelectron spectrometry and XRD to characterize the oxides formed on SS 430 in an O_2/N_2 environment at 1000 °C for up to 20 min [236].

Table 7.4: Calculated surface properties of the porous parts (hatch distance 0.12-0.16 mm and laser current 1000-1200 mA).

Sample	Hatch Distance (mm)	Laser current (mA)	Porosity ϵ (%)	Surface roughness Sa (µm)	K_D (m^2)	K_F (m)
S1	0.12	1000	33.87	23.70	2.77×10^{-12}	3.37×10^{-8}
S2	0.13	1000	35.91	26.04	7.02×10^{-12}	4.66×10^{-8}
S3	0.14	1000	41.40	31.06	2.25×10^{-11}	4.42×10^{-8}
S4	0.16	1000	55.47	44.96	1.98×10^{-9}	4.87×10^{-8}
S5	0.12	1200	28.62	23.30	1.55×10^{-12}	3.48×10^{-8}
S6	0.13	1200	31.63	22.17	1.99×10^{-12}	3.93×10^{-8}
S7	0.14	1200	34.44	25.50	7.77×10^{-12}	4.06×10^{-8}
S8	0.16	1200	44.41	40.91	1.57×10^{-11}	4.01×10^{-8}

The investigation disclosed that within the first 15 s to 30 s of oxidation, a single-phase oxide layer with a corundum structure is evident. Initially resembling Fe_2O_3 in chemical composition, this layer rapidly transitions to Cr_2O_3. After

30 s of oxidation, an $MnCr_2O_4$ spinel phase emerges, coinciding with a shift in the oxidation state of Mn from +3 (Mn_2O_3) to +2 ($MnCr_2O_4$). The study showed that the induction period for spinel formation corresponds to the time taken for Mn_2O_3 to reach its maximum solubility in Cr_2O_3 (12-17 wt.%). Once this threshold is exceeded, the $MnCr_2O_4$ spinel nucleates on the surface and grows through a reaction involving Mn_2O_3 and Cr_2O_3 [236, 237]. If this mechanism is applicable to the formation of the two-phase scale in the Crofer 22 APU samples under investigation, it suggests that the scale microstructure could be governed by the initial nucleation rate of chromia. This is since the nucleation rate dictates the chromia grain size, and grain boundary diffusion of transition metals through Cr_2O_3 is significantly faster (3-5 orders of magnitude) than bulk diffusion [239]. Additionally, it has been reported that the grain boundary diffusion of Mn is 1-2 orders of magnitude faster than the grain boundary diffusion of Cr or Fe in Cr_2O_3 [239, 240]. Magdefrau et al. [241] investigated the annealing treatment of Crofer 22 APU for long-tem (750 h) and also short time (5 h). Based on their results, the microstructures of the scale in samples oxidized for just 5 h revealed that the nucleation of Cr_2O_3 and $MnCr_2O_4$ phases during the initial oxidation stages influenced the ultimate scale microstructures. Larger alloy grain sizes resulted in lower nucleation rates, larger spinel grains, and enhanced oxidation resistance. It is deduced from these findings that larger alloy grain sizes in heat-treated samples diminish the initial supply of Mn to the alloy surface. This, in turn, leaves more Cr available to form a thicker initial Cr_2O_3 scale with coarser grains. Consequently, alloy heat treatment proves to be an effective method for slowing the oxidation of Crofer 22 APU [241].

7.4.2 Screen Printing Coating

To apply a protective layer to the permeable sections of the additively manufactured plates, the screen printing technique was employed. This method is well-suited for coating flat structures with varying layer thicknesses, depending on the number of print jobs. In this study, no pretreatment such as polishing of the AM samples was performed. A printing paste consisting of ytteria-stablized zirconia (8-YSZ,

Tosoh co.), Terpineol $98\,\%$ (Alfa Aesar), dispersant (Hypermer KD1-SO-(AP)), and ethyl cellulose (viscosity 100 cp, Aldrich) was prepared. After mixing the ingredients on a heater stirrer, the formed paste was rolled for $30\,\mathrm{min}$ by three-roll milling. All print jobs were carried out under consistent conditions for all samples simultaneously. After screen printing, the printed samples were held in an oven at $40\,^{\circ}\mathrm{C}$ for $2\,\mathrm{h}$. Before each new print job, the deposited weight of the previous step was recorded. Calcination at $550\,^{\circ}\mathrm{C}$ for $2\,\mathrm{h}$ with heating rate of $2\,\mathrm{K\,min^{-1}}$ was performed after several printing-drying jobs.

7.5 Results of additive manufactured permeable structures

This section describes the processing of Crofer 22 APU by PBF-LB/M for the first time. The capabilities of this material are demonstrated by the successful fabrication of the key elements of a membrane reactor. This target application requires the characterization of a coating on the permeable AM part.

7.5.1 Results of coated porous parts

Figure 7.8 shows the weight deposition changes versus surface properties of samples S1-S8. It is seen, with enlarging in hatch distance from samples S1 to S4 and also from samples S5 to S8, the weight of depositing increases. It might be justified with the effect of surface roughness and also the volume of paste in contact with plates that penetrate inside the pores [242].

Sample S4 with maximum hatch distance and minimum laser current compared to other samples shows the maximum loading of 8-YSZ (73.9 mg), while sample S5 possesses the lowest deposition (37.5 mg). Given that all screen printer parameters were kept constant, this variation indicates that the paste primarily covers the surface levels of the samples after 16 printing steps. The quality of the coated samples also were analyzed by SEM imaging. Figure 7.9 shows the surface

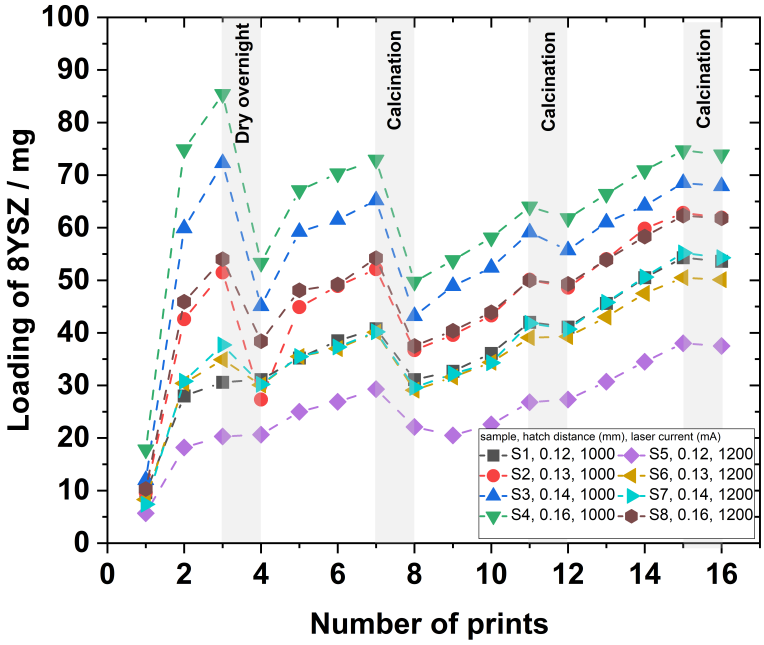

Figure 7.8: Deposition weight records versus number of screen printing jobs for printed samples S1-S8 (hatch distance 0.12 mm to 0.16 mm and laser current 1000 mA to 1200 mA).

view of the coated samples after screen printing process. At a magnification of 25 ×, defects such as uncovered spots were observed in samples S2-S4 and also S6-S8. These defects are attributed to the surface roughness of these samples.

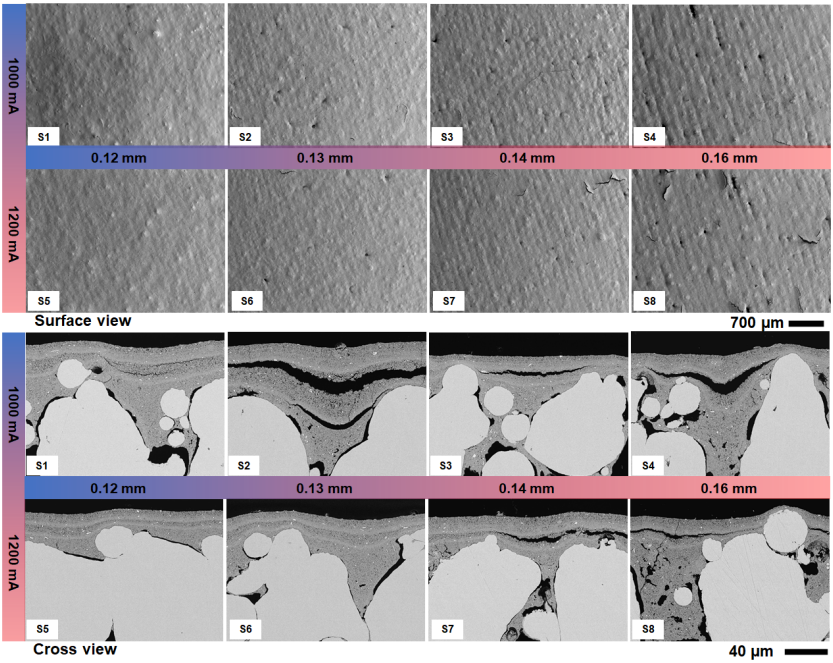

Figure 7.9: Surface view of coated samples with 8-YSZ with screen-printing technique (hatch distance 0.12 mm to 0.16 mm and laser current 1000 mA to 1200 mA).

Although additional printing jobs could improve coverage and coating on these samples, it is not advisable due to potential increases in mass transfer resistance and mechanical instability of the layer. According to the results, sample S5 depicts a non-defect surface that provides a rather smooth surface for any later coating such as a Pd-based active layer. Moreover, Figure 7.10 shows the cross-section view of the samples S1-S8 highlighting the depth of 8-YSZ paste penetration into the porous support following the screen printing process. It is found that the penetration depth depends on the porous part structure and the sample S4 depicts a penetration depth of approximately 30 % of the substrate thickness. It was not

possible to measure the water contact angle (wettability test) for all samples as they were highly hydrophilic.

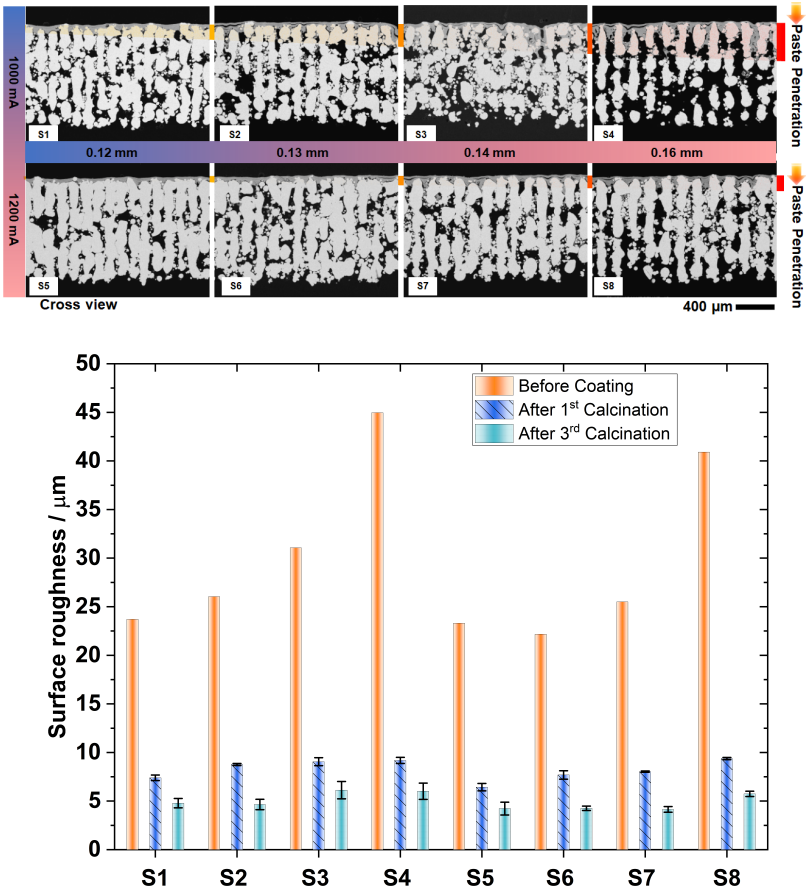

Figure 7.10: Top) Cross view of coated samples S1-S8; with magnification 50X, Bottom) The effect of paste penetration when printing is shown (hatch distance 0.12 mm to 0.16 mm and laser current 1000 mA to 1200 mA).

The reason why sample S5 was opted as the optimal case for scaling-up and printing final membrane substrates is the surface quality. Although the more porous structures like S4 give more permeability, the aim is to coat a defect-free ceramic layer or later dense Pd layer while the layer thickness should remain as thin as possible.

7.5.2 Integration of AM parts into a MR system

As shown in Figure 7.2, instead of welding the porous part to the dense part, AM of an integrated design in one job is proposed. The membrane support on one side is in contact with reforming channels, while the other side is faced with permeate channels. These plates are piled up together and welded later one by one through a pre-defined weld path.

After optimization of the PBF-LB/M process and successfully coating a DBL on samples, the final geometry was additively manufactured and coated by screen printing. To reduce the laser-welding steps for assembling the plates, the membrane support, the micro-structured permeate plate, and the two interface plates are produced in one job. This saves time and costs while reducing the complexity of supply chain and assembly. Figure 7.11 indicates the merged plates.

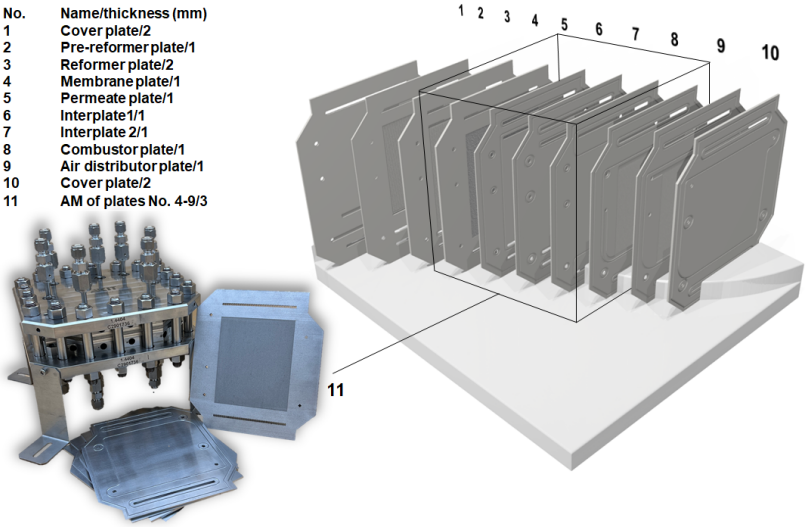

Figure 7.11: One-go printing of integrated plates of an MR with PBF-LB/M technique (No. 4-9); printing the composite plates of porous-dense (No. 11), thickness of 3 mm.

Moreover, by AM of the plate (No. 11 instead of No. 5-9), the final cell (including whole plates) undergoes not only less thermal stress when laser welding but also might be produced in thinner thickness (plate No. 11 saves up to 2 mm in thickness). The idea of such a planner structure allows for the scale-up of the system through the number of stacks, while the ratio of the surface area of the membrane to the volume of the system remains high.

7.5.3 Using permeable parts for mixing air-fuel in microreactors

Figure 7.12 illustrates a comparison highlighting a novel application of AM for a CCR reactor. The comparison between design A (using conventional manufacturing techniques like chemical etching and laser cutting) and design B demonstrates the flexibility of AM in reactor design. A simulation was conducted, revealing the benefits of AM in heat management over an MR system (see Section 6.9).

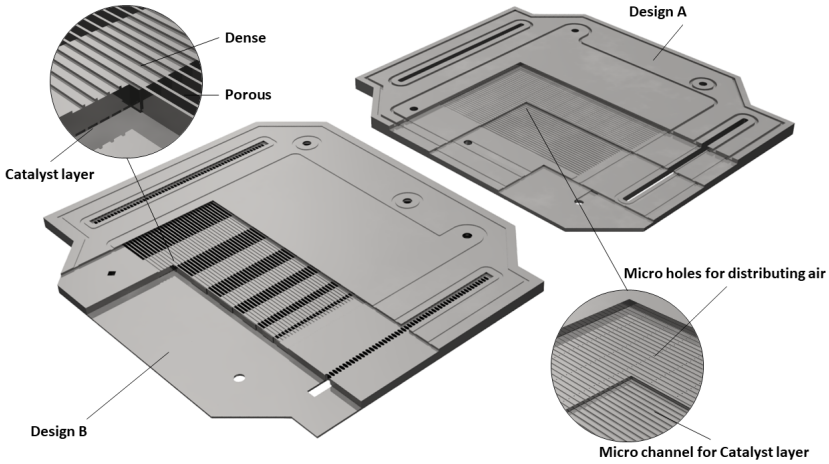

Figure 7.12: An ultra-compact planar catalytic reactor composed of catalytic plates designed for CCR.

Figure 7.13 shows a few show-cases for process intensification, especially for high-temperature processes.

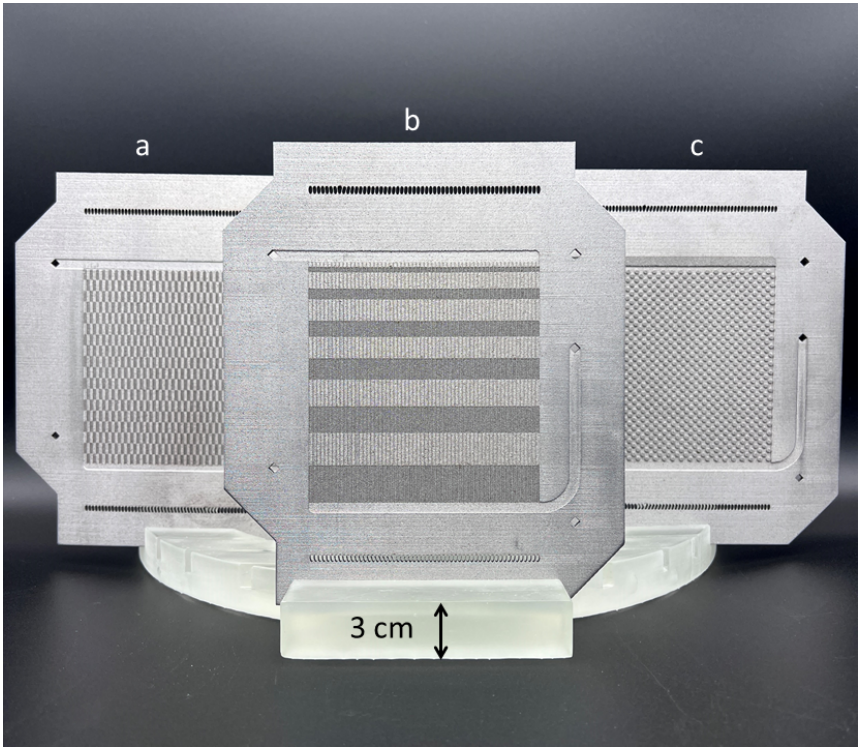

Figure 7.13: Additively manufactured Crofer 22 APU parts for a high-temperature reaction like catalytic combustion ; (a) special design for air distribution to avoid the hot spot formation, (b) design for distributing air along the catalyst bed (fuel channel) to distribute the heat along the reactor channel, (c) micro-packed bed with porous pillars (for air diffusion) for catalyst loading.

As shown in Figure 7.13, the plates printed for a catalytic combustor can be designed and optimized freely depending on the process requirement. Conventionally in the literature, segmentation of the catalyst beds (for a catalytic combustor) or air distribution are reported [243, 244]. However, with the aid of AM, the design can come with more flexibility and novelty to increase the overall reactor

efficiency. Moreover, for packed bed systems, Figure 7.13 C, the gases can penetrate the catalyst bed in different directions as the pillars on the plate are porous and are connected to the other side of the plate.

7.6 Summary and conclusion

For the first time, the process parameters were developed for processing Crofer 22 APU using laser-based powder bed fusion. The capabilities of additively manufactured Crofer 22 APU were demonstrated on a metallic Pd membrane support as part of a membrane reformer for high-temperature applications. Through systematic parameter optimization, composite substrates comprising dense and porous structures were developed. Variations in hatch distance and laser power were used to evaluate the porosity and permeability of the substrates. A protective layer of 8-YSZ was coated on the samples and analyzed. Additionally, objects built with different up-facing and down-facing angles of printing were examined. The integrated design simplifies assembly, reduces the number of welding operations, and allows for a thinner membrane reformer. The combination of screen printing coating and additively manufactured Crofer 22 APU reduces fabrication costs and time for membrane reactor plates, facilitating industrial scaling-up. The positive results of this study demonstrate the potential use of additively manufactured Crofer 22 APU not only as a membrane support but also for other reactor designs. This high-temperature, corrosion-resistant material expands opportunities in terms of operating conditions and design perspectives in chemical process engineering.

8 Summary and outlook

8.1 Summary

This work focused on the development of the third generation of ultra-compact membrane reformers for hydrogen production and separation at IMVT. The primary objective of this system is to deliver H_2 to end-users in decentralized applications through a modular and compact design that is easy to scale up while achieving high efficiency in product purity and energy usage and reducing the CO_2 footprint by eliminating the need for large supply plants. Chapter 4 discusses two techniques based on plasma spraying for depositing thin layers of Pd. Despite the advantages of this rapid coating method and its reduced chemical waste compared to conventional Pd coating techniques, the results indicated that the produced Pd layers were not fully selective for H_2. Consequently, commercially available self-supported thin Pd foils were chosen for integration into the MR. These foils were incorporated into the reactor using a laser welding technique. Systematic optimization of the welding parameters for the alloy Crofer 22 APU (the housing of the MR and substrate for the Pd membrane) was carried out using both continuous and pulsed wave techniques. The welding parameters were precisely adjusted to ensure a leak-tight integration between the membrane and its support, using microstructured foils. A key challenge was optimizing the energy input to achieve a secure bond without evaporating the thin Pd foil or deforming the entire assembly. However, for the prototype-scale reactor, which had a larger Pd substrate area, the integration and assembly process faced difficulties, as air gaps between the substrate and the Pd foils were not fully eliminated.

In Chapter 5, two sets of highly active catalysts based on novel metals were synthesized and characterized for the MSR and CCR processes. This chapter also describes the optimization of the screen printing technique used for coating these catalysts, allowing for a fast and reproducible application method. The coated layers were tested in microstructured reactors on a lab scale and characterized.

The prototype of the MR was designed and fabricated based on insights gained from previous versions at IMVT. In this generation, Crofer 22 APU was used for the MR construction, providing excellent compatibility between the Pd membrane and substrate, with similar low thermal expansion coefficients. The μ-EnH$_2$cer V 3.0 was tested without a membrane due to the lack of suitable techniques during the research period. A detailed 2D model was developed to simulate the performance of μ-EnH$_2$cer V 3.0 for further evaluation of the MR in autothermal mode.

To address challenges such as reducing the number of plates used in μ-EnH$_2$cer V 3.0, eliminating curved surfaces between porous and dense regions of the Pd support, and minimizing laser welding steps, advanced additive manufacturing techniques were employed. Simulation results indicated that temperature uniformity could be improved by either segmenting the catalyst in the CCR and applying a screen printing technique or by 3D printing the porous components for better fuel distribution along the CCR channel, which is feasible using additive manufacturing with Crofer 22 APU.

8.2 Outlook

Due to time constraints in this research, several ideas are proposed for future work:

- Re-optimization of the MR for scalability: In the current version, it is suggested to integrate the Pd substrate as the outer component of a cell, with assembly occurring as the final welding step, reducing stress during preparation and assembly.
- Alternative coating methods: since a successful coating technique was not developed in this research, and considering the challenges associated with handling commercially available defect-free thin Pd foils, exploring alternative coating methods to achieve thin layers is necessary.
- Electrified or hybrid MR systems: a hybrid MR that combines electrical heating with CCR is proposed for applications where a constant electricity supply is feasible, as it can reduce the CO_2 footprint and offer faster start-up times.
- Additive manufacturing of the entire MR: while it may be challenging to use this method for coating the catalyst and Pd membrane, it is possible to reduce the components to three parts, significantly decreasing assembly time and cost.
- Development of a full 3D simulation model: further refinement of the MR simulation to a comprehensive 3D model could allow for the simulation of different cells with periodic boundary conditions, enabling more precise calculations of MR efficiency.

As a final remark on H_2 production for decentralized applications through steam reforming of NG using a membrane reformer, it is worth noting that other technologies, such as water electrolysis powered by renewable energies (assuming the cost of renewable energies becomes more affordable), have gained more popularity compared to the beginning of this study. Additionally, significant challenges

remain, such as the implementation of thin and stable Pd-based membranes for scaled-up membrane reformers. However, the development of compact modular reactors, which can enhance mass and heat transfer, and their associated challenges—such as flexible design, ease of manufacturing, sealing, and mechanical and thermal stability—remain general topics in process engineering. These techniques might also be applicable to other processes, such as ammonia (NH_3) cracking for decentralized applications.

This thesis brings the message that process intensification of autothermal membrane/ reformers can be further addressed by conducting research on new designs, fully automated reactor manufacturing, and eliminating intermediate assembly procedures and techniques.

A Appendix

A.1 Equilibrium composition calculation

It is possible to determine the equilibrium methane conversion, which is represented as $X^{eq}_{CH_4}$, and the equilibrium mole fraction of methane, $y^{eq}_{CH_4}$, using the equilibrium constants for the MSR reaction 2.1 and the WGS reaction 2.2. The equilibrium constants are found in [30, 31] as follows:

$$K_{eq,1} = \frac{y^3_{H_2} y_{CO}}{y_{CH_4} y_{H_2O}} P_t^2 = \frac{n^3_{H_2} n_{CO}}{n_{CH_4} n_{H_2O}} P_t^2 = exp[30.114 - \frac{26830}{T}] bar^2 \quad \text{(A.1)}$$

$$K_{eq,2} = \frac{y_{H_2} y_{CO_2}}{y_{CO} y_{H_2O}} = \frac{n_{H_2} n_{CO_2}}{n_{CO} n_{H_2O}} = exp[-4.036 + \frac{4400}{T}] \quad \text{(A.2)}$$

In the given equation, P_t refers to the total pressure in bar, T represents the temperature (K), and y and n refer to the mole fraction and mole number of gas species, respectively. If a reformer is operated under constant total pressure and S/C ratio, the equilibrium composition can differ in various locations depending on the temperature. To determine the equilibrium composition, it is assumed that a reactor initially contains 1 mole of methane and SC moles of water vapor. The reactor is assumed to undergo MSR and WGS reactions, with $r1$ and $r2$ moles of reactants participating, respectively. The initial changed, and final mole numbers of gas species can be organized in tabular form as follows [245, 246]: The equilibrium constraints stated in equations A.1 and A.2 must be met by the final composition, which gives rise to a series of nonlinear algebraic equations expressed as:

Table A.1: Composition changes of reactions for a basis of 1 mole of CH_4 and SC as the steam to methane ratio for SR and WGS

Gas species	Initial	Changed	Final
CH_4	1	$-r1$	$1-r1$
H_2O	SC	$-r1-r2$	$SC-r1-r2$
H_2	0	$3r1+r2$	$3r1+r2$
CO	0	$r1-r2$	$r1-r2$
CO_2	0	$r2$	$r2$
$TotalMoles$	$1+SC$	$2r1$	$1+SC+2r1$

$$f_1(r_1,r_2)=0: K_{eq,1}(1-r1)(SC-r1-r2)(1+SC+2r1)^2-P_t^2(3r1+r2)^3(r1-r2)=0 \tag{A.3}$$

$$f_2(r_1,r_2)=0: K_{eq,2}(r1-r2)(SC-r1-r2)-(3r1+r2)(r2)=0 \tag{A.4}$$

these equations can be solved numerically through e.g. a multivariable Newton-Raphson method or via the $fsolve$ solver in MATLAB using the "trust-region-dogleg algorithm". The initial guesses are generated randomly by MATLAB in the range of $0 < r_{i,0} < 1$, and it is solved when the tolerance ζ is less than $1e^{-6}$. After calculating the values for equations A.3 and A.4, the equilibrium level of methane conversion, $X_{CH_4}^{eq}$, and the mole fraction of methane, $y_{CH_4}^{eq}$, can be computed.

$$X_{CH_4}^{eq}=r_1 \tag{A.5}$$

$$y_{CH_4}^{eq}=\frac{1-r_1}{1+SC+2r_1} \tag{A.6}$$

A.2 Membrane

This graph shows the good compatibility of the Crofer 22 APU, Pd, and 8-YSZ for a composite membrane operating at moderate to elevated temperatures.

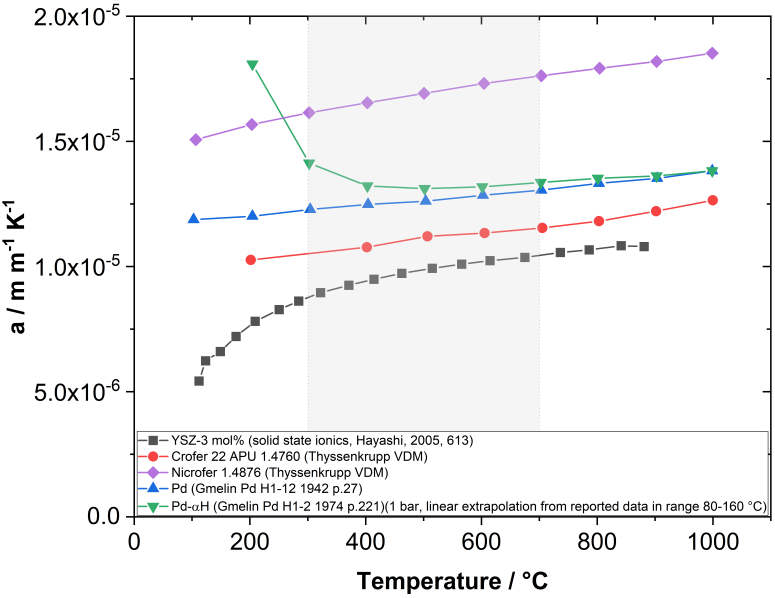

Figure A.1: Thermal expansion coefficients of different components of a composite pd membrane.

The following figure shows the lab-scale adapter for testing small plate Pd membranes (composite membranes or foil-based modules).

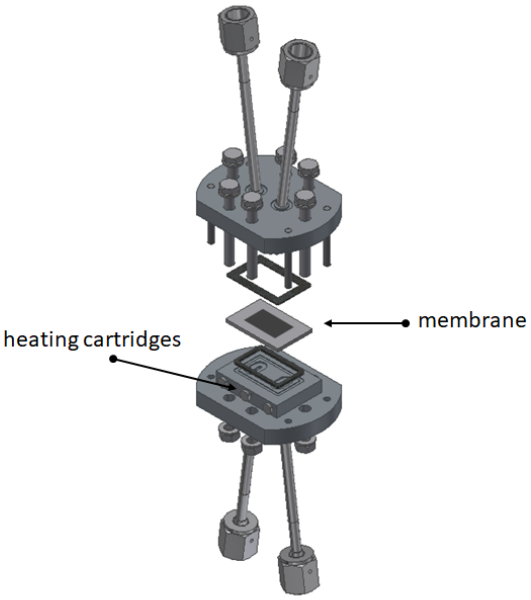

Figure A.2: Membrane adaptor sketch for gas test of the synthesized Pd membrane for lab test.

A.3 Catalyst characterization techniques and test reactor sketch

A.3.1 Electron Probe Microanalyzer

An electron probe microanalyzer (EPMA) with field emission-cathode JXA-8530F was employed to investigate the quality of the microstructured channels, and also catalyst layers, and elemental maps of the materials were detected by WDS (wavelength dispersive spectroscopy). The coated layers were characterized by a top-surface view and a cross-section view. The latter was carried out in this way first of all, the samples were cut in the middle and then mounted into epoxy and finally polished to a shiny level. As the last step, the prepared samples were coated with a conductive carbon layer by evaporation deposition technique with heated carbon filament.

A.3.2 Transmission Electron Microscopy

A Transmission Electron Microscopy (TEM) analysis was performed for the synthesized Pt/Pd nano-particles on the Al_2O_3 support by dispersing a small amount of each powder in alcohol and then briefly treating it in an ultrasonic bath to obtain a good distribution of the powder particles. Then, by using an ultrasonic generator, a drop of the dispersion was nebulized onto a 3-mm-diameter copper TEM support mesh (Ted Pella, Inc., Item No. 01824) covered with a Lacey carbon film and, in addition, an ultra-thin carbon film (approximately $3\,\mathrm{nm}$ thick). TEM analyses were performed on a 200 kV FEI Tecnai Osiris microscope. The microscope has a thermally assisted field emission cathode (Schottky emitter) as an electron source. With the TEM Osiris, a point resolution of $0.24\,\mathrm{nm}$ can be achieved in high-resolution TEM imaging (HRTEM) at $200\,\mathrm{kV}$ accelerating voltage. The minimum probe diameter of the focused electron beam is $0.18\,\mathrm{nm}$, and this value also determines the maximum achievable resolution of scanning transmission electron microscopy (STEM) imaging. They were recorded with a

bright-field detector and with a ring-shaped dark-field detector for electrons scattered at wide angles (High-Angle Annular Dark Field - HAADF). The microscope is also equipped with a ChemiSTEM system including four silicon drift detectors (SDD) from Bruker, which allows chemical analysis by energy-dispersive X-ray spectroscopy (EDXS). TEM images were registered by a $2k \times 2k$ CCD camera (Gatan UltraScan 1000 P), and the image acquisition time for TEM bright-field images was typically $1\,\mathrm{sec}$ to $2\,\mathrm{sec}$. The digital micro-graph program (Gatan) was used for image acquisition. The size, shape, and distribution of both the metallic nanoparticles and the Al_2O_3 support particles were characterized using conventional TEM bright-field imaging and STEM imaging. An example of the structural nature of the material was also performed using HRTEM. For the analysis of the chemical composition and elemental distribution, the method combination STEM/EDXS was used. For this purpose, two-dimensional point-by-point spectra showing the qualitative elemental distribution were accumulated in the so-called Hypermap mode of the Bruker EDXS system. The measurement time was typically 10 to 25 min, and a possible drift of the sample area was automatically corrected by cross-correlation of reference images. The achievable lateral resolution is down to $1\,\mathrm{nm}$.

A.3.3 Physi- and Chemisorption

Physisorption was carried out with a 3Flex Series 3058 instrument from Micrometrics. The adsorption isotherm at 77 K for the catalyst support using the BET (Brunauer-Emmett-Teller) method can be expressed as [247]:

$$\frac{P/P_0}{a.(1-P/P_0)} = \frac{1}{a_m.c} + \frac{c-1}{c.a_m}.\frac{P}{P_0} \tag{A.7}$$

where the coefficient a quantifies the molar amount of adsorbate, while a_m represents the molar amount of an adsorbed monolayer. The dimensionless BET constant c describes the relationship between the adsorption energy of the first layer and the interaction between the adsorbate and adsorbent. In this case, the

coefficient a was determined through experimental measurement using a 5-point BET method.

$$a = \frac{a_m}{1/P/P_0} \tag{A.8}$$

The specific geometric surface area of the catalyst support can then be calculated using the following equation:

$$S_{BET} = \frac{a_m.N_A.S_0}{m_{cat}} \tag{A.9}$$

The mass of the catalyst, denoted as m_{cat}, was determined using two methods: (1) directly with powdered samples. The specific surface area of the catalyst denoted as S_0, was determined using N_2 adsorption measurements. The evaluation of pore size and pore size distribution was carried out using two different methods. The Dubinin-Radushkevich (DR) method was used for micropores, which are defined as pores with sizes less than $2\,\mathrm{nm}$, while the Barret-Joyner-Halenda (BJH) method was used for mesopores, which are pores with sizes ranging from $2\,\mathrm{nm}$ to $50\,\mathrm{nm}$. The DR method establishes a correlation between $\log(W)$ and $\log^2(p/p_0)$, resulting in a linearized isotherm based on the principles of micropore filling.

$$W = W_0.exp(-B.(\frac{T}{\beta})^2.log^2(p/p_0)) \tag{A.10}$$

In Equation A.3.3, W represents the total volume of the liquid adsorbate, W_0 represents the total volume of the micropores, B is a constant specific to the adsorbent, and b is a constant specific to the adsorbate. Extrapolation of Equation A.3.3 provides an estimate for the volume of the micropores, denoted as W_0. The presence of mesopores and the calculation of pore size distribution can be determined from hysteresis in adsorption isotherms. The BJH method uses a modified Kelvin equation to estimate the actual radius of a pore r_p, which is the sum of the Kelvin radius of a pore r_k and the thickness of the adsorbed film t:

$$r_p = r_k + t \tag{A.11}$$

The Kelvin equation provides a prediction of the pressure at which the adsorbate will undergo spontaneous condensation (and evaporation) in cylindrical pores with a specified size. The Rh dispersion was assessed using H_2 chemisorption on the same samples.

Rh/Pd-Pt dispersion in the catalysts was determined using pulse chemisorption of H_2 on an automatic analyzer (Micromeritics 3FLEX). A certain amount of sample was loaded in a reactor and reduced in pure H_2 $30\,\mathrm{mL\,min^{-1}}$ at $400\,^\circ\mathrm{C}$ for $1\,\mathrm{h}$. After reduction, the samples were purged with Ar ($30\,\mathrm{mL\,min^{-1}}$) at the same temperature for $1\,\mathrm{h}$ and then cooled down to $30\,^\circ\mathrm{C}$. Then, precise $1\,\mathrm{mL}$ pulses of a mixture of 10 vol.% of H_2 in Ar were injected into the reactor at 4-minute intervals. The Rh dispersion was calculated from the cumulative volume of H_2 adsorbed from all the pulses, and the Rh loading was determined by ICP-AES assuming an adsorption stoichiometry of H:Rh = 1:1 [248]. In order to calculate the dispersion of any noble metal into the catalyst the following relationship with assuming all particles in a spherical form has been considered [249]:

$$D = 6\frac{\nu_m/a_m}{d} \tag{A.12}$$

the variables in this equation are the volume occupied by an atom in the bulk metal (ν_m), the area occupied by a surface atom (a_m), and the particle diameter (d). For Rhodium (Rh), the ν_m and a_m are 13.78 $\mathrm{Å^3}$ and 7.58 $\mathrm{Å^2}$, respectively [249].

A.3.4 Rheometry

Examining the rheological properties and thixotropy of screen printing pastes is crucial for ensuring the uniformity of applied layers. For characteristics of the pastes, a rotating disk rheometer (Rheostress 1, Thermo Scientific, Haake, cone geometry C60/1 ° with a diameter of 60 mm and an angle of 1 °) at a temperature of 25 °C was used. The paste was positioned between the holder and the cone with a side angle of 1 °. A shear stress linear ramp ranging from 0.1 Pa to 1200 Pa was applied, and the resulting shear rate was recorded to generate a flow plot.

Thixotropic behavior was determined by measuring paste viscosity at various shear rates through a step function ($0.1\ \mathrm{sec}^{-1} \rightarrow 100\ \mathrm{sec}^{-1} \rightarrow 0.1\ \mathrm{sec}^{-1}$).

A.3.5 Profilometer

The layer thickness of the coated catalysts and also the surface roughness of the catalyst channels are estimated and mapped with a 3D optical profilometer (S-Neox, Sensofar) based on a light beam reflection from the object surface.

A.3.6 Inductively coupled plasma atomic emission spectroscopy

Inductively coupled plasma atomic emission spectroscopy (ICP-AES) was used to determine the elemental composition of the synthesized catalysts for CCR reaction. ICP-AES usually provides good detection limits and a wide linear range for most elements. The elements of Pd and Pt were determined by ICP-AES spectroscopy (iCAP 7600 DUO von Thermofisher Scientific). About 30 – 40 mg of the samples (accuracy ± 0.05 mg) was dissolved in 4 ml hydrochloric acid, 4 ml sulfuric acid, and 2 ml hydrogen peroxide at 523 K for 6 h in the pressure digestion vessel DAB-2 (Berghof). The analysis of the elements was accomplished with four different calibration solutions and an internal standard (Sc). The range of the calibration solutions did not exceed a decade. Three wavelengths of the elements have been used for calculation.

A.3.7 X-ray diffraction

X-ray diffraction (XRD) measurements were carried out for the co-planner (out of the plane, OP) orientation on a Bruker D8 Advance equipped with a position sensitive detector (PSD) Lynxeye in $\theta - \theta$ geometry, variable divergence slit, and 2.3° Soller-slit on the secondary side was used. The XRD data was acquired with

Cu $K\alpha 1$, 2-radiation (λ=0.154 018 nm). in order to determine the crystalline size, the Sherrer equation is described as follows:

$$d = \frac{k\lambda}{\beta \cos\theta} \tag{A.13}$$

Where d, k, λ, β, and θ are the mean size of crystalline, dimensionless shape factor, X-ray wavelength, line broadening at half the maximum intensity (FWHM), and Bragg angle, respectively.

A.3.8 Test reactor sketch

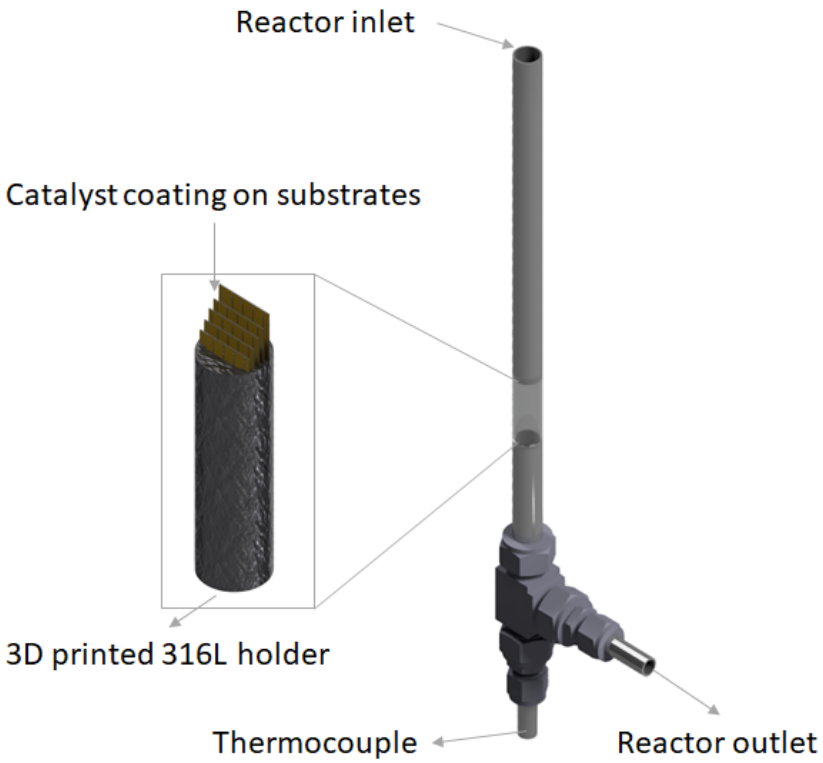

Figure A.3: Testing of coated catalysts of CCR for activity test in 3D-printed housing (holder) which is adjustable for small catalytic plates. The reactor is made of stainless steel 1.4435 suitable for testing up to 500 °C and 10 bar.

A.4 Autothermal membrane reformer

As part of the modeling procedure, mesh dependence is checked to select the optimal mesh size, ensuring high accuracy and low computation time.

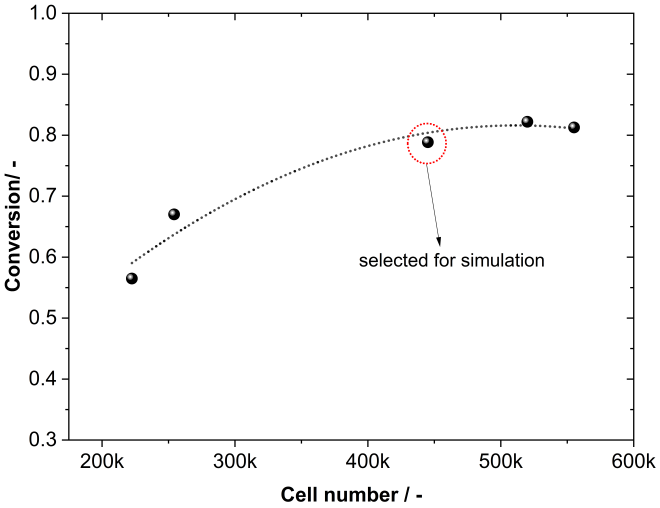

Figure A.4: Cell independence test for simulation of MR (Case A), see Section 6.6.2.

Evaluation of the performance of the modeled autothermal MR in this study, with variations in catalyst thickness and CH_4 flow rate in the CCR section.

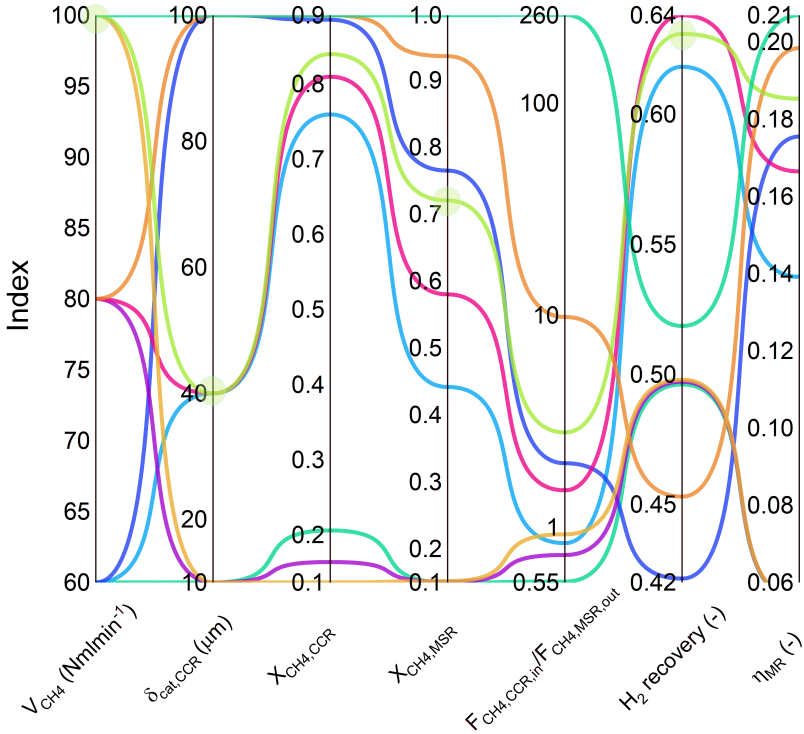

Figure A.5: Results of the simulation for a non-isothermal MR by changing flow rate of CH_4 and thickness of coating in CCR. The conditions are $W/F_{reforming}$ 1.80 $gr_{cat}h/mol$ and Sweep gas of N_2: 500 N mL min^{-1}, T_{inlet}=673 K, P_{ret}=1.5 bar, P_{perm}=1 bar, Air/CH_4:10 and S/C=3.

Table A.2: Results of the simulation for a non-isothermal MR by changing flow rate of CH_4 and thickness of coating in CCR. The conditions are $W/F_{reforming}$ 1.80 $gr_{cat}h/mol$ and Sweep gas of N_2: $500\,\mathrm{N\,mL\,min^{-1}}$, T_{inlet}=673 K, P_{ret}=1.5 bar, P_{perm}=1 bar, Air/CH_4:10 and S/C=3.

$CH_{4in,CCR}$ ($\mathrm{N\,mL\,min^{-1}}$)	$\delta_{cat,CCR}$ (μm)	$X_{CH_4,CCR}$ (-)	$X_{CH_4,MSR}$ (-)	ϕ_{H_2} (-)	Std. T (K)	DaPe (-)	η_{MR} (-)	$CH_{4in,CCR}/CH_{4out,MSR}$ (-)
60	10	0.21	0.15	0.50	8.55	0.98	0.06	0.55
60	40	0.76	0.44	0.62	32.75	0.94	0.14	0.84
60	100	0.89	0.77	0.42	29.57	0.86	0.18	2.01
80	10	0.16	0.15	0.50	8.23	0.99	0.06	0.74
80	40	0.81	0.58	0.64	42.74	0.81	0.17	1.50
80	100	0.89	0.94	0.45	39.86	0.74	0.20	9.83
100	10	0.14	0.15	0.50	8.00	0.99	0.06	0.93
100	40	0.84	0.72	0.63	49.22	0.67	0.19	2.81
100	100	0.89	1.00	0.52	59.05	0.59	0.21	261

Table A.3: CH_4 conversion and H_2 recovery, MR efficiency, and DaPe number. The conditions are $\delta_{cat,com}$:40 μm, combustion fuel flow of CH_4: 100 N mL min^{-1} $W/F_{reforming}$ 1.80 $gr_{cat}h/mol$ and Sweep gas of N_2: 100-1000 N mL min^{-1}, T_{inlet}=673 K, P_{ret}=1.5-6 bar, P_{perm}=1 bar, Air/CH_4:10 and S/C=3.

P (bar)	$N_{2in,sweep}$ (N mL min^{-1})	$CH_{4in,MSR}$ (N mL min^{-1})	$X_{CH_4,CCR}$ (-)	$X_{CH_4,MSR}$ (-)	$CH_{4in,CCR}/CH_{4out,MSR}$ (-)	ϕ_{H_2} (-)	η_{MR} (-)	DaPe (-)	Std. T (-)
1.5	100	75	0.90	0.90	13.06	0.43	0.12	0.41	48.15
1.5	100	125	0.82	0.63	2.09	0.34	0.10	0.31	42.88
1.5	100	250	0.58	0.27	0.55	0.19	0.04	0.28	32.52
3	100	75	0.92	1.00	742.66	0.52	0.16	0.28	75.94
3	100	125	0.89	0.83	4.75	0.31	0.12	0.31	55.84
3	100	250	0.83	0.49	0.79	0.18	0.06	0.30	43.90
6	100	75	0.96	1.00	61102.00	0.74	0.20	0.15	106.54
6	100	125	0.95	0.90	8.14	0.42	0.16	0.21	83.33
6	100	250	0.94	0.57	0.93	0.23	0.09	0.24	69.44
1.5	500	75	0.89	1.00	276.92	0.75	0.21	0.96	44.65
1.5	500	125	0.84	0.72	2.81	0.63	0.19	0.67	49.22
1.5	500	250	0.58	0.30	0.57	0.43	0.08	0.48	34.55
3	500	75	0.90	1.00	141220.00	0.81	0.23	0.36	88.00
3	500	125	0.88	0.92	9.43	0.49	0.19	0.40	57.39
3	500	250	0.82	0.54	0.87	0.31	0.11	0.37	41.33
6	500	75	0.96	1.00	1780600.00	0.93	0.25	0.17	116.91
6	500	125	0.95	0.97	24.17	0.58	0.23	0.24	88.34
6	500	250	0.93	0.61	1.05	0.34	0.13	0.27	70.38
1.5	1000	75	0.87	1.00	2912.50	0.86	0.25	1.24	42.11
1.5	1000	125	0.84	0.77	3.44	0.72	0.22	0.89	50.60
1.5	1000	250	0.57	0.31	0.58	0.52	0.10	0.59	35.48
3	1000	75	0.90	1.00	716350.00	0.88	0.26	0.39	91.11
3	1000	125	0.88	0.94	12.94	0.55	0.23	0.43	58.14
3	1000	250	0.82	0.55	0.90	0.36	0.13	0.39	40.29
6	1000	75	0.96	1.00	3185800.00	0.96	0.26	0.17	119.21
6	1000	125	0.94	0.98	39.05	0.64	0.25	0.25	90.07
6	1000	250	0.92	0.63	1.08	0.38	0.15	0.28	70.50

A.5 Additive manufacturing

Supplementary information for the AM Study of Crofer 22 APU.

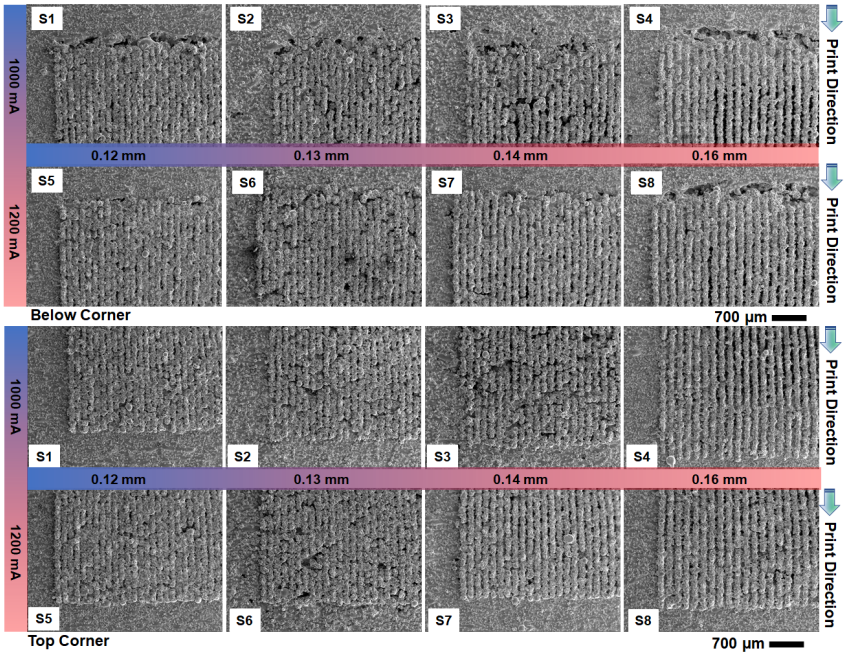

Figure A.6: Top view and cross-section view of printed samples with different hatch distances and laser power; dense/porous part connection on the edges (hatch distance 0.12-0.16 mm and laser current 1000-1200 mA).

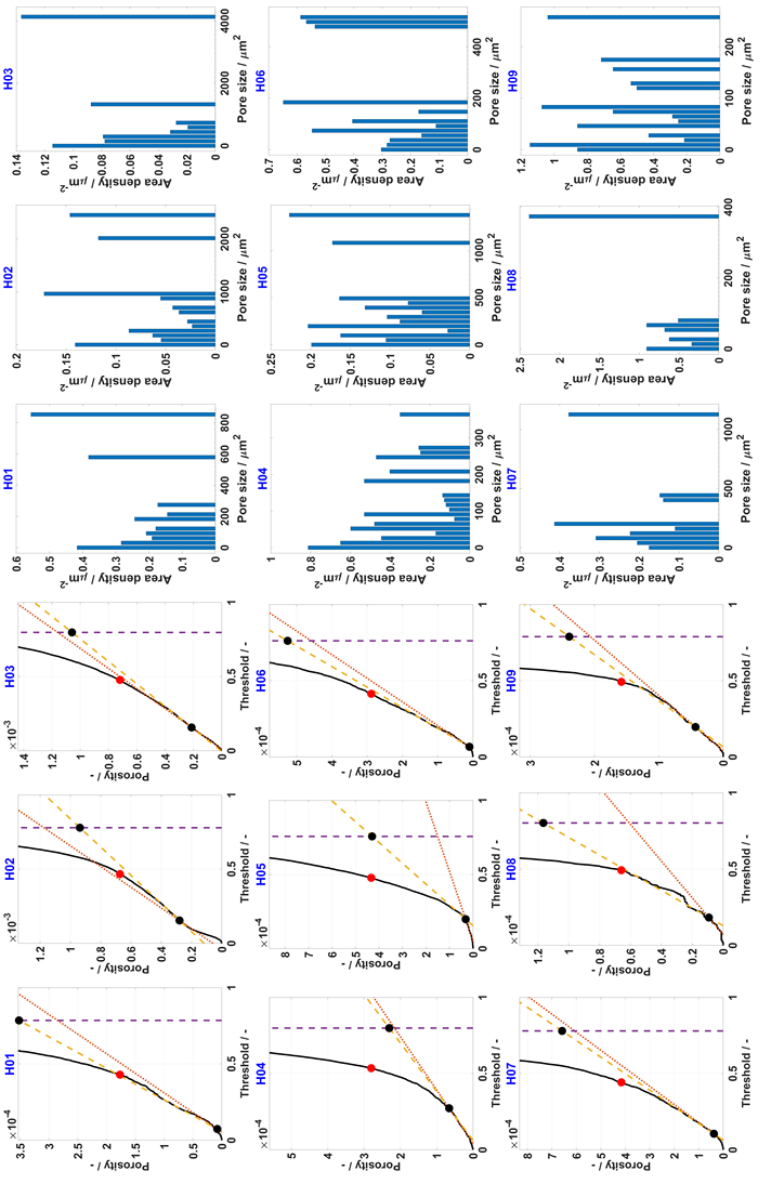

Figure A.7: Gas-tight wall parameter optimization for a PBF-LB/M object.

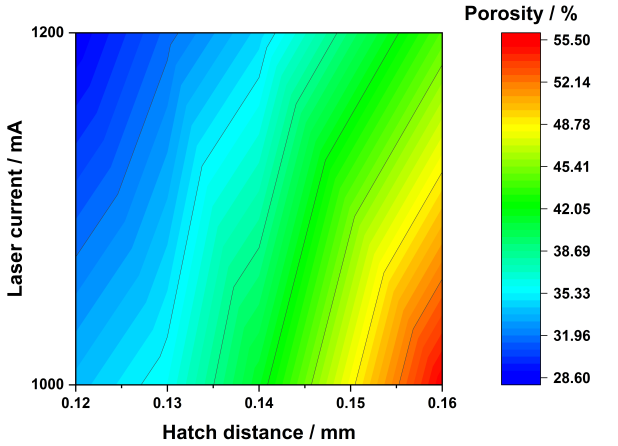

Figure A.8: Contour plot of the porosity dependency on hatch distance and laser current for porous part in this study (hatch distance 0.12-0.16 mm and laser current 1000-1200 mA).

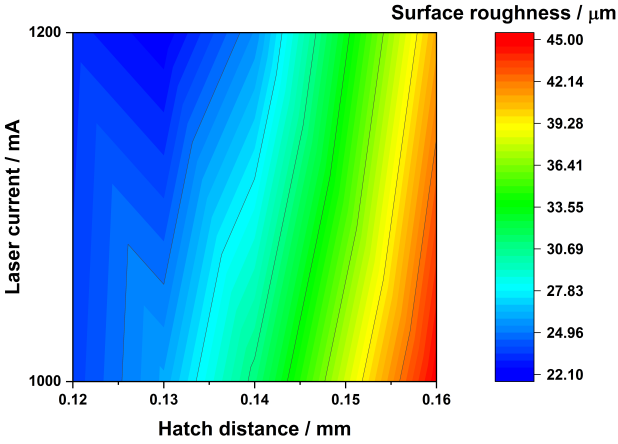

Figure A.9: Contour plot of the porous part surface roughness dependency on hatch distance and laser current in this study (hatch distance 0.12-0.16 mm and laser current 1000-1200 mA).

Table S1: Overview of the PBF-LB/M parameters. All objects were printed with hatch distance of $0.08\,\mathrm{mm}$ and layer thickness of $50\,\mu\mathrm{m}$. The parameters are shown in the Table as; Laser current L_C, point distance P_D, exposure time P_S, scan speed v_s, and volumetric energy density E_L.

	Hatch					Contour		
Sample	L_C (mA)	P_D (µm)	P_S (µs)	v_S ($\mathrm{mm\,s^{-1}}$)	E_L ($\mathrm{J\,mm^{-3}}$)	L_C (mA)	P_D (µm)	P_S (µs)
C01	2000	35	20	-	-	1000	30	20
C02	2000	35	20	-	-	1400	30	20
C03	2000	35	20	-	-	1400	40	20
C04	2000	35	20	-	-	1800	40	20
C05	2000	35	20	-	-	1800	15	20
C06	2000	35	20	-	-	1400	10	20
C07-90°	2000	35	20	-	-	1800	15	20
C08-90°	2000	35	20	-	-	1400	10	20
H01	1800	30	20	1.50	30.00	1400	15	20
H02	1800	30	20	1.50	30.00	1800	15	20
H03	1800	30	20	1.50	30.00	1400	10	20
H04	1900	35	20	1.75	27.14	1400	15	20
H05	1900	35	20	1.75	27.14	1800	15	20
H06	1900	35	20	1.75	27.14	1400	10	20
H07	2000	35	20	1.75	28.58	1400	15	20
H08	2000	35	20	1.75	28.58	1800	15	20
H09	2000	35	20	1.75	28.58	1400	10	20

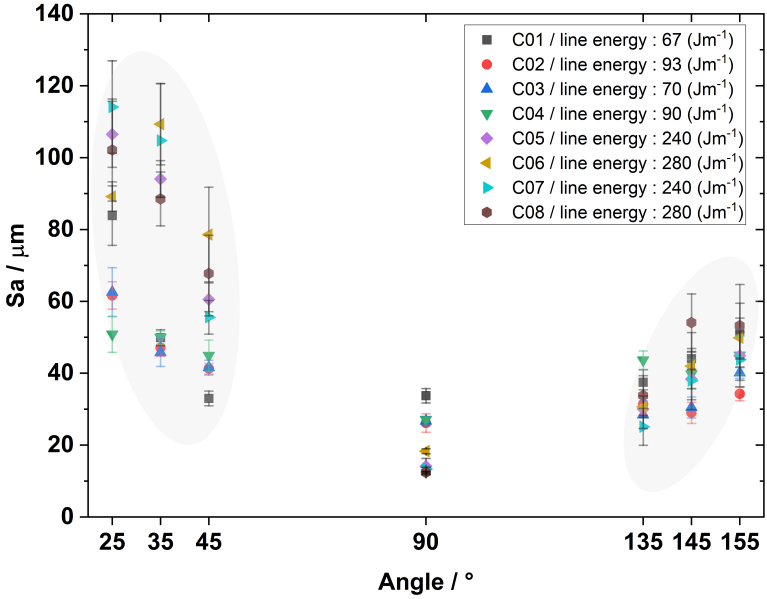

Figure A.10: The line energy effect on the surface roughness (S_a) for different down-facing/up-facing angles. The line energy is calculated based on the power per scan speed (see Table S1).

List of Figures

2.1 Schematic illustration of the methane steam reforming process, used with permission from Springer [16]. 5

2.2 A) Equilibrium constants for reactions 2.1, 2.2, and 2.3 were determined as a function of temperature at a pressure of 1 bar. B) Mole fractions and CH_4 conversion of the components at equilibrium condition P:1 bar S/C:3 versus temperature. C) at constant temperature of 823 K and S/C:3 versus pressure. 9

3.1 Illustration representing the four transport mechanisms through a porous membrane: (a) Knudsen diffusion, (b) surface diffusion, (c) capillary condensation, and (d) molecular sieving. This figure was regenerated according to reference [41]. 19

3.2 Diffusion model for hydrogen in metals according to Kehr's theory. This figure was regenerated according to reference [42]. . . . 20

3.3 Phase diagram of palladium hydride as a function of pressure and temperature. Adapted from [59]; based on the original data from [60]. 25

3.4 Images depicting the configuration of the catalyst-membrane assembly within the reformer tubes of the pilot membrane reformer operating with molten salt heating are presented. These images include a close-up perspective of the catalyst/membrane assembly (a), a lateral view (b), an overhead view (c), and a rearview that showcases the sealed end of the tubular membrane (d) [82] (re-printed with permission from Elsevier). 32

3.5 Photography of the membrane modules: (a) 13 tubular palladium membranes supported by alumina, (b) 5 plate PdAg (palladium-silver) membranes, (c) 3 tubular PdAg membranes supported by alumina [102]. 39

3.6 The evolution of the μ-EnH_2ancer from version V 1.0 to V 3.0 is marked by notable changes. In the case of V 1.0, testing was conducted under isothermal conditions. However, for version V 2.0, the focus shifted to incorporating a combustion plate reactor into the design, and V 3.0 aimed at increasing the area of reacting surface to volume of the module. 42
3.7 Different strategies to supply the heat needed for MSR. 44
4.1 (a) Schematic of the tape-casting process for the fabrication of porous metallic substrates using Crofer 22 APU slurry, (b) Top view of the sintered tape-cast substrate after being treated under Ar at 1150 °C for 3 hours. 51
4.2 Schematic representation outlining the setup of the test apparatus for conducting experiments on the permeation of gases. 53
4.3 Schematic representation of the SPS (or APS) technique under atmospheric pressure (top) and VPS using dry powder of Pd (bottom) for preparation of Pd composite membranes [150]. 57
4.4 SEM images of the powders were captured using a voltage of 20 kV, a current of 1.6 nA, and an ETD detector. These images illustrate the average particle characteristics of the (a) Daiken Chemicals Pd powder, (b) C. Hafner powder, and (c) presents the EDX analysis of the powders, revealing insights into their purity levels [150]. 58
4.5 SEM images APS and VPS samples with a 30 kV, 1.6 nA beam. The surface morphology illustrates the layer roughness for SPS (a) and VPS (c) samples. Cross-sectional views of the SPS (b) and VPS (d) layers were also analyzed. Additionally, a backscattered detector cross-section image (e) and EDX elemental mapping analysis (f) were conducted for the SPS sample [150]. 60
4.6 a) SEM images of the VPS samples with a 20 kV, 1.6 nA beam. This sample is the delaminated layer of Pd, lamella prepared for TEM analysis. b) Elemental mapping is shown as line and point in this Figure for the Pd layer and bottom of the Pd layer, respectively. 61

4.7 TEM analysis was conducted on two grains with distinct orientations in the APS sample [150]. 62
4.8 TEM bright field images of the samples are depicted in (a) and (d). Many dark field images of the coatings, superposed with different colors indicating various orientations and grain sizes, are shown in (b) and (e). The SADP of each sample, confirming the presence of pure palladium, are presented in (c) and (f) [150]. . 63
4.9 Gas test with N_2 at room temperature for samples of APS, VPS, metallic porous substrate of Crofer 22 APU (denoted as sinter metal), and dip-coated substrate with 8-YSZ. 64
4.10 Gas test results for sample TMC-5 (APS) at T:723 K, for single gases of H_2 and N_2. For comparison, the results of the test module studied by Tim Boeltken [141] tested at 673 K is shown in the graph. 66
4.11 SEM analysis of TMC-5 with different magnification and views for before and after gas test of N_2 and H_2 at 723 K. Cracks were found after the assembly based on the images from the surface and cross-section view. 67
4.12 Results of the welded pieces of Crofer 22 APU to Pd-membrane based on the numbers listed in Table 4.4. 72
4.13 Results of the welded pieces of SS-316L to Pd-membrane based on the numbers listed in Table 4.4. 74
4.14 Flux of H_2 gas versus pressure difference of retentate and permeate side with power of 0.5 for modules TMF-1 and TMF-3 at 623.15 K. 76
4.15 Estimation of activation energy and permanence coefficient based on an Arrhenius plot for sample TMF-1. 77
4.16 Cross-section view of samples TMF-1 and TMF-3 after gas test for estimation of the size of each layer. 79

5.1 Potential reaction pathways for MSR as outlined by Niu et al. [167]. The reaction network for MSR is segmented into five parts: H_2O dissociation (enclosed in a dashed green rectangle), CH_4 dissociation (enclosed in a dashed red rectangle), CH oxidation (enclosed in a dashed orange rectangle), C oxidation (enclosed in a dashed light blue rectangle), and H_2 formation (enclosed in a dashed dark blue rectangle). (reprinted with permission from Elsevier). 82
5.2 Schematic of FSP system for synthesis of catalyst in this study. The left drum shows the batch configuration and the right drum shows the semi-continuous configuration. 84
5.3 The flowchart showing the procedure for catalyst preparation for MSR and CCR in this study. 85
5.4 High-angle annular dark-field scanning transmission electron microscopy (HAADF-STEM) images were captured for 1RhSAL catalyst (up). The SAL particle size seen by STEM images (down). . 88
5.5 The XRD patterns of different loading of Pd onto SAL and FAL for as prepared catalysts by FSP. 91
5.6 The XRD patterns of different loading of Pt onto 1.5PdSAL for as prepared catalysts by FSP. 92
5.7 TEM images of 1.5PdSAL with different magnifications and elemental mapping. 93
5.8 TEM images of 1.5PdFAL with different magnifications and elemental mapping. 94
5.9 N_2 adsorption-desorption isotherms (top) and porse size distribution (bottom) for samples 1.5PdSAL and 1RhSAL in the fresh mode and after calcination at $550\,^{\circ}\mathrm{C}$. It should be noted that the isotherms for the 1RhSAL sample are shifted upwards by 50 units to clearly distinguish the results within a single graph. 95
5.10 Flowchart of the paste preparation and coating with screen printing. . 98
5.11 Cross sectional view and surface view of the coated catalyst of 1RhSAL into the microchannels with screen printing technique. . . . 99
5.12 Cross sectional view and surface view of the coated catalyst of 1.5Pd1.5PtSAL into the microchannels with screen printing technique.100

5.13 Rheological properties of the pastes prepared based on 1RhSAL and 1.5Pd1.5PtSAL catalysts for screen printing; (A) shear stress and viscosity versus shear rate, (B) shear rate and viscosity versus time. 102
5.14 Test rig flow diagram for a microchannel reactor used for catalyst activity tests for MSR and CCR in this work. 104
5.15 CH_4 conversion versus time on stream for catalyst 1PdAl-comm at P_{abs}:1 bar, Air/CH_4:10, W/F:0.0064 $gr_{cat}.min/ml_{CH_4}$. 108
5.16 CH_4 conversion versus temperature for catalyst 1.5PdSAL at P_{abs}:1 bar, Air/CH_4:10, W/F:0.0082 $gr_{cat}.min/ml_{CH_4}$. 109
5.17 CH_4 conversion; (A) versus time for (B) against temperature catalyst; for 1.5PdSAL and 1.5Pd1.5PtSAL , P_{abs}:1 bar, Air/CH_4:10, W/F:0.0082 $gr_{cat}.min/ml_{CH_4}$. 110
6.1 The top illustration depicts the stacking principle of the modular microstructured membrane reactor, while the bottom schematic showcases the channel configuration within the microchannel membrane module, highlighting heat integration through combustion. 115
6.2 The diagram illustrating the flow scheme of the test rig utilized to experimentally assess the μ-EnH_2ancer V 3.0. 117
6.3 Assembly procedure for μ-EnH_2ancer V 3.0 plates: a) Integration of all plates, a porous substrate (Crofer 22 APU), and a 12.5 μm Pd foil. b) Foil cracking occurred during the He test due to mechanical force applied during rubber tightening. c) Successful testing and coupling of the reactor without the membrane part in this configuration. 119
6.4 MSR test at μ-EnH_2ancer V 3.0 plates: A) conversion of CH_4 versus temperature B) Dry gas molar fraction of the gases C) CO selectivity and CO_2 selectivity versus temperature D) 2D model validation against experiments. The 2D model was simulated based on the kinetics of Halabi et. al and Xu, Froment at S/C:3.7 and W/F:1.53 $\mathrm{gr_{cat}\,h/mol_{CH_4}}$. 121

6.5 MSR test at μ-EnH_2ancer V 3.0 plates: A) conversion of CH_4 versus temperature for different N_2 flow rates B) conversion of CH_4 along the reactor length for kinetics of Halabi et al. and Xu, Froment (simulation) at T:808 K, S/C:3.7 W/F:1.53 $\mathrm{gr_{cat}\,h/mol_{CH_4}}$, C) conversion and CO selectivity versus S/C ratio T:808 K, P:1 bar, W/F:1.53 $\mathrm{gr_{cat}\,h/mol_{CH_4}}$. 123
6.6 Air distributor plate used in the CCR test for controlling the heat reduce along the reactor bed. 124
6.7 CCR test at μ-EnH_2ancer V 3.0 plates: A) conversion of CH_4 and mole fraction of the dry gas in the outlet of the reactor for 40$CH_4$600Air ($\mathrm{N\,mL\,min^{-1}}$), W/F:3.85 $\mathrm{gr_{cat}\,h/mol_{CH_4}}$ B) simulation results against experiments C) effect of air to CH_4 versus temperature for different Air to CH_4 ratios D) Conversion versus at different temperatures versus W/F:3.85-15.4 $\mathrm{gr_{cat}\,h/mol_{CH_4}}$. Tests were carried out at atmospheric pressure. . . 126
6.8 Effect of air for tests carried out at A) conversion of CH_4/mole fraction of the gases (dry basis) 5$CH_4$75Air ($\mathrm{N\,mL\,min^{-1}}$), W/F:30 $\mathrm{gr_{cat}\,h/mol_{CH_4}}$, and B) conversion of CH_4 versus temperature and Air to CH_4 ratios. 127
6.9 Mole fraction of O_2 in mixture of CH_4 and air with different flow rates of 5CH_4-75Air, 80CH_4-320Air, and 60CH_4-340Air $\mathrm{mL\,min^{-1}}$ where no reaction term is considered. 129
6.10 Velocity vector in direction of the micro-hole depths of O_2 in mixture of CH_4 and air with different flow rates of 5CH_4-75Air, 80CH_4-320Air, and 60CH_4-340Air $\mathrm{mL\,min^{-1}}$ where no reaction term is considered. 131
6.11 A graphical representation of the stacked cells of the autothermal membrane reformer and a cross view of one cell for a 2D modeling. . 133

6.12 Validation of 2D simulation vs experimental results μ-EnH_2ancer V 1.0 [205] under assumed isothermal condition. A) CH_4 conversion (left axis) and CO selectivity (right axis) against residence time (W/F), B) CH_4 conversion versus hydrogen recovery. C) CH_4 conversion (left axis) and CO selectivity (right axis) against pressure difference (bar) at W/F 0.33 $\mathrm{gr_{cat}\,h/mol_{CH_4}}$ D) hydrogen recovery and flux of permeated H_2 against pressure difference (bar) at W/F 0.33 $\mathrm{gr_{cat}\,h/mol_{CH_4}}$ and without sweep gas. Operating conditions are T=773 K, P_{ret}=6 (A,B), P_{perm}=1 bar and S/C=3. The solid lines, dashed lines, and points present the 2D simulation results, equilibrium curves, and experiments, respectively. 146

6.13 Results of the simulation for a non-isothermal MR by changing flow rate of CH_4 and thickness of coating in CCR. The conditions are $W/F_{reforming}$ 1.80 $gr_{cat}h/mol$ and Sweep gas of N_2: $500\,\mathrm{N\,mL\,min^{-1}}$, T_{inlet}=673 K, P_{ret}=1.5 bar, P_{perm}=1 bar, Air/CH_4:10 and S/C=3. 150

6.14 Temperature profile of different sections of the autothermal MR for different flow rates of fuel (CH_4) at combustion section A) Combustion section, B) Pre-reforming section, C) Reforming section, and D) Permeate section and temperature profile of the whole geometry. The conditions are $W/F_{reforming}$ 1.80 $\mathrm{gr_{cat}\,h/mol_{CH_4}}$ and Sweep gas of N_2: $500\,\mathrm{N\,mL\,min^{-1}}$, $\delta_{\text{cat,CCR}}$: 40 μm, T_{inlet}=673 K, P_{ret}=1.5 bar, P_{perm}=1 bar, Air/CH_4:10 and S/C=3. 152

6.15 Temperature profile of different sections of the autothermal MR for different coating thicknesses at combustion section A) Combustion section, B) Pre-reforming section, C) Reforming section, and D) Permeate section and temperature profile of the whole geometry. The conditions are $W/F_{reforming}$ 1.80 $gr_{cat}h/mol$ and Sweep gas of N_2: $500\,\mathrm{N\,mL\,min^{-1}}$, F_{CH4}:100 $\mathrm{N\,mL\,min^{-1}}$, T_{inlet}=673 K, P_{ret}=1.5 bar, P_{perm}=1 bar, Air/CH_4:10 and S/C=3. 154

6.16 CH_4 conversion and CO selectivity of MSR for different flow rates of fuel (CH_4) at combustion section A) conversion in pre-reforming section, B) conversion in reforming section, C) selectivity in pre-reforming section, and D) selectivity in reforming section. The conditions are $W/F_{reforming}$ 1.80 $gr_{cat}h/mol$ and Sweep gas of N_2: 500 Nml/min, $\delta_{\text{cat,CCR}}$: 40 μm, T_{inlet}=673 K, P_{ret}=1.5 bar, P_{perm}=1 bar, Air/CH_4:10 and S/C=3. 155

6.17 CH_4 conversion and CO selectivity of MSR for different coating thicknesses at combustion section A) conversion in pre-reforming section, B) conversion in reforming section, C) selectivity in pre-reforming section, and D) selectivity in reforming section. The conditions are $W/F_{reforming}$ 1.80 $gr_{cat}h/mol$ and Sweep gas of N_2: 500 N mL min^{-1}, F_{CH4}:100 N mL min^{-1}, T_{inlet}=673 K, P_{ret}=1.5 bar, P_{perm}=1 bar, Air/CH_4:10 and S/C=3. . 156

6.18 Time scales for different fuel flow rates and CR coating thicknesses. The conditions are $\delta_{cat,com}$:10-100 μm, combustion fuel flow of CH_4: 60-100 N mL min^{-1} $W/F_{reforming}$ 1.80 $gr_{cat}h/mol$ and Sweep gas of N_2: 100-500 N mL min^{-1}, T_{inlet}=673 K, P_{ret}=1.5-2.5 bar, P_{perm}=1 bar, Air/CH_4:10 and S/C=3. 158

6.19 CH_4 conversion and H_2 recovery, MR efficiency, and DaPe number. The conditions are $\delta_{cat,com}$:40 μm, combustion fuel flow of CH_4: 100 N mL min^{-1} $W/F_{reforming}$ 1.80 $gr_{cat}h/mol$ and Sweep gas of N_2: 100-1000 N mL min^{-1}, T_{inlet}=673 K, P_{ret}=1.5-6 bar, P_{perm}=1 bar, Air/CH_4:10 and S/C=3. 159

6.20 Effect of sweeping gas N_2 flow rate at conditions of $\delta_{cat,com}$:40 μm, combustion fuel flow of CH_4: 100 N mL min^{-1} $W/F_{reforming}$ 3 $\text{gr}_{\text{cat}}\,\text{h}/\text{mol}_{\text{CH}_4}$ and Sweep gas of N_2: 100-1000 N mL min^{-1}, T_{inlet}=673 K, P_{ret}=6 bar, P_{perm}=1 bar, Air/CH_4:10 and S/C=3. . . 161

6.21 Effect of pressure of MSR at conditions of $\delta_{cat,com}$:40 μm, combustion fuel flow of CH_4: 100 N mL min^{-1} $W/F_{reforming}$ 3 $\text{gr}_{\text{cat}}\,\text{h}/\text{mol}_{\text{CH}_4}$ and Sweep gas of N_2: 1000 N mL min^{-1}, T_{inlet}=673 K, P_{perm}=1 bar, Air/CH_4:10 and S/C=3. 162

6.22 Comparison of different configurations for CR, Case A: base case where air and fuel are pre-mixed with uniform coated layer, Case B: pre-mixed inflow with uniform segmented catalyst layer, Case C: additively manufactured porous segments for air distribution along the CR with descending design, and Case D: additively manufactured porous segments with ascending design. 164
6.23 Results of the simulated configurations of CCR, A) Temperature in the gas channel (fuel section) along the reactor, B) CH_4 conversion of CCR, and C) velocity magnitude in the center-line of fuel channel. The conditions are $\delta_{cat,com}$:40 μm, combustion fuel flow of CH_4: 100 $\mathrm{N\,mL\,min^{-1}}$ $W/F_{reforming}$ 3 $\mathrm{gr_{cat}\,h/mol_{CH_4}}$ and Sweep gas of N_2: 1000 $\mathrm{N\,mL\,min^{-1}}$, T_{inlet}=673 K, P_{ret}=6 bar, P_{perm}=1 bar, Air/CH_4:10 and S/C=3. . . 165
6.24 Results of the simulated configurations of CR, A) Temperature in gas channel (fuel section) along the reactor, B) CH_4 conversion of CR, C) concentration ratio of O_2 to CH_4, and D) velocity magnitude in the center-line of fuel channel. The conditions are $\delta_{cat,com}$:40 μm, combustion fuel flow of CH_4: 100 $\mathrm{N\,mL\,min^{-1}}$ $W/F_{reforming}$ 3 $\mathrm{gr_{cat}\,h/mol_{CH_4}}$ and Sweep gas of N_2: 1000 $\mathrm{N\,mL\,min^{-1}}$, T_{inlet}=673 K, P_{ret}=6 bar, P_{perm}=1 bar, Air/CH_4:10 and S/C=3. 168
7.1 Cross-sectional view of a composite Pd membrane consisting of porous sinter metal of Crofer 22 APU, 8YSZ diffusion barrier layer, and Pd layer (selective towards hydrogen) for hydrogen separation from a gas mixture. More details regarding the Pd coating can be found in [150]. 172
7.2 Comparison of preparation of planar metal-based membrane support through PBF-LB/M and tape-casting plus welding techniques. 174
7.3 Particle size distribution of the Crofer 22 APU powder. 177

7.4 Sample for the evaluation of surface roughness of AM Crofer 22 APU, (a) Front view of manufactured test pieces showing all three printed angles $25°$, $35°$ and $45°$, (b) isometric view of printed test pieces and (c) view of down-facing surface of all test pieces (the schematic was reprinted with permission from Elsevier) [229]. 180
7.5 Top view and cross-sectional view of printed samples with different hatch distances and laser power (hatch distance 0.12-$0.16\,\mathrm{mm}$ and laser current 1000-$1200\,\mathrm{mA}$). 182
7.6 Water permeability of additively manufactured samples, the effect of hatch distance ranging from $0.12\,\mathrm{mm}$ to $0.16\,\mathrm{mm}$, a: Laser current $1000\,\mathrm{mA}$, b: $1200\,\mathrm{mA}$. 185
7.7 Heat treatment under Air atmosphere for sample S5, at $800\,°\mathrm{C}$ for $2\,\mathrm{h}$. 187
7.8 Deposition weight records versus number of screen printing jobs for printed samples S1-S8 (hatch distance $0.12\,\mathrm{mm}$ to $0.16\,\mathrm{mm}$ and laser current $1000\,\mathrm{mA}$ to $1200\,\mathrm{mA}$). 190
7.9 Surface view of coated samples with 8-YSZ with screen-printing technique (hatch distance $0.12\,\mathrm{mm}$ to $0.16\,\mathrm{mm}$ and laser current $1000\,\mathrm{mA}$ to $1200\,\mathrm{mA}$). 191
7.10 Top) Cross view of coated samples S1-S8; with magnification 50X, Bottom) The effect of paste penetration when printing is shown (hatch distance $0.12\,\mathrm{mm}$ to $0.16\,\mathrm{mm}$ and laser current $1000\,\mathrm{mA}$ to $1200\,\mathrm{mA}$). 192
7.11 One-go printing of integrated plates of an MR with PBF-LB/M technique (No. 4-9); printing the composite plates of porous-dense (No. 11), thickness of 3 mm. 194
7.12 An ultra-compact planar catalytic reactor composed of catalytic plates designed for CCR. 195
7.13 Additively manufactured Crofer 22 APU parts for a high-temperature reaction like catalytic combustion ; (a) special design for air distribution to avoid the hot spot formation, (b) design for distributing air along the catalyst bed (fuel channel) to distribute the heat along the reactor channel, (c) micro-packed bed with porous pillars (for air diffusion) for catalyst loading. 196

A.1 Thermal expansion coefficients of different components of a composite pd membrane. 205
A.2 Membrane adaptor sketch for gas test of the synthesized Pd membrane for lab test. 206
A.3 Testing of coated catalysts of CCR for activity test in 3D-printed housing (holder) which is adjustable for small catalytic plates. The reactor is made of stainless steel 1.4435 suitable for testing up to $500\,^{\circ}\mathrm{C}$ and 10 bar. 213
A.4 Cell independence test for simulation of MR (Case A), see Section 6.6.2. 214
A.5 Results of the simulation for a non-isothermal MR by changing flow rate of CH_4 and thickness of coating in CCR. The conditions are $W/F_{reforming}$ 1.80 $gr_{cat}h/mol$ and Sweep gas of N_2: $500\,\mathrm{N\,mL\,min^{-1}}$, T_{inlet}=673 K, P_{ret}=1.5 bar, P_{perm}=1 bar, Air/CH_4:10 and S/C=3. 215
A.6 Top view and cross-section view of printed samples with different hatch distances and laser power; dense/porous part connection on the edges (hatch distance 0.12-$0.16\,\mathrm{mm}$ and laser current 1000-$1200\,\mathrm{mA}$). 218
A.7 Gas-tight wall parameter optimization for a PBF-LB/M object. . . . 219
A.8 Contour plot of the porosity dependency on hatch distance and laser current for porous part in this study (hatch distance 0.12-$0.16\,\mathrm{mm}$ and laser current 1000-$1200\,\mathrm{mA}$). 220
A.9 Contour plot of the porous part surface roughness dependency on hatch distance and laser current in this study (hatch distance 0.12-$0.16\,\mathrm{mm}$ and laser current 1000-$1200\,\mathrm{mA}$). 220
A.10 The line energy effect on the surface roughness (S_a) for different down-facing/up-facing angles. The line energy is calculated based on the power per scan speed (see Table S1). 222

List of Tables

2.1 Overview of key benefits and drawbacks of major hydrogen production technologies available in the market [16]. 6
3.1 Comparison of the commercial small reformer units after [36, 37]. . . 12
3.2 Characteristics of the different types of hydrogen-selective membranes, derived from Kluiters [38]. 14
3.3 Crystallographic information for metals with FCC and BCC structures [43]. 22
3.4 Hydrogen permeability in certain metals and the corresponding enthalpy for hydride formation. 23
3.5 Palladium-based supported membranes that were produced for the prototype membrane reactors [79]. 37
3.6 Characteristics of the μ-EnH_2ancer generations developed at IMVT. . 41
4.1 The thermal expansion coefficient of the principal elements in a metallic composite, Pd-based membrane designed for H_2 separation. . 52
4.2 Samples of Pd-composite membranes prepared with plasma spraying coating with two techniques of APS and VPS in this study. 65
4.3 Compositions and physical properties of the material used in parameter study for laser welding in this section. 71
4.4 Integration of Pd23Ag ($5\,\mu$m, SINTEF) to Crofer 22 APU and SS 316L via laser welding. 71
4.5 Leak test of the welded modules at different stages. 73
4.6 Module specification for the samples of TMF-1 and TMF-3. 75

4.7 Review of the experimental gas test results for Pd membranes in literature and this study as a comparison. $P_{H_2,perm}$: 101.3 kPa id permeate side was atmospheric pressure and no other stand in the paper. CR: cold-rolled, CHF: ceramic hollow fiber, ELP: electroless plating, MC: microchannel, PSS: porous stainless steel. 78
5.1 Charactersitics of the 1Rh/SAL based on the H_2 chemisorption and TEM analysis. 89
5.2 Prepared catalysts with different loadings of Pd and Pt onto SAL and FAL for CCR. 90
5.3 Chemical composition of Crofer 22 APU in [%] by min. and max. by specification [137] and analysis of the virgin powder. 105
6.1 Parameters applied for laser welding of μ-EnH_2ancer V 3.0 components. 118
6.2 Parameters for catalyst characteristics implemented in prototype reactor. 120
6.3 Physical properties of the porous parts (coated catalysts and printed Crofer 22 APU) used for simulation. 139
6.4 Arrhenius kinetic parameters. 141
6.5 Van't Hoff adsorption parameters 142
7.1 Chemical composition of Crofer 22 APU in [%], min. and max. by specification [137] and analysis of the virgin powder. 176
7.2 Arithmetical mean height of the surface Sa of additive manufactured Crofer 22 APU with a surface angle α to the build plate. 180
7.3 Process parameters for dense part printing with Crofer 22 APU powder. 181
7.4 Calculated surface properties of the porous parts (hatch distance 0.12-0.16 mm and laser current 1000-1200 mA). 187
A.1 Composition changes of reactions for a basis of 1 mole of CH_4 and SC as the steam to methane ratio for SR and WGS 204
A.2 Results of the simulation for a non-isothermal MR by changing flow rate of CH_4 and thickness of coating in CCR. The conditions are $W/F_{reforming}$ 1.80 $gr_{cat}h/mol$ and Sweep gas of N_2: 500 N mL min^{-1}, T_{inlet}=673 K, P_{ret}=1.5 bar, P_{perm}=1 bar, Air/CH_4:10 and S/C=3. 216

A.3 CH_4 conversion and H_2 recovery, MR efficiency, and DaPe number. The conditions are $\delta_{cat,com}$:40 μm, combustion fuel flow of CH_4: 100 $\mathrm{N\,mL\,min^{-1}}$ $W/F_{reforming}$ 1.80 $gr_{cat}h/mol$ and Sweep gas of N_2: 100-1000 $\mathrm{N\,mL\,min^{-1}}$, T_{inlet}=673 K, P_{ret}=1.5-6 bar, P_{perm}=1 bar, Air/CH_4:10 and S/C=3. 217

S1 Overview of the PBF-LB/M parameters. All objects were printed with hatch distance of $0.08\,\mathrm{mm}$ and layer thickness of $50\,\mu\mathrm{m}$. The parameters are shown in the Table as; Laser current L_C, point distance P_D, exposure time P_S, scan speed v_s, and volumetric energy density E_L. 221

List of Publications

Journal articles

- Masoud Mahmoudizadeh, Christoph Klahn, and Roland Dittmeyer. Powder bed fusion of solid and permeable crofer 22 apu parts for applications in chemical process engineering. Progress in Additive Manufacturing, DOI:10.1007/s40964-024-00811-w.
- Masoud Mahmoudizadeh, Christoph Klahn, and Roland Dittmeyer. Innovative autothermal reactor design via additive manufacturing: Optimization of catalytic exothermic reactions using porous media for heat management. Procedia CIRP, DOI:10.1016/j.procir.2024.04.011.
- Masoud Mahmoudizadeh, Michael Rubin, and Roland Dittmeyer. Simulation study of a compact autothermal membrane reformer for hydrogen production. Submitted.
- Efi Hadjixenophontos, Masoud Mahmoudizadeh, Michael Rubin, Dirk Ullmer, Fatemeh Razmjooei, Alexander C Hanf, Jan Brien, Roland Dittmeyer, and Asif Ansar. Palladium membrane with high density of large-angle grain boundaries to promote hydrogen diffusivity. Membranes, DOI: 10.3390/membranes12060617.

Conference talks

- Masoud Mahmoudizadeh, Dongxu Xie, Paul Kant, Martin Bram, Efi Hadjixenophontos, Fatemeh Razmjooei, Drik Ullmer, Asif Ansar, Michael Klumpp, and Roland Dittmeyer. Micro membrane reactor for methane steam reforming–concept and preparation of the porous metal supported pd-membrane sandwich structure. The 16th International Conference on Inorganic Membranes (ICIM 16), Taiwan, 2022.
- Masoud Mahmoudizadeh, Christoph Klahn, and Roland Dittmeyer. Innovative autothermal reactor design via additive manufacturing: Optimization of catalytic exothermic reactions using porous media for heat management. 34thCIRP Design Conference, Cranfiled, 2024.

Book chapter

- T. Gietzelt, M. Mahmoudizahdeh, T. Wunsch and R. Dittmeyer, Chapter 10. Laser Welding for Micro Process Devices, A Guide to Laser Welding, Manuel de Bastos Pereira, António and Vaz Marques, Eva Soledade and Gomes da Silva, Francisco José, Nova Science Publishers, DOI: 10.52305/MCBI4234.

Patent application

- T. Gietzelt, M. Mahmoudizadeh, R. Dittmeyer, T. Wunsch and J. Näther, Non-Pd metallic composite membranes for H_2 separation from gas mixtures, EM24018.

Master thesis

As part of this work, the author has initiated and supervised following thesis

- Schahrsad Arpanahsadeh, Development of a Method for Synthesis and Coating of Pd/Pt-Based Catalysts for Catalytic Combustion of Methane, Master thesis, 2021.

Other publications

- Mahmoudizadeh et al., Development of a replaceable microreactor coated with a CuZnFe nanocatalyst for methanol steam reforming, Chemical Engineering & Technology, DOI:10.1002/ceat.201500101.
- Mahmoudizadeh et al., A performance study on the electrocoating process with a CuZnAl nanocatalyst for a methanol steam reformer: the effect of time and voltage, RSC Advances, DOI:10.1039/C5RA18371E.
- Roshan et al., Single-stage water gas shift reaction over structural modified Cu–Ce catalysts at medium temperatures: Synthesis and catalyst performance, Chem. Eng. Res. Des, DOI:10.1016/j.cherd.2018.02.038.

Permissions

This thesis includes content reproduced with friendly permission from Springer Nature and Elsevier. Specific sections and figures have been adapted from previously published works (list of publications) to support the research presented herein.

Bibliography

[1] Marco Martino, Concetta Ruocco, Eugenio Meloni, Pluton Pullumbi, and Vincenzo Palma. Main hydrogen production processes: An overview. *Catalysts*, 11(5):547, 2021.

[2] Pavlos Nikolaidis and Andreas Poullikkas. A comparative overview of hydrogen production processes. *Renewable and Sustainable Energy Reviews*, 67:597–611, 2017.

[3] Jose M Marín Arcos and Diogo MF Santos. The hydrogen color spectrum: techno-economic analysis of the available technologies for hydrogen production. *Gases*, 3(1):25–46, 2023.

[4] Vincenzo Spallina, G Matturro, C Ruocco, E Meloni, V Palma, Ekain Fernandez, J Melendez, AD Pacheco Tanaka, JL Viviente Sole, M van Sint Annaland, et al. Direct route from ethanol to pure hydrogen through autothermal reforming in a membrane reactor: Experimental demonstration, reactor modelling and design. *Energy*, 143:666–681, 2018.

[5] Neha Pal, Madhu Agarwal, Karishma Maheshwari, and Yogendra Singh Solanki. A review on types, fabrication and support material of hydrogen separation membrane. *Materials Today: Proceedings*, 28:1386–1391, 2020.

[6] Can Zeng Liang, Tai-Shung Chung, and Juin-Yih Lai. A review of polymeric composite membranes for gas separation and energy production. *Progress in Polymer Science*, 97:101141, 2019.

[7] Fausto Gallucci, JA Medrano, Ekain Fernandez, Jon Melendez, Martin Van Sint Annaland, and DA Pacheco-Tanaka. Advances on high temperature pd-based membranes and membrane reactors for hydrogen purifcation and production. *Journal of Membrane Science & Research*, 3(3):142–156, 2017.

[8] N Kruse, Y Schießer, S Kämnitz, H Richter, I Voigt, G Braun, and JU Repke. Carbon membrane gas separation of binary CO_2 mixtures at high pressure. *Separation and Purification Technology*, 164:132–137, 2016.

[9] Hong-Joo Lee, Hiroyuki Suda, Kenji Haraya, and Seung-Hyeon Moon. Gas permeation properties of carbon molecular sieving membranes derived from the polymer blend of polyphenylene oxide (PPO)/polyvinylpyrrolidone (PVP). *Journal of Membrane Science*, 296(1-2):139–146, 2007.

[10] Jun-ichiro Hayashi, Hirotaka Mizuta, Masatake Yamamoto, Katsuki Kusakabe, and Shigeharu Morooka. Pore size control of carbonized BPDA-pp ODA polyimide membrane by chemical vapor deposition of carbon. *Journal of Membrane Science*, 124(2):243–251, 1997.

[11] Hui-Hsing Tseng, Itta Arun Kumar, Tzu-Hsiang Weng, Chi-Yuan Lu, and Ming-Yen Wey. Preparation and characterization of carbon molecular sieve membranes for gas separation—the effect of incorporated multi-wall carbon nanotubes. *Desalination*, 240(1-3):40–45, 2009.

[12] Pei Shi Tin, Huey Yi Lin, Rui Chin Ong, and Tai-Shung Chung. Carbon molecular sieve membranes for biofuel separation. *Carbon*, 49(2):369–375, 2011.

[13] Anil Kumar Pabby, Syed SH Rizvi, and Ana Maria Sastre Requena. *Handbook of membrane separations: chemical, pharmaceutical, food, and biotechnological applications*. CRC press, 2015.

[14] Ho Bum Park, Youn Kook Kim, Ji Min Lee, Sun Yong Lee, and Young Moo Lee. Relationship between chemical structure of aromatic polyimides and gas permeation properties of their carbon molecular sieve membranes. *Journal of Membrane Science*, 229(1-2):117–127, 2004.

[15] Seong-Joong Kim, You-In Park, Seung-Eun Nam, Hosik Park, and Pyung Soo Lee. Separations of f-gases from nitrogen through thin carbon membranes. *Separation and Purification Technology*, 158:108–114, 2016.

[16] Fausto Gallucci, Jose Antonio Medrano, and Emma Palo. Conventional processes for hydrogen production. In *CO_2 and CO as Feedstock: Sustainable Carbon Sources for the Circular Economy*, pages 19–40. Springer, 2024.

[17] Kinetics Technologies (2018) KT Reformers. *http://www.kt-met.com/en/business/hydrogen- syngas-technology*, Accessed 10 Mar 2018.

[18] McDermott (2018) Steam methane reformers. *https://www.cbi.com/What-We-Do/Technology/Gas-Processing/Hydrogen Synthesis-Gas-Production/Steam-Methane-Reformers*, Accessed 10 Mar 2018.

[19] Haldor Topsoe. Tubular radiant wall steam reformer. *https://www.topsoe.com/products/tubular-radiant-wall-steam-reformer*, Accessed 10 Mar 2018.

[20] Chandra Ratnasamy and Jon P Wagner. Water gas shift catalysis. *Catalysis Reviews*, 51(3):325–440, 2009.

[21] Jamie D Holladay, Jianli Hu, David L King, and Yong Wang. An overview of hydrogen production technologies. *Catalysis Today*, 139(4):244–260, 2009.

[22] Bernhard Neumann and Kurt Jacob. Die gleichgewichtsverhältnisse bei der methanbildung aus kohlenoxyd und wasserstoff, bzw. kohlendioxyd und

wasserstoff. *Zeitschrift für Elektrochemie und angewandte physikalische Chemie*, 30(23-24):557–576, 1924.

[23] Jens Rostrup-Nielsen. Steam reforming of hydrocarbons. a historical perspective. In *Studies in surface science and catalysis*, volume 147, pages 121–126. Elsevier, 2004.

[24] Joshua O Ighalo, Kanika Dulta, Setyo Budi Kurniawan, Fredrick O Omoarukhe, Ugochukwu Ewuzie, Steve O Eshiemogie, Alaba U Ojo, and Siti Rozaimah Sheikh Abdullah. Progress in microalgae application for CO_2 sequestration. *Cleaner Chemical Engineering*, page 100044, 2022.

[25] Kayode A Adegoke, Kabir O Oyedotun, Joshua O Ighalo, James F Amaku, Chijioke Olisah, Adedapo O Adeola, Kingsley O Iwuozor, Kovo G Akpomie, and Jeanet Conradie. Cellulose derivatives and cellulose-metal-organic frameworks for CO_2 adsorption and separation. *Journal of CO_2 Utilization*, 64:102163, 2022.

[26] Chitta Sahana, Sudipta De, and Subha Mondal. Integration of CO_2 power and refrigeration cycles with a desalination unit to recover geothermal heat in an oilfield. *Applied Thermal Engineering*, 189:116744, 2021.

[27] Xuan Peng and Qibing Jin. Molecular simulation of methane steam reforming reaction for hydrogen production. *International Journal of Hydrogen Energy*, 47(12):7569–7585, 2022.

[28] Gilbert F Froment, Kenneth B Bischoff, and Juray De Wilde. *Chemical reactor analysis and design*, volume 2. Wiley New York, 1990.

[29] MH Halabi, MHJM De Croon, J Van Der Schaaf, PD Cobden, and JC Schouten. Intrinsic kinetics of low temperature catalytic methane–steam reforming and water–gas shift over $Rh/Ce_{\alpha}\mathrm{Zr}_{1-\alpha}O_2$ catalyst. *Applied Catalysis A: General*, 389(1-2):80–91, 2010.

[30] Jianguo Xu and Gilbert F Froment. Methane steam reforming, methanation and water-gas shift: I. intrinsic kinetics. *AIChE Journal*, 35(1):88–96, 1989.

[31] Jianguo Xu and Gilbert F Froment. Methane steam reforming: Ii. diffusional limitations and reactor simulation. *AIChE Journal*, 35(1):97–103, 1989.

[32] Peter Häussinger, Reiner Lohmüller, and Allan M Watson. Hydrogen, 2. production. *Ullmann's Encyclopedia of Industrial Chemistry*, 2000.

[33] K Aasberg-Petersen, I Dybkjær, CV Ovesen, NC Schjødt, J Sehested, and SG Thomsen. Natural gas to synthesis gas–catalysts and catalytic processes. *Journal of Natural gas science and engineering*, 3(2):423–459, 2011.

[34] G Eklund and O Von Krusenstierna. Storage and transportation of merchant hydrogen. *International Journal of Hydrogen Energy*, 8(6):463–470, 1983.

[35] Joan M Ogden. Review of small stationary reformers for hydrogen production. *Report to the international energy agency*, 609, 2001.

[36] Benjamin Dittmar. Entwicklung eines technischen H_2-membranreaktors. *Karlsruhe Institute of Technology (KIT), PhD thesis*, 2014.

[37] Tim Boeltken. Microstructured reactors with integrated metallic membranes for on-site production of pure hydrogen. *Karlsruhe Institute of Technology (KIT), PhD thesis*, 2014.

[38] SCA Kluiters. Status review on membrane systems for hydrogen separation. *Energy Center of the Netherlands, Petten, The Netherlands*, 2004.

[39] SA Steward. Review of hydrogen isotope permeability through materials. Technical report, Lawrence Livermore National Lab.(LLNL), Livermore, CA (United States), 1983.

[40] William J Koros and GK Fleming. Membrane-based gas separation. *Journal of Membrane Science*, 83(1):1–80, 1993.

[41] Joseph O Hirschfelder, Charles F Curtiss, and R Byron Bird. *The molecular theory of gases and liquids*. John Wiley & Sons, 1964.

[42] KW Kehr. Theory of the diffusion of hydrogen in metals. *Hydrogen in Metals I: Basic Properties*, pages 197–226, 2005.

[43] MD Dolan. Non-Pd BCC alloy membranes for industrial hydrogen separation. *Journal of Membrane Science*, 362(1-2):12–28, 2010.

[44] MI Darby and MN Read. Energy of hydrogen in bcc transition metals. *Journal of the Less Common Metals*, 91(2):209–215, 1983.

[45] M Lagos and H Cerón. Quantum mechanism of hydrogen diffusion in tantalum. *Solid State Communications*, 65(6):535–538, 1988.

[46] AL Companion, Frank Liu, and DP Onwood. On the location of a hydrogen atom in body-centered cubic 3d transition metal lattices. *Journal of the Less Common Metals*, 107(1):131–138, 1985.

[47] Jingcheng Xu and Jijun Zhao. First-principles study of hydrogen in perfect tungsten crystal. *Nuclear Instruments and Methods in Physics Research Section B: Beam Interactions with Materials and Atoms*, 267(18):3170–3174, 2009.

[48] Andrea Latgé, Rejane M Ribeiro-Teixeira, and JR Iglesias. Binding energy of a hydrogen impurity in an fcc lattice. *Solid State Communications*, 52(2):87–91, 1984.

[49] MA Khan, JC Parlebas, and C Demangeat. Electronic structure and ordering of hydrogen in fcc transition metals. *Journal of the Less Common Metals*, 77(1):P1–P8, 1981.

[50] KG McLennan, E MacA Gray, and JF Dobson. Deuterium occupation of tetrahedral sites in palladium. *Physical Review B*, 78(1):014104, 2008.

[51] Georg Alefeld and Johann Völkl. Hydrogen in metals i-basic properties. *Berlin and New York*, 28, 1978.

[52] Takashi Kiriyama and Tetsuo Tanabe. Interaction of hydrogen atoms with metals. *Journal of Nuclear Materials*, 220:873–877, 1995.

[53] Peter Cotterill. The hydrogen embrittlement of metals. *Progress in Materials Science*, 9(4):205–301, 1961.

[54] Robert E Buxbaum and Terry L Marker. Hydrogen transport through non-porous membranes of palladium-coated niobium, tantalum and vanadium. *Journal of Membrane Science*, 85(1):29–38, 1993.

[55] KHJ Buschow, PCP Bouten, and AR Miedema. Hydrides formed from intermetallic compounds of two transition metals: a special class of ternary alloys. *Reports on Progress in Physics*, 45(9):937, 1982.

[56] Thomas Graham. Xviii. on the absorption and dialytic separation of gases by colloid septa. *Philosophical Transactions of the Royal Society of London*, (156):399–439, 1866.

[57] F Sakamoto, Y Kinari, FL Chen, and Y Sakamoto. Hydrogen permeation through palladium alloy membranes in mixture gases of 10% nitrogen and ammonia in the hydrogen. *International Journal of Hydrogen Energy*, 22(4):369–375, 1997.

[58] MLH Wise, JPG Farr, and IR Harris. X-ray studies of the α/β miscibility gaps of some palladium solid solution-hydrogen systems. *Journal of the Less Common Metals*, 41(1):115–127, 1975.

[59] Ying Chen, Yucheng Hou, Gennady Govor, Olga Demidenko, and Yujing Li. Hydrogen absorption in palladium-based nanocrystals for electrocatalysis investigation. *ChemElectroChem*, 11(12):e202400071, 2024.

[60] H Frieske and E Wicke. Magnetic susceptibility and equilibrium diagram of PdH_n. *Berichte der Bunsengesellschaft für physikalische Chemie*, 77(1):48–52, 1973.

[61] E Wicke, H Brodowsky, and H Züchner. Hydrogen in palladium and palladium alloys. *Hydrogen in Metals II: Application-Oriented Properties*, pages 73–155, 2005.

[62] Gioele Di Marcoberardino, Jasper Knijff, Marco Binotti, Fausto Gallucci, and Giampaolo Manzolini. Techno-economic assessment in a fluidized bed membrane reactor for small-scale H_2 production: Effect of membrane support thickness. *Membranes*, 9(9):116, 2019.

[63] Taher Yousefi Amiri, Kamran Ghasemzageh, and Adolfo Iulianelli. Membrane reactors for sustainable hydrogen production through steam reforming of hydrocarbons: A review. *Chemical Engineering and Processing-Process Intensification*, 157:108148, 2020.

[64] Fausto Gallucci, Ekain Fernandez, Pablo Corengia, and Martin van Sint Annaland. Recent advances on membranes and membrane reactors for hydrogen production. *Chemical Engineering Science*, 92:40–66, 2013.

[65] Xavier Quek and Hugh Hamilton. Palladium membrane technology for hydrogen production, carbon capture and other applications. *Johnson Matthey Technology Review*, 60(3):190–195, 2016.

[66] Takafumi Tanaka, Akira Hirano, Shoukei Kobayashi, Takuya Oda, Seiki Kuwabara, Andrew Lord, Paul Gunning, Oscar González de Dios, Victor Lopez, Arturo Mayoral Lopez de Lerma, et al. Autonomous network diagnosis from the carrier perspective. *Journal of Optical Communications and Networking*, 12(1):A9–A17, 2020.

[67] TA Peters, Per Martin Rørvik, TO Sunde, M Stange, Frode Roness, TR Reinertsen, JH Ræder, Yngve Larring, and Rune Bredesen. Palladium (Pd) membranes as key enabling technology for pre-combustion CO_2 capture and hydrogen production. *Energy Procedia*, 114:37–45, 2017.

[68] Anwu Li, Tony Boyd, Jim Choon Lim, and John Ross Grace. Development of palladium-alloy membranes for hydrogen separation and purification. *Journal of Membrane Science and Research*, 6(1):99–106, 2020.

[69] G Iaquaniello, A Borruto, E Lollobattista, Giovanni Narducci, and D Katsir. Hydrogen palladium selective membranes: an economic perspective. *Membrane Reactors for Hydrogen Production Processes*, pages 57–78, 2011.

[70] Ekain Fernandez, Kai Coenen, Arash Helmi, Jon Melendez, Jon Zuñiga, DA Pacheco Tanaka, Martin van Sint Annaland, and Fausto Gallucci. Preparation and characterization of thin-film pd–ag supported membranes for high-temperature applications. *International Journal of Hydrogen Energy*, 40(39):13463–13478, 2015.

[71] K Atsonios, KD Panopoulos, A Doukelis, AK Koumanakos, E Kakaras, T Peters, and YC van Delft. Introduction to palladium membrane technology. *Palladium Membrane Technology for Hydrogen Production, Carbon Capture and Other Applications: Principles, Energy Production and Other Applications. Elsevier*, pages 1–21, 2014.

[72] Toshiaki Tanaka, Tomonobu Hasegawa, Keiichi Ozono, Hiroyuki Tanaka, Susumu Kanzaki, Susumu Yokoya, Kazuo Chihara, Noriyuki Iwamoto, and Yoshiki Seino. Effect of growth hormone treatment on quality of life in japanese children with growth hormone deficiency: an analysis from a prospective observational study. *clinical pediatric endocrinology*, 23(3):83–92, 2014.

[73] Ekain Fernandez, A Helmi, JA Medrano, K Coenen, A Arratibel, J Melendez, NCA de Nooijer, V Spallina, JL Viviente, J Zuñiga, et al. Palladium based membranes and membrane reactors for hydrogen production and purification: An overview of research activities at tecnalia and TU/e. *International Journal of Hydrogen Energy*, 42(19):13763–13776, 2017.

[74] Richard Beavis. The $EU\ FP6$ cachet project-final results. *Energy Procedia*, 4:1074–1081, 2011.

[75] F Giroudière, JL Ambrosino, B Fischer, D Pavone, E Sanz-Garcia, A Le Gall, E Soutif, and H Vleeming. Hygensys: a flexible process for hydrogen and power production with reduction of CO_2 emission. *Oil & Gas Science and Technology–Revue d'IFP Energies nouvelles*, 65(5):673–688, 2010.

[76] Jan Wilco Dijkstra, Johannis AZ Pieterse, Hui Li, Jurriaan Boon, Yvonne C van Delft, Gunabalan Raju, Gerard Peppink, Ruud W van den Brink, and

Daniel Jansen. Development of membrane reactor technology for power production with pre-combustion CO_2 capture. *Energy Procedia*, 4:715–722, 2011.

[77] D Jansen, JW Dijkstra, RW Van den Brink, TA Peters, M Stange, R Bredesen, A Goldbach, HY Xu, A Gottschalk, and A Doukelis. Hydrogen membrane reactors for CO_2 capture. *Energy Procedia*, 1(1):253–260, 2009.

[78] A Iulianelli, A Basile, H Li, and RW Van den Brink. Inorganic membranes for pre-combustion carbon dioxide (CO_2) capture. In *Advanced membrane science and technology for sustainable energy and environmental applications*, pages 184–213. Elsevier, 2011.

[79] Final report summary -CACHET. available from: https://cordis.europa.eu/.

[80] JL Viviente Sole, DA Pacheco Tanaka, JA Medrano, and Fausto Gallucci. An overview of some recent european projects on metallic membranes. *Current Trends and Future Developments on (Bio-) Membranes*, pages 313–379, 2020.

[81] Alberto Giaconia, Luca Turchetti, Giulia Monteleone, Barbara Morico, Gaetano Iaquaniello, Keren Shabtai, Moshe Sheintuch, Daniella Boettge, Joerg Adler, Vicenzo Palma, et al. Development of a solar-powered, fuel-flexible compact steam reformer: The comethy project. *Chem Eng Trans*, 35, 2013.

[82] Alberto Giaconia, Gaetano Iaquaniello, Giampaolo Caputo, Barbara Morico, Annarita Salladini, Luca Turchetti, Giulia Monteleone, Antonella Giannini, and Emma Palo. Experimental validation of a pilot membrane reactor for hydrogen production by solar steam reforming of methane at maximum 550 °C using molten salts as heat transfer fluid. *International Journal of Hydrogen Energy*, 45(58):33088–33101, 2020.

[83] Alberto Giaconia, G Monteleone, B Morico, A Salladini, K Shabtai, M Sheintuch, Daniela Böttge, Jörg Adler, V Palma, S Voutetakis, et al.

Multi-fuelled solar steam reforming for pure hydrogen production using solar salts as heat transfer fluid. *Energy Procedia*, 69:1750–1758, 2015.

[84] Vincenzo Palma, Daniela Barba, Eugenio Meloni, Simona Renda, and Concetta Ruocco. Ultracompact biofuels catalytic reforming processes for distributed renewable hydrogen production. In *Studies in Surface Science and Catalysis*, volume 179, pages 317–333. Elsevier, 2020.

[85] Alberto Giaconia, Gaetano Iaquaniello, Barbara Morico, Annarita Salladini, and Emma Palo. Techno-economic assessment of solar steam reforming of methane in a membrane reactor using molten salts as heat transfer fluid. *International Journal of Hydrogen Energy*, 46(71):35172–35188, 2021.

[86] F Gallucci, M van Sint Annaland, L Roses, and G Manzolini. Using palladium membrane-based fuel reformers for combined heat and power (CHP) plants. *Palladium Membrane Technology for Hydrogen Production, Carbon Capture and Other Applications: Principles, Energy Production and Other Applications*, page 319, 2014.

[87] Simon Martinez, Ghislain Michaux, Patrick Salagnac, and Jean-Louis Bouvier. Micro-combined heat and power systems (micro-CHP) based on renewable energy sources. *Energy Conversion and Management*, 154:262–285, 2017.

[88] Trevor Hocksun Kwan, Xiaofeng Wu, and Qinghe Yao. Performance comparison of several heat pump technologies for fuel cell micro-CHP integration using a multi-objective optimisation approach. *Applied Thermal Engineering*, 160:114002, 2019.

[89] Gioele Di Marcoberardino and Giampaolo Manzolini. Investigation of a 5 kW micro-CHP PEM fuel cell based system integrated with membrane reactor under diverse EU natural gas quality. *International Journal of Hydrogen Energy*, 42(19):13988–14002, 2017.

[90] Alba Arratibel, Jose Antonio Medrano, Jon Melendez, D Alfredo Pacheco Tanaka, Martin van Sint Annaland, and Fausto Gallucci. Attrition-resistant membranes for fluidized-bed membrane reactors: Double-skin membranes. *Journal of membrane science*, 563:419–426, 2018.

[91] Alba Arratibel, Alfredo Pacheco Tanaka, Iker Laso, Martin van Sint Annaland, and Fausto Gallucci. Development of Pd-based double-skinned membranes for hydrogen production in fluidized bed membrane reactors. *Journal of Membrane Science*, 550:536–544, 2018.

[92] Jose Luis Viviente, Jon Meléndez, David Alfredo Pacheco Tanaka, Fausto Gallucci, Vincenzo Spallina, Giampaolo Manzolini, Stefano Foresti, Vincenzo Palma, Concetta Ruocco, and Leonardo Roses. Advanced m-CHP fuel cell system based on a novel bio-ethanol fluidized bed membrane reformer. *International Journal of Hydrogen Energy*, 42(19):13970–13987, 2017.

[93] Jose Antonio Medrano, Ekain Fernandez, Jon Melendez, Maria Parco, David Alfredo Pacheco Tanaka, Martin van Sint Annaland, and Fausto Gallucci. Pd-based metallic supported membranes: High-temperature stability and fluidized bed reactor testing. *International Journal of Hydrogen Energy*, 41(20):8706–8718, 2016.

[94] Ekain Fernandez, Jose Antonio Medrano, Jon Melendez, Maria Parco, Jose Luis Viviente, Martin van Sint Annaland, Fausto Gallucci, and DA Pacheco Tanaka. Preparation and characterization of metallic supported thin Pd–Ag membranes for hydrogen separation. *Chemical Engineering Journal*, 305:182–190, 2016.

[95] Ekain Fernandez, Jose Angel Sanchez-Garcia, Jose Luis Viviente, Martin van Sint Annaland, Fausto Gallucci, and David A Pacheco Tanaka. Morphology and N_2 permeance of sputtered Pd-Ag ultra-thin film membranes. *Molecules*, 21(2):210, 2016.

[96] Ekain Fernandez, Jose Angel Sanchez-Garcia, Jon Melendez, Vincenzo Spallina, Martin van Sint Annaland, Fausto Gallucci, DA Pacheco Tanaka,

and Radha Prema. Development of highly permeable ultra-thin Pd-based supported membranes. *Chemical Engineering Journal*, 305:149–155, 2016.

[97] G Iaquaniello, E Palo, A Salladini, and B Morico. Membrane reactors for hydrogen production. In *Current Trends and Future Developments on (Bio-) Membranes*, pages 261–292. Elsevier, 2020.

[98] Emma Palo, Annarita Salladini, Barbara Morico, Vincenzo Palma, Antonio Ricca, and Gaetano Iaquaniello. Application of Pd-based membrane reactors: An industrial perspective. *Membranes*, 8(4):101, 2018.

[99] M Colozzi, G Galdieri, F Gallucci, JA Medrano Jimenez, L Mosca, E Palo, S Taraschi, and SA Wassie. Process design for green hydrogen production. *International Journal of Hydrogen Energy*, 2019.

[100] G Iaquaniello, E Palo, and A Salladini. Renewable sources to biorefineries, biomass conversion, and membrane technology. In *Membrane Engineering in the Circular Economy*, pages 177–196. Elsevier, 2022.

[101] G Iaquaniello, E Palo, A Salladini, and B Cucchiella. *Using palladium membrane reformers for hydrogen production*. Woodhead Publishing: Sawston, UK, 2014.

[102] Diego Barba, Mauro Capocelli, Marcello De Falco, Giovanni Franchi, and Vincenzo Piemonte. Mass transfer coefficient in multi-stage reformer/membrane modules for hydrogen production. *Membranes*, 8(4):109, 2018.

[103] Barbara Morico, Annarita Salladini, Emma Palo, and Gaetano Iaquaniello. Solar energy assisted membrane reactor for hydrogen production. *ChemEngineering*, 3(1):9, 2019.

[104] C Cremers, A Pelz, U Stimming, K Haas-Santo, O Görke, P Pfeifer, and K Schubert. Micro-structured methane steam reformer with integrated catalytic combustor. *Fuel Cells*, 7(2):91–98, 2007.

[105] P Pfeifer, T Böltken, R Dürrschnabel, R Dittmeyer, E Hansjosten, T Gietzelt, T Wunsch, and F Dallmann. Membrane reformer. WO2020228982A1, 2020.

[106] Ib Chorkendorff and Johannes W Niemantsverdriet. *Concepts of modern catalysis and kinetics*. John Wiley & Sons, 2017.

[107] K Aasberg-Petersen, J-H Bak Hansen, TS Christensen, I Dybkjaer, P Seier Christensen, C Stub Nielsen, SEL Winter Madsen, and JR Rostrup-Nielsen. Technologies for large-scale gas conversion. *Applied Catalysis A: General*, 221(1-2):379–387, 2001.

[108] Ankur Kumar, Michael Baldea, and Thomas F Edgar. A physics-based model for industrial steam-methane reformer optimization with non-uniform temperature field. *Computers & Chemical Engineering*, 105:224–236, 2017.

[109] Yong Ho Yu and Mihail H Sosna. Modeling for industrial heat exchanger type steam reformer. *Korean Journal of Chemical Engineering*, 18:127–132, 2001.

[110] Jens Rostrup-Nielsen and Lars J Christiansen. *Concepts in syngas manufacture*, volume 10. World Scientific, 2011.

[111] Gregor D Wehinger, Matthias Kraume, Viktor Berg, Oliver Korup, Katharina Mette, Robert Schlögl, Malte Behrens, and Raimund Horn. Investigating dry reforming of methane with spatial reactor profiles and particle-resolved cfd simulations. *AIChE journal*, 62(12):4436–4452, 2016.

[112] Martyn V Twigg. *Catalyst handbook*. Routledge, 2018.

[113] Mohsen Behnam and Anthony G Dixon. 3D CFD simulations of local carbon formation in steam methane reforming catalyst particles. *International Journal of Chemical Reactor Engineering*, 15(6):20170067, 2017.

[114] Dean A Latham, Kimberley B McAuley, Brant A Peppley, and Troy M Raybold. Mathematical modeling of an industrial steam-methane reformer

for on-line deployment. *Fuel Processing Technology*, 92(8):1574–1586, 2011.

[115] P Darvishi and F Zareie-Kordshouli. A rigorous mathematical model for online prediction of tube skin temperature in an industrial top-fired steam methane reformer. *Chemical Engineering Research and Design*, 126:32–44, 2017.

[116] Dante Bonaquist. Analysis of CO_2 emissions, reductions, and capture for large-scale hydrogen production plants. *Praxair. Our-company/sustainable-development/greentechnologies-and-climate-change/less-carbon-more-green*, 2010.

[117] Ali T-Raissi and David L Block. Hydrogen: automotive fuel of the future. *IEEE Power and Energy Magazine*, 2(6):40–45, 2004.

[118] Energy Efficiency. Tracking industrial energy efficiency and CO_2 emissions. *International Energy Agency*, 34(2):1–12, 2007.

[119] Pamela L Spath and Margaret K Mann. Life cycle assessment of hydrogen production via natural gas steam reforming. Technical report, National Renewable Energy Lab.(NREL), Golden, CO (United States), 2000.

[120] Angela M Moreno and Benjamin A Wilhite. Autothermal hydrogen generation from methanol in a ceramic microchannel network. *Journal of Power Sources*, 195(7):1964–1970, 2010.

[121] Xinhai Xu, Peiwen Li, and Yuesong Shen. Small-scale reforming of diesel and jet fuels to make hydrogen and syngas for fuel cells: A review. *Applied Energy*, 108:202–217, 2013.

[122] Amin Delparish, Sinan Koc, Burcu Selen Caglayan, and Ahmet K Avci. Oxidative steam reforming of glycerol to synthesis gas in a microchannel reactor. *Catalysis Today*, 323:200–208, 2019.

[123] Albert Renken. Microstructured reactors for heterogeneous catalytic processes. In *Basic Principles in Applied Catalysis*, pages 521–542. Springer, 2004.

[124] LL Makarshin, VA Sadykov, DV Andreev, AG Gribovskii, VV Privezentsev, and VN Parmon. Syngas production by partial oxidation of methane in a microchannel reactor over a $Ni - Pt/La_{0.2}Zr_{0.4}Ce_{0.4}O_x$ catalyst. *Fuel Processing Technology*, 131:21–28, 2015.

[125] Ugurcan Tozar and Ahmet K Avci. Strategies for improving CO_2 utilization in microchannel enabled production of dimethyl ether. *Chemical Engineering and Processing-Process Intensification*, 151:107914, 2020.

[126] Paul Watts and Charlotte Wiles. Recent advances in synthetic micro reaction technology. *Chemical communications*, (5):443–467, 2007.

[127] Sylvia Andrea Cruz Torres, Oihane Sanz Iturralde, Rosalía Poyato Galán, Oscar Hernando Laguna Espitia, F Javier Echave, Luis C Almeida, Miguel Ángel Centeno Gallego, Gurutze Arzamendi, LM Gandia, EF Souza-Aguiar, et al. Design and testing of a microchannel reactor for the prox reaction. *Chemical Engineering Journal, 167, 634-642.*, 2011.

[128] M O'Connell, G Kolb, K-P Schelhaas, M Wichert, D Tiemann, H Pennemann, and R Zapf. Towards mass production of microstructured fuel processors for application in future distributed energy generation systems: a review of recent progress at imm. *Chemical Engineering Research and Design*, 90(1):11–18, 2012.

[129] K Venkataraman, JM Redenius, and LD Schmidt. Millisecond catalytic wall reactors: dehydrogenation of ethane. *Chemical Engineering Science*, 57(13):2335–2343, 2002.

[130] Grigorios Kolios, Achim Gritsch, Arístides Morillo, Ute Tuttlies, Jens Bernnat, Frank Opferkuch, and Gerhart Eigenberger. Heat-integrated reactor concepts for catalytic reforming and automotive exhaust purification. *Applied Catalysis B: Environmental*, 70(1-4):16–30, 2007.

[131] Joseph William Pratt. A fischer-tropsch synthesis reactor model framework for liquid biofuels production. Technical report, Sandia National Laboratories (SNL), Albuquerque, NM, and Livermore, CA . . . , 2012.

[132] Dionisios G Vlachos. Microreactor engineering: Processes, detailed design and modeling. *Microfabricated Power Generation Devices: Design and Technology*, pages 179–198, 2009.

[133] B Dittmar, A Behrens, N Schödel, M Rüttinger, Th Franco, G Straczewski, and R Dittmeyer. Methane steam reforming operation and thermal stability of new porous metal supported tubular palladium composite membranes. *International Journal of Hydrogen Energy*, 38(21):8759–8771, 2013.

[134] Adam Jan Kot. *Entwicklung eines metallbasierten Substratkonzepts für energieeffiziente Gastrennmembranen*. Number FZJ-2016-02520. Werkstoffsynthese und Herstellungsverfahren, 2016.

[135] P Kant. Palladiumkompositmembranen durch suspensionsplasmaspritzen auf planaren substraten und deren integration in kompakte membranreaktoren, 2017.

[136] BN Dutta and B Dayal. Lattice constants and thermal expansion of palladium and tungsten up to 878 °C by X-ray method. *physica status solidi (b)*, 3(12):2253–2259, 1963.

[137] VDM Metals International GmbH. VDM®Crofer 22 APU. *Material Data Sheet No. 414*, 2021.

[138] Sonun Ulan kyzy, Rainer Voelkl, Oliver Munz, Tim Fischer, Sarah Welzenbach, and Uwe Glatzel. Thermo-physical properties of Hastelloy X and Haynes 214 close to the melting range. *Materials Science and Technology*, 36(10):1012–1019, 2020.

[139] S Raju, K Sivasubramanian, R Divakar, G Panneerselvam, A Banerjee, E Mohandas, and MP Antony. Thermal expansion studies on Inconel-600® by high temperature X-ray diffraction. *Journal of Nuclear Materials*, 325(1):18–25, 2004.

[140] Thyssenkrupp AG. *https://www.thyssenkrupp.com*, 2023.

[141] Tim Boeltken, Dennis Soysal, Seungcheol Lee, Grazyna Straczewski, Uta Gerhards, Peter Peifer, Johannes Arnold, and Roland Dittmeyer. Perspectives of suspension plasma spraying of palladium nanoparticles for preparation of thin palladium composite membranes. *Journal of Membrane Science*, 468:233–241, 2014.

[142] P Quicker, V Höllein, and R Dittmeyer. Catalytic dehydrogenation of hydrocarbons in palladium composite membrane reactors. *Catalysis today*, 56(1-3):21–34, 2000.

[143] Volker Höllein, Matthew Thornton, Peter Quicker, and Roland Dittmeyer. Preparation and characterization of palladium composite membranes for hydrogen removal in hydrocarbon dehydrogenation membrane reactors. *Catalysis Today*, 67(1-3):33–42, 2001.

[144] Lech Pawlowski. Suspension and solution thermal spray coatings. *Surface and Coatings Technology*, 203(19):2807–2829, 2009.

[145] Andreas Killinger, Rainer Gadow, Georg Mauer, Alexandre Guignard, Robert Vaßen, and Detlev Stöver. Review of new developments in suspension and solution precursor thermal spray processes. *Journal of Thermal Spray Technology*, 20:677–695, 2011.

[146] Holger Kassner, Roberto Siegert, Dag Hathiramani, Robert Vassen, and Detlev Stoever. Application of suspension plasma spraying (SPS) for manufacture of ceramic coatings. *Journal of Thermal Spray Technology*, 17:115–123, 2008.

[147] Pierre Fauchais, Aurélien Joulia, Simon Goutier, Christophe Chazelas, Michel Vardelle, Armelle Vardelle, and Sylvie Rossignol. Suspension and solution plasma spraying. *Journal of Physics D: Applied Physics*, 46(22):224015, 2013.

[148] A Killinger. Status and future trends in suspension spray techniques. *Future Development of Thermal Spray Coatings*, pages 81–122, 2015.

[149] Tae H Lee, Chan Y Park, Geunhee Lee, Stephen E Dorris, and U Balu Balachandran. Hydrogen transport properties of palladium film prepared by colloidal spray deposition. *Journal of Membrane Science*, 415:199–204, 2012.

[150] Efi Hadjixenophontos, Masoud Mahmoudizadeh, Michael Rubin, Dirk Ullmer, Fatemeh Razmjooei, Alexander C Hanf, Jan Brien, Roland Dittmeyer, and Asif Ansar. Palladium membrane with high density of large-angle grain boundaries to promote hydrogen diffusivity. *Membranes*, 12(6):617, 2022.

[151] Felipe Miranda, Felipe Caliari, Alexei Essiptchouk, and Gilberto Pertraconi. Atmospheric plasma spray processes: From micro to nanostructures. In *Atmospheric Pressure Plasma-from Diagnostics to Applications*. IntechOpen, 2018.

[152] Satyapal Mahade, Karthik Narayan, Sivakumar Govindarajan, Stefan Björklund, Nicholas Curry, and Shrikant Joshi. Exploiting suspension plasma spraying to deposit wear-resistant carbide coatings. *Materials*, 12(15):2344, 2019.

[153] Tim Boeltken, M Belimov, P Pfeifer, TA Peters, Rune Bredesen, and Roland Dittmeyer. Fabrication and testing of a planar microstructured concept module with integrated palladium membranes. *Chemical Engineering and Processing: Process Intensification*, 67:136–147, 2013.

[154] FA Lewis. The palladium-hydrogen system: Structures near phase transition and critical points. *International Journal of Hydrogen Energy*, 20(7):587–592, 1995.

[155] H Amandusson, L-G Ekedahl, and Helen Dannetun. Hydrogen permeation through surface modified pd and pdag membranes. *Journal of Membrane Science*, 193(1):35–47, 2001.

[156] Lei Shi, Andreas Goldbach, Gaofeng Zeng, and Hengyong Xu. Direct H_2O_2 synthesis over Pd membranes at elevated temperatures. *Journal of Membrane Science*, 348(1-2):160–166, 2010.

[157] XL Pan, N Stroh, H Brunner, GX Xiong, and SS Sheng. Pd/ceramic hollow fibers for H_2 separation. *Separation and Purification Technology*, 32(1-3):265–270, 2003.

[158] XL Pan, GX Xiong, SS Sheng, N Stroh, and H Brunner. Thin dense Pd membranes supported on $\alpha - Al_2O_3$ hollow fibers. *Chemical Communications*, (24):2536–2537, 2001.

[159] Peter P Mardilovich, Ying She, Yi Hua Ma, and Min-Hon Rei. Defect-free palladium membranes on porous stainless-steel support. *AIChE Journal*, 44(2):310–322, 1998.

[160] Jiafeng Yu, Zhe Zhang, Felix Dallmann, Jixin Zhang, Dengyun Miao, Hengyong Xu, Andreas Goldbach, and Roland Dittmeyer. Facile synthesis of highly active Rh/Al_2O_3 steam reforming catalysts with preformed support by flame spray pyrolysis. *Applied Catalysis B: Environmental*, 198:171–179, 2016.

[161] Somaye Mohammadi and Zeinab Mohammadi. Functionalized $NiFe_2O_4$/mesopore silica anchored to guanidine nanocomposite as a catalyst for synthesis of 4H-chromenes under ultrasonic irradiation. *Journal of Composites and Compounds*, 3(7):84–90, 2021.

[162] Doan Pham Minh, Tan Ji Siang, Dai-Viet N Vo, Thanh Son Phan, Cyrille Ridart, Ange Nzihou, and Didier Grouset. Hydrogen production from biogas reforming: An overview of steam reforming, dry reforming, dual reforming, and tri-reforming of methane. *Hydrogen Supply Chains*, pages 111–166, 2018.

[163] Haotian Zhang, Zhuxing Sun, and Yun Hang Hu. Steam reforming of methane: Current states of catalyst design and process upgrading. *Renewable and Sustainable Energy Reviews*, 149:111330, 2021.

[164] Jens R Rostrup-Nielsen, Jens Sehested, and Jens K Nørskov. Hydrogen and synthesis gas by steam-and CO_2 reforming. 2002.

[165] Gabriella Garbarino, Federico Pugliese, Tullio Cavattoni, Guido Busca, and Paola Costamagna. A study on CO_2 methanation and steam methane reforming over commercial ni/calcium aluminate catalysts. *Energies*, 13(11):2792, 2020.

[166] Emmett D Goodman, Jay A Schwalbe, and Matteo Cargnello. Mechanistic understanding and the rational design of sinter-resistant heterogeneous catalysts. *ACS Catalysis*, 7(10):7156–7173, 2017.

[167] Juntian Niu, Yalan Wang, Yanying Qi, Anh H Dam, Hongmin Wang, Yi-An Zhu, Anders Holmen, Jingyu Ran, and De Chen. New mechanism insights into methane steam reforming on pt/ni from dft and experimental kinetic study. *Fuel*, 266:117143, 2020.

[168] Agustín Salcedo, Pablo G Lustemberg, Ning Rui, Robert M Palomino, Zongyuan Liu, Slavomir Nemsak, Sanjaya D Senanayake, José A Rodriguez, M Verónica Ganduglia-Pirovano, and Beatriz Irigoyen. Reaction pathway for coke-free methane steam reforming on a Ni/CeO_2 catalyst: active sites and the role of metal–support interactions. *ACS Catalysis*, 11(13):8327–8337, 2021.

[169] Reto Strobel, Frank Krumeich, Wendelin J Stark, Sotiris E Pratsinis, and Alfons Baiker. Flame spray synthesis of Pd/Al_2O_3 catalysts and their behavior in enantioselective hydrogenation. *Journal of Catalysis*, 222(2):307–314, 2004.

[170] Giulia Baracchini. *Optimization of Layered Bifunctional Catalytic Systems for One-step Synthesis of Dimethyl Ether*. PhD thesis, Karlsruher Institut für Technologie (KIT), 2020.

[171] Jose M Gatica, Richard T Baker, Paolo Fornasiero, Serafin Bernal, Ginesa Blanco, and Jan Kašpar. Rhodium dispersion in a $Rh/Ce_{0.68}Zr_{0.32}O_2$ catalyst investigated by HRTEM and H_2 chemisorption. *The Journal of Physical Chemistry B*, 104(19):4667–4672, 2000.

[172] Katarina Persson, Lisa D Pfefferle, William Schwartz, Anders Ersson, and Sven G Järås. Stability of palladium-based catalysts during catalytic combustion of methane: The influence of water. *Applied Catalysis B: Environmental*, 74(3-4):242–250, 2007.

[173] Reto Strobel, Sotiris E Pratsinis, and Alfons Baiker. Flame-made $Pd/La_2O_3/Al_2O_3$ nanoparticles: thermal stability and catalytic behavior in methane combustion. *Journal of Materials Chemistry*, 15(5):605–610, 2005.

[174] Wenjie Qi, Jingyu Ran, Ruirui Wang, Xuesen Du, Jun Shi, Juntian Niu, Peng Zhang, and Mingchu Ran. Kinetic consequences of methane combustion on Pd, Pt and Pd-Pt catalysts. *RSC advances*, 6(111):109834–109845, 2016.

[175] Kenneth SW Sing. Reporting physisorption data for gas/solid systems with special reference to the determination of surface area and porosity (recommendations 1984). *Pure and Applied Chemistry*, 57(4):603–619, 1985.

[176] Shaoping Wei, Yitong Zhao, Guoli Fan, Lan Yang, and Feng Li. Structure-dependent selective hydrogenation of cinnamaldehyde over high-surface-area $CeO_2 - ZrO_2$ composites supported Pt nanoparticles. *Chemical Engineering Journal*, 322:234–245, 2017.

[177] Jaekyeong Yoo, Seungwon Park, Ji Hwan Song, Sangbeom Yoo, and In Kyu Song. Hydrogen production by steam reforming of natural gas over butyric acid-assisted nickel/alumina catalyst. *International Journal of Hydrogen Energy*, 42(47):28377–28385, 2017.

[178] A Mileva, G Issa, J Henych, V Štengl, D Kovacheva, and T Tsoncheva. CeO_2 and TiO_2 obtained by urea assisted homogeneous hydrolyses method as catalysts for environmental protection: Effect of Ti/Ce ratio. *BULGARIAN CHEMICAL COMMUNICATIONS*, 49:77–83, 2017.

[179] Zeid A ALOthman. A review: fundamental aspects of silicate mesoporous materials. *Materials*, 5(12):2874–2902, 2012.

[180] Yanet Piña-Pérez, Francisco Tzompantzi-Morales, Raúl Pérez-Hernández, Rubén Arroyo-Murillo, Próspero Acevedo-Peña, and Ricardo Gómez-Romero. Photocatalytic activity of Al_2O_3 improved by the addition of Ce^{3+}/Ce^{4+} synthesized by the sol-gel method. photodegradation of phenolic compounds using uv light. *Fuel*, 198:11–21, 2017.

[181] David E Motaung, Gugu H Mhlongo, Peter R Makgwane, Baban P Dhonge, Franscious R Cummings, Hendrik C Swart, and Suprakas Sinha Ray. Ultra-high sensitive and selective H_2 gas sensor manifested by interface of n–n heterostructure of $CeO_2 - SnO_2$ nanoparticles. *Sensors and Actuators B: Chemical*, 254:984–995, 2018.

[182] Mahendra R Somalu, Andanastuti Muchtar, Wan Ramli Wan Daud, and Nigel P Brandon. Screen-printing inks for the fabrication of solid oxide fuel cell films: A review. *Renewable and Sustainable Energy Reviews*, 75:426–439, 2017.

[183] Hung-Wen Lin, Chang-Pin Chang, Wen-Hwa Hwu, and Ming-Der Ger. The rheological behaviors of screen-printing pastes. *Journal of Materials Processing Technology*, 197(1-3):284–291, 2008.

[184] O Görke, P Pfeifer, and K Schubert. Kinetic study of ethanol reforming in a microreactor. *Applied Catalysis A: General*, 360(2):232–241, 2009.

[185] Katarina Persson, Anders Ersson, K Jansson, N Iverlund, and Sven Järås. Influence of co-metals on bimetallic palladium catalysts for methane combustion. *Journal of Catalysis*, 231(1):139–150, 2005.

[186] Kohji Narui, Hirohide Yata, Keiichi Furuta, Akio Nishida, Yasuhiko Kohtoku, and Tokuo Matsuzaki. Effects of addition of Pt to PdO/Al_2O_3 catalyst on catalytic activity for methane combustion and tem observations of supported particles. *Applied Catalysis A: General*, 179(1-2):165–173, 1999.

[187] Shuwu Yang, A Maroto-Valiente, M Benito-Gonzalez, I Rodriguez-Ramos, and A Guerrero-Ruiz. Methane combustion over supported palladium catalysts: I. reactivity and active phase. *Applied Catalysis B: Environmental*, 28(3-4):223–233, 2000.

[188] Anders Ersson, Henrik Kušar, Richard Carroni, Timothy Griffin, and Sven Järås. Catalytic combustion of methane over bimetallic catalysts a comparison between a novel annular reactor and a high-pressure reactor. *Catalysis Today*, 83(1-4):265–277, 2003.

[189] CF Cullis, TG Nevell, and DL Trimm. Role of the catalyst support in the oxidation of methane over palladium. *Journal of the Chemical Society, Faraday Transactions 1: Physical Chemistry in Condensed Phases*, 68:1406–1412, 1972.

[190] RFFJ Burch, FJ Urbano, and PK Loader. Methane combustion over palladium catalysts: The effect of carbon dioxide and water on activity. *Applied Catalysis A: General*, 123(1):173–184, 1995.

[191] R Burch, PK Loader, and FJ Urbano. Some aspects of hydrocarbon activation on platinum group metal combustion catalysts. *Catalysis today*, 27(1-2):243–248, 1996.

[192] JC Van Giezen, FR Van den Berg, JL Kleinen, AJ Van Dillen, and JW Geus. The effect of water on the activity of supported palladium catalysts in the catalytic combustion of methane. *Catalysis Today*, 47(1-4):287–293, 1999.

[193] Dragos Ciuparu, Nikolaos Katsikis, and Lisa Pfefferle. Temperature and time dependence of the water inhibition effect on supported palladium catalyst for methane combustion. *Applied Catalysis A: General*, 216(1-2):209–215, 2001.

[194] Dragos Ciuparu, Emily Perkins, and Lisa Pfefferle. In situ dr-ftir investigation of surface hydroxyls on $\gamma - Al_2O_3$ supported PdO catalysts during methane combustion. *Applied Catalysis A: General*, 263(2):145–153, 2004.

[195] TE Hoost and K Otto. Temperature-programmed study of the oxidation of palladium/alumina catalysts and their lanthanum modification. *Applied Catalysis A: General*, 92(1):39–58, 1992.

[196] MH Halabi, MHJM De Croon, J Van der Schaaf, PD Cobden, and JC Schouten. Low temperature catalytic methane steam reforming over ceria–zirconia supported rhodium. *Applied Catalysis A: General*, 389(1-2):68–79, 2010.

[197] Yueh-Heng Li, Guan-Bang Chen, Hung-Wei Hsu, and Yei-Chin Chao. Enhancement of methane combustion in microchannels: effects of catalyst segmentation and cavities. *Chemical Engineering Journal*, 160(2):715–722, 2010.

[198] MARIA ANNA Murmura, M Diana, R Spera, and Maria Cristina Annesini. Modeling of autothermal methane steam reforming: Comparison of reactor configurations. *Chemical Engineering and Processing-Process Intensification*, 109:125–135, 2016.

[199] Nicolaas Engelbrecht, Raymond C Everson, Dmitri Bessarabov, and Gunther Kolb. Microchannel reactor heat-exchangers: A review of design strategies for the effective thermal coupling of gas phase reactions. *Chemical Engineering and Processing-Process Intensification*, 157:108164, 2020.

[200] Bruce E Poling, John M Prausnitz, and John P O'connell. *Properties of gases and liquids*. McGraw-Hill Education, 2001.

[201] R.B. Bird, W.E. Stewart, and E.N. Lightfoot. *Transport Phenomena*. J. Wiley, 2002.

[202] Jacob Bear and Carol Braester. On the flow of two immscible fluids in fractured porous media. In *Developments in soil science*, volume 2, pages 177–202. Elsevier, 1972.

[203] Ronald G Munro. Evaluated material properties for a sintered alpha-alumina. *Journal of the American Ceramic Society*, 80(8):1919–1928, 1997.

[204] Bernhard Tjaden, Samuel J Cooper, Daniel JL Brett, Denis Kramer, and Paul R Shearing. On the origin and application of the bruggeman correlation for analysing transport phenomena in electrochemical systems. *Current Opinion in Chemical Engineering*, 12:44–51, 2016.

[205] T Boeltken, A Wunsch, T Gietzelt, P Pfeifer, and R Dittmeyer. Ultra-compact microstructured methane steam reformer with integrated palladium membrane for on-site production of pure hydrogen: Experimental demonstration. *International journal of hydrogen energy*, 39(31):18058–18068, 2014.

[206] M Arsalan Ashraf, Oihane Sanz, Mario Montes, and Stefania Specchia. Insights into the effect of catalyst loading on methane steam reforming and controlling regime for metallic catalytic monoliths. *International Journal of Hydrogen Energy*, 43(26):11778–11792, 2018.

[207] Norbert Kockmann. *Transport phenomena in micro process engineering*. Springer Science & Business Media, 2007.

[208] Divesh Bhatia, Robert W McCabe, Michael P Harold, and Vemuri Balakotaiah. Experimental and kinetic study of NO oxidation on model Pt catalysts. *Journal of Catalysis*, 266(1):106–119, 2009.

[209] Pranit S Metkar, Nelson Salazar, Rachel Muncrief, Vemuri Balakotaiah, and Michael P Harold. Selective catalytic reduction of NO with NH_3 on iron zeolite monolithic catalysts: Steady-state and transient kinetics. *Applied Catalysis B: Environmental*, 104(1-2):110–126, 2011.

[210] Saurabh Y Joshi, Michael P Harold, and Vemuri Balakotaiah. On the use of internal mass transfer coefficients in modeling of diffusion and reaction in catalytic monoliths. *Chemical Engineering Science*, 64(23):4976–4991, 2009.

[211] Mamadou Mbodji, Jean-Marc Commenge, and Laurent Falk. Preliminary design and simulation of a microstructured reactor for production of synthesis gas by steam methane reforming. *Chemical Engineering Research and Design*, 92(9):1728–1739, 2014.

[212] Donald A Nield, Adrian Bejan, et al. *Convection in porous media*, volume 3. Springer, 2006.

[213] Lihua Shen and Zhangxin Chen. Critical review of the impact of tortuosity on diffusion. *Chemical Engineering Science*, 62(14):3748–3755, 2007.

[214] AY Tonkovich, Steve Perry, Yong Wang, Dongming Qiu, T LaPlante, and William A Rogers. Microchannel process technology for compact methane steam reforming. *Chemical Engineering Science*, 59(22-23):4819–4824, 2004.

[215] Toshinori Tsuru, Koji Yamaguchi, Tomohisa Yoshioka, and Masashi Asaeda. Methane steam reforming by microporous catalytic membrane reactors. *AIChE journal*, 50(11):2794–2805, 2004.

[216] Dongxu Xie and Roland Dittmeyer. Correlations of laser scanning parameters and porous structure properties of permeable materials made by laser-beam powder-bed fusion. *Additive Manufacturing*, 47:102261, 2021.

[217] Milan Kundra, Tom Grall, Derrick Ng, Zongli Xie, and Christian H Hornung. Continuous flow hydrogenation of flavorings and fragrances using 3d-printed catalytic static mixers. *Industrial & Engineering Chemistry Research*, 60(5):1989–2002, 2021.

[218] Jie Liu, Yu Gao, Yanbin Fan, and Wei Zhou. Fabrication of porous metal by selective laser melting as catalyst support for hydrogen production microreactor. *International Journal of Hydrogen Energy*, 45(1):10–22, 2020.

[219] Flaviana Calignano, Tonia Tommasi, Diego Manfredi, and Alessandro Chiolerio. Additive manufacturing of a microbial fuel cell—a detailed study. *Scientific reports*, 5(1):1–10, 2015.

[220] Caterina Rizzi, Angelo Oreste Andrisano, Francesco Leali, Francesco Gherardini, Fabio Pini, and Alberto Vergnano. Design tools and methods in industrial engineering. In *Conference proceedings ADM*, page 14. Springer, 2019.

[221] Hanns Stoffregen, Jakob Fischer, Christian Siedelhofer, and Eberhard Abele. Selective laser melting of porous structures. In *Proceedings of the 22nd Annual International Solid Freeform Fabrication (SFF) Symposium*, pages 680–695, Austin, TX, 2011. University of Texas.

[222] Dongdong Gu and Yifu Shen. Processing conditions and microstructural features of porous 316L stainless steel components by DMLS. *Applied Surface Science*, 255(5):1880–1887, 2008.

[223] Igor Yadroitsev, I. Shishkovsky, Ph. Bertrand, and Igor Smurov. Manufacturing of fine-structured 3D porous filter elements by selective laser melting. *Applied Surface Science*, 255(10):5523–5527, 2009.

[224] Christoph Klahn. *Laseradditiv gefertigte, luftdurchlässige Mesostrukturen: Herstellung und Eigenschaften für die Anwendung*. Light Engineering für die Praxis. Springer, Berlin and Heidelberg, 2015.

[225] Christoph Klahn and Mirko Meboldt. Integration of gas-permeable structures in laser additive manufactured products. In T. S. Srivatsan and T. S. Sudarshan, editors, *Additive manufacturing: Innovations, advances, and applications*, pages 285–310. CRC Press LLC, 2015.

[226] Dongxu Xie, Bernd Fränkle, Christoph Klahn, and Roland Dittmeyer. Fabrication of sectionally permeable components with curved surface by laser-beam powder-bed fusion. *Chemie Ingenieur Technik*, 94(7):983–992, 2022.

[227] Ruidi Li, Jnhui Liu, Yusheng Shi, Mingzhang Du, and Zhan Xie. 316L stainless steel with gradient porosity fabricated by selective laser melting. *Journal of Materials Engineering and Performance*, 19(5):666–671, 2010.

[228] Evren Yasa, Jan Deckers, Tom Craeghs, Mohsen Badrossamay, and Jean-Pierre Kruth. Investigation on occurance of elevated edges in selective laser melting. In *Proceedings of the 20th Annual International Solid Freeform Fabrication (SFF) Symposium*, pages 180–192, Austin, TX, 2009. University of Texas.

[229] Amal Charles, Ahmed Elkaseer, Umberto Paggi, Lore Thijs, Veit Hagenmeyer, and Steffen Scholz. Down-facing surfaces in laser powder bed fusion of Ti6Al4V: Effect of dross formation on dimensional accuracy and surface texture. *Additive Manufacturing*, 46:102148, 2021.

[230] Julian Ferchow, Manuel Biedermann, Pascal Müller, Bernhard Auchmann, André Brem, and Mirko Meboldt. Harnessing manufacturing elements to select local process parameters for metal additive manufacturing: A case study on a superconducting solenoid coil. *Additive Manufacturing*, 46:102140, 2021.

[231] Hussain Najmi, Eddy El-Tabach, Khaled Chetehouna, Nicolas Gascoin, and François Falempin. Effect of flow configuration on darcian and forchheimer permeabilities determination in a porous composite tube. *International Journal of Hydrogen Energy*, 41(1):316–323, 2016.

[232] Zhengwen Zeng and Reid Grigg. A criterion for non-darcy flow in porous media. *Transport in porous media*, 63(1):57–69, 2006.

[233] JP Martins, D Milton-Tayler, and HK Leung. The effects of non-darcy flow in propped hydraulic fractures. In *SPE Annual Technical Conference and Exhibition*, pages SPE–20709–MS. OnePetro, SPE, 1990.

[234] Majid Hassanizadeh and William G Gray. General conservation equations for multi-phase systems: 3. constitutive theory for porous media flow. *Advances in water resources*, 3(1):25–40, 1980.

[235] S Majid Hassanizadeh and William G Gray. High velocity flow in porous media. *Transport in porous media*, 2(6):521–531, 1987.

[236] I Saeki, H Konno, and R Furuichi. Initial oxidation of type 430 stainless steels with 0.09–0.9 Mn in $O_2 - N_2$ atmosphere at 1273 K. *Corrosion science*, 38(9):1595–1612, 1996.

[237] I Saeki, H Konno, R Furuichi, T Nakamura, K Mabuchi, and M Itoh. The effect of the oxidation atmosphere on the initial oxidation of type 430 stainless steel at 1273 K. *Corrosion Science*, 40(2-3):191–200, 1998.

[238] J Rufner, P Gannon, P White, M Deibert, S Teintze, R Smith, and H Chen. Oxidation behavior of stainless steel 430 and 441 at 800 °C in single (air/air) and dual atmosphere (air/hydrogen) exposures. *International Journal of Hydrogen Energy*, 33(4):1392–1398, 2008.

[239] RE Lobnig, HP Schmidt, K Hennesen, and HJ Grabke. Diffusion of cations in chromia layers grown on iron-base alloys. *Oxidation of Metals*, 37:81–93, 1992.

[240] ACS Sabioni, AM Huntz, LC Borges, and F Jomard. First study of manganese diffusion in Cr_2O_3 polycrystals and thin films by sims. *Philosophical Magazine*, 87(12):1921–1937, 2007.

[241] Neal J Magdefrau, Lei Chen, Ellen Y Sun, and Mark Aindow. Effects of alloy heat treatment on oxidation kinetics and scale morphology for Crofer 22 APU. *Journal of Power Sources*, 241:756–767, 2013.

[242] Sarah Krainer and Ulrich Hirn. Contact angle measurement on porous substrates: Effect of liquid absorption and drop size. *Colloids and Surfaces A: Physicochemical and Engineering Aspects*, 619:126503, 2021.

[243] Richard C Pattison, Forrest E Estep, and Michael Baldea. Pseudodistributed feed configurations for catalytic plate microchannel reactors. *Industrial & Engineering Chemistry Research*, 53(13):5028–5037, 2014.

[244] Han Wang, Guogang Yang, Shian Li, Qiuwan Shen, Zheng Li, and Biaojie Chen. Numerical study on the effect of discrete catalytic layer arrangement on methane steam reforming performance. *RSC Advances*, 11(5):2958–2967, 2021.

[245] Jason Keith. Equilibrium simulation of a methane steam reformer. *Michigan Technological University*, 2008.

[246] H Scott Fogler. *Elements of chemical reaction engineering*. Pearson Boston, 2020.

[247] Stephen Brunauer, Paul Hugh Emmett, and Edward Teller. Adsorption of gases in multimolecular layers. *Journal of the American chemical society*, 60(2):309–319, 1938.

[248] Niels van Vegten, Davide Ferri, Marek Maciejewski, Frank Krumeich, and Alfons Baiker. Structural properties of flame-made Rh/Al_2O_3 and catalytic behavior in chemoselective hydrogenation. *Journal of Catalysis*, 249(2):269–277, 2007.

[249] Completely Revised Second, Enlarged Edition, Gerhard Ertl, Helmuth Knözinger, Ferdi Schüth, Jens Weitkamp, and Wiley-VCH Verlag GmbH& Co KGaA. Handbook of heterogeneous catalysis, 2008.